Institut d'Estudis Espacials de Catalunya (IEEC)
Institut de Ciències de l'Espai (CSIC)
Universitat Politècnica de Catalunya (UPC)

Observation and interpretation of type IIb supernova explosions

by

Antonia Morales Garoffolo

A thesis submitted for the degree of

Doctor in Physics

Advisors:
Dr. Nancy Elias-Rosa
Prof.Dr. Jordi Isern
Tutor:
Prof.Dr. Eduardo Bravo

Barcelona, 2016

To my parents Pepe and Maria, for helping me to make this happen.

Contents

Abstract

Core-collapse supernovae (CC-SNe) explosions represent the final demise of massive stars. Among the various types, there is a group of relatively infrequent CC-SNe termed type IIb, which appear to be hybrids between normal type II SNe (those characterised by H emission) and type Ib (those that lack H features in their spectra but exhibit prominent He I lines). The nature of the stellar progenitors leading to type IIb SNe is currently unknown, although two channels are contemplated: single massive stars that have lost part of their outer envelope as a consequence of stellar winds, and massive stars that shed mass by Roche-Lobe overflow to a companion. The latter is in fact the favoured scenario for most of the objects observed up to now. In the majority of cases, when there are no direct progenitor detections, some hints about type IIb SN progenitors (e.g., initial mass) can be derived indirectly from the objects' light curves (LCs) and spectra. Motivated by the relatively few well-sampled observational datasets that exist up to date for type IIb SNe and the unknowns on their progenitors, we carried out extensive observations (mainly in the optical domain) for the young type IIb SNe 2011fu and 2013df. Both these SNe are particularly interesting because they show a first LC peak caused by shock breakout, followed by a secondary ^{56}Ni-decay-powered maximum. The analysis of the data for SNe 2011fu and 2013df points to precursors that seem to have been stars with large radii (of the order of 100 $R_\odot$), with low mass hydrogen envelopes (tenths of $M_\odot$), and relatively low initial masses (12–18 $M_\odot$), which could have formed part of interacting binary systems.

The nature of a third SN IIb candidate, OGLE-2013-SN-100, proved to be enigmatic. OGLE-2013-SN-100, shows a first peak in the LC, and other characteristics somewhat similar to those of type IIb SNe. However, after a deeper analysis, we conclude OGLE-2013-SN-100 is likely not a SN of type IIb. We provide an alternative possible explanation for this object, which implies a combination of a SN explosion and interaction of its ejecta with circumstellar-material.

SNe 2011fu and 2013df were included in a larger sample of type IIb SNe to carry out a comparative study of their observables and environment. Regarding the host galaxies, 90 % of the objects are located in giant ($r < -18$ mag) hosts. In addition, the SNe are about equally split in low star formation and high star formation rate spiral galaxies. Concerning the SN ultra-violet (UV), optical, and near-infrared

(NIR) LCs, we find a dispersion in both shape and brightness. Particularly, a few objects show a sharp declining early phase in the UV and double-peaked optical-NIR LCs. However, the absence of a first LC peak, in some of the cases, may be due to lack of early observations. In addition, we found dispersion in the evolution of the colour indices of the SNe, making the colour comparison method not suitable to estimate extinction toward a type IIb SN. In the optical domain, the study of the (secondary) peak brightness in the R band shows that low luminosity events could be uncommon and the average brightness of the sample is ~ -17.5 mag. As for the spectral properties, the SNe that show an early spike in their LCs exhibit blue, shallow-lined early-time spectra and arise from extended progenitors ($R \sim 100$ $R_{\odot}$). Additionally, while there is an overall resemblance of the measured ejecta velocities, there is also dispersion of equivalent widths, nebular line luminosities and ratios among all the objects that could indicate differences in the ionisation state of the ejecta and mixing. All in all, we find heterogeineity in the studied observables of the sample of type IIb SNe, which reflects the variety of their explosion parameters and progenitor properties.

Acknowledgements

This thesis was carried out thanks to financial support by the Institut de Estudis Espacials de Catalunya (IEEC). Additional resources were provided by the Spanish Ministry of Science and Innovation (MICINN) grant AYA2011-24704/ESP, and by the Spanish *Ministerio de Economía y Competitividad* (MINECO) grant ESP2013-41268-R.

"It takes a village to raise a child," and what a village has helped me through this 4-year adventure!

Thank you Nancy, ¡muchas gracias!, for dedicating part of your time to me and this thesis, even in complicated times and at long distances. Thank you so much for taking me along to discover some of the Chile-Argentina wonders of the world during our PESSTO break. I am so glad you conviced me to go! Moltes gràcies Jordi per haver-me donat l'oportunitat de treballar en l'ICE (CSIC-IEEC), i crec que he après a posar bé les afiliacions i tot. Thank you Eduardo for being the bridge to the UPC, and always being ready to help.

I would like to say thanks to all the people who have contributed with observations and/or models to this thesis. Unfortunately, there are too many names to include here. Without their help, this thesis would not have come to term.

I also want to thank the ICE research group to which I have belonged during these years. Thank you Margarita for your support, and for always making it easy to travel to do observations or go to congresses and stays, all of which have been a very important part of this thesis. Thank you Aldo, Baybars, and Martin for teaching me lots of new things at the Friday-group meetings, and making me a little less afraid to ask silly questions. Thank you Nataly for your help at the beginning of it all. And of course, thanks to the two shinning stars Laura and Nùria, always there to light the way. I sure am going to miss you ladies.

Thanks to Guadalupe, Isabel, and Josefa for their hard work taking care of the paper-work involving trips, etc. and being so nice about it. Thank you Josep Guerrero for not placing thumbtacks on my chair after all... Thank you also for the less important things, like taking care of Greta and making it always work even after the several transformations it has undergone during these years. Thank you Ana Maria Ortega for always being patient, kind, and extremely helpful.

Thank you to the Padova-Asiago Supernova Group for helping me with observations and giving me a lot of input throughout these years, and also for always welcoming me and making me feel part of the group during my stays at the Osservatorio.

Thanks a lot Massimo and Rubina for all your help and patience reviewing the thesis, and of course for your helpful comments.

Thank you cyber buddies for helping me survive the cyber. Although it is true that I abandoned you at one point, fortunately we were re-born into oxygen, light, and velociraptors, and re-united stronger and with new incorporations as the *ICE machines*. Thank you all for the special lunches and coffee breaks, you will all be dearly missed.

Another thank you goes to my friends the Chevalier Jesús de Vilallonga and his dame Katherine Slusher. Thanks for making everything easier, especially at the beginning, and also for the fun and delicious paellas, the end-of-May Gemini birthday parties, etc.

And then there is the architecture connection that lead me to Carmen and Javi and the great extra-curricular times we lived together. Thank you so much guys.

Thank you from the bottom of my heart to my dear Barcelona friends: Ale (+2), Ana, Choni, Giovanna, Rosanna, and Viviana. I feel so fortunate to have coincided with you and for having spent so many special and unforgettable moments together during these years. Thank you for each and everyone of them.

I simply do not have enough words to thank my family, for all they have done for me. I am so fortunate, that my parents not only have given me all their love and support during these years, but also have contributed directly to this thesis by reading it and editing the English. Thank you so much Maria and Pepe, you guys are amazing. This thesis is for and because of you. Thank you uncle Nicky, you are simply the best! Thanks Vincent and Juan Antonio for always believing in me. Thank you Joaquín, Maite, and their two little doves Itziar and Maitane, for always being able to make me smile.

And finally, the miracle. The girl from New Mexico/Utrera meets the engineer from Jerez de la Frontera (*donde las papas se comen enteras*) in Barcelona. If I had known you were here, I would have come sooner, to have the time of my life everyday by your side. Thank you Nacho for making me feel the luckiest girl in the Universe.

¡Garrote!

Barcelona, January 2016

List of Figures

List of Tables

List of Acronyms

ADC	Analog-to-digital Converter
ADU	Analog-to-digital Units
ASC	Asiago Supernova Catalogue
ATel	Astronomer's Telegram
CALIFA	Calar Alto Legacy Integral Field Area
CCD	Charged Coupled Device
CC-SN	Core-Collapse Supernova
CSIC	Consejo Superior de Investigaciones Científicas
CSM	Circumstellar Material
ESO	European Southern Observatory
FWHM	Full Width at Half Maximum
GELATO	GEneric cLAssification TOol
HST	Hubble Space Telescope
IAU	International Astronomical Union
ICE	Institut de Ciències de l'Espai
IEEC	Institut d'Estudis Espacials de Catalunya
IRAF	Image Reduction and Analysis Facility
JC	Johnson Cousins
JD	Julian Date
LBV	Luminous Blue Variable
LTE	Local Thermodynamic Equilibrium
LC	Light Curve

NASA	National Aeronautics and Space Administration
NED	NASA/IPAC Extragalactic Database
NIR	Near Infrared
PESSTO	Public ESO Spectroscopic Survey for Transient Objects
PSF	Point Spread Function
PTF	Palomar Transient Factory
QE	Quantum Efficiency
SDSS	Sloan Digital Sky Survey
SED	Spectral Energy Distribution
SE-SNe	Stripped-Envelope Supernovae
S/N	Signal-to-noise Ratio
SN	Supernova
SNe	Supernovae
SNID	Supernova Identification
SNR	Supernova Remnant
SNOOPY	SuperNOvaPhotometrY
UPC	Universitat Politècnica de Catalunya
UT	Universtal Time
UV	Ultraviolet
WD	White Dwarf
WISeREP	Weizmann Interactive Supernova data REPository
WR	Wolf-Rayet

Chapter 1

Introduction

A supernova (SN) is the explosive endpoint in the evolution of a star. The term supernova derives from the Latin *nova* (new; as Supernovae – SNe – appear to be new stars in the sky) and the prefix *super-* (above; indicating that SNe are brighter than *nova* explosions). SNe are interesting astrophysical objects from a variety of perspectives. For example, they drive galactic chemical evolution, since they return to the interstellar medium the chemical elements which were formed along the progenitor's life and in the SN explosion itself. SNe induce star formation, since the shock waves generated in their explosion heat and compress interstellar molecular clouds. They are very energetic extra-terrestrial particle accelerators, and probably originate cosmic rays. Moreover, they can be used as cosmological distance indicators, and to set constraints on the equation of state of Dark Energy. Together with the interest of studying individual SNe, due, for example, to the insight that they bring to stellar evolution theories, all of these facts have made SNe research of great interest over the years.

Possibly, the first supernova for which written reports exist is SN 185, which took place in the year AD 185 in the Milky Way Galaxy. Five other Galactic SNe are known to have exploded since: SN 1006 and SN 1054 both recorded by Chinese, Middle Eastern astronomers, and possibly native American Indians, SN 1572 (also coined Tycho's SN, since Tycho Brahe performed an extensive observational study of the object), SN 1604 (also known as Kepler's SN because Johannes Kepler observed it for over a year and published a book about its optical display), and lastly Cas A, thought to have exploded around the year 1680. All these historic SNe have been confirmed as such thanks to the observation of their SN-remnants (SNRs; ejecta expelled in a SN explosion which are presently interacting with circumstellar or interstellar material). Ancient reports about other candidate SNe exist; however, no SNRs have been located at the sites at which they supposedly took place. In Figure 1.1, we show an example of the SNR associated to SN 1054 observed at different wavelengths.

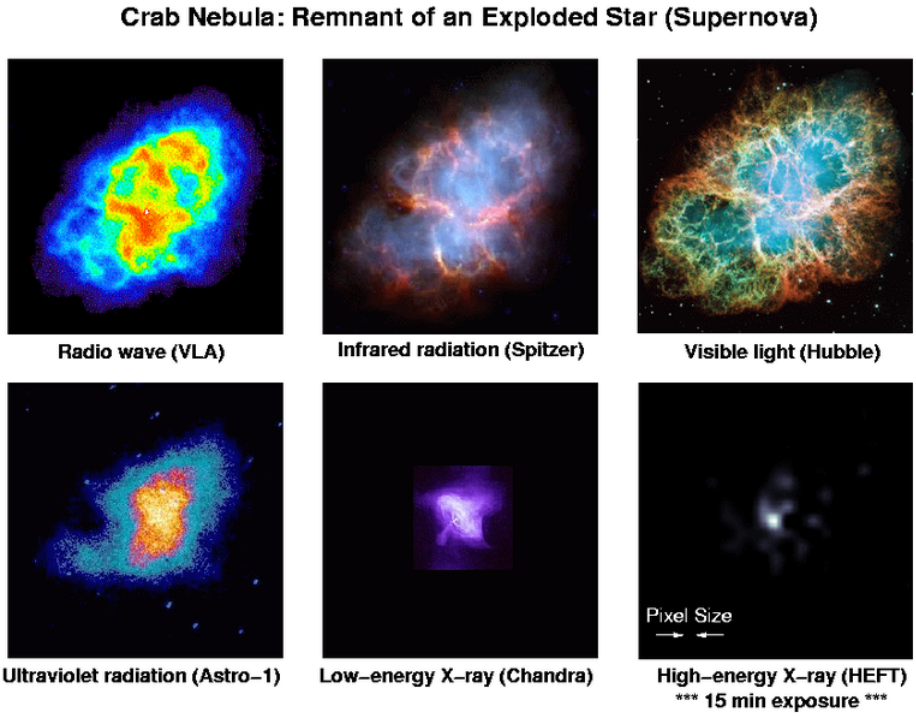

Figure 1.1: Crab Nebula (SNR associated to SN 1054) as observed at various wavelengths. Credit: The National Aeronautics and Space Administration (NASA).

The birth of modern SN astronomy occurred in 1885, when the first extra-Galactic SN (S Andromedae or SN 1885A[1]) was detected with a telescope, and its announcement in a telegram (Hartwig, 1885) led to follow-up observations by different astronomers around the world (see e.g., de Vaucouleurs & Corwin 1985).

In the 20$^{\text{th}}$ century, Walter Baade and Fritz Zwicky made important progress in the field of SN observations. They carried out the first regular supernova searches with the 18-inch Palomar Telescope (California, U.S.A.) between 1936 and 1941 and discovered 19 SNe. Spectroscopic SN observations soon reflected that there are at least two different types of SNe: those that show hydrogen lines in their spectra (type II) and those that do not (type I). This global classification, first proposed by Minkowski (1941) is actually the basis of the classification used today. By the 1960s more SNe had been discovered and Fritz Zwicky added types III, IV, and V that

[1]Note that historic SNe are named SN followed by the year in which they took place. From S Andromedae onward, the year in which they exploded is followed by capital letters in alphabetical order (i.e., SN 1885A was the first SN discovered in the year 1885), and once the alphabet has been completed, double lower case letters in alphabetical order are used (e.g. SN 2000aa, SN 2000ab, SN 2000ac, ..., SN 2000az, SN 2000ba, SN 2000bb, etc.). In addition, other notations are used associated to the different transient surveys that discover SNe.

consisted of a few individual SNe whose observational properties did not seem to fit in types I or II. Specifically, among these, and included in type V, was SN 1961V, whose spectral similarities to η Carinae still today pose the question of whether it was a genuine supernova or rather a transient related to a luminous blue variable (LBV) massive outburst.

In the 1980s type I SNe were further sub-categorised attending to the presence/absence of chemical elements other than hydrogen. For example, SNe with strong Si II lines in their spectra at around maximum light were named type Ia while those with and without prominent helium features were termed Ib and Ic, respectively. Currently, it is known that type Ia SNe arise from the thermonuclear runaway of an acreeting white dwarf (WD) while type Ib and Ic are core-collapse-SNe (CC-SNe) although their progenitors are massive stars that had lost their H or H plus He envelopes before explosion, respectively. Type II SNe are also believed to be CC-SNe whose progenitors have retained (at least part of) their outer envelopes before exploding (see the upper panel of Figure 1.2 for an example of SN spectroscopic classification of the main types). The sub-classification into type IIP (Plateau) and IIL (Linear) is done attending to light curve (LC) shape. While the former show a plateau after maximum light, the latter show LCs that decline linearly after peak (see the bottom panel of Figure 1.2). Type IIn (narrow) SNe, show narrow emission lines in their spectra indicative of ejecta-circumstellar-material (CSM) interaction. Type IIb SNe, the object of study of this thesis, are SNe whose spectra undergo a transition from being hydrogen-dominated at early phases in their evolution to resembling the spectra of type Ib SN (H-deficient) at later times. This traditional SN classification scheme is shown in Figure 1.3 (see e.g., Filippenko 1997 and Turatto 2003 for reviews on SN classification).

In the late eighties, SN 1987A, the closest ever extragalactic SN (at a distance of ~ 50 kpc in the Large Magellanic Cloud) was discovered and thoroughly observed in a wide range of the electromagnetic spectrum. For the first time ever, the neutrino signal from a SN was detected, and the progenitor directly identified in archival images (see e.g. Arnett et al. 1989 for a review). Due to the unusual behaviour of its LC (slow rise to maximum, faint, and broad LC), SN 1987A was termed a peculiar type II SN that did not fall into any of the traditional SN categories. Nowadays, a few SNe 1987A-like events have been further discovered and studied (see e.g. Taddia et al. 2012). As technology improves and SN observations continue to increase, additional new subclasses are being added to the traditional classification scheme. For example, broad-line SNe Ic, also known as hypernovae, show fast expanding ejecta (> 20000 km s^{-1}) and at times are associated to long duration gamma ray bursts or X-ray flashes (e.g. SN 1998bw; Galama et al. 1998). Type Ia SNe are now divided in several groups. One one hand, there have been discoveries of luminosity extremes with respect to normal type Ia SNe ($M_{\rm Vpeak} \sim -19$ mag), which yield two other types, overluminous (like SN 1991T, Filippenko et al. 1992b) and underluminous 91bg-like events (Filippenko et al., 1992a). Additionally, there are Ia-CSM SNe,

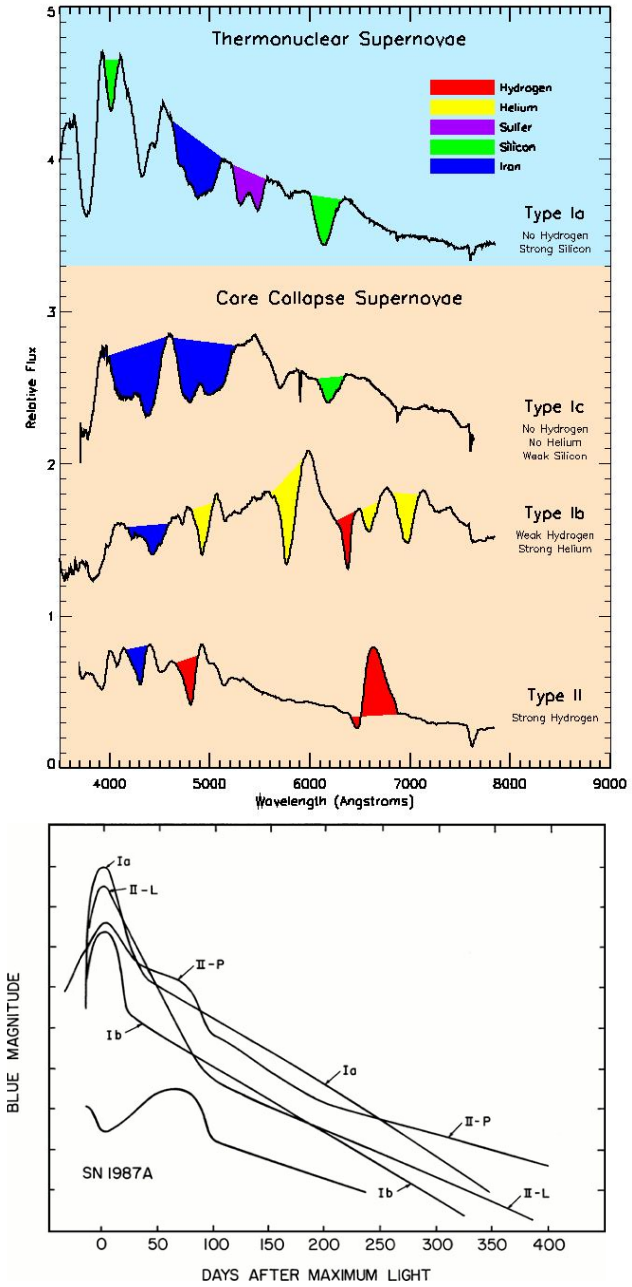

Figure 1.2: Top panel: Spectral identification of different SN types (from http://supernova.lbl.gov/∼dnkasen/tutorial/). Bottom panel: Schematic SN LCs for different SN types compared to that of SN 1987A (from Wheeler & Harkness 1990).

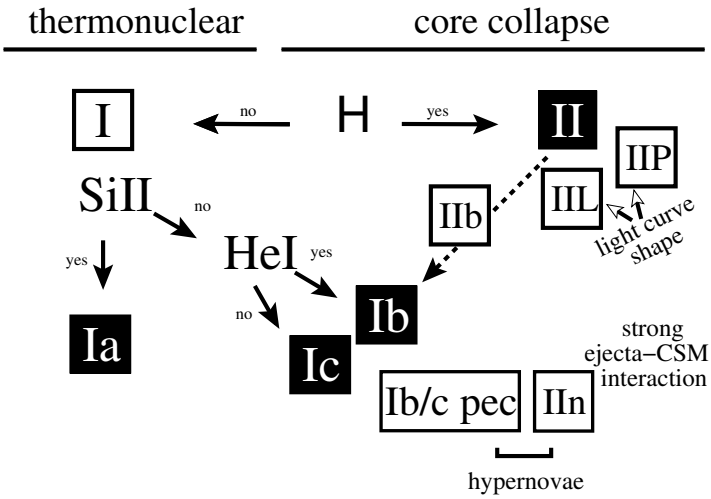

Figure 1.3: Traditional SN classification scheme based on the presence/absence of H, He, and Si in the SN spectra and the shape of their LCs (from Turatto 2003).

thermonuclear SNe whose ejecta interact with CSM causing the apparition of emission lines in their spectra (Hamuy et al., 2003). In the context of CC-SNe, Ibn SNe are believed to be SNe whose ejecta interact with helium-rich CSM, the prototype of such objects being SN 2006jc (Pastorello et al., 2007). Subluminious type IIP SNe represent another relatively rare group of the current SNe zoo (e.g. SN 1997D; Turatto et al. 1998). Other intriguing objects are Super-Luminous SNe (SL-SNe), which are considerably bright ($M_{\rm V}< -21$ mag). Some of these were first thought to arise from pair-instability explosions of very massive stars (SN 2007bi; Gal-Yam et al. 2009), while the LCs of others like PTF12dam could be powered by magnetars (Nicholl et al., 2013).

There is also a group of objects that sometimes challenge SN classifications since their spectra are similar to those of type IIn SNe, although they are in fact luminous stellar outbursts and not terminal SN explosions. These transients are named SN impostors (Van Dyk et al., 2000). One example of such a transient could be the above-mentioned SN 1961V.

The number of SNe discovered per year has dramatically increased with time, mainly due to the improvement of technology (the use of CCDs, etc.). For example, at the beginning of the 20th century about less than 20 SNe were discovered per year. By the beginning of the 21st century the number had increased to ~ 200, and currently, counting both those announced by the International Astronomical Union (IAU) and other channels, about ~ 1000 SNe are discovered per year (see Figure 1.4). In this context, other than the dedicated SN surveys (e.g. Catalina Real-Time Transient Survey – CRTS –, La Silla Quest – LSQ –), amateur astronomers have been of great help to the field.

Most likely, the current dedicated transient surveys will discover further variety among the known SN subclasses and possibly transients unknown up to now. This may continue to expand the current SN classification scheme presented above.

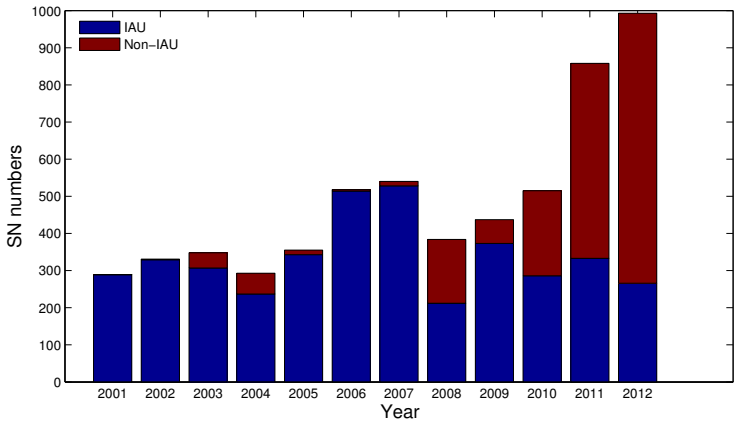

Figure 1.4: Number of SNe discovered per year during the 21st century. The objects in blue are those spectroscopically confirmed and reported by the IAU, and the ones in red are those distributed by other channels and in most cases not confirmed spectroscopically (from Gal-Yam et al. 2013).

1.1 CC-SNe observables

The observational and theoretical study of individual SNe over the whole range of the electromagnetic spectrum is of the utmost importance, for example, to assess the nature of the progenitors, their explosion parameters, their nucleosynthesis (as well as that produced by the explosion), and to probe late-time stellar evolution. In this context, it is of interest to collect photometric data to construct LCs and to obtain a spectral time series to evaluate the ejecta evolution. In this section, we briefly describe the mechanisms that power CC-SN LCs and the information that can be extracted from them, as well as the formation of SN spectra and some of the things that can be learned from them.

1.1.1 CC-SNe light curves

CC-SNe arise from the explosion of massive stars ($M > 8$ M$_\odot$; see e.g. Heger et al. 2003). During their evolution, these stars undergo nuclear fusion from H to heavier elements, up to the formation of an Fe core. At this point, the radiation pressure is not able to sustain the outer layers of the star, which start to collapse onto the core. During this process, electron captures onto protons take place, forming neutrons and

emitting neutrinos. The neutron degeneracy pressure halts the collapse of the outer stellar layers. A shock wave is formed and propagates outwards. During the passage of the shock wave through the stellar layers, explosive nucleosynthesis forms iron peak elements, one of the most important being ^{56}Ni. The shock wave suffers energy losses through the outward propagation and is halted before disrupting the star. An extra energy source is thus needed to further *push* the shock wave. However, the origin of this energy source is still under debate. One of the possibilities is that the neutrinos formed during the neutronization processes of the collapse provide this additional energy (Janka et al., 2007). Another option is that the extra pressure needed comes from core oscillation g-modes (Burrows et al., 2007). In any case, when the shock wave reaches the stellar surface, the electromagnetic display associated to the SN explosion begins, with a flash of soft X-rays and ultra-violet (UV) radiation that is known as shock breakout. For the type Ib SN 2008D, shock breakout was directly observed in the X-rays (Soderberg et al., 2008). In the optical and UV bands shock breakout signatures appear as an early and short-lasting spike in the SN LCs. Such signatures are rarely observed, although they are present in the LCs of two of the SNe studied in this thesis, namely SNe 2011fu and 2013df, as we discuss in Chapters 3 and 4.

Following shock breakout, SN ejecta adiabatically (and homologously $v \propto r$) expand and cool, which produces a drop in the LC, until the radioactive decay of the ^{56}Ni (to ^{56}Co) produced in the explosion becomes important and the luminosity starts to increase until reaching a peak. After this maximum the ejecta continue to expand and cool. In the case of type IIP SNe, this causes the H envelope to recombine. While the recombination wave moves inward through the ejecta, the temperature remains practically constant producing the plateau of the LC. Once all the hydrogen has recombined, the LC declines at the rate of the decay of ^{56}Co$\rightarrow^{56}$Fe (0.0098 mag d^{-1}). For CC-SNe other than type IIP, after the radioactively powered peak the LC begins to drop and then settles to the ^{56}Co$\rightarrow^{56}$Fe exponential tail. At times later than $\sim$ 1000 d since explosion, other radioactive isotopes such as ^{57}Co and ^{44}Ti also contribute to the luminosity evolution of CC- SNe.

The formation of dust in the SN ejecta can affect the observed LC late-time decline rate, since dust grains may absorb optical photons and re-emit them in the near infrared (NIR), causing a steeper optical slope. In the case of SN 1987A, another effect, termed freeze out, was believed to take place at around 1000 days since explosion. This is thought to be caused by material that was ionised at explosion but recombined at a much longer time-scale than the ejecta expansion and possibly caused the slope of the LC tail to decrease (Leibundgut & Suntzeff, 2003).

In a CC-SN explosion a total energy of about 10^{53} erg is released, of which 99 % is carried away by neutrinos, 1 % is converted to ejecta kinetic energy, and 0.01 % becomes photons. From the radioactively powered bolometric LC, one can obtain not only the ejecta kinetic energy, but also the total ejected mass, and the mass of ^{56}Ni sythesised in the explosion. This may be done by semi-analytical

modelling (Arnett, 1982), according to which the mass of ^{56}Ni is related to the peak of the LC, and the kinetic energy (E_{51}) plus total ejected mass ($M_{\rm ej}$) are related to the LC width ($\tau_{\rm LC} \approx 8 M_{\rm ej}^{3/4} E_{51}^{-1/4}$). In Chapter 4 we use an analytical approach based on the simple model of Arnett (1982) to derive the explosion parameters of SN 2013df. Another method to obtain the physical parameters of SNe is to perform hydrodynamical modelling of the LCs (e.g. Blinnikov et al. 1998). We have used this approach to derive the parameters of SN 2011fu in Chapter 3.

1.1.2 SN spectra

SN spectral time series can be considered a scan through the SN ejecta. During the early phases of SN evolution, the ejecta are not completely transparent (photospheric phase) and only the outer layers of the ejecta are observed, but as the SN ejecta expand and cool, opacity drops and the inner layers of the matter expelled in the SN explosion are revealed (nebular phase). During the photospheric phase spectra are characterised by showing a thermal black-body continuum superposed by absorption and/or emission lines, often with P-Cygni profiles. In Figure 1.5 we show a sketch of the formation of such a profile. The shaded zone in the line of sight of the observer produces a blue shifted absorption, while the lightly shaded emission gives rise to the emission component centred at the rest wavelength of the chemical element to which it corresponds. The absorption component of the P-Cygni profile allows the measurement of the velocity of the region at which the line predominantly forms through the Doppler effect.

During the nebular phase the spectra are dominated by forbidden emission lines superposed on a faint continuum. The γ-rays produced by the radioactive decay of ^{56}Co undergo Compton scattering, which produces non-thermal electrons that induce atom and ion excitation followed by radiation emission that causes line formation. Nebular emission line profiles in SN spectra are of great interest, since they trace possible asymmetries of the line emitting regions or the radioactive source exciting the lines. The profile widths, on the other hand, are a measure of the radial extent of the emitting species.

For SNe with ejecta that interact with CSM, the spectra present a blue continuum with superposed narrow emission lines provoked by shock interaction emission. Broad emission lines due to the ionised SN ejecta can also be observed if the CSM is thin.

One way to analyse the kinematics of the SN ejecta and constrain progenitor masses of SNe is through the radiative-transport modelling of their ejecta to fit late-time spectra (e.g. Jerkstrand et al. 2012). We have performed such an analysis by comparing our late-time spectra of SN 2011fu to late-time spectral models in Chapter 3.

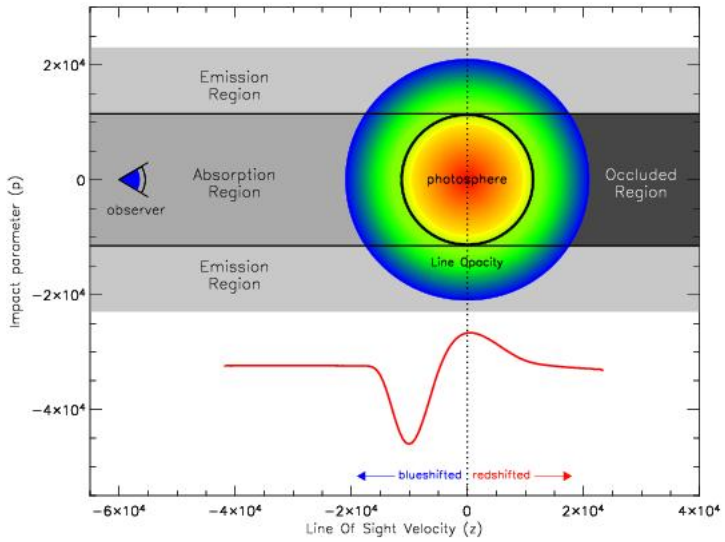

Figure 1.5: Sketch of a P-Cygni profile formation in SN ejecta. As the ejecta expand homologously, the absorption region in the line of sight of the observer produces a Doppler-shifted absorption component, and the emission region gives rise to the emission component centred at the rest wavelength. Credit: http://supernova.lbl.gov/∼dnkasen/tutorial/.

1.2 Type IIb SNe

SNe IIb are the subject of this thesis. They are hybrid objects that undergo a transition from being H-dominated at early phases of their spectral evolution to being He-dominated at later times. Type IIb SNe, along with types Ib and Ic, are many times referred to as stripped-envelope SNe (SE-SNe; Clocchiatti et al. 1996), since their progenitors are thought to have lost part of their H, practically their whole H, or their H and He envelopes before their terminal explosions as SNe, respectively. Two mechanisms have been proposed by which type IIb SN progenitors lose part of their H envelope before exploding, namely stripping by a close companion after Roche-Lobe overflow (e.g., Podsiadlowski et al. 1992), and wind-driven stellar mass loss in a single star (e.g., Heger et al. 2003).

Type IIb SNe are relatively rare objects. Their rate among a volume-limited sample of 81 type II SNe was estimated by Li et al. (2011) to be $11.9\,\%^{+3.9}_{-3.6}$ (see Figure 1.6). Since they are not very frequent objects, not very many of them have been extensively monitored.

One important issue that could potentially affect type IIb SN rates is possible mis-classifications. That is, a single epoch spectrum could lead to a wrong classification as a type Ib SN (Milisavljevic et al., 2013). On the other hand, there have been (ambiguous) hydrogen identifications in the spectra of some type Ib SNe, e.g.

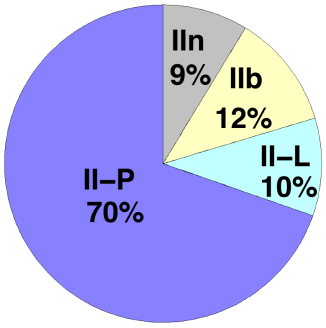

Figure 1.6: Type II SN rates from a volume-limited sample of 81 SNe (from Li et al. 2011).

SNe 2000H (Branch et al., 2002), 2008D (Soderberg et al., 2008), which poses the question of whether type IIb and Ib SNe are related to similar progenitors solely differentiated by H envelope mass. A recent study of a large dataset of SE-SN spectra (Liu et al., 2015) elucidates both of these questions. The spectral comparison of the samples of type IIb and Ib SNe shows that type IIb SNe exhibit systematically stronger (greater equivalent width; EW) Hα, a fact that can be used to differentiate between the two subtypes by using the comparison to the mean spectra produced in the study. This fact also confirms that the progenitors of SN of type IIb have more hydrogen than those of type Ib. Moreover, an observational overlap is found in most of the spectroscopic measurements performed (velocities and EWs), thus suggesting an observational continuum between both subclasses, which translates into a likely continuum of sizes or masses of the progenitors' hydrogen layers.

1.2.1 Individual studies

In this section we provide a summary of the main results of the analysis of the observational data for some individual type IIb SNe, including those for which there have been progenitor detections and/or about which individual studies have been carried out.

SN 1993J

The first type IIb SN to have shown a spectral transition from type II to type Ib-like spectra was SN 1987K (Filippenko, 1988). However, the SN that for years has been considered the prototype of the subclass is the well-observed SN 1993J (Filippenko et al., 1994; Richmond et al., 1994), which in fact is one of the best studied CC-SNe to date. SN 1993J took place in M81, at a distance of $\sim$ 3.6 Mpc from the Milky Way. The object has been extensively followed-up at different wavelengths. Its optical-NIR bolometric LC shows a fast rise to an early peak followed by a rapid decline, thought to be the consequence of the cooling of the progenitor's stellar envelope after shock

breakout. Subsequently, it presented a secondary maximum attributed to input from the radioactive decay of ^{56}Ni (e.g. Nomoto et al. 1993; Podsiadlowski et al. 1993; Woosley et al. 1994). Some of the models used to reproduce the SN LC invoked the explosion of a star that had lost part of its hydrogen envelope due to stripping by a binary companion (e.g. Woosley et al. 1994). A K-type supergiant star at the position of SN 1993J was detected in archival images (Aldering et al., 1994), and Maund & Smartt (2009) claimed its disappearance, confirming that it was the SN progenitor. Moreover, Maund et al. (2004) detected signatures of the possible hot blue companion star of the progenitor of SN 1993J in near UV spectra, and recent spectroscopic observations of the SN field (Fox et al., 2014) further reveal the likely contribution of a hot B-type star and the SN, thus supporting the nowadays-accepted binary system progenitor scenario for SN 1993J.

Regarding the optical spectroscopic observations, other than a clear transition from type II to type Ib-like SN spectra (see e.g. Barbon et al. 1995), SN 1993J showed evidence of clumpy ejecta (Matheson et al., 2000b) indicating asymmetries in the SN explosion, and at late times Hα emission features (Patat et al., 1995) reflecting the existence of a circumstellar hydrogen-rich shell interacting with the SN ejecta.

An extensive radio data analysis for SN 1993J is presented in Weiler et al. (2007).[2] The observations are well described by the interaction of the forward SN shock with a pre-SN shell. The X-ray LCs of SN 1993J (Zimmermann & Aschenbach, 2003) display a similar behaviour to the radio LCs, and both suggest there was an increase in mass loss rate $\sim$ 8000 yr before the SN explosion. A UV spectrum was obtained $\sim$ 19 d after explosion (Jeffery et al., 1994) with Hubble Space Telescope (HST). It recently has been modelled by Ben-Ami et al. (2015), and these authors suggest that the continuum flux excess that the spectrum exhibits and that the modelling does not account for has its origin above the SN photosphere caused by ejecta-CSM interaction.

SN 1996cb

SN 1996cb is a type IIb SN which was reasonably well observed in the optical (Qiu et al., 1999). It was discovered in NGC 3510 at a distance $\sim$ 9.7 Mpc from the Milky Way. The main observational difference between it and SN 1993J is the lack of the primary peak in the LC. The analysis of the observational data led Qiu et al. (1999) to invoke a stripped but more compact progenitor than for SN 1993J.

[2]Radio and X-ray data studies of CC-SNe provide unique information about the forward shock-CSM interaction. With them, one can trace the properties of the CSM and the progenitor's mass loss history, which in turn can help constrain the SN progenitor (see e.g., Weiler et al. 2002; Immler & Lewin 2003). SN radio LCs are characterised by a steep rise to a peak (reached first at higher frequencies), followed by a turnover to a declining phase. The multi-frequency radio LCs can be modelled, from which best LC fit parameters are obtained, and with these an estimate of the mass loss rate of the SN progenitor can be calculated (Sramek & Weiler, 2003).

Radio observations of this object show that the main difference with those of SN 1993J is that the LCs could have peaked at an earlier phase than SN 1993J (Van Dyk et al., 1996).

SN 2001gd

SN 2001gd is a SN for which practically only radio and X-ray observations exist (Pérez-Torres et al., 2005; Stockdale et al., 2007). The object was discovered after maximum light in NGC 5033 at a distance of ~ 17.2 Mpc. The radio and X-ray data suggest that the SN shock underwent CSM interaction. Pérez-Torres et al. (2005) suggest that the observed radio and X-ray properties are somewhat similar to those of SN 1993J.

SN 2001ig

SN 2001ig is another type IIb SN for which observational data at different wavelengths exist is SN 2001ig. This SN exploded in NGC 7424 at a distance of $\sim$ 13.1 Mpc. The analysis of optical spectra presented in Silverman et al. (2009) led to an estimate for the progenitor's initial mass: ~ 15 $M_\odot$. Radio observations showed modulations in the LCs (Ryder et al., 2004), which were proposed to have their origin in the progenitor's binary companion. In fact, the possible binary companion of the progenitor of SN 2001ig was found by Ryder et al. (2006). However, the modulations in the radio LCs can also be explained in terms of stellar variability prior to CC (Soderberg et al., 2006). Moreover, Kotak & Vink (2006) propose single LBVs undergoing S Doradus-type variations as possible progenitors of SNe like 2001ig which show radio LCs with quasi-periodical variations.

Analysis of UV spectra at ~ 11 and 19 d since explosion is presented in Ben-Ami et al. (2015). The spectra, contrary to that of SN 1993J, are line-dominated, and show no continuum flux excess.

SN 2003bg

SN 2003bg took place at a distance of $\sim$ 17.7 Mpc in ESO 420-G009. The SN LC lacked the first maximum present in the LC of SN 1993J (Hamuy et al., 2009). The object exhibited high luminosity and explosion kinetic energy (Mazzali et al., 2009), consistent with the parameters of a hypernova. The modelling of the late-time spectra constrained the progenitor initial mass to $\sim$ 20–25 $M_\odot$.

The radio properties of SN 2003bg are similar to those of SN 2001ig (Soderberg et al., 2006), with the LCs showing fluctuations interpreted as wind density variations caused by stellar variability before SN explosion. The average mass loss rate derived from the X-ray and radio observations is $\dot{M} = 3 \times 10^{-4}$ $M_\odot$ yr^{-1}, consistent with the mass loss rate of galactic Wolf-Rayet (WR) stars. However, there is no proposed mechanism for WR variability that could account for the radio LC variations, so S

Doradus-like variations of an LBV progenitor, as in the case of SN 2001ig, could be an alternative explanation (Kotak & Vink, 2006).

SN 2008ax

SN 2008ax is another example of a well-studied type IIb SN (see e.g., Pastorello et al. 2008; Taubenberger et al. 2011). This object exploded in NGC 4490, at a distance of $\sim$ 9.6 Mpc from the Milky Way. The progenitor was found in archival images (Li, 2008; Crockett et al., 2008), but there were multiple configurations that matched its observed colours. Two scenarios were proposed, one consisting of a single massive WR-like progenitor, and another based on a binary system. Recent modelling of SN 2008ax late-time nebular spectra by Jerkstrand et al. (2015) points to a progenitor not massive enough to have been a WR-like star. Moreover, recent observations of the SN field indicate that the light of the first identified progenitor candidate was contaminated by several identified nearby sources, which makes the plausible progenitor fainter and bluer than firstly measured (Folatelli et al., 2015). Thereby two new scenarios are contemplated: one involving a single star whose physical parameters are incompatible with a WR, and another invoking a binary system with modelled properties compatible with the observations.

The lack of an early spike in the LC of SN 2008ax (except for some residual cooling after a first maximum observed in the UV bands by Roming et al. 2009) is one of the main differences between SN 2008ax's observed LC and that of SN 1993J. Other than that, the LC shows a radioactively powered phase with similar timescales to those of SN 1993J. The spectra show a II$\rightarrow$Ib SN transition, and at late times Hα emission can be identified in the spectra, although it may not originate from ejecta-CSM interaction as speculated for SN 1993J (Taubenberger et al., 2011).

Early X-ray observations (Roming et al., 2009) reveal that the mass loss rate of SN 2008ax's progenitor was probably below that of SN 1993J ($\dot{M} = (9 \pm 3) \times 10^{-6}$ M$_\odot$ yr^{-1}). Additionally, the radio LC behaviour is somewhat different to that of SN 1993J, peaking at an earlier phase and exhibiting short-timescale modulations (5 to 10 d), which Roming et al. (2009) interpret as the progenitor being in a binary system, but could also be caused by stellar variability prior to explosion.

SN 2008bo

SN 2008bo, exploded in NGC 6643 at a distance of $\sim$ 21 Mpc. Its early spectra resembled those of SN 2008ax (Navasardyan et al., 2008), and late-time spectral analysis (Milisavljevic et al., 2010) further supported that the object was a type IIb SN. The SN was detected in radio and X-rays, specifically the radio properties showed a re-brightening as a possible consequence of CSM density variations (Stockdale et al., 2008), similarly to SNe 2001ig, 2003bg, and 2008ax.

SN 2010as

SN 2010as is another type IIb SNe for which there has been a possible progenitor detection, and for which a reasonable dataset exists (Folatelli et al., 2014b). This object was in principle classified as a transitional type Ib/c SN (SE-SNe whose He lines become prevalent with time). However, since it showed evidence of hydrogen in the early phases after discovery, which gradually disappeared, it is considered a type IIb event. Differently to SN 1993J, the LC does not show an early peak, hydrogen lines are weaker, and its He velocities show a peculiar *flat* evolution at early phases. A massive WR-like progenitor for SN 2010as is consistent with the observations in archival HST images ($M_{\mathrm{ZAMS}} \sim$ 28–29 $\mathrm{M}_{\odot}$). However, the hydrodynamical modelling of the observed LC implies an initial mass of $M_{\mathrm{ZAMS}} \sim 15\ \mathrm{M}_{\odot}$ for the progenitor. The apparent inconsistency between the two progenitor mass estimates can be solved if a binary system is the detected source at the SN position in the HST images.

SN 2010P

SN 2010P took place in Arp 299 at a distance of $\sim$ 45 Mpc. The NIR LCs of the object did not show any signs of a first peak (Kankare et al., 2014). The spectral evolution was not covered by observations, but a single optical spectrum of the SN showed it to be similar to e.g. SN 2008ax. The radio LC had a long rise to maximum ($\sim$ 100 d), as did that of e.g. SN 1993J (Romero-Cañizales et al., 2014).

SN 2011dh

SN 2011dh is an additional example of a very well monitored type IIb SN. This SN took place in M51 at a distance of $\sim$ 7.8 Mpc, and its yellow supergiant progenitor has been identified in archival images (Maund et al., 2011; Van Dyk et al., 2011) and confirmed to have disappeared after the SN explosion (Van Dyk et al., 2013). Extensive analysis of UV, optical, and NIR data is presented in Ergon et al. (2014). The LC showed a shock breakout cooling phase in the UV and g bands, which was missed in other bands. The hydrodynamical modelling of the observed LC leads to progenitor parameters consistent with those of the detected SN-precursor (Bersten et al., 2012). Nebular spectral modelling further constrains the SN progenitor initial mass to $\sim$ 12 $\mathrm{M}_{\odot}$, which supports a binary companion as the cause for the stripping of its outer envelope (Ergon et al., 2015; Jerkstrand et al., 2015). Furthermore, the modelling of a progenitor binary system is consistent with observations (Benvenuto et al., 2013), and there has been a likely detection of the stellar companion of the progenitor of SN 2011dh (Folatelli et al. 2014a; see also Maund et al. 2015).

A $\sim$ 24 d UV spectrum of SN 2011dh was modelled by Ben-Ami et al. (2015), which showed a less significant UV excess than that of SN 1993J. This was interpreted as a less significant SN ejecta-CSM interaction at an early phase. The radio data

follow the shock-CSM shell interaction scenario similarly to other CC-SNe, and the LCs peak at earlier phase than for SN 1993J (see e.g., Maeda 2012; Horesh et al. 2013). X-ray observations indicate that the progenitor's mass loss rate prior to explosion was $\sim 3 \times 10^{-6}$ $M_\odot$ yr^{-1}, smaller than for SN 1993J (Maeda et al., 2014).

SN 2011ei

This is another well-monitored type IIb SN, which occurred at a distance of $\sim$ 28.5 Mpc in NGC 6925. The analysis of the multi-wavelength observations presented in Milisavljevic et al. (2013) implies that the LC, as opposed to that of SN 1993J, did not show an early peak due to shock breakout cooling. The spectra metamorphose from type II to SN Ib-like in a relatively short timescale ($\sim$ 1 week). A progenitor's mass loss rate of $\dot{M} = 1.4 \times 10^{-5}$ $M_\odot$ yr^{-1} is estimated from radio and X-ray data analysis. The observations of the object are consistent with the explosion of a compact star ($\sim$ 1 $R_\odot$) with initial mass 10–15 $M_\odot$ embedded in a circumstellar wind.

SN 2011hs

SN 2011hs is another type IIb SN for which panchromatic observations have been obtained (Bufano et al., 2014). The LC showed a trace of cooling after shock breakout in the R band but was missed in the rest. The spectra show relatively broad lines indicative of high expansion velocities. The observations are consistent with the explosion of an extended star ($\sim$ 500–600 $R_\odot$) of initial mass $\sim$ 12–15 $M_\odot$.

The radio LC shows a peak luminosity similar to that of SN 1993J but the progenitor's mass loss rate seems to be higher.

SN 2013cu

SN 2013cu is another interesting type IIb object, since it was discovered very few hours after explosion (Gal-Yam et al., 2014). Although a WR wind-like spectrum was obtained for this SN few hours after explosion, recent work has shown that the progenitor star for SN 2013cu was unlikely a WR; instead a LBV or a yellow hypergiant undergoing an eruptive phase are compatible with the spectrum modelling (Groh, 2014; Shivvers et al., 2014; Smith et al., 2015).

1.2.2 Other major studies on type IIb SNe

Chevalier & Soderberg (2010) proposed that bright early luminosity from the shock-heated progenitor stellar envelope, low radio shell velocities, and thermal X-ray emission were characteristic of extended progenitors with $R \sim 100$ $R_\odot$, while compact progenitors with $R \sim 1$ $R_\odot$ had faint early optical LCs, had high radio shell velocities, and showed non-thermal X-ray emission. These authors proposed that SN 1993J

and 2001gd belonged to the extended category, while SN 1996cb, 2001ig, 2003bg, 2008ax, and 2008bo were part of the compact. However, SNe 2010P exhibits radio properties that can be attributed to an extended progenitor although its LC lacks a first early peak. On the contrary, both 2011dh, and 2011hs show radio properties that are in agreement with compact precursors even though the detection of the progenitor and/or modelling of the hydrodynamical LCs indicate opposite-wise. This possibly means that the relation between the radio properties of type IIb SNe and the extended versus compact nature of their progenitor stars may be more complicated than previously understood.

Recently, Ben-Ami et al. (2015), have proposed a correlation between a set of type IIb SNe observables and the SN progenitor properties and their environment. They suggest that the UV Spectral Energy Distribution (SED) shape is correlated with the ^{56}Ni mass synthesised in the SN explosion and that UV flux excess is correlated with a longer duration of cooling phase after shock breakout and slower radio shell velocities, which in turn implies the presence of greater CSM. However, these findings are limited by a small-sized SN sample.

Another recent study on type IIb SNe is that performed by Strotjohann et al. (2015), in which they investigate Palomar Transient Factory[3] (PTF) archival images in the search for progenitor eruptions prior to SN explosion. In their sample of 27 SNe, they solely found one possible outburst case, which leads them to conclude that bright precursor explosions are uncommon among type IIb SN progenitors.

1.3 Objectives and structure of the thesis

In view of the observational variety among type IIb SNe, an important question is which of the observed properties of SNe IIb can be connected with the characteristics of their progenitor systems. As we have indicated above, a few direct progenitor detections of type IIb SNe have been achieved over the course of time. However, even in these special cases, SN photometric and spectroscopic observations provide a method to constrain progenitor properties and investigate their nature as well as that of their environment. Ideally, it is convenient to have SN observations in all the electromagnetic spectrum wavelength range. However when this is not possible, observations in the optical and NIR wavelengths can provide very useful information.

Motivated by the relatively few well-sampled observational datasets that exist up to date for type IIb SNe and the unknowns on their progenitors/environment, the main goals of this thesis are, on one hand, to contribute to the small sample of well-studied objects by observationally characterising, in the optical and NIR, new IIb SNe candidates exploded during the course of the thesis. Tied to modelling, observational data can provide valuable clues about the individual properties of the SNe. On the other hand, we aim to perform a comparative study of our sample

[3] http://www.ptf.caltech.edu/

together with the published data of other type IIb objects in order to find possible correlations or differences among their individual properties and investigate what these can tell us about their progenitors.

Our sample of individual SNe consists of a total of three candidates, which after a deeper investigation revealed in two true IIb objects: SNe 2011fu and 2013df. The third candidate, OGLE-2013-SN-100, revealed more complex and we cannot certify that this peculiar object is a type IIb SN. Data acquisition for these three SNe was possible thanks to the New Technology Telescope-*Telescopio Nazionale Galileo* Large Program (NTT-TNG LP; P.I. Stefano Benetti), a scientific collaboration between many European Institutions; our own observational time at several telescopes such as the Liverpool Telescope (LT), the *Gran Telescopio Canarias* (GTC), and the *Telescopi Joan Oró* (TJO); and the Public European Southern Observatory Spectroscopic Survey of Transient Objects (PESSTO; see Appendix A). The literature SNe selected to perform the comparative study includes those SNe described in Section 1.2.1.

This thesis is structured in the following way:

- In **Chapter 2** we describe the observational data acquisition and processing techniques. Specifically, we present the characteristics of the set of telescopes and instruments used to observe SNe 2011fu, 2013df, and OGLE-2013-SN-100. We also delineate the data reduction techniques which are necessary to be performed before analysing the SN data.

- **Chapter 3** is dedicated to SN 2011fu. We first describe the distance and reddening adopted for the SN. Next, we show our photometric and spectroscopic observational results, which have been modelled in collaboration with other SN research groups.

- In **Chapter 4** we present SN 2013df. We begin with a description of the distance and reddening assumed for the object, secondly we exhibit the SN LCs and spectral time series and their analysis, among which is the modelling of the radioactively-powered phase of the SN LC thanks to an external collaboration. We then attempt to set constraints on the progenitor's properties by applying an analytical investigation of the early photometric data.

- The analysis of the observational data of the peculiar transient OGLE-2013-SN-100 is presented in **Chapter 5**. We start by expounding the distance and reddening supposed for the object. Next we present the dataset that we have collected for this object. Finally, we discuss possible scenarios that could be giving rise to the observed properties.

- **Chapter 6** is devoted to the comparison of observables of a sample of literature type IIb SNe along with SNe 2011fu and 2013df. We first investigate several

properties of the host galaxies of the objects (colours, and morphology), to next compare SN observables such as the UV, optical (R band), and NIR LCs and colours, and their optical spectra.

- The main conclusions of this thesis are discussed in **Chapter 7**.
- **Appendix A** describes PESSTO and my participation in the survey as an observer and data reducer, which has involved the classification of a number of transients.

Chapter 2

Data Acquisition and Processing

This chapter describes the processes of data acquisition, including the instruments used to collect the data, and the data processing techniques that were performed before analysing the observations of SNe 2011fu, 2013df and OGLE-2013-SN-100.

2.1 Data acquisition

In order to study SNe, both photometric and spectroscopic data are fundamental. With the former we can construct the objects' LCs that describe the overall emission energy evolution of the event, while the latter are useful to evaluate the time evolution of the main physical parameters of their ejecta. Ideally, the data should span from the generally fast-evolving early phases after explosion (when daily observations are aspired), to slower evolving phases after LC maxima (when observations can be carried out in a more relaxed manner), and up to the nebular phase when the ejecta are transparent and a few observations are sufficient. In general, the decision of observationally following-up a SN depends on the scientific objectives. In our project we were interested in type IIb SNe discovered soon after explosion with a large temporal range of visibility. Since it is important to have extended datasets, after deciding to follow-up an object, observational campaigns were coordinated, which made use of both our own observational time at different sites and that available to our collaborators around the world. Specifically, the follow-up of SN 2011fu was possible thanks to the NTT-TNG Large Program led by Stefano Benetti, which involved the cooperation of several European institutions. Collaboration with the Padova-Asiago SN group helped to complement the follow-up campaign of SN 2013df, and some of the visitor time available to the PESSTO survey at the NTT (see Appendix A) was used to collect OGLE-2013-SN-100 data.

2.2 Telescopes and instrumentation

A brief summary of the characteristics of the professional telescopes and instrumentation used for the data acquisition of the SNe described in Chapters 3, 4, and 5 is given below:

GTC + OSIRIS: The 10.4-m *Gran Telescopio de Canarias* (GTC) located on the island of La Palma at the *Roque de los Muchachos* Observatory (ORM; Spain) equipped with OSIRIS was used to obtain Sloan *gri* photometry and spectroscopy with grisms R300B R300R. OSIRIS consists of two 2048 × 4096 pixel Marconi Charged Coupled Devices (CCDs) 42–82 (with a 9.4″ gap between them), has a total field of view of 7′.8 × 8′.5 and a pixel scale of 0″.127 pix^{-1}. Its readout noise is 4.5 e$^-$ and gain 0.95 e$^-$/ADU. The spectral coverages of R300B and R300R are 3600–7200 Å and 4800–10000 Å respectively, while the resolving power for a reference wavelength of 6500 Å is ∼ 400 for both grisms.
http://www.gtc.iac.es/instruments/osiris/osiris.php

WHT + ACAM: The 4.2-m William Hershel Telescope (WHT) located at the ORM equipped with ACAM was used to obtain Sloan *griz* photometry and spectroscopy with grism V400. ACAM consists of a 2 k × 4 k pixel EEV CCD, has a field of view of 9′.0 × 10′.4 and a pixel scale of 0″.250 pix^{-1}. Its readout noise is 3.0 e$^-$ and gain 1.16 e$^-$/ADU. The spectral range of V400 is 3500–9400 Å and its resolving power for a reference wavelength of 6500 Å is 500.
http://www.ing.iac.es/Astronomy/instruments/acam/

WHT + ISIS: The WHT equipped with ISIS, which consists of a EEV12 of 4096 × 2048 (13.5 micron) pixels CCD, was used to obtain spectroscopy with the blue arm R300B and red arm R158R grisms. The R300B grism covers the range 3200–5300 Å and has a resolving power of ∼ 1000 for a reference wavelength of 5500 Å. The R158R grism was used along with the gg495 blocking filter and has a wavelength coverage of 5300–10000 Å, and a resolving power ∼ 1000 for a reference wavelength of 6500 Å.
http://www.ing.iac.es/Astronomy/instruments/isis/

NTT + EFOSC2: The 3.58-m NTT located at the *Observatorio de La Silla* (Chile) equipped with EFOSC2 was used to obtain Bessell *BVRI* photometry and spectroscopy with grisms 13 and 16. EFOSC2 is a Loral/Lesser, thinned, AR coated, UV flooded, MPP chip controlled by ESO-FIERA. Its size is 2048 × 2048 pixels, and it has a field of view of 30′ × 30′ and a pixel scale of 0″.24 pix^{-1}. Its readout noise is 7.8 e$^-$ and gain 0.9 e$^-$/ADU. Grism 13 covers a spectral range 3650–9250 Å and has a resolving power of ∼ 355, while grism 16 was used along with blocking filter OG530 and covers a spectral range of 6000–9995 Å and has a resolving power of 595

for a reference wavelength of 6500 Å.
http://www.eso.org/sci/facilities/lasilla/instruments/efosc/overview.html

TNG + DOLORES: The 3.58-m TNG located at the ORM equipped with DOLORES was used to obtain Bessell *UBVRI* photometry and spectroscopy with grisms LRB and LRR. DOLORES consists of a 2048 × 2048 pixel e2v 4240 Thinned back-illuminated, deep-depleted, Astro-BB coated CCD, has a field of view of $8'.6 \times 8'.6$ and a pixel scale of $0.''252$ pix^{-1}. Its readout noise is 9 e$^-$ and gain 0.97 e$^-$/ADU. The spectral ranges of LRB/R are 3000–8800 and 4470–10360 Å respectively, and both grisms have a resolving power of ~ 460 for a reference wavelength of 6500 Å.
http://www.tng.iac.es/instruments/lrs/

NOT + ALFOSC: The 2.5-m Nordic Optical Telescope (NOT) located at the ORM equipped with ALFOSC was used to obtain Bessell *UBVRI* photometry and spectroscopy with grisms 4 and 5. ALFOSC consists of a 2048 × 2048 pixel e2v nimo back illuminated CCD42-40, has a field of view of $6'.4 \times 6'.4$ and a pixel scale of $0''.190$ pix^{-1}. Its readout noise is 4.2 e$^-$ and gain 0.33 e$^-$/ADU. The spectral ranges of grisms 4 and 5 are 3200–9100 Å and 5000–10250 Å respectively, and the resolving power of both grisms for a reference wavelength of 6500 Å is ~ 500.
http://www.not.iac.es/instruments/detectors/CCD8/

CA2p2 + CAFOS: The 2.2-m telescope located at the *Observatorio Hispano Alemán de Calar Alto* (CAHA; Almería, Spain) equipped with CAFOS was used to obtain Bessell *UBVRI* photometry and spectroscopy with grisms B200, R200, and G200 (with blocking filter gg495). CAFOS consists of a 2048 × 2048 pixel SITe#1d CCD, has a field of view of $9' \times 9'$ and a pixel scale of $0''.53$ pix^{-1}. Its readout noise is 5.06 e$^-$ and gain 2.3 e$^-$/ADU. The spectral ranges of grisms B200, R200, and G200 are 3200–8000, 6300–11000, and 4800–9500 Å respectively, and the resolving power of the three grisms for a reference wavelength of 6500 Å is ~ 500.
https://www.caha.es/alises/cafos/cafos.html

FTN + EM01: The 2.0-m Faulkes Telescope North (FTN) located on Mt. Haleakala at the Manua Kea Observatories (Hawaii, U.S.A.) equipped with EM01 was used to obtain Bessel *BVRI* photometry. EM01 consists of a e2v 42–40 CCD which has a field of view of $4'.7 \times 4'.7$ and a pixel scale of $0''.278$ pix^{-1}. Its readout noise is 4.0 e$^-$ and gain 2.0 e$^-$/ADU.
http://lcogt.net/observatory/instruments/merope/

FTN + fs02: The FTN equipped with fs02 was used to obtain Bessel *BVRI* photometry. fs02 consists of a Fairchild CCD-486 which has a field of view of $10'.5 \times 10'.5$ and a pixel scale of $0''.304$ pix^{-1}. Its readout noise is 11.31 e$^-$ and gain 8.09 e$^-$/ADU.
http://lcogt.net/observatory/instruments/spectral/

LT + RATCam: The 2.0-m Liverpool Telescope (LT) located at the ORM equipped with RATCam was used to obtain Sloan *uriz* and Bessell BV photometry. RATCam consists of a 2048×2048 pixel EEV CCD42-40 and has a field of view of $4'.6 \times 4'.6$, and a pixel scale of $0''.135$ pix^{-1}. Its readout noise is 8 e$^-$ and gain 1.62 e$^-$/ADU.
http://telescope.livjm.ac.uk/TelInst/Inst/RATCam/

LT + IO:O: The LT equipped with IO:O was used to obtain Sloan *uri* and Bessell BV photometry. IO:O consists of a 4096×4112 pixel e2v CCD 231 and has a field of view of $10' \times 10'$, and a pixel scale of $0''.30$ pix^{-1}. Its readout noise is 5.0 e$^-$ and gain 2.2 e$^-$/ADU.
http://telescope.livjm.ac.uk/TelInst/Inst/IOO/

A1p82 + AFOSC: The Copernico 1.82-m telescope located on Mt. Ekar at the Asiago Observatory (Italy) equipped with AFOSC was used to obtain Bessell *UBVRi* photometry and spectroscopy with grisms 2, 4, and VPH6. AFOSC consists of a Tektronix TK1024 thinned back-illuminated 1024×1024 pixel CCD and has a field of view of $8'.1 \times 8'.1$ and a pixel scale of $0''.473$ pix^{-1}. Its readout noise is 7.06 e$^-$ and gain 2.73 e$^-$/ADU. The spectral range and resolving power (for a reference wavelength of 6500 Å) of grism 2 are 3720–10000 Å and $\sim$ 200 respectively, while grism 4 covers 3500 to 8450 Å and has a resolving power of 300, and VPH6 has a range of 4500–10000 Å and resolving power of 500.
http://archive.oapd.inaf.it/asiago/2000/2300/2310.html

TCS + CAIN-III: The 1.52-m Telescopio Carlos Sánchez (TCS) located at the *Observatorio del Teide* equipped with CAIN-III was used to obtain JHK_s photometry. CAIN consists of 256×256 pixel HgCdTe photoelectric elements (NICMOS 3 technology), it has a field of view of $4'.2 \times 4'.2$ and a pixel scale of $1''.00$ pix^{-1}. Its readout noise is 70 e$^-$ and gain 8.5 e$^-$/ADU.
http://www.iac.es/telescopes/pages/es/inicio/instrumentos/cain.php#1

WT + OGLE III: The 1.3-m Warsaw Telescope (WT) located at the *Observatorio de Las Campanas* (Chile) equipped with a 32 detector mosaic was used to obtain Bessell VI photometry. The detector consists of 32 thin e2v44-82 2048×4096 pixel CCD chips, has a field of view of $1.4^\circ \times 1.4^\circ$ and a pixel scale of $0''.26$ pix^{-1}. Its readout noise is 6.3 e$^-$ and gain 1.7 e$^-$/ADU.
http://ogle.astrouw.edu.pl/∼ogle/

A1p22 + B&C: The Galileo 1.22-m telescope located on Mt. Pennar at the Asiago Observatory (Italy) equipped with the Boller & Chivens spectrograph was used to obtain grism 300 spectroscopy, which is characterized by having a 300 lines mm^{-1} grating, a spectral range of 3350–7850 Å and a resolving power of 700 for a reference

wavelength of 6500 Å.
http://archive.oapd.inaf.it/asiago/7000/7200/7200.html

ASch + SCAM: The Schmidt 0.92-m telescope located on Mt. Ekar at the Asiago Observatory (Italy) equipped with SCAM was used to obtain Bessell *BVRI* photometry. SCAM consists of a LORAL thick front illuminated CCD sensor, which has a field of view of $48'.7 \times 48'.7$ and a pixel scale of $1.437''$ pix^{-1}. Its readout noise is 12 e$^-$ and gain 0.92 e$^-$/ADU.
http://archive.oapd.inaf.it/asiago/3000/3200.html

TJO + MEIA: The 0.82-m *Telescopi Joan Oró* (TJO) located at the *Observatori Astronómic del Montsec* (OAdM; Catalunya, Spain) equipped with MEIA was used to obtain Bessell *UBVRI* photometry. MEIA consists of a 2048 × 2048 pixel e2v CCD42-40-1-B, has a field of view of $12'.3 \times 12'.3$ and a pixel scale of $0''.13$ pix^{-1}. Its readout noise is 8.67 e$^-$ and gain 1.21 e$^-$/ADU.
http://www.oadm.cat/en/content/55/meia.htm

TED + ST9XE: The 0.6-m Esteve Duran Telescope (TED) located at the *Observatori Esteve Duran* in Seva (Catalunya, Spain) equipped with a ST9XE CCD was used to obtain Bessell *VI* photometry. ST9XE has a field of view of $11'.7 \times 11'.7$ and a pixel scale of $1''.370$ pix^{-1}. Its readout noise is 15 e$^-$ and gain 1.6 e$^-$/ADU.
http://astrogea.org/foed/oed.htm

OAC + ST8XE: The 0.4-m telescope located at the *Observatorio Astrofísico de Cantabria* (OAC) equipped with a ST8XE CCD was used to obtain Bessell *VRI* photometry. ST8XE has a field of view of $24'.0 \times 26'.0$ and a pixel scale of $0''.900$ pix^{-1}. Its readout noise is 15 e$^-$ and gain 2.63 e$^-$/ADU.
http://max.ifca.unican.es/OAC/

SWIFT + UVOT: The 0.3-m modified Ritchey-Chretien UV/optical telescope (UVOT) equipped with a micro channel plate intensified CCD (MIC) on board the *SWIFT* satellite obtained Bessell optical *UBV* and ultraviolet *UVW2*, *UVM2*, and *UVW1* photometry. MIC has a field of view of $17' \times 17'$ and a pixel scale of $0''.502$ pix^{-1}. Its readout noise is 0.0 e$^-$ and gain 1.0 e$^-$/ADU.
https://www.swift.psu.edu/uvot/

In addition to the photometry obtained at professional observatories, amateur astronomers supplied very useful early-time data for SNe 2011fu and 2013df. Below we summarize the photometry they have provided along with a brief description of the instrumentation they used to acquire it:

- SN 2011fu:
  - **Fabrizio Ciabattari** (F.C.) and **Enrico Mazzoni** (E.M.) from the Italian SNe search program (ISSP)[1] provided unfiltered images taken with a FLI Proline CCD (field of view of $20'.4 \times 19'.8$, pixel scale of $2''.32$ pix^{-1}), at the Newtonian Telescope (0.5 m) of the *Osservatorio di Monte Agliale*[2] (Lucca, Italy). The instrument they used has a quantum efficiency (QE) that peaks at an effective wavelength consistent with that of the R band.
  - **Xing Gao** provided unfiltered images taken with a QHY9 CCD (field of view of $25'.0 \times 19'.0$, pixel scale of $0''.450$ pix^{-1}) at a 0.36-m Celestron C14 telescope of the Xingming Observatory (China). The instrument reaches its maximum sensitivity at a wavelength consistent with the effective wavelength of the V band.
- SN 2013df:
  - **Fabrizio Ciabattari** from the ISSP provided an unfiltered image taken with the FLI Proline CCD at the Newtonian Telescope of the *Osservatorio di Monte Agliale*.
  - **Sauro Donati** (S.D.) provided an unfiltered image taken with a SBIG ST10 dual camera (field of view of $12'.4 \times 18'.4$, pixel scale of $1''.52$ pix^{-1}) with a Schmidt-Cassegrain Telescope (0.3 m) at San Vito (Lucca, Italy). The QE reaches its maximum at a wavelength consistent with the effective wavelength of the R band.
  - **Stan Howerton**[3] provided an unfiltered image taken with a KAF-6303 CCD (field of view of $37'.41 \times 24'.94$, pixel scale of $0''.73$ pix^{-1}) at the iTelescope.net T18 (0.32 m; Spain). The detector reaches its maximum QE at the V band.
  - **Stan Howerton** provided V images taken with a SBIG ST-10XME CCD camera (field of view of $40'.4 \times 60'$, pixel scale of $1''.65$ pix^{-1}) at the iTelescope.net T5 (0.25 m; New Mexico, USA).
  - **Koichi Itagaki**[4] provided an unfiltered image taken with a Bitran BT-214E CCD (KAF 1001E) (field of view of $28'.2 \times 28'.2$, pixel scale of $1''.65$ pix^{-1}) with a reflector telescope (0.5 m at f/6) at the Itagaki Astronomical Observatory (Japan).The QE of the detector peaks at the R band effective wavelength.

[1] http://italiansupernovae.org/
[2] http://www.oama.it/
[3] http://www.itelescope.net/
[4] http://www.k-itagaki.jp/

– **Norbert Schramm**[5] provided images taken with a Orion Star Shoot Pro V2 one shot colour camera (field of view of $66.5' \times 100'$, pixel scale of $1''.98$ pix^{-1}) at a Schmidt/Newtonian telescope (0.20 m; Oxford, U.S.A.). The colour camera has a filter colour array or Bayer mask that arranges the red, green, and blue response on each pixel of the CCD. Once each of the frames was divided into blue, green, and red images, they could be treated as B, V, and R data respectively.

2.3 Data reduction

The SN data reduction was performed within IRAF.[6] Specifically for the pre-reduction (Section 2.3.1) we made use of the *ccdproc* package, and the measurements of the instrumental photometry (Section 2.3.2) were done with SNOOPY,[7] a package intended to assist the process of obtaining SN light curves from multi-band data obtained at different sites. SNOOPY is based on a code written by F. Patat in 1996, was implemented in the IRAF environment by E. Cappellaro of the Padova-Asiago SN group in 2000, and has been recently upgraded to a set of Python/PyRAF scripts.

2.3.1 Data pre-reduction

Data pre-reduction is a preliminary process that is needed to correct the raw SN images from detector and telescope signatures. It consists of the following steps:

Bias subtraction. An offset, or bias level, is added to the signal read by the CCD to make sure that the Analog-to-digital Converter (ADC) does not receive negative values. The ADC examines the charge accumulated in a CCD pixel and converts it to a digital value that is proportional to the number of electrons by a factor known as the 'gain'. In practice, to correct for bias, several images (~ 10) are taken with the telescope shutter closed and with 0 s exposures, then a master bias is created from the combination of these and is subtracted from all the images. In this way statistics are improved, random noise is reduced, and cosmic rays removed.

Overscan correction. In principle, there can be bias level fluctuations over the night caused for example by temperature variations. To account for this, a part of the CCD consisting of several non-illuminated columns and/or rows is used as the 'overscan' region, used to determine the mean bias level to remove.

[5] http://njstargazer.org/

[6] Image reduction and Analysis Facility, a software system distributed by the National Optical Astronomy Observatories (NOAO).

[7] Cappellaro 2014, SNOOPY: http://sngroup.oapd.inaf.it/snoopy.html

Trimming. The overscan region and any other parts of the frames close to the edge that are not important for the scientific analysis, can be cut off after correcting for overscan.

Flatfielding. Vignetting of the telescope optics, spatial variations in the CCD coating and/or dust on the CCD or the filter can cause pixel-to-pixel variations of the CCD sensitivity. This can be corrected dividing the frames by a flat-field. For photometry, these are images obtained by exposing the CCD to a uniform source of light at the wavelength of interest which can be an illuminated screen inside the telescope dome (dome-flats) or a region of the sky at dawn or twilight (sky-flats). For spectroscopy, flat-fields are usually quartz continuum spectra. In practice, several flat-fields are obtained for each of the filters or grisms used to acquire the scientific data. As with the bias, the reason for the repeated exposures is to improve statistics and get rid of artefacts like cosmic rays or stars (in the case of sky-flats). All flat-fields are bias-subtracted, and overscan-corrected, and the ones corresponding to the same filters/grisms are median-combined. In the case of spectroscopy, an additional step is required before dividing the data, which consists in normalising the flat-field along the dispersion axis to get rid of large scale variations of the quartz continuum spectra and to retain only the pixel-to-pixel variations.

2.3.2 Photometry

Our SN photometric data consists of broad-band Bessel *UBVRI*, Sloan *ugriz*, and near infrared (NIR) *JHKs* images. In general, at early bright phases single exposures are sufficient in each of the optical bands, but at later times multiple and longer exposures are necessary in order to increase the photon statistics and remove cosmic rays and CCD defects, especially in the bluer bands. In the latter cases, the images corresponding to the same filters are aligned and combined to produce a single image of improved Signal-to-noise ratio (S/N) with respect to the single exposures.

In the case of the NIR photometry, dithered short multiple exposures in each band are always necessary due to the high background emission. CAINDR, a package in the IRAF environment developed by José A. Acosta Pulido and Rafael Barrena for the instrument CAIN at the TCS, was used for the data pre-reduction. The images of each specific filter are corrected for flat field, and bad pixels. Then background images are constructed by median-combining the dithered science frames without aligning them, and subsequently subtracted. Finally the scientific images corresponding to the same filter are combined taking into account the dithering pattern.

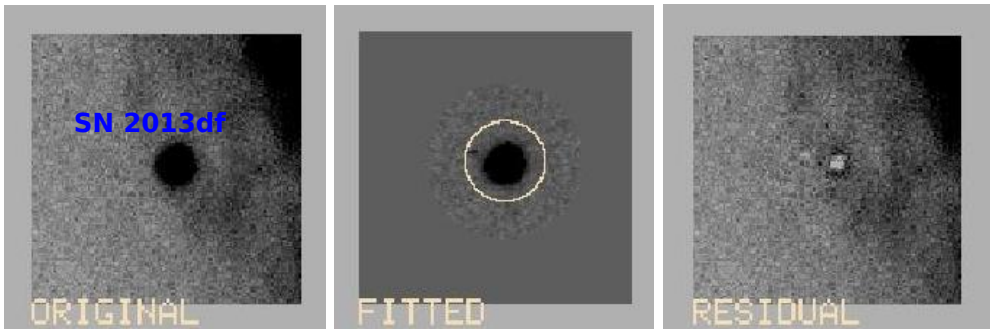

Figure 2.1: Example of the PSF fitting technique for SN 2013df: The left panel is the original image of a region around the SN position, the middle panel is the fitted profile after the background's contribution has been estimated with a low order polynomial, and the right panel represents the residual background.

Measurement of instrumental magnitudes

One of the main issues in determining SN magnitudes is differentiating the actual SN light from that of the underlying host galaxy. This can be especially difficult when the SN has faded and/or if it is located in a position of a complicated background (close to the galaxy nucleus, in a spiral arm, near an HII region, etc.). Depending on the situation, different approaches are applied to measure the SN photometry. When the SNe are bright and dominate over the background, the SN magnitudes are estimated by Point Spread Function (PSF)[8] fitting by means of SNOOPY, whereas in the cases in which the SNe have faded considerably and their signal is not clearly discernible from that of the background, the template-subtraction technique is used.

- **PSF-fitting technique**

  This process consists in constructing the PSF of unsaturated and isolated stars in the SN field, then the SN profile is obtained with a PSF scaled to match the stellar profile of the object. The background near the SN is determined by fitting low order polynomials to that region, and the SN instrumental magnitude is obtained as $-2.5\log(N_{\rm SN})$, where $N_{\rm SN}$ is the number of counts from the SN after subtracting the background. In Figure 2.1 we show an example of the utilisation of this approach in the case of SN 2013df (Chapter 4) in a phase near the minimum after first peak of the LC. Sometimes, like in this particular case, bright residuals may be left at the SN position.

- **Template subtraction**

[8]The PSF of a punctual astronomical object is an analytic two-dimensional function of the distribution of light from the source on the detector.

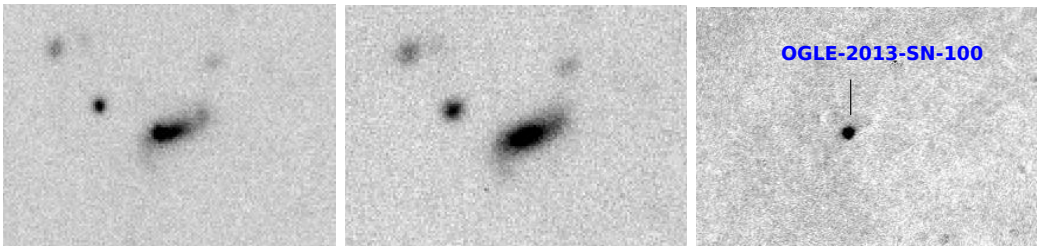

Figure 2.2: Example of the template subtraction technique for the transient OGLE-2013-SN-100. Left panel: Original R band image of the region around OGLE-2013-SN-100. Middle panel: R band template image for OGLE-2013-SN-100. Right panel: Resulting R band image of OGLE-2013-SN-100 after performing the template subtraction.

This method consists in eliminating the galactic contribution before taking the measurement of the instrumental magnitude of the SN. This method uses a template image taken before the SN explosion or at very late times when the SN has completely faded, which is then subtracted from the frames with the SN. Ideally, the SN images and the templates should be taken with the same instrument and under the same conditions, but usually this is not the case, and some additional steps must be taken before image subtraction. In practice, both the template and SN images are astrometrized and their seeing calculated. Then both images are registered, that is, corrected for pixel scale differences and rotation. Afterwards, the image with better seeing is manipulated to match the one with poorer seeing and both are calibrated to the same intensity. Once this is done, image subtraction can be performed. Specifically for this purpose SNOOPY makes use of HOTPANTS.[9] The resulting difference image should only contain the SN, but sometimes other variable objects, such as bad pixels or bad columns can appear as well. In any case, finally the instrumental magnitude of the SN is measured on the difference image by PSF fitting. An example of this method for OGLE-2013-SN-100 is shown in Figure 2.2. Although the template subtraction technique is the best choice to obtain SN instrumental magnitudes, it is not always applicable because of the lack of template images, filter mismatch between template and science frames, etc.

Both the PSF-fitting and template subtraction approaches have been used in this thesis. In the case of SN 2011fu (see Chapter 3), template subtraction was necessary for all the Bessell U and Sloan u data, since the SN was very faint in these bands. In the rest of the bands, we found differences below 0.1 mag between applying the PSF-fitting and the template subtraction before PSF-fitting, so the SN magnitudes were obtained directly by PSF-fitting. In the case of SN 2013df (see Chapter 4),

[9] http://www.astro.washington.edu/users/becker/v2.0/hotpants.html

we only did PSF-fitting since we did not have a template image at the time we performed the analysis of the object. Given the location of SN 2013df, in a spiral arm of its host and far from its nucleus in a zone where the background is smooth, the difference between applying or not template subtraction is likely < 0.1 mag as for SN 2011fu. Finally, for OGLE-2013-SN-100 (see Chapter 5), all magnitudes were obtained after doing the template subtraction, since the object was quite faint in all bands.

Basic calibration

In the first place, the instrumental magnitudes $m_{\lambda,\mathrm{ins}}$ in a filter λ, obtained with PSF-fitting or template subtraction, is scaled to a 1 s exposure (t_{exp}) and corrected for the atmospheric extinction (k_λ) of the site where the observation was obtained:

$$m'_\lambda = m_{\lambda,\mathrm{ins}} + 2.5\,\log(t_{\mathrm{exp}}) - k_\lambda\; z_{\mathrm{air}}, \tag{2.1}$$

where z_{air} is the airmass.

Given that each SN observation is unique, in order to make the most of all observations including those obtained under non-photometric conditions, the set of invariable, preferably isolated, non-saturated stars in the SN field used for the PSF fit are also used as local standards. In turn, these local standards are calibrated by means of the observation of Landolt fields (Landolt, 1992) and *ugriz* standards (Smith et al., 2002). These observations lead to a system of equations for the standards for each night and instrumental configuration:

$$m_\lambda^{\mathrm{stand}} - m_\lambda'^{\mathrm{stand}} = Zp_{\lambda\lambda^*} + ct_{\lambda\lambda^*}\;(m_\lambda^{\mathrm{stand}} - m_{\lambda^*}^{\mathrm{stand}}), \tag{2.2}$$

where $m_\lambda^{\mathrm{stand}}$ is the apparent magnitude of the standard, $m_\lambda'^{\mathrm{stand}}$ is the scaled instrumental magnitude (equation 2.1), $Zp_{\lambda\lambda^*}$ and $ct_{\lambda\lambda^*}$ are the zero point and colour term for the instrumental configuration, and λ, λ^* are two in general neighbouring bands. Once the zero points and colour terms are known, equation 2.2 can be applied to derive the apparent magnitudes of the local standards and the SN for each night and configuration. The mean value of the apparent magnitudes of the local standards obtained on photometric nights can then be used to calculate (if necessary) a shift to the zero points for the nights that are not photometric. These modified zero points are used to obtain the final calibrated SN photometry for the non-photometric nights.

For both SNe 2011fu and 2013df we have some unfiltered and colour amateur frames. All instrumental magnitudes of the SNe were obtained by PSF fit. As mentioned above, the Bayer-masked frames obtained for SN 2013df (see Section 2.2) were subdivided in blue, green, and red images. One of the main problems when doing this is that gaps result between the pixels of the images of the same

colour. To minimise this effect when deriving the instrumental magnitudes, we re-binned the images before performing the PSF fit. The magnitude calibration was done by re-scaling (taking into account the required zero points for the local standards) to B, V, and R band magnitudes those derived from the blue, green and red images respectively. The calibration of the unfiltered data was done re-scaling the magnitudes to V and R depending on the wavelength at which the detectors used reached their maximum sensitivity. Magnitudes of this type are affected by large errors.

Only in the case of SN 2011fu (Chapter 3) we have data in the NIR. The NIR instrumental magnitudes were obtained by PSF-fitting and the calibration was done in a slightly different manner than described above. Since some of the stars in the SN field were in the 2-MASS catalogue (Skrutskie et al., 2006), the SN data were calibrated with respect to these. That is, we obtained the instrumental magnitudes of those stars by PSF-fitting and then estimated transformation coefficients to the J,H, K_s bands by linearly interpolating the instrumental and the 2-MASS magnitudes of the local sequence.

In the case of SN 2013df (Chapter 4), in addition to the optical data obtained with on-ground telescopes, we made use of the publicly available optical UBV and Ultra-violet (UV) photometry obtained by *SWIFT*. The calibrated UVOT SN images were retrieved from the *SWIFT* data archive.[10] Estimates of the SN magnitudes were obtained by using the task *uvotsource* included in the *ftools* packages distributed by NASA's HEASARC. The task performs aperture photometry, corrected for the detector coincidence losses, integrating the flux in a user defined aperture. In the particular case to reduce the contamination by galaxy background, the SN magnitude was measured with a $3''$ aperture. We also measured, as reference, the magnitude of field stars with the same $3''$ aperture along with a $5''$ aperture. The reference stars were used to derive an aperture correction and, by including some of the local standards, were used to cross-check the photometric calibration for the optical bands obtained at other telescopes.

S-correction: Correction to standard photometric bands

The canonical way to calibrate magnitudes of objects with black-body SEDs is by using colour equations like 2.2. However, the use of these equations is not completely correct for SNe, especially in advanced phases in their evolution when their SEDs are line-dominated and can lead to significant scattering in the SN LCs if the photometric data are obtained with different instruments. The correction applied to the colour equation to calibrate SN magnitudes is called S-correction, and it was first introduced by Stritzinger et al. (2002) and Krisciunas et al. (2003), additional changes in the

[10] https://heasarc.gsfc.nasa.gov/cgi-bin/W3Browse/swift.pl

technique to calculate it were added by Pignata et al. (2004). Basically, the S-correction is a term which must be added to the colour equation in place of the colour term:

$$m_{\lambda}^{\mathrm{SN}} = m_{\lambda}^{\prime\,\mathrm{SN}} + Zp_{\lambda\lambda^*} + \delta S, \tag{2.3}$$

where $m_{\lambda}^{\mathrm{SN}}$ is the SN apparent magnitude, $m_{\lambda}^{\prime\,\mathrm{SN}}$ is its scaled instrumental magnitude, and δS is the S-correction, that depends on the SN SED and the difference between the used passband and the original passband of the system.

The basic idea underlying the S-correction is to synthetically compute SN magnitudes in an instrumental configuration and in a standard configuration, in our case the Bessel system. The difference between these two synthetically computed magnitudes is δS and can be expressed as

$$\delta S = m_{\mathrm{SN}}^{\mathrm{Bess}} - m_{\mathrm{SN}}^{\mathrm{ins}}, \tag{2.4}$$

where $m_{\mathrm{SN}}^{\mathrm{Bess}}$ is the SN apparent magnitude in the Bessell system (Bessell & Murphy, 2012) and $m_{\mathrm{SN}}^{\mathrm{ins}}$ in the instrumental system. The synthetically computed SN magnitudes in the Bessell and instrumental systems are given by

$$m_{\mathrm{SN}}^{\mathrm{Bess}} = -2.5 \log \frac{f_{\mathrm{SN}}^{\mathrm{Bess}}}{f_{\mathrm{Vega}}^{\mathrm{Bess}}}, \tag{2.5}$$

$$m_{\mathrm{SN}}^{\mathrm{ins}} = -2.5 \log \frac{f_{\mathrm{SN}}^{\mathrm{ins}}}{f_{\mathrm{Vega}}^{\mathrm{ins}}}. \tag{2.6}$$

$f_{\mathrm{Vega}}^{\mathrm{Bess}}$ is Vega's flux for a standard Bessell passband and is given by

$$f_{\mathrm{Vega}}^{\mathrm{Bess}} = \int_{\lambda_{\mathrm{min}}}^{\lambda_{\mathrm{max}}} M_{\mathrm{Bess}}(\lambda) Sp_{\mathrm{Vega}}(\lambda) d\lambda, \tag{2.7}$$

where $M_{\mathrm{Bess}}(\lambda)$ is one of the standard Bessell passbands ($M_{\mathrm{Bess}}(\lambda) = U, B, V, R, I$) and Sp_{Vega} is Vega's SED.

$f_{\mathrm{SN}}^{\mathrm{Bess}}$ is the SN flux for a standard Bessel passband:

$$f_{\mathrm{SN}}^{\mathrm{Bess}} = \int_{\lambda_{\mathrm{min}}}^{\lambda_{\mathrm{max}}} M_{\mathrm{Bess}}(\lambda) Sp_{\mathrm{SN}}(\lambda) d\lambda, \tag{2.8}$$

where $Sp_{\mathrm{SN}}(\lambda)$ is the SED of the SN.

The flux values of Vega ($f_{\mathrm{Vega}}^{\mathrm{ins}}$) and the SN ($f_{\mathrm{SN}}^{\mathrm{ins}}$) in the instrumental configuration are given by

$$f_{\mathrm{Vega}}^{\mathrm{ins}} = \int_{\lambda_{\mathrm{min}}}^{\lambda_{\mathrm{max}}} M_{\mathrm{ins}}(\lambda) Sp_{\mathrm{Vega}}(\lambda) d\lambda \tag{2.9}$$

and

$$f_{\rm SN}^{\rm ins} = \int_{\lambda_{\rm min}}^{\lambda_{\rm max}} M_{\rm ins}(\lambda) Sp_{\rm SN}(\lambda) d\lambda, \tag{2.10}$$

where $M_{\rm ins}$ is the instrumental passband

$$M_{\rm ins}(\lambda) = QE(\lambda) \times T(\lambda) \times R(\lambda) \times A(\lambda). \tag{2.11}$$

$QE(\lambda)$ is the instrumental quantum efficiency, $T(\lambda)$ is the filter transmission, $R(\lambda)$ the telescope's mirror reflectivity, and $A(\lambda)$ is the atmospheric transmission profile. As an example, in Figure 2.3 we have represented the $BVRI$ passbands of the instruments used to obtain the photometry for SN 2011fu.

S-correction calculations are generally limited to the availability of all the terms in equation 2.11. Another limitation is the spectral coverage of the SN both in wavelength and in time. For example, for SN 2011fu the spectra did not cover the U,u,z,J,H,K_s passbands, and thus we were unable to calculate S-corrections for those bands. On the other hand, for the nights in which there were no spectra available, the S-correction terms were determined by linear interpolation of the adjacent nights with spectra.

Photometric errors

The errors of the instrumental magnitudes (obtained via PSF-fitting or template subtraction) were estimated by placing artificial stars with profiles similar to those of the SN at positions near the SN (a few arcsec) and calculating the standard deviation of their recovered magnitudes. The total error of the SN magnitudes is given by

$$\Delta m_{\rm tot} = \sqrt{\Delta m_{\rm art}^2 + \Delta Zp^2 + \Delta\delta S^2}, \tag{2.12}$$

where $\Delta m_{\rm art}$ is the error of the instrumental magnitude, ΔZp is the quadratic sum of deviations of the stellar sequence's magnitudes with respect to their calibrated values, and $\Delta\delta S$ is the error associated to the S-correction (if applicable).

2.3.3 Spectroscopy

Pre-reduction and extraction

All 2-D spectra were corrected for bias, trimmed, flat-fielded, and then were variance-weighed extracted with the IRAF task *apall*. This task makes it possible to choose an aperture perpendicular to the direction of the dispersion axis around the SN spectrum, and sums up the counts inside. A background region which consists of night sky lines and galaxy foreground or background emission is defined to both

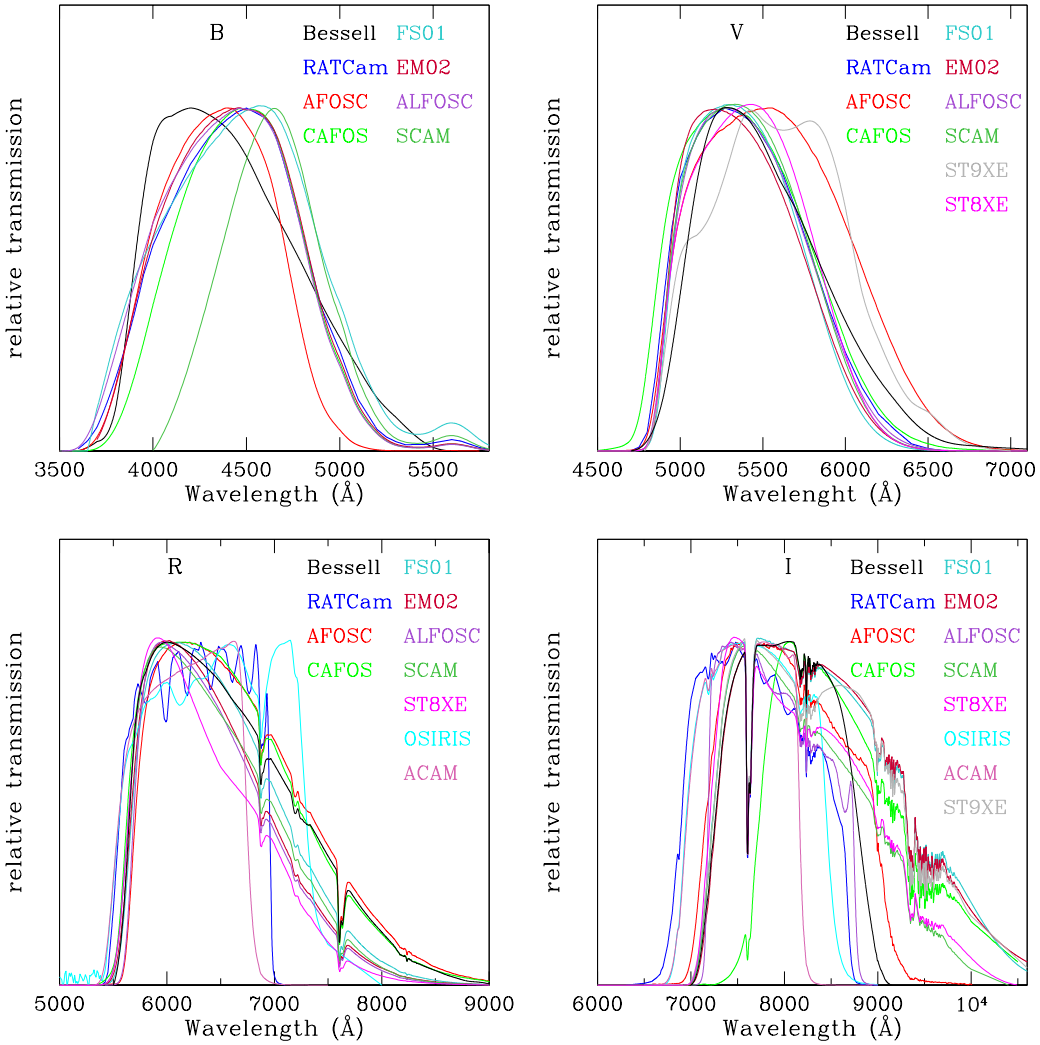

Figure 2.3: *BVRI* passbands of the instruments used to obtain the photometry of SN 2011fu. The Bessell 2012 passbands (Bessell & Murphy 2012) have also been represented for reference.

sides of the aperture, and it is then fit and subtracted from the spectrum. Next the aperture tracing is checked since there could be possible misalignments between the grism and the CCD.

Wavelength calibration

After the 1-D spectral extraction, the next step is the wavelength calibration, which is achieved with arc lamp spectra (e.g. Hg-Cd, He-Ne, He-Ar) taken with the same set-up and usually with the same pointing position as the SN to avoid a modification in the dispersion solution due to the telescope flexure. The identification of the arc lamp spectral lines and polynomial fit to the dispersion solution give the pixel to wavelength transformation which is then applied to the SN. The wavelength calibration is checked against night sky lines, and the errors typically do not exceed 1-2 Å. We would like to remark that in most cases the spectra were obtained with the slit aligned with the paralactic angle to avoid differential flux losses caused by differential atmospheric refraction (Filippenko, 1982).

Flux calibration

The instrumental sensitivity curves to flux calibrate the spectra were obtained by comparing the tabulated flux data of spectrophotometric standards typically taken from Oke (1990); Hamuy et al. (1992, 1994), with their observed extracted and wavelength calibrated spectra. If no standard was observed that night, a sensitivity function derived for another night with the same telescope and instrumental configuration was applied. Correction for atmospheric extinction was taken into account by considering the tabulated values for each observatory. Sometimes the SN spectra are obtained under non-photometric conditions or the SN and/or the standard are not perfectly centred in the slit, which may cause flux losses and errors in the flux calibration. For these reasons the spectral flux calibration was checked against the SN photometry at a contemporaneous phase, and if necessary scaled by:

$$\delta I_\lambda = 10^{-0.4\,(m_{\lambda,\mathrm{phot}} - m_{\lambda,\mathrm{spec}})} \tag{2.13}$$

where $m_{\lambda,\mathrm{phot}}$ is the observed SN magnitude in band λ and $m_{\lambda,\mathrm{spec}}$ is the synthetically computed SN magnitude from the spectrum.

Telluric correction

Owing mainly to the presence of water vapour and O_2 in the Earth's atmosphere, broad telluric absorption bands 'contaminate' the SN spectra. By eliminating the telluric bands from the spectroscopic standard spectrum and using the resulting

spectrum to divide the original one, we obtain a spectrum which is equal to 1 in the whole wavelength range except in the region of the telluric lines. The SN spectra are then divided by this spectrum, and the telluric lines practically disappear, although some residuals may still be present.

Chapter 3

SN 2011fu

In this chapter we show the results of the analysis of the observational data that we have collected for SN 2011fu, which have also been published in Morales-Garoffolo et al. (2015a). We give a short introduction of the SN, present its photometric and spectroscopic analysis and conclude with an estimation of its explosion and progenitor parameters by hydrodynamical modelling of its pseudo bolometric LC and comparison with late-time spectral models.

3.1 SN 2011fu: distance, reddening, and explosion date

SN 2011fu, with coordinates $\alpha = 02^{\rm h}08^{\rm m}21^{\rm s}.26$ and $\delta = 41^{\rm o}29'9''.9$ (J2000) (see Figure 3.1), was discovered in a spiral arm of the galaxy UGC 1626 by F. Ciabattari and E. Mazzoni of the ISSP, on 2011 September 21.04 UT and classified by Tomasella et al. (2011) as a young type II SN on 2011 September 23.84 UT. An analysis of optical data of SN 2011fu was presented by Kumar et al. (2013), which confirmed it was a type IIb SN.

Thanks to an extensive collaboration between many European institutions, we have collected optical photometry and spectroscopy, as well as some NIR photometric data of SN 2011fu, at several sites. Some early-time amateur data taken by F. Ciabattari and E. Mazzoni from Italy, and Xing Gao from China were also included in our analysis. Our data cover the period between a few days post-discovery, until the SN disappeared behind the Sun (end of 2012 February). After that, one more spectrum and one epoch of *gri* photometric data were obtained well into the nebular phase of the SN, 2012 July 20 UT.

The rise to a first maximum in the V and R LCs (see the inset of Figure 3.2) implies that SN 2011fu was discovered very soon after explosion. In fact, models show that the evolution of the SN LC during this rise should be very fast, and lasts $\sim$ 1 d for a number of configurations (e.g. Blinnikov et al. 1998; Bersten et al. 2012). By adopting $\mathrm{JD_{explo}} = 2455824.5 \pm 0.7$ as the explosion date of SN 2011fu,

we have obtained the best fit of the early phase of the pseudo-bolometric LC with the hydrodynamical models presented in Section 3.4.1. Thus, we have chosen $JD_{explo} = 2455824.5 \pm 0.7$ as the explosion date of SN 2011fu, which is in agreement with the discovery epoch, the last non-detection of the object, which was 2011 August 10 (JD = 2455783.5), the pre-discovery image taken by Xing Gao 2011 September 20 (JD = 2455825.2), and the classification as a young object. Note that this assumed explosion date also agrees, within the uncertainties, with the explosion epoch adopted by Kumar et al. (2013). All phases related to SN 2011fu in the rest of this chapter are given with respect to $JD_{explo} = 2455824.5 \pm 0.7$.

UGC 1626 is an SAB(rs)c type galaxy whose heliocentric recessional velocity given by the NASA/IPAC Extragalactic Database (NED) is 5543 ± 11 km s^{-1}. We have taken measurements of the SN redshift from the narrow Hα emissions in its spectra and have obtained the same redshift as for its host galaxy, which we have adopted in the rest of this thesis. The redshift derived distance to UGC 1626, also provided by NED assuming $H_0 = 73 \pm 5$ km s^{-1} Mpc^{-1}, $\Omega_m = 0.27$, $\Omega_v = 0.73$, and accounting for the Virgo, Great Attractor, and Shapley infalls, is 74.5 ± 5.2 Mpc, i.e. $\mu = 34.36 \pm 0.15$ mag (Mould et al., 2000).

The reddening in the line of sight of UGC 1626 due to the Milky Way is $E(B-V)_{MW} = 0.068 \pm 0.002$ mag (Schlafly & Finkbeiner, 2011). We have detected a narrow absorption probably due to Na ID $\lambda\lambda$5890, 5896 at the host galaxy redshift. The equivalent width of this line is 0.33 ± 0.03 Å, which, using the relations for unresolved Na ID given by Poznanski et al. (2012), provides an estimate of the reddening in the host galaxy as: $E(B-V)_{host} = 0.035^{+0.042}_{-0.029}$ mag. In fact, a similar value of reddening due to the host galaxy is obtained by using the relations of Turatto et al. (2003). In the rest of this manuscript we have adopted $E(B-V)_{total} = 0.10^{+0.04}_{-0.03}$ mag as the total reddening towards SN 2011fu. We note that in Kumar et al. (2013) the relations of Munari & Zwitter (1997) were used to estimate the contribution to the reddening due to the host galaxy, and they obtained $E(B-V)_{total} = 0.22 \pm 0.11$, which is consistent with the value we have adopted within the uncertainties.

3.2 Photometry

3.2.1 Light curves

All the photometric data were pre-reduced as described in Section 2.3.1 except for data obtained at the LT, which were automatically reduced with the instruments' specific pipelines. The instrumental magnitudes of the SN were derived via PSF fitting as indicated in Section 2.3.2. In the case of the U and u photometry, the measurements were done after performing template subtraction as specified in Section 2.3.2. For all other bands, PSF photometry at late time was verified by performing

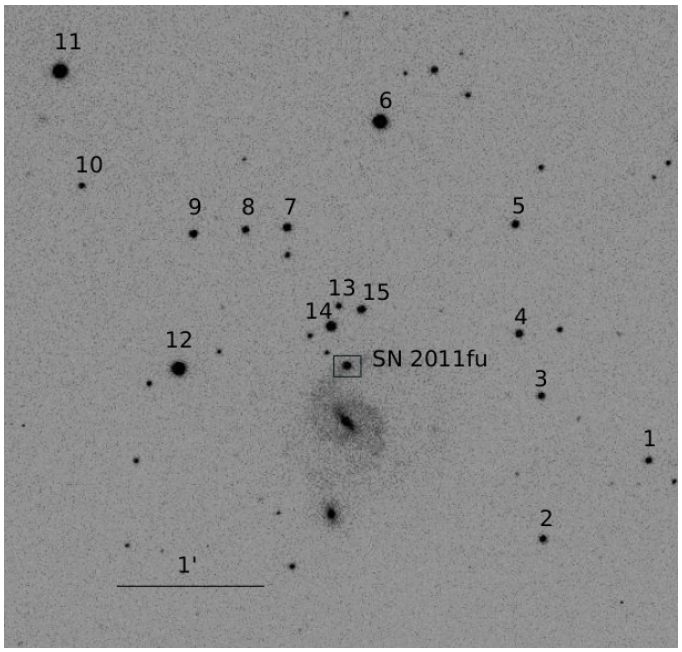

Figure 3.1: V-band image of UGC 1626 taken with the 2.2-m Calar Alto Telescope + CAFOS on 2011 October 16. The stars used for the photometric calibration of SN 2011fu are labelled. North is toward the top and East toward the left.

template subtractions, and differences were below 0.1 mag[1]. A set of 15 local stars in the SN field (Figure 3.1) were used to trace the photometric calibration.

Given the fact that several instruments with different passbands were used to acquire our data, we carried out S-corrections of our *BVrRiI* photometry to the Bessell system (see Section 2.3.2). In order to derive the S-correction terms, we used our spectral sequence of the SN. Note that we were not able to perform S-corrections to the U-, u-, and z-band photometry given the fact that our spectra do not cover completely these passbands. The SN magnitudes together with their errors, calculated by adding in quadrature the uncertainties associated with the calibration and the PSF fit, are reported in Tables 3.1–3.3.

The unfiltered photometry provided by F. Ciabattari was rescaled to the R band after considering that the detector sensitivity peaks at this wavelength. With the same argument the data provided by X. Gao were rescaled to V.

Note that stars 2, 6, 9, 12, and 14 from our sequence coincide with stars 2, 1, 4, 3 and 5 used for photometric calibration by Kumar et al. (2013). The greatest difference between the two sequences is 0.1 mag found for star 2 in the U band. For

[1]The *UBVRI* band templates were obtained on 2012 October 23 with AFOSC at the 1.82 m telescope in the Asiago Observatory, while the *uri* band templates were obtained on 2014 October 25 at the LT with IO:O in the *Roque de los Muchachos* Observatory.

the rest of the bands differences are found to be less than 0.1 mag.

The NIR data were reduced within IRAF with the help of CAINDR as described in Section 2.3.2. Similarly to the optical data, we measured the instrumental SN magnitudes by PSF fitting. The SN calibration was done relative to 2MASS stars in the field (Skrutskie et al. 2006; see Table 3.4).

The optical-NIR LCs of SN 2011fu are presented in Figure 3.2. In addition to the data presented in the figure, we obtained two epochs of Sloan g-band data, which are listed in Table 3.2. In the optical, the LCs clearly present two peaks in all bands, but not in the NIR since the data do not cover the early phases. The rise to primary peak in the V and R bands can be seen thanks to the early-time data provided by amateur astronomers (see inset in the top-right of the figure).

By making low-order polynomial fits to the optical LCs, we have estimated the phases and magnitudes at which the minima after first peak and secondary maxima take place. The results are presented in Table 3.6. Note that we obtain different absolute magnitudes at secondary peak from Kumar et al. (2013) due to the fact that we have adopted different distance and reddening towards the host. However, our values agree within the uncertainties. We also fitted low-order polynomials to the first peaks in the R and V LCs. In the V band, the first peak at 16.3 mag is reached $\sim$ 2.3 d after explosion while in the R band the 16.0 mag first peak is obtained $\sim$ 2.8 d post-explosion.

We have also estimated the decline rates of the tails of the $BVRIz$ LCs (Table 3.6). These rates are steeper than expected from ^{56}Co decay, which is 0.98 mag (100 d)$^{-1}$. This is a common characteristic to stripped envelope SNe (e.g., SN 2008ax; Taubenberger et al. 2011) and is possibly due to increasing transparency for γ rays in their lower mass ejecta.

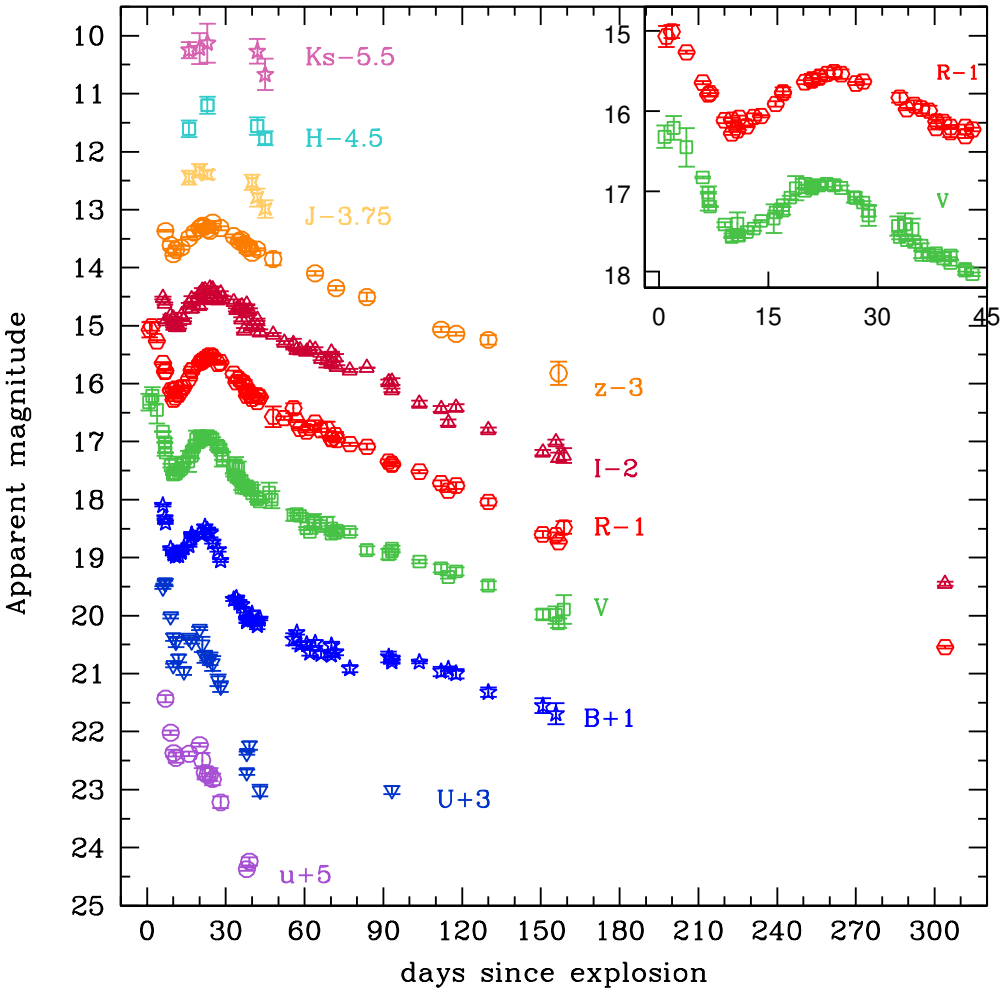

Figure 3.2: Optical-NIR light curves of SN 2011fu. The assumed explosion epoch is JD = 2455824.5 ± 0.7. The LCs have been shifted for clarity by the values indicated in the figure. The inset at the top right corner of the figure is a zoom of the V and R LCs up to 45 d.

Table 3.1: Optical Bessell photometry of SN 2011fu. The U data are not S-corrected, note that the reported RI LT data are the S-corrected Sloan ri magnitudes

Date	JD (+2400000.00)	Phase[a] (d)	U (mag)	B (mag)	V (mag)	R (mag)	I (mag)	Key[b]
2011/09/20	55825.2	0.7	–	–	16.32 ± 0.14	–	–	Xing Gao
2011/09/21	55825.5	1.0	–	–	–	16.07 ± 0.13	–	F.C.+E.M.
2011/09/21	55826.4	1.9	–	–	16.21 ± 0.15	–	–	Xing Gao
2011/09/21	55826.4	1.9	–	–	–	16.01 ± 0.08	–	F.C.+E.M.
2011/09/23	55828.3	3.8	–	–	–	16.27 ± 0.02	–	A1p82+AFOSC
2011/09/23	55828.4	3.9	–	–	16.45 ± 0.24	–	–	Xing Gao
2011/09/25	55830.5	6.0	16.52 ± 0.02	17.10 ± 0.02	16.83 ± 0.01	16.65 ± 0.02	16.52 ± 0.02	A1p82+AFOSC
2011/09/26	55831.2	6.7	–	–	17.09 ± 0.15	–	–	Xing Gao
2011/09/26	55831.4	6.9	16.43 ± 0.03	17.31 ± 0.02	17.02 ± 0.01	16.80 ± 0.02	16.62 ± 0.02	A1p82+AFOSC
2011/09/27	55831.5	7.0	–	17.40 ± 0.02	17.19 ± 0.01	16.78 ± 0.04	16.92 ± 0.03	LT+RATCam
2011/09/29	55833.5	9.0	–	17.85 ± 0.02	17.41 ± 0.03	17.12 ± 0.04	16.84 ± 0.03	LT+RATCam
2011/09/29	55834.5	10.0	17.86 ± 0.03	17.93 ± 0.02	17.57 ± 0.01	17.28 ± 0.02	17.00 ± 0.02	A1p82+AFOSC
2011/09/29	55834.6	10.1	–	17.91 ± 0.02	17.55 ± 0.02	17.11 ± 0.02	16.87 ± 0.03	LT+RATCam
2011/09/30	55835.3	10.8	–	–	17.40 ± 0.14	–	–	Xing Gao
2011/09/30	55835.4	10.9	–	17.97 ± 0.02	17.55 ± 0.02	17.24 ± 0.01	16.98 ± 0.05	A1p82+AFOSC
2011/10/01	55835.5	11.0	–	17.95 ± 0.01	17.55 ± 0.03	17.08 ± 0.03	17.02 ± 0.03	LT+RATCam
2011/10/01	55836.4	11.9	17.74 ± 0.06	17.96 ± 0.02	17.51 ± 0.01	17.19 ± 0.01	17.02 ± 0.03	A1p82+AFOSC
2011/10/03	55837.5	13.0	–	17.91 ± 0.02	17.46 ± 0.03	17.07 ± 0.43	16.83 ± 0.05	LT+RATCam
2011/10/03	55838.5	14.0	17.96 ± 0.06	17.84 ± 0.02	17.37 ± 0.01	17.06 ± 0.01	16.90 ± 0.03	A1p82+AFOSC
2011/10/05	55840.2	15.7	–	–	17.34 ± 0.18	–	–	Xing Gao
2011/10/06	55840.5	16.0	–	17.79 ± 0.02	17.26 ± 0.02	16.91 ± 0.03	16.64 ± 0.04	LT+RATCam
2011/10/06	55841.4	16.9	17.45 ± 0.04	17.64 ± 0.03	17.17 ± 0.02	16.78 ± 0.02	16.71 ± 0.06	Ca2p2 + CAFOS
2011/10/07	55841.5	17.0	–	17.60 ± 0.03	17.24 ± 0.05	16.77 ± 0.06	16.54 ± 0.05	LT+RATCam
2011/10/08	55842.5	18.0	–	–	17.08 ± 0.02	–	–	LT+RATCam
2011/10/08	55843.3	18.8	–	–	16.96 ± 0.15	–	–	Xing Gao
2011/10/10	55844.5	20.0	–	17.58 ± 0.02	16.99 ± 0.03	16.64 ± 0.03	16.46 ± 0.03	LT+RATCam
2011/10/10	55844.5	20.0	–	–	16.90 ± 0.06	–	16.66 ± 0.05	TED+ST9XE
2011/10/11	55845.5	21.0	–	17.60 ± 0.04	16.97 ± 0.03	16.61 ± 0.07	16.40 ± 0.05	LT+RATCam
2011/10/11	55845.5	21.0	–	–	16.94 ± 0.04	16.62 ± 0.03	–	OAC+ST8XE
2011/10/11	55845.5	21.0	–	–	16.94 ± 0.02	–	16.56 ± 0.03	TED+ST9XE
2011/10/12	55846.5	22.0	–	17.47 ± 0.03	16.92 ± 0.04	16.57 ± 0.03	16.39 ± 0.03	LT+RATCam
2011/10/12	55846.5	22.0	–	–	–	16.58 ± 0.05	16.50 ± 0.06	OAC+ST8XE
2011/10/13	55847.5	23.0	–	17.53 ± 0.04	16.90 ± 0.04	16.54 ± 0.04	16.45 ± 0.03	LT+RATCam
2011/10/14	55848.5	24.0	–	17.58 ± 0.07	16.92 ± 0.06	16.52 ± 0.06	16.36 ± 0.04	LT+RATCam
2011/10/15	55849.5	25.0	–	17.73 ± 0.03	16.96 ± 0.03	16.54 ± 0.06	16.37 ± 0.04	LT+RATCam
2011/10/16	55851.4	26.9	–	–	17.07 ± 0.07	–	16.56 ± 0.04	TED+ST9XE

Table 3.1: (continued)

Date	JD (+2400000.00)	Phase[a] (d)	U (mag)	B (mag)	V (mag)	R (mag)	I (mag)	Key[b]
2011/10/16	55851.5	27.0	18.12 ± 0.10	17.87 ± 0.03	17.08 ± 0.02	16.66 ± 0.02	16.56 ± 0.04	Ca2p2 + CAFOS
2011/10/18	55852.5	28.0	–	18.05 ± 0.02	17.14 ± 0.02	16.63 ± 0.03	16.44 ± 0.03	LT+RATCam
2011/10/18	55853.2	28.7	–	–	17.30 ± 0.13	–	–	Xing Gao
2011/10/18	55853.4	28.9	–	–	17.24 ± 0.07	–	16.53 ± 0.04	TED+ST9XE
2011/10/22	55857.2	32.7	–	–	17.43 ± 0.12	–	–	Xing Gao
2011/10/23	55857.6	33.1	–	18.72 ± 0.03	17.57 ± 0.03	16.83 ± 0.06	16.59 ± 0.04	LT+RATCam
2011/10/23	55858.2	33.7	–	–	17.41 ± 0.14	–	–	Xing Gao
2011/10/24	55858.6	34.1	–	18.70 ± 0.02	17.61 ± 0.01	16.98 ± 0.01	16.73 ± 0.03	A1p82+AFOSC
2011/10/24	55859.2	34.7	–	–	17.47 ± 0.13	–	–	Xing Gao
2011/10/25	55859.5	35.0	–	18.78 ± 0.04	17.63 ± 0.03	16.92 ± 0.06	16.70 ± 0.04	LT+RATCam
2011/10/25	55860.4	35.9	–	–	17.79 ± 0.05	–	16.89 ± 0.04	TED+ST9XE
2011/10/26	55860.5	36.0	–	18.81 ± 0.04	17.68 ± 0.03	16.97 ± 0.06	16.67 ± 0.04	LT+RATCam
2011/10/27	55861.5	37.0	–	18.91 ± 0.04	17.79 ± 0.03	16.99 ± 0.06	17.08 ± 0.04	LT+RATCam
2011/10/28	55862.5	38.0	19.70 ± 0.05	19.10 ± 0.03	17.77 ± 0.02	17.13 ± 0.02	16.64 ± 0.01	NOT+ALFOSC
2011/10/28	55862.5	38.0	–	19.08 ± 0.04	17.80 ± 0.03	17.21 ± 0.02	16.76 ± 0.02	LT+RATCam
2011/10/29	55863.5	39.0	–	19.06 ± 0.04	17.83 ± 0.03	17.14 ± 0.06	16.74 ± 0.04	LT+RATCam
2011/10/30	55864.5	40.0	–	19.07 ± 0.07	17.80 ± 0.05	17.26 ± 0.06	–	LT+RATCam
2011/10/30	55864.5	40.0	–	18.97 ± 0.06	17.89 ± 0.03	17.20 ± 0.03	17.01 ± 0.03	A1p82+AFOSC
2011/10/31	55866.5	42.0	–	19.10 ± 0.06	17.97 ± 0.03	17.31 ± 0.02	17.03 ± 0.03	A1p82+AFOSC
2011/11/01	55866.6	42.1	–	19.17 ± 0.06	17.99 ± 0.05	17.20 ± 0.03	16.90 ± 0.02	LT+RATCam
2011/11/01	55867.4	42.9	20.02 ± 0.10	19.06 ± 0.02	18.03 ± 0.02	17.23 ± 0.02	17.12 ± 0.05	Ca2p2 + CAFOS
2011/11/05	55871.1	46.6	–	–	17.88 ± 0.17	–	–	Xing Gao
2011/11/06	55872.1	47.6	–	–	18.00 ± 0.15	–	–	Xing Gao
2011/11/07	55872.6	48.1	–	–	–	17.57 ± 0.18	17.15 ± 0.03	WHT+ACAM
2011/11/11	55876.9	52.4	–	–	–	17.59 ± 0.03	17.30 ± 0.03	FTN+fs02
2011/11/14	55880.2	55.7	–	19.41 ± 0.10	18.27 ± 0.10	17.42 ± 0.09	17.32 ± 0.09	ASch+SCAM
2011/11/15	55881.4	56.9	–	19.29 ± 0.04	18.25 ± 0.03	17.65 ± 0.02	17.42 ± 0.02	Ca2p2 + CAFOS
2011/11/17	55882.9	48.4	–	19.51 ± 0.06	18.28 ± 0.05	17.78 ± 0.03	17.43 ± 0.03	FTN+fs02
2011/11/19	55885.4	60.9	–	19.49 ± 0.04	18.49 ± 0.02	17.82 ± 0.02	17.45 ± 0.03	A1p82+AFOSC
2011/11/21	55886.5	62.0	–	19.64 ± 0.05	18.56 ± 0.03	17.76 ± 0.04	17.39 ± 0.02	A1p82+AFOSC
2011/11/22	55888.1	63.6	–	–	18.38 ± 0.13	–	–	Xing Gao
2011/11/23	55888.5	64.0	–	19.47 ± 0.05	18.40 ± 0.06	17.67 ± 0.04	17.42 ± 0.05	LT+RATCam
2011/11/25	55890.8	66.3	–	19.66 ± 0.06	18.45 ± 0.05	17.80 ± 0.03	17.57 ± 0.03	FTN+fs02
2011/11/27	55893.0	68.5	–	–	18.41 ± 0.11	17.78 ± 0.13	17.59 ± 0.13	FTN+fs02
2011/11/29	55894.9	70.4	–	19.52 ± 0.07	18.50 ± 0.05	17.94 ± 0.04	17.66 ± 0.03	FTN+fs02
2011/11/29	55894.9	70.4	–	19.68 ± 0.03	18.59 ± 0.02	17.96 ± 0.02	17.46 ± 0.01	NOT+ALFOSC

Table 3.1: (continued)

Date	JD (+2400000.00)	Phase[a] (d)	U (mag)	B (mag)	V (mag)	R (mag)	I (mag)	Key[b]
2011/11/30	55896.4	71.9	–	19.63 ± 0.05	18.57 ± 0.06	17.89 ± 0.05	17.55 ± 0.06	LT+RATCam
2011/12/01	55896.8	72.3	–	–	18.53 ± 0.05	17.97 ± 0.04	17.71 ± 0.03	FTN+fs02
2011/12/06	55901.8	77.3	–	19.91 ± 0.06	18.56 ± 0.05	18.04 ± 0.03	17.77 ± 0.03	FTN+EM01
2011/12/12	55908.4	83.9	–	–	18.87 ± 0.07	18.09 ± 0.05	17.73 ± 0.01	LT+RATCam
2011/12/20	55916.4	91.9	–	19.71 ± 0.09	18.94 ± 0.09	18.34 ± 0.04	17.97 ± 0.05	A1p82+AFOSC
2011/12/22	55917.8	93.3	20.01 ± 0.07	19.80 ± 0.03	18.88 ± 0.03	18.38 ± 0.03	17.96 ± 0.06	NOT+ALFOSC
2011/12/22	55917.8	93.3	–	19.75 ± 0.06	18.85 ± 0.05	18.40 ± 0.03	18.11 ± 0.03	FTN+EM01
2012/01/01	55928.3	103.8	–	19.80 ± 0.02	19.07 ± 0.03	18.52 ± 0.03	18.34 ± 0.05	Ca2p2 + CAFOS
2012/01/09	55936.5	112.0	–	19.96 ± 0.08	19.18 ± 0.07	18.72 ± 0.05	18.44 ± 0.05	LT+RATCam
2012/01/12	55939.4	114.9	–	19.92 ± 0.03	19.33 ± 0.03	18.85 ± 0.02	18.67 ± 0.05	Ca2p2 + CAFOS
2012/01/15	55942.3	117.8	–	20.00 ± 0.08	19.24 ± 0.07	18.76 ± 0.06	18.41 ± 0.06	LT+RATCam
2012/01/27	55954.4	129.9	–	20.32 ± 0.08	19.48 ± 0.07	19.04 ± 0.06	18.80 ± 0.04	LT+RATCam
2012/02/17	55975.3	150.8	–	20.55 ± 0.13	19.98 ± 0.09	19.60 ± 0.06	19.19 ± 0.05	A1p82+AFOSC
2012/02/22	55980.3	155.8	–	20.69 ± 0.18	19.99 ± 0.15	19.61 ± 0.04	19.01 ± 0.04	A1p82+AFOSC
2012/02/23	55981.4	156.9	–	–	20.13 ± 0.08	19.73 ± 0.03	19.27 ± 0.08	LT+RATCam
2012/02/25	55983.4	148.9	–	–	19.89 ± 0.25	19.48 ± 0.11	19.24 ± 0.13	LT+RATCam
2012/07/20	56128.6	304.1	–	–	–	21.54 ± 0.02	21.45 ± 0.04	GTC+OSIRIS

[a]Phase in days with respect to the adopted explosion date JD = 2455824.5 ± 0.7.

[b]More information about the telescopes and instruments can be found in Section 2.2.

3.3 Spectroscopy

3.3.1 Spectral evolution of SN 2011fu

The list with our spectroscopic observations is presented in Table 3.7. All spectra were pre-reduced, extracted, wavelength and flux calibrated as indicated in Sections 2.3.1 and 2.3.3.

In Figure 3.3 we show the spectral evolution of SN 2011fu ranging from $\sim$ 4 to $\sim$ 304 d after explosion. The early spectra show a blue continuum and shallow features. Starting at around 6 d Hα, Hβ (with some possible Fe II contamination), He I λ5876, Ca II H & K, Ca II NIR $\lambda\lambda\lambda$8498, 8542, 8662, and Fe II λ5169 appear to grow. The Hα P-Cygni absorption component at 11.1 d shows a small trough at around 6300 Å in addition to a broader and deeper one centred at approximately 6190 Å. These double Hα absorption features have been seen before in some type IIb SNe (e.g. SN 2011hs; Bufano et al. 2014) and have been claimed to be either due to Si II (Hachinger et al., 2012) or to the presence of a double density distribution of hydrogen in the ejecta of the SNe as claimed for some type II SNe (e.g. Inserra et al. 2013). Note that in the first spectrum and the one at 14 d, there is a narrow emission line at approximately the rest wavelength of Hα. This line is also seen in some of our subsequent spectra. However, as we will explain below, we believe it is not associated with the SN or its CSM. After the LC's secondary maximum, at 34.1 d, two new lines with fairly narrow absorptions at approximately 4840 and 4890 Å are discernible, which we believe are associated with Fe II λ4924 and Fe II λ5018 + He I λ5015, respectively. In addition, there is an absorption that could be associated with O I λ7774. A major change occurs at $\sim$ 40 d, when He I λ6678 and He I λ7065 appear and, together with He I λ5876, become progressively stronger. At 62 d a double-peaked emission associated with [O I] $\lambda\lambda$ 6300, 6364 with components at approximately 6240 and 6300 Å is observed, as well as an emission which has increased in intensity with respect to previous spectra and is possibly associated with [O I] λ5577. Starting at 103.8 d, [N II] $\lambda\lambda$6548, 6583 produces an emission between $\sim$ 6400 and $\sim$ 6700 Å (Jerkstrand et al., 2015). At phase 155.8 d we notice a decrease in the intensity of Na I around 5890 Å (which is possibly contaminated by residual He I λ5876; Jerkstrand et al. 2015). In addition we identify [Ca II] $\lambda\lambda$7291, 7324 and two strong emission lines, a narrow one at approximately the rest position of Hα (on top of N II $\lambda\lambda$6572, 6583) and the other at $\sim$ 6723 Å. In the last spectrum of our sequence, beside [O I] $\lambda\lambda$ 6300, 6364, [Ca II] $\lambda\lambda$7291, 7324, O I λ7774, we also distinguish Mg I] λ4571, [Fe II] λ7155. The Ca II NIR line has diminished significantly from our previous spectra and is now blended with [C I] λ8727. The narrow emissions at Hα and the one at $\sim$ 6700 Å are still present although the first seems to have diminished in intensity while the second has become broader and now is centred at approximately 6735 Å. The unresolved narrow Hα emission line seen in our last two spectra, and also observed in some of the earlier-time spectra, is detected mainly on

Table 3.2: Optical Sloan photometry of SN 2011fu in the Vega system.

Date	JD (+2400000.00)	Phase[a] (d)	u (mag)	g (mag)	z (mag)	Key[b]
2011/09/27	55831.5	7.0	16.43 ± 0.06	–	16.37 ± 0.03	LT+RATCam
2011/09/29	55833.5	9.0	17.02 ± 0.04	–	16.61 ± 0.04	LT+RATCam
2011/09/30	55834.6	10.1	17.37 ± 0.06	–	16.77 ± 0.03	LT+RATCam
2011/10/01	55835.5	11.0	17.45 ± 0.09	–	16.70 ± 0.03	LT+RATCam
2011/10/03	55837.5	13.0	–	–	16.66 ± 0.05	LT+RATCam
2011/10/06	55840.5	16.0	17.38 ± 0.04	–	16.49 ± 0.04	LT+RATCam
2011/10/08	55842.5	18.0	–	–	16.40 ± 0.06	LT+RATCam
2011/10/10	55844.5	20.0	17.23 ± 0.03	–	16.32 ± 0.03	LT+RATCam
2011/10/11	55845.5	21.0	17.50 ± 0.13	–	16.28 ± 0.05	LT+RATCam
2011/10/12	55846.5	22.0	17.71 ± 0.11	–	16.30 ± 0.03	LT+RATCam
2011/10/13	55847.5	25.0	17.75 ± 0.03	–	16.34 ± 0.05	LT+RATCam
2011/10/14	55848.5	24.0	17.74 ± 0.11	–	16.36 ± 0.05	LT+RATCam
2011/10/15	55849.5	25.0	17.82 ± 0.10	–	16.22 ± 0.05	LT+RATCam
2011/10/18	55852.5	28.0	18.22 ± 0.10	–	16.32 ± 0.03	LT+RATCam
2011/10/23	55857.6	33.1	–	–	16.46 ± 0.05	LT+RATCam
2011/10/25	55859.5	35.0	–	–	16.54 ± 0.05	LT+RATCam
2011/10/26	55860.5	36.0	–	–	16.52 ± 0.05	LT+RATCam
2011/10/27	55861.5	37.0	–	–	16.59 ± 0.05	LT+RATCam
2011/10/28	55862.5	38.0	19.37 ± 0.03	–	16.66 ± 0.02	LT+RATCam
2011/10/29	55863.5	39.0	19.24 ± 0.07	–	16.65 ± 0.04	LT+RATCam
2011/10/30	55864.5	40.0	–	–	16.75 ± 0.04	LT+RATCam
2011/11/01	55866.6	42.1	–	–	16.69 ± 0.02	LT+RATCam
2011/11/07	55872.6	48.1	–	18.72 ± 0.29	16.85 ± 0.05	WHT+ACAM
2011/11/23	55888.5	64.0	–	–	17.10 ± 0.06	LT+RATCam
2011/11/30	55896.4	71.9	–	–	17.35 ± 0.05	LT+RATCam
2011/12/12	55908.4	83.9	–	–	17.51 ± 0.05	LT+RATCam
2012/01/09	55936.5	112.0	–	–	18.07 ± 0.07	LT+RATCam
2012/01/15	55942.3	117.8	–	–	18.14 ± 0.08	LT+RATCam
2012/01/27	55954.4	129.9	–	–	18.25 ± 0.07	LT+RATCam
2012/02/23	55981.4	156.9	–	–	18.82 ± 0.16	LT+RATCam
2012/07/20	56128.6	304.1	–	22.41 ± 0.15	–	GTC+OSIRIS

[a]Phase in days with respect to the adopted explosion date JD = 2455824.5 ± 0.7.
[b]More information about the telescopes and instruments can be found in Section 2.2.

Table 3.3: NIR photometry of SN 2011fu.

Date	JD (+2400000.00)	Phase[a] (d)	J (mag)	H (mag)	K_s (mag)	Key[b]
2011/10/06	55840.6	16.1	16.20 ± 0.12	16.10 ± 0.14	15.75 ± 0.14	TCS+CAIN3
2011/10/10	55844.6	20.1	16.08 ± 0.12	–	15.72 ± 0.27	TCS+CAIN3
2011/10/12	55847.4	23.0	16.15 ± 0.08	15.70 ± 0.15	15.63 ± 0.34	TCS+CAIN3
2011/10/29	55864.5	40.0	16.28 ± 0.13	–	–	TCS+CAIN3
2011/10/31	55866.5	42.0	16.54 ± 0.15	16.06 ± 0.15	15.77 ± 0.21	TCS+CAIN3
2011/11/04	55869.5	45.0	16.74 ± 0.15	16.27 ± 0.12	16.17 ± 0.27	TCS+CAIN3

[a]Phase in days with respect to the adopted explosion date JD = 2455824.5 ± 0.7.
[b]More information about the telescopes and instruments can be found in Section 2.2.

Table 3.4: Johnson-Cousins optical and 2MASS NIR magnitudes and associated errors for the stellar sequence used in the calibration process of SN 2011fu's photometry.

Star	U (mag)	B (mag)	V (mag)	R (mag)	I (mag)	J (mag)	H (mag)	K_s (mag)
1	19.26 ± 0.10	18.66 ± 0.02	17.74 ± 0.02	17.20 ± 0.03	16.65 ± 0.03	–	–	–
2	18.25 ± 0.10	18.17 ± 0.02	17.52 ± 0.02	17.10 ± 0.05	16.79 ± 0.03	–	–	–
3	18.26 ± 0.06	18.25 ± 0.02	17.55 ± 0.02	17.24 ± 0.02	16.87 ± 0.03	16.24 ± 0.12	15.96 ± 0.19	15.79 ± 0.26
4	18.98 ± 0.09	18.14 ± 0.02	17.18 ± 0.02	16.63 ± 0.02	16.14 ± 0.03	15.45 ± 0.06	14.81 ± 0.08	14.81 ± 0.11
5	17.75 ± 0.04	17.83 ± 0.02	17.25 ± 0.02	16.90 ± 0.02	16.58 ± 0.02	15.91 ± 0.08	15.77 ± 0.15	15.51 ± 0.20
6	15.68 ± 0.09	15.51 ± 0.02	14.88 ± 0.07	14.47 ± 0.07	14.11 ± 0.06	13.49 ± 0.02	13.16 ± 0.03	13.07 ± 0.03
7	17.88 ± 0.04	17.77 ± 0.02	17.14 ± 0.03	16.77 ± 0.03	16.41 ± 0.02	15.83 ± 0.08	15.30 ± 0.10	15.42 ± 0.19
8	19.94 ± 0.05	18.82 ± 0.02	17.58 ± 0.03	16.82 ± 0.02	16.15 ± 0.03	15.11 ± 0.05	14.54 ± 0.05	14.28 ± 0.07
9	17.60 ± 0.04	17.61 ± 0.02	17.07 ± 0.02	16.75 ± 0.03	16.42 ± 0.02	15.97 ± 0.09	15.73 ± 0.15	15.25*
10	19.48 ± 0.10	18.89 ± 0.02	18.02 ± 0.02	17.57 ± 0.02	17.14 ± 0.02	–	–	–
11	15.21 ± 0.04	15.21 ± 0.02	14.71 ± 0.02	14.37 ± 0.02	14.03 ± 0.02	–	–	–
12	16.33 ± 0.05	15.74 ± 0.03	14.87 ± 0.02	14.42 ± 0.06	14.00 ± 0.05	13.24 ± 0.02	12.82 ± 0.03	12.74 ± 0.03
13	19.37 ± 0.07	18.77 ± 0.01	17.99 ± 0.02	17.52 ± 0.03	17.08 ± 0.03	16.35 ± 0.13	15.68 ± 0.13	15.93 ± 0.29
14	16.83 ± 0.04	16.79 ± 0.01	16.24 ± 0.03	15.92 ± 0.06	15.57 ± 0.02	14.95 ± 0.04	14.73 ± 0.06	14.79 ± 0.11
15	18.52 ± 0.04	17.84 ± 0.01	16.97 ± 0.03	16.46 ± 0.03	16.03 ± 0.03	15.26 ± 0.05	14.79 ± 0.07	14.70 ± 0.10

* No value for the uncertainty is given by the 2MASS catalogue.

Table 3.5: Sloan Vega magnitudes and associated errors for the stellar sequence used in the calibration process of SN 2011fu's photometry.

Star	u (mag)	g^* (mag)	r (mag)	i (mag)	z (mag)
1	–	–	17.20 ± 0.01	16.64 ± 0.01	16.28 ± 0.01
2	–	17.38 ± 0.01	17.15 ± 0.01	16.77 ± 0.01	16.52 ± 0.03
3	–	17.44 ± 0.01	17.22 ± 0.01	16.83 ± 0.01	16.59 ± 0.01
4	–	17.19 ± 0.01	16.63 ± 0.01	16.13 ± 0.01	15.82 ± 0.01
5	17.85 ± 0.02	17.04 ± 0.01	16.89 ± 0.01	16.54 ± 0.01	16.34 ± 0.02
6	15.52 ± 0.03	–	14.45 ± 0.01	14.06 ± 0.01	13.83 ± 0.01
7	17.59 ± 0.05	16.96 ± 0.01	16.75 ± 0.01	16.36 ± 0.01	16.12 ± 0.01
8	–	17.73 ± 0.01	16.83 ± 0.01	16.16 ± 0.01	15.71 ± 0.01
9	17.59 ± 0.05	16.88 ± 0.01	16.72 ± 0.01	16.38 ± 0.01	16.16 ± 0.02
10	–	17.96 ± 0.01	17.57 ± 0.01	17.12 ± 0.01	16.84 ± 0.03
11	15.05 ± 0.02	–	14.32 ± 0.02	13.98 ± 0.02	13.84 ± 0.04
12	16.15 ± 0.03	–	14.38 ± 0.04	13.97 ± 0.01	13.68 ± 0.01
13	–	17.87 ± 0.01	17.53 ± 0.01	17.05 ± 0.01	16.78 ± 0.02
14	–	–	15.88 ± 0.01	15.52 ± 0.01	15.29 ± 0.01
15	–	15.95 ± 0.01	16.46 ± 0.01	16.00 ± 0.01	15.71 ± 0.01

* The stars were only measured in one epoch in this band.

Table 3.6: Optical and NIR magnitudes of the minimum and secondary maximum of SN 2011fu, the corresponding times at which they occurred, and tail decline rates in the *BVRIz* LCs.

Band	$t^a_{\rm min}$ (d)	App. min. mag.[b] (mag)	$t^a_{\rm max}$ (d)	App. max. mag.[c] (mag)	Ab. max. mag.[d] (mag)	Decline tail (mag/100d)[e]
U	13.6 ± 1.1	17.90 ± 0.01	18.8 ± 0.8	17.29 ± 0.01	-17.58 ± 0.16	–
B	11.8 ± 1.0	17.96 ± 0.01	21.8 ± 1.6	17.52 ± 0.01	-17.26 ± 0.15	1.25 ± 0.07
V	10.6 ± 0.7	17.55 ± 0.01	22.9 ± 0.7	16.92 ± 0.01	-17.76 ± 0.15	1.78 ± 0.04
R	11.1 ± 2.1	17.18 ± 0.01	24.2 ± 1.2	16.53 ± 0.01	-18.08 ± 0.15	2.04 ± 0.04
I	11.4 ± 1.5	16.95 ± 0.01	24.1 ± 1.2	16.42 ± 0.01	-18.12 ± 0.15	1.97 ± 0.05
z	10.5 ± 0.7	17.29 ± 0.01	24.1 ± 1.0	16.29 ± 0.01	-18.22 ± 0.15	1.82 ± 0.04
J	–	–	24.5 ± 2.6	16.08 ± 0.01	-18.38 ± 0.15	–
H	–	–	29.6 ± 0.7	15.62 ± 0.01	-18.80 ± 0.15	–
K_s	–	–	29.2 ± 4.5	15.56 ± 0.01	-18.84 ± 0.15	–

[a] $t_{\rm min}$ and $t_{\rm max}$ are calculated with respect to our adopted explosion date JD $= 2455824.5 \pm 0.7$. The errors in the NIR are large due to less photometric coverage of the maxima.
[b] App. min. mag. = Apparent minimum magnitude.
[c] App. max. mag. = Apparent maximum magnitude.
[d] Ab. max. mag. = Absolute maximum magnitude estimated considering $\mu = 34.36 \pm 0.15$ mag and $E(B-V)_{\rm total} = 0.10^{+0.04}_{-0.03}$.
[e] Considering the interval starting ~ 40 d after explosion to ~ 160 d.

Table 3.7: List of spectroscopic observations of SN 2011fu.

Date	JD (+2400000.00)	Phase[a] (d)	Telescope+Instrument[b]	Grism+Filter	Spectral Range Å
2011/09/23	55828.3	3.8	AS1p82+AFOSC	g4	3500–8450
2011/09/24	55828.5	4.0	WHT+ISIS	R158R+R300B+gg495	3200–10000
2011/09/25	55830.4	5.9	AS1p82+AFOSC	g2+g4	3500–10200
2011/09/26	55831.3	6.8	AS1p82+AFOSC	g4	3500–8450
2011/09/29	55833.6	9.1	NOT+ALFOSC	g4	3200–9100
2011/09/30	55835.3	10.8	AS1p82+AFOSC	g2+g4	3500–10200
2011/10/01	55836.4	11.9	AS1p82+AFOSC	g4	3500–8450
2011/10/03	55838.5	14.0	AS1p82+AFOSC	g4	3500–8450
2011/10/06	55841.4	16.9	Ca2p2+CAFOS	B200+R200	3200–11000
2011/10/10	55844.6	20.1	NOT+ALFOSC	g4	3200–9100
2011/10/17	55851.5	27.0	Ca2p2+CAFOS	B200+R200	3200–11000
2011/10/17	55851.6	27.1	WHT+ACAM	V400	3500–9400
2011/10/24	55858.5	34.0	AS1p82+AFOSC	g4	3500–8450
2011/10/27	55862.4	37.9	NOT+ALFOSC	g4	3200–9100
2011/10/30	55864.6	40.1	AS1p82+AFOSC	g4	3500–8450
2011/10/31	55866.4	41.9	AS1p82+AFOSC	g4	3500–8450
2011/11/01	55867.4	42.9	Ca2p2+CAFOS	G200	3700–9500
2011/11/07	55872.5	48.0	WHT+ISIS	R158R+R300B+gg495	3200–10000
2011/11/15	55881.4	56.9	Ca2p2+CAFOS	G200	3700–9500
2011/11/20	55886.4	61.9	AS1p82+AFOSC	g4	3500–8450
2011/11/29	55894.5	70.0	NOT+ALFOSC	g4	3200–9100
2011/11/29	55895.4	70.9	Ca2p2+CAFOS	R200	6300–11000
2011/12/17	55913.5	89.0	TNG+DOLORES	LRR+LRB	3000–10000
2011/12/20	55916.4	91.9	AS1p82+AFOSC	g4	3500–8450
2011/12/21	55917.4	92.9	NOT+ALFOSC	g4+g5	3200–10250
2012/01/01	55928.4	103.9	Ca2p2+CAFOS	G200+gg495	4800–9500
2012/02/22	55980.3	155.8	AS1p82+AFOSC	g4	3500–8450
2012/07/20	56128.6	304.1	GTC+OSIRIS	R300B+R300R	3600–10000

[a] Phase with respect to our adopted explosion epoch JD = 2455824.5 ± 0.7.
[b] More information about the telescopes and instruments can be found in Section 2.2.

nights in which the seeing was not good or the SN was faint, so it is probably due to contamination from a nearby H II region.

Concerning the line at ∼ 6700 Å, in the models presented by Jerkstrand et al. (2015), there is an emission associated with [S II] λλ6716, 6731 about an order of magnitude weaker than the observed line. However, uncertainties in the temperature and ionization state might cause it to be stronger for SN 2011fu. Another possibility is due to contamination by the nearby H II region which we believe is causing the narrow Hα emission. In fact, in the 156 d spectrum both the narrow Hα and the ∼ 6700 Å feature have similar Full Width at Half Maximum (FWHM) and are unresolved, thus suggesting a common origin not related to the SN. Similar narrow Hα and [S II] λλ6716, 6731 emissions caused by nearby H II regions are detected, e.g. in the spectra of the type IIb SNe 1987K (Filippenko, 1988) and 2008ax (Milisavljevic et al., 2010). However, in H II regions, [S II] λλ6716, 6731 lines are less intense than Hα and this is not the case of the 304 d spectrum of SN 2011fu. In addition, the

line at $\sim$ 6700 Å at this phase is clearly resolved. For these reasons, an [S II] $\lambda\lambda$6716, 6731 emission associated with the SN is the favoured possibility at 304 d.

3.3.2 Line profiles

On the left-hand panel of Figure 3.4, we have presented the evolution of SN 2011fu's [O I] $\lambda\lambda$ 6300, 6364 nebular profile in velocity space. As seen in the figure, the profile shows two peaks, one at approximately 0 km s^{-1} and the other at ~ -2800 km s^{-1}. On the middle panel of Figure 3.4 we have shown the nebular profiles of [O I] λ5577 and Mg I] λ4571. Finally, on the right-hand panel of the figure we have artificially added a component with 1/3 the intensity of the original [O I] λ5577 and Mg I] λ4571 profiles and red-shifted by 3000 km s^{-1} in order to compare them with the [O I] $\lambda\lambda$6300, 6364 doublet.[2] As can be seen on this last panel, the shapes of the oxygen and magnesium profiles are quite similar to one another. Taubenberger et al. (2009) already found a great similarity between the oxygen and magnesium profiles in nebular spectra of some stripped envelope SNe, supporting the idea that Mg and O have similar spatial distributions within their ejecta, which is expected from the models (Maeda et al., 2006). Moreover, in the case of the type IIb SN 2011dh the components of the small-scale fluctuations of the [O I] $\lambda\lambda$6300, 6364 and Mg I] λ4571 in its late-time spectra coincide, which in addition to the results of Jerkstrand et al. (2015) implies that the oxygen lines are mostly formed in the O/Ne/Mg zone.

A possible explanation of the shape of the profiles of SN 2011fu is that the bulk of oxygen and magnesium is distributed in spherically symmetric expanding ejecta and that there is a clump with emission from both these elements expanding at $\sim$ 2800 km s^{-1} towards the observer. A second possibility is that the radioactivity exciting the lines is distributed asymmetrically. Given the similarity of the [O I] $\lambda\lambda$6300, 6364 and the [O I] λ5577 and Mg I] λ4571 when an artificial component is added to the last two, a Hα high-velocity absorption, as found by Maurer et al. (2010) for some type IIb SNe, may not be the main cause of the double-peaked [O I] $\lambda\lambda$6300, 6364 line, although it could contribute to the profile. On the other hand, the narrow blue-shifted component of the [O I] $\lambda\lambda$6300 carries a significant fraction of the flux even at 300 d. Residual opacity in the core or line blocking explains blue-shifted emission lines of stripped envelope and specifically type IIb SNe (Taubenberger et al. 2009; Jerkstrand et al. 2015). But in the case of SN 2011fu, the persistence of the blue shifted emission from the [O I] $\lambda\lambda$6300, 6364 line over time suggests some degree of asymmetry in the SN ejecta. So, in principle, either clumping or an asymmetrical distribution of the radioactive material seems to be

[2]The relative intensity of [O I] λ6364 to [O I] λ6300 can be 1 or 1/3 depending on whether the O I density is above or below n $\approx 10^{10}$ cm^{-3}, respectively (see e.g., Spyromilio 1991). At the times at which our spectra were taken it is reasonable to assume the intensity ratio between both lines to be 1:3, since O I densities can reasonably be assumed to be on the lower end (Taubenberger et al., 2009).

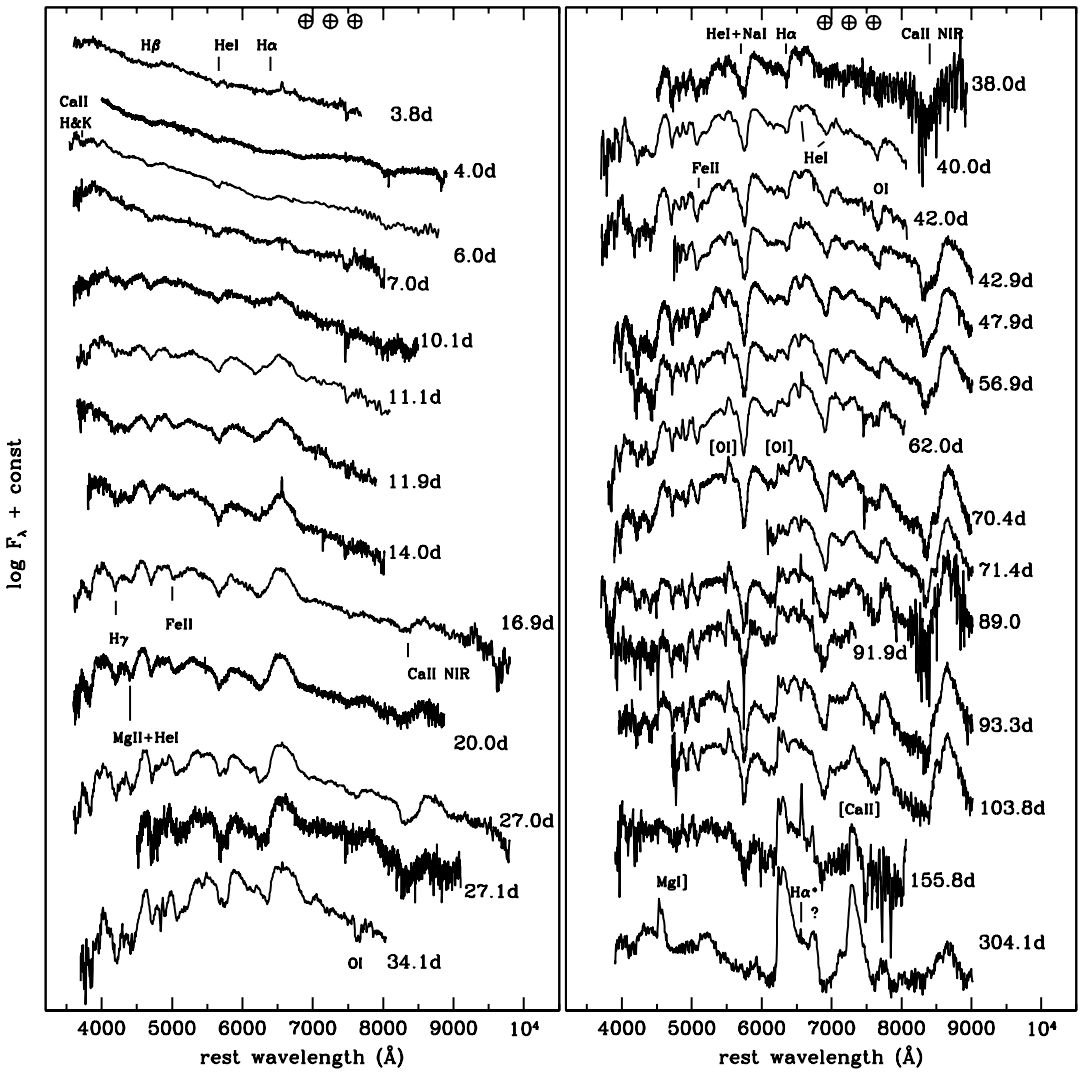

Figure 3.3: Optical spectral evolution of SN 2011fu, where the most relevant features in the spectra are indicated. The wavelengths at which there are residual telluric features have been marked with $\oplus$. The spectra have been corrected for the host galaxy redshift. Epochs indicated in the plot are with respect to our assumed explosion date of JD = 2455824.5$\pm$0.7. Spectra have been shifted vertically for clarity. Hα* is the narrow Hα emission, which we believe is associated to the H II region. The question mark at $\sim$ 6700 Å marks the line discussed in Section 3.3.1.

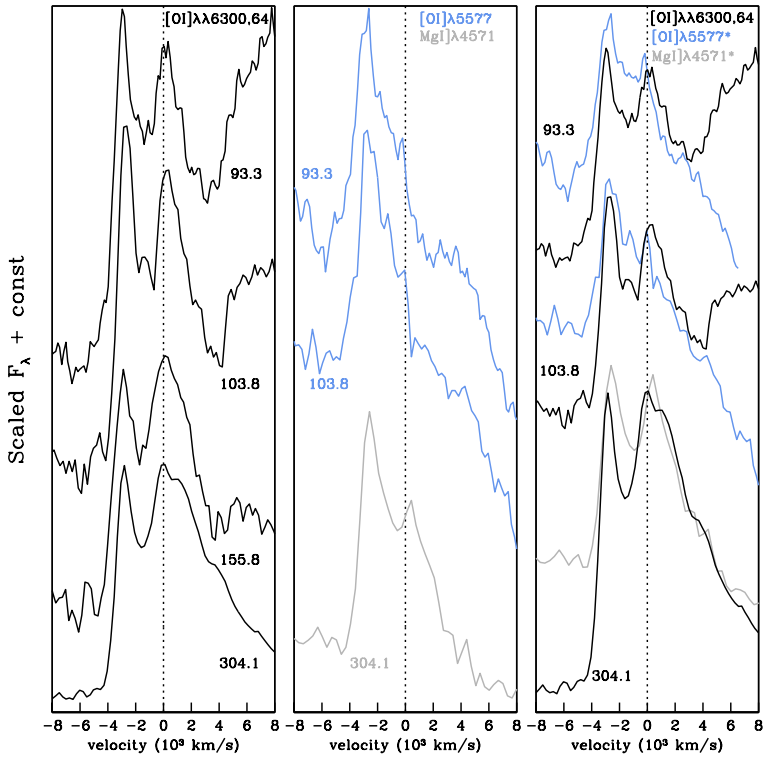

Figure 3.4: Late-time profiles of [O I] $\lambda\lambda$6300, 6364,[O I] λ5577, and Mg I] λ4571. Left-hand panel: evolution of the late-time profiles of [O I] $\lambda\lambda$6300, 6364 in velocity space. The 0 km s^{-1} vertical line corresponds to 6300 Å. Middle panel: [O I] λ5577 and Mg I] λ4571 profiles between 93 and 304 d since explosion. Right-hand panel: comparison of the [O I] $\lambda\lambda$6300, 6364 profiles with [O I] λ5577* and Mg I] λ4571*, which are the original profiles plus an artificial component, scaled to 1/3 the intensity and redshifted by 3000 km s^{-1}, added to account for the doublet nature of [O I] $\lambda\lambda$6300, 6364.

the most likely explanation for the profiles. Intriguingly, we have found two other SNe in the literature that have blue shifted double-peaked [O I] $\lambda\lambda$6300, 6364 profiles similar to SN 2011fu: types Ib SN 1996aq (Taubenberger et al., 2009) and SN 2005bf (Modjaz et al., 2008; Milisavljevic et al., 2010) at 216d. For SN 1996aq, Taubenberger et al. (2009) speculated that the most likely explanation for its profile shape is that a clump is moving in the line of sight at high velocity, and this is probably also the case for SNe 2011fu and 2005bf.

Finally, we note that the shape of SN 2011fu's [Ca II] $\lambda\lambda$7291, 7324 line (not shown in the figure) is not similar to the oxygen and magnesium profiles, implying that, as expected, they are forming at different locations within the ejecta.

3.4 Discussion

3.4.1 Hydrodynamical modelling of the pseudo-bolometric LC

To obtain the pseudo-bolometric optical-NIR LC, first we converted the apparent magnitudes of SN 2011fu (corrected for extinction) to effective fluxes. At the phases at which there were no data, the missing points were obtained by interpolation, or as in the cases of the U and u bands at more than ~ 90 d, and NIR prior and past secondary maximum, by extrapolation, assuming a constant colour from the data at the nearest epoch. The fluxes were integrated over wavelength following a trapezoidal rule, and finally converted to luminosities taking into account the adopted distance to the SN. The resulting pseudo-bolometric LC along with the hydrodynamical models used to fit it (explained below) are presented in Figures 3.5 (left panel) and 3.6.

One approach to derive physical parameters of SNe is to compare LCs and expansion velocities derived from hydrodynamical models with observations. From this comparison it is possible to constrain the explosion energy, the ejecta and the nickel masses as well as the distribution of the radioactive material. These parameters can be estimated by focusing the modelling around the "main peak" of the LC (i.e. the nickel powered phase). Information on the size of the progenitor is given by the post shock breakout cooling phase.

We calculated a set of hydrodynamical models, by integrating the hydrodynamical equations assuming a spherically symmetric self-gravitating gas, using as initial structures those derived from stellar evolutionary calculations. A one-dimensional Lagrangian Local Thermodynamic Equilibrium (LTE) radiation hydrodynamics code (Bersten et al., 2011) is used to explode the initial configuration. As pre-SN structure, we adopted helium (He) stars with a thin hydrogen envelope ($< 1\,\mathrm{M}_\odot$) which have successfully reproduced the LCs and the spectral features of other SNe IIb (see e.g. Shigeyama et al. 1994; Blinnikov et al. 1998, and more recently Bersten et al. 2012). The He core models used here were calculated by Nomoto & Hashimoto (1988) following the stellar evolution until the collapse of the core. We have smoothly attached a low-mass hydrogen-rich envelope in hydrostatic and thermal equilibrium to the He core to take into account the thin H-envelope required for an SN IIb. The SN explosion is produced by applying a certain amount of energy near the centre of the progenitor's core, which provokes a shock wave that propagates outward converting the internal and kinetic energy in energy radiated from the stellar surface. The thermalization of the γ-rays produced in the decay of $^{56}\mathrm{Ni}\rightarrow{}^{56}\mathrm{Co}\rightarrow{}^{56}\mathrm{Fe}$ provides another source of energy that is taken into account by including in the code γ-ray transfer in the grey approximation, that is assuming constant gamma-ray opacity. A mass cut of 1.5 $\mathrm{M}_\odot$ is assumed to collapse to form a neutron star or black hole after explosion. The code makes it possible to calculate consistently the shock wave propagation in the stellar interior, the shock breakout and the posterior phases of the LC evolution until the SN becomes nebular. An update of the micro physics (equation of state and

opacities) appropriate for the study of stripped-envelope SNe was incorporated in the code by Bersten et al. (2012). One-dimensional nucleosynthesis calculations lead to a ^{56}Ni distribution concentrated in the inner zones of the progenitor. However, Rayleigh-Taylor instabilities are expected to occur during shock-wave propagation, thus a certain degree of mixing of ^{56}Ni with the outer zones is believed to take place. To take into account this effect, we have assumed that 98 % of the total mass is mixed following a linear function of the radial coordinate, thus the amount of ^{56}Ni in the outer layers is in fact small.

First, we have focused our analysis on the modelling of the LC and the photospheric velocities around the secondary peak without taking into account the cooling part of the LC. The photospheric velocities are expected to be similar to those derived from the Fe II λ5169 line (see e.g. figure 14 of Dessart & Hillier 2005), which we have estimated from the minima of the lines' P-Cygni absorptions present in the object's spectra. Figure 3.5 shows the results of the LC modelling for three different He core masses, 4 (He4), 5 (He5), and 8 $M_\odot$ (He8), which correspond to the stellar evolution of single stars with main-sequence masses of 15, 18, and 25 $M_\odot$, respectively. For each model, different explosion energies and ^{56}Ni masses were explored. Here we show the best set of parameters for each of the models. Specifically, an explosion energy of 1, 1.3, and 2 foe (1 foe $= 1 \times 10^{51}$ erg), and a ^{56}Ni mass of 0.15 $M_\odot$ were found for model He4 (He4E1Ni15), He5 (He5E13Ni15), and He8 (He8E2Ni15), respectively.[3] As can be seen in the figure, model He5 provides the best representation of the observed data. The He8 model is too massive to reproduce the LC unless we assume a more energetic explosion but this would fail to fit the expansion velocities. On the other hand, a lower mass model, He4, gives a worse fit of the LC and underestimates the early photospheric velocities.

Our favoured model, He5, is a H-free object with an initial radius of ≈ 2 $R_\odot$. Although this model gives a good representation of the data around the secondary peak, it fails to reproduce the cooling phase due to the compact structure of the progenitor. Figure 3.6 shows the fits to the LC for models with different progenitor radius. The size of the progenitor was modified by attaching thin H-rich envelopes to the core of the He5 model (solid line). Note that the presence of a thin envelope mostly affects the shape of the LC during the cooling phase. Figure 3.6 shows models with radii of 400, 450, and 500 $R_\odot$ and envelope masses ($M_{\rm env}$) of ≈ 0.3 $M_\odot$. The model with $R = 450$ $R_\odot$ provides the closest match to the data. However, all the models give an initial peak brighter than the observations. The differences may be due to uncertainties in the bolometric calculation (note that we have no UV data for the SN, which are important at these early phases) or/and limitations of the model such as the LTE approximation or variation of the density profile of the outermost layers, among other possible reasons. It is noteworthy that to

[3] We have estimated the uncertainty of the model-derived ^{56}Ni mass by considering only the photometric errors to be 0.02 $M_\odot$.

reproduce the early phase of the LC it was not only needed to assume an extended envelope but it was also necessary to adopt a slightly more massive envelope than in previous modelling of SNe IIb, where e.g. $M_{\rm env} = 0.1$ M$_\odot$ was required for SN 2011dh and SN 1993J (Bersten et al. 2012; see also Nakar & Piro 2014). The need for a more massive envelope was mainly due to the high luminosity of the minimum after primary maximum of the LC. For lower $M_{\rm env}$, the cooling occurs faster and the minimum occurs at a lower luminosity even for a large radius. As mentioned in Section 3.1, we estimated the explosion epoch of SN 2011fu on the basis of the rise to first peak of its pseudo-bolometric LC. Models show that from explosion to a rising phase to a first (shock breakout) peak, approximately $\lesssim 1$ d goes by (see for example figure 10 of Blinnikov et al. 1998). This means that the first data point in our observed pseudo bolometric LC should have occurred $\lesssim 1$ d since explosion. Consistent time-scales for the first peak in SN 2011fu's pseudo-bolometric LC are obtained by choosing this point to have taken place 0.7 d after explosion, i.e. adopting as the explosion epoch JD $= 2455824.5 \pm 0.7$.

A summary of all the parameters obtained from the best core and envelope model that fit the observed LC is shown in Table 3.8. Similar to Kumar et al. (2013) we have obtained a kinetic energy which is relatively higher than that obtained for other type IIb SNe but still lower than that derived for SN 2011ei (Milisavljevic et al., 2013) and the type IIb hypernova SN 2003bg (Hamuy et al., 2009). Note that we have obtained a lower ^{56}Ni mass than Kumar et al. (2013) (0.21 M$_\odot$) possibly due to the different distance and extinction to SN 2011fu that we have adopted. On the other hand, our estimate of the ejected mass is larger than theirs (1.1 M$_\odot$).

Regarding the progenitor radius, core mass, and hydrogen envelope, we have obtained overall larger values than those obtained by Kumar et al. (2013) with analytical models. Specifically they obtained a progenitor radius of ~ 150 R$_\odot$, an He core mass of 1 M$_\odot$, and a hydrogen envelope mass of 0.1 M$_\odot$. But as they noted, their results should be considered only order-of-magnitude estimates. With hydrodynamical modelling, we obtained a radius that is three times larger and consistent with that of an extended supergiant similar to the progenitors of SNe 1993J (~ 600 R$_\odot$; Maund et al. 2004; Van Dyk et al. 2013) and 2013df (~ 550 R$_\odot$; Van Dyk et al. 2014). All in all, our calculations show that the progenitor of SN 2011fu was not a WR star but a supergiant.

3.4.2 Comparison with late-time spectral models

With the objective of further understanding the nature of the progenitor of SN 2011fu and its ejecta, we have compared the last three spectra of our sequence (104, 156, 304 d) to the late-time spectral models presented in Jerkstrand et al. (2015). These models are obtained with a code described in detail in Jerkstrand (2011) with updates reported in Jerkstrand et al. (2012) and Jerkstrand et al. (2014). In summary, the code computes energy deposition by radioactive isotopes in the ejecta using a Monte

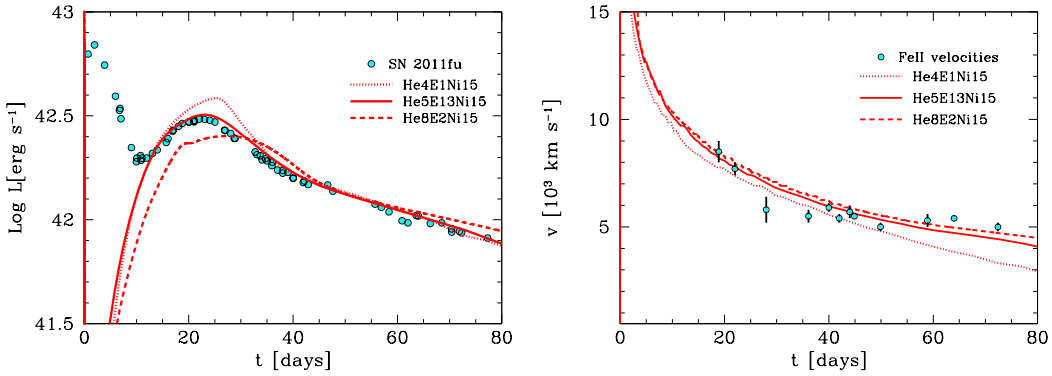

Figure 3.5: Left-hand panel: Observed bolometric light curve of SN 2011fu (dots) compared to the results of the light curve calculations for models He4E1Ni15 (dotted line), He5E13Ni15 (solid line) and He8E2Ni15 (dashed line), omitting the first peak. Right-hand panel: Evolution of the photospheric velocity for models He4E1Ni15 (dotted line), He5E13Ni15 (solid line) and He8E2Ni15 (dashed line) compared with measured Fe II line velocities of SN 2011fu (dots).

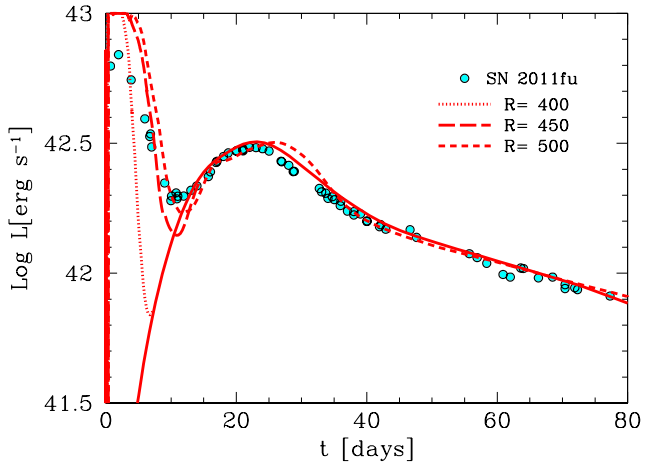

Figure 3.6: Observed bolometric LC of SN 2011fu (dots) compared to the bolometric LCs for models with the same physical parameters as our preferred model (He5E13Ni15; solid line), but with different initial radii. The radius variation is accomplished by attaching thin H-rich envelopes to the He5 model. An extended progenitor with $R \approx 450\,\mathrm{R}_\odot$ (long dashed) is needed to reproduce the cooling phase of SN 2011fu.

Table 3.8: Explosion parameters and progenitor properties for the best fitting models to the observed data of SN 2011fu.

Parameters	Explosion/Progenitor
$E_{\rm kin}$ (10^{51}erg)	1.3
^{56}Ni mass ($M_\odot$)	0.15
$M_{\rm ej}$ ($M_\odot$)	3.5*
Progenitor Radius ($R_\odot$)	450
Initial mass ($M_\odot$)	18
Hydrogen envelope mass ($M_\odot$)	0.3

*Assuming that 1.5 $M_\odot$ collapsed to form a compact remnant and the rest of the mass that formed the core was ejected.

Carlo simulation method to obtain the excitation, ionization, and heating rates. The input nucleosynthesis is given by the calculations of the evolution and explosion of solar metallicity, non-rotating stars with $M_{\rm ZAMS}$ in the range 12-17 $M_\odot$ given by Woosley & Heger (2007). The ejecta are divided in zones reflecting the layer composition resulting from both the stellar evolution and explosion simulations. In order to take into account the likely hydrodynamical mixing in the inner layers, the ejecta structure was divided in three main components, a mixed core, a partially mixed He envelope and an unmixed H envelope. The core contains metal zones, namely Fe/Co/He, SI/S, O/Si/S, O/Ne/Mg, and O/C designated after their most abundant elements. The He envelope is constituted by He/C and He/N zones. Finally, the H envelope also includes CNO burning products. The code does not include molecule formation reaction networks, instead molecule formation is parametrised by temperature cooling in the O/C and O/Si/S zones following the findings for SN 1987A. Two limiting cases are studied, complete molecular cooling and no molecular cooling. Both models with and without dust are investigated, with dust formation in the ejecta included in the models as a grey opacity in the core.

To begin with, we compared our spectra with the three models (best-fit to SN 2011dh) with the same settings for mixing, clumping, molecule, and dust, and differing only in progenitor mass (12, 13, and 17 $M_\odot$). These are models 12C, 13G, and 17A (see table 4 in Jerkstrand et al. 2015). In order to do this, we scaled the models accounting for differences in ^{56}Ni mass synthesized in the explosion, phase (if the difference in phase between models and spectra is Δt, the factor $\exp(-2\Delta t/111.4)$ is used to scale the models), and distances assumed for the models and the SN. The models have been calculated at a distance of 7.8 Mpc and assuming a ^{56}Ni mass of 0.075 $M_\odot$ (since they were constructed to compare with SN 2011dh), while in Section 3.4.1 we have estimated 0.15 ± 0.02 $M_\odot$ of ^{56}Ni from SN 2011fu. Overall, the model spectra are dimmer than the SN spectra. We note that for ^{56}Ni on the higher end of its uncertainty, the flux difference between modelled and observed spectra diminishes. Given that the errors in the extinction are not large, redenning uncertainty

is likely not to be the cause of the discrepancy between the flux levels. Another possibility is that the ejecta structure of SN 2011fu is different from the one used in the models and the IIb SNe fit with the models. Note that the Jerkstrand et al. (2015) models have an imposed dust extinction of $\tau = 0.25$ from 200 d. If no dust is produced in SN 2011fu this introduces a 25 % flux error for the last spectrum.

At all phases, the overall best-fitting model is 13G. The oxygen lines produced by the 17A model are more intense than those observed, while the 12C model underestimates the oxygen intensities. In Figure 3.7, we present the three late-time SN spectra compared to the 13G spectral models at coeval phase. We have also indicated in the plot some of the most important features that arise in the late spectral modelling.[4] In the middle panel of the figure we have also plotted model 17A and 12C to reflect the discrepancy between the oxygen lines of the model and those observed of the spectrum. In Figure 3.8 we present a comparison of the [O I] $\lambda\lambda$ 6300, 6364 late-time luminosities of SN 20111fu and those corresponding to models 12C, 13G and 17A. All in all, these comparisons indicate that the progenitor of SN 2011fu was probably at the lower end of the tested range, with $M_{ZAMS} \sim 13$ $M_\odot$. The model that best fits the observed LC, however, corresponds to a progenitor star with a 5 $M_\odot$ He core, i.e. $M_{ZAMS} = 18$ $M_\odot$. This value is higher but not inconsistent with the estimate we have obtained here. In fact, it is not surprising to have found different values for the progenitor's initial mass since the initial conditions and the methodology used in both modelling methods are rather different. The hydrodynamical modelling of the LC uses stellar evolutionary models with different progenitor M_{ZAMS} and explodes these structures for different values of explosion energies and nickel masses to compare with the data of SN 2011fu. The greatest degeneracy in the model is between mass and energy. This is the reason for modelling both the LC and the expansion velocities. Another source of uncertainty is introduced by the initial stellar evolutionary models. The code treats in a very approximate way the radiation transportation but correctly simulates the explosion hydrodynamics from the propagation of the shock wave and ejection of the envelope.

The nebular spectral models use ejecta with nucleosynthesis from the evolution and explosion of stars of different M_{ZAMS}. While the dynamic structure of the core is manually arranged to match the observed metal line widths in type IIb SNe (~ 3500 km s^{-1}), as well as to capture effects of macroscopic mixing and clumping seen in 2D simulations and inferred from observed line profiles, the envelope follows a profile obtained in a 1D explosion simulation by Bersten et al. (2012). Uncertainty is introduced by two sources: the dynamic structure of the ejecta and the margin of error in the spectral modelling. Since the model reproduces well the metal line profiles of SN 2011fu, the core velocity of 3500 km s^{-1} is likely to be accurate. The envelope absorbs quite little of the gamma-ray energy (see appendix A in Jerkstrand

[4] Hα* is the narrow Hα emission which we believe is associated with an H II region. The question mark at ~ 6700 Å marks the line we discussed in Section 3.3.1.

et al. 2015), so an uncertainty in its density profile introduces only a moderate dispersion for the flux levels. Thus, the model uncertainty is likely to be dominated by the error in the ^{56}Ni mixing as well as by molecule and dust formation. The ^{56}Ni mixing used in 13G is chosen to match both the diffusion phase LC and the nebular spectra of SN 2011dh, but may be somewhat different in SN 2011fu.

It would be interesting to analyse whether the differences between the two modelling approaches persist if the post-explosion density structure of our preferred LC model for SN 2011fu is used as the initial condition of the spectral modelling. However, this analysis is beyond the scope of this work. In any case, the mass estimates obtained from the two methods are consistent in the sense that we can discard the possibility of the progenitor being a single WR star (with $M_{\mathrm{ZAMS}} \geq 25$ M$\odot$).

To check for evidence of molecule formation in the ejecta of the SN, we compared models 12C (no molecular cooling; see table 4 of Jerkstrand et al. 2015) and 12D (with molecular cooling) with our late-time spectra. In the bottom panel of Figure 3.7 the comparison at 300 d is shown. The oxygen lines are the ones that are most sensitive to molecule formation at 100 and 150 d along with [C I] λ8727 at 300 d. In our case, the model without molecular cooling is favoured, similarly to the case of SN 2011dh. We also looked at the contrast factor or oxygen zone density, i.e. the density ratio between the metal zones in the core and the Fe/Co/He zone, but the models with different oxygen zone densities do not show palpable differences. However, we do note that the Mg I] λ4571 line at 304 d is quite strong, which favours a high oxygen zone density, since the line is quite sensitive to this parameter, and this is in agreement with the results found for SN 2011dh in Jerkstrand et al. (2015).

In summary, the comparisons of our nebular spectra with the models presented in Jerkstrand et al. (2015) point to a progenitor with an initial mass of ~ 13 M$_\odot$. Probably no molecules were formed in the ejecta, and the oxygen zone density was possibly high.

3.5 Summary

In this chapter we have analysed optical and NIR data for the double-peaked type IIb SN 2011fu spanning from a few to approximately 300 d after explosion.

The first peak in the V band LC occurred ~ 2.3 d after our estimated explosion date and reached an absolute magnitude of -18.06 mag. Subsequently the LC underwent a decline, reaching a minimum ~ 10.6 d after explosion, and then re-brightened to a secondary maximum at -17.76 mag ~ 23 d after explosion. Afterwards the LC declined, specifically the LC tail followed a decline rate of 1.78 ± 0.04 mag 100d^{-1}.

SN 2011fu's spectra evolve in a similar fashion to those of SN 1993J (see e.g. Barbon et al. 1995). During the first phases after explosion Balmer, He, Ca, and Fe lines are present in the spectra. At around 40 d, He lines dominate the spectra although Hα is still present and persists up to later phases. Forbidden oxygen lines

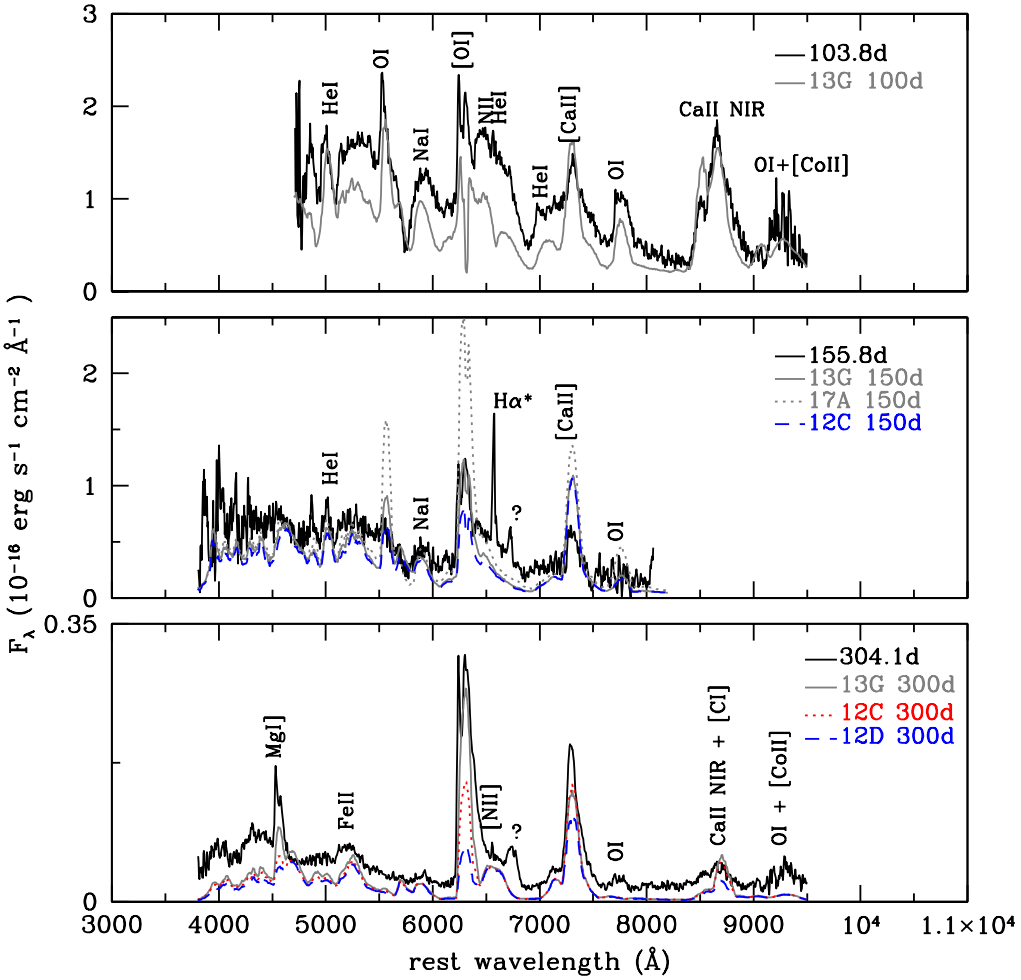

Figure 3.7: Late-time spectra of SN 2011fu compared to the best fitting spectral model 13G presented in Jerkstrand et al. 2015. In the middle panel we show our spectrum at $\sim$ 156 d and the three models that vary only in progenitor mass. In the bottom panel other than model 13G, we show models 12C and 12D, which are the ones used to study molecule formation in the SN ejecta. The spectral models have been scaled accounting for difference in phase with respect to the SN spectra (Δt) by the factor $\exp(-2\Delta t/111.4)$, difference in ^{56}Ni synthesized mass, and distance assumed for the models and the SN.

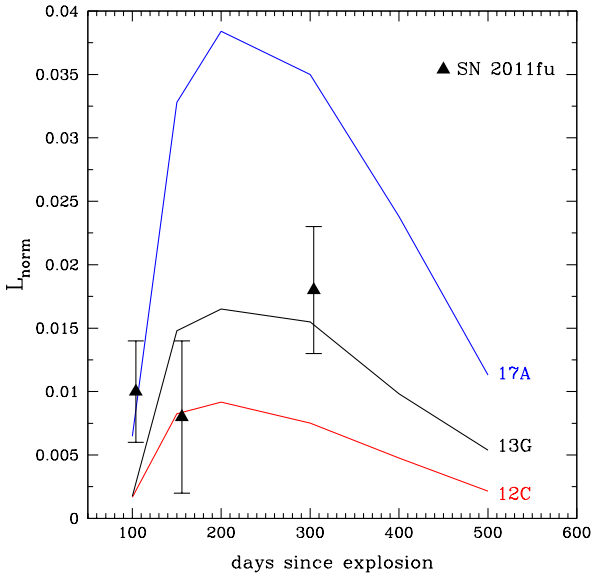

Figure 3.8: Late-time [O I] $\lambda\lambda$6300, 6364 luminosities of SN 2011fu (triangles) compared to the model tracks 12C, 13G, and 17A of Jerkstrand et al. 2015.

are clearly visible at $\sim$ 62 d, which indicates that the SN is entering the nebular phase. At late times the most important features are [O I] $\lambda\lambda$ 6300, 6364, and [Ca II] $\lambda\lambda$7291, 7324. In addition in our latest spectrum taken at 304 d, Mg I] λ4571 and a line that could be due to [S II] $\lambda\lambda$6713, 6730 are detected.

The nebular profiles of oxygen and magnesium indicate that the oxygen/magnesium zone is clumped. Calcium lines do not show similar profiles indicating, as expected, that they are formed at a different location.

Thanks to the hydrodynamical modelling of the pseudo-bolometric LC we conclude that SN 2011fu was the explosion of an extended object ($R \approx 450$ R$_\odot$), with an He core mass of 5 M$_\odot$ ($M_{\rm ZAMS} \approx 18$ M$_\odot$) and an ejecta mass of 3.5 M$_\odot$, an explosion energy of 1.3 $\times 10^{51}$ erg, and a ^{56}Ni mass of 0.15 M$_\odot$. The stellar envelope of its progenitor ($\sim$ 0.3 M$_\odot$) also seems to have been more massive than for other type IIb SNe (see e.g. Bersten et al. 2012), implying the presence of more H in the SN ejecta.

We have compared our late-time spectra ($\geq$100 d) with late-time spectral models for type IIb SNe presented in Jerkstrand et al. (2015). From this analysis, the overall best fitting value of the progenitor mass is 13 M$_\odot$, similar to the $M_{\rm ZAMS}$ values that have previously been derived for SNe 1993J, 2008ax, and 2011dh (12-16 $M_{\rm ZAMS}$, Jerkstrand et al. 2015). As for these other IIb SNe, we find also for SN 2011fu that molecule formation is non-existent.

The extensive dataset of SN 2011fu presented in this chapter have permitted us to

derive some of the characteristics of the ejecta of one more type IIb SN presenting a double-peaked LC, as well as to set constraints on some of its progenitor's properties. SN 2011fu is another example of a type IIb SN which shows evidence that the progenitor mass was in the range 13-18 $M_{\odot}$. This is in the higher range of stars that are seen to explode (Smartt, 2015), which supports type IIb progenitor detections being significantly more luminous than the II-P progenitors. Furthermore, as for all previously modelled IIb SNe, we have determined a M_{ZAMS} value much lower that what would have been needed for a wind-stripped WR progenitor, and evidence is piling up that most, if not all, type IIb SNe come from binary stripped progenitors.

Chapter 4

SN 2013df

In this chapter we present the results of the analysis of our observational data for SN 2013df, which have also been published in Morales-Garoffolo et al. (2014) and Morales-Garoffolo et al. (2015b). We begin with a short introduction of the SN, next we describe our photometric and spectroscopic results, and we finish with an estimation of some constraints on the SN progenitor's characteristics.

4.1 SN 2013df: distance, reddening, and explosion date

SN 2013df (Figure 4.1), having coordinates $\alpha = 12^{\rm h}26^{\rm m}29.33^{\rm s}$ and $\delta = +31^{\rm o}13'38.''3$ (J2000), was discovered in the galaxy NGC 4414 by F. Ciabattari and E. Mazzoni of the ISSP, on 2013 June 7.87 UT (Ciabattari et al., 2013). SN 2013df is the second SN discovered in NGC 4414, the first being the type Ia SN 1974G. A spectrum of SN 2013df taken soon after discovery (2013 June 10.8 UT) showed characteristics of a type II supernova resembling early spectra of the type IIb SN 1993J (Ciabattari et al., 2013). The identification of the probable 13–17 $M_\odot$ yellow supergiant precursor of SN 2013df as well as some early time optical data of the transient were presented in Van Dyk et al. (2014). Soon after discovery of the SN, X-ray detection coming from a source at the SN position (2.1 arcsec offset) was reported by Li & Kong (2013). The absorption corrected average luminosity (0.3–10 keV) of their observations, which spanned from 2013 June 13 to 2013 June 19, was 7×10^{39}erg s^{-1}, falls in the range of other X-ray detected SNe. A recent analysis of the X-ray and radio emission arising from SN 2013df during the interval between 10 and 250 d after explosion has been published in Kamble et al. (2015). Modelling of the observed radio and X-ray data presented in this manuscript suggest that the progenitor of SN 2013df suffered significant mass loss in the years prior to explosion.

We have adopted $\mu = 31.65 \pm 0.30$ mag as the distance modulus to NGC 4414. This estimate was obtained as the weighted mean value of distance moduli provided by NED. The heliocentric redshift for SN 2013df is assumed to be that of its host

Table 4.1: Magnitudes and associated errors in the Johnson-Cousins and Sloan systems of the stellar sequence used in the calibration process of SN 2013df's photometry.

Band (mag)	1	2	3	4	5
U		16.41 ± 0.04	16.47 ± 0.04	16.55 ± 0.04	
B	17.36 ± 0.03	16.40 ± 0.04	15.88 ± 0.03	16.62 ± 0.05	17.74 ± 0.04
V	15.83 ± 0.02	15.78 ± 0.03	14.87 ± 0.02	16.01 ± 0.03	16.29 ± 0.03
R	14.73 ± 0.02	15.33 ± 0.02	14.29 ± 0.03	15.70 ± 0.03	15.48 ± 0.02
I	13.28 ± 0.02	14.97 ± 0.02	13.74 ± 0.02	15.31 ± 0.02	14.71 ± 0.02
u	19.49 ± 0.01*	17.43 ± 0.06	17.32 ± 0.03		
r	15.24 ± 0.02	15.68 ± 0.01	14.59 ± 0.01		
i	14.04 ± 0.06	15.50 ± 0.01	14.28 ± 0.03		

* The star was only measured in one epoch.

galaxy as given by NED ($v_{recession} = 716 \pm 6$ km s^{-1}). The reddening in the line of sight of the SN due to the Milky Way (Schlafly & Finkbeiner, 2011) is $E(B-V)_{MW} = 0.017 \pm 0.001$ mag. Thus, adopting $E(B-V)_{NGC\ 4414} = 0.081 \pm 0.016$ mag as the SN reddening in the host-galaxy (Van Dyk et al., 2014), we assume in the rest of this manuscript $E(B-V)_{Total} = 0.098 \pm 0.016$ mag as the total reddening toward SN 2013df.

To estimate the explosion date of SN 2013df we rely on the similarity of its R band light curve with that of SN 1993J. In Figure 4.3 we compared the template for type IIb SN LCs derived from the R band data of SN 1993J in Li et al. (2011), and the early time data for SN 2013df. As can be seen in the figure, similarly to SN 1993J, we perceive the rise to the first maximum in the LC of SN 2013df. Assuming that the rise to the first peak in the R band is the same in SN 1993J and SN 2013df, we estimate that the explosion of SN 2013df took place on JD = 2456450.0 ± 0.9 (2013 June 6.50 UT). This date is consistent with the discovery date on 2013 June 7.87 UT (JD = 2456451.37) and the last non-detection of the SN (2013 May 25 UT down to a magnitude of 18.5, Van Dyk et al. 2014). We also ran comparisons between our sequence of spectra and those in Supernova Identification (SNID; Blondin & Tonry 2007) and GEneric cLAssification TOol (GELATO; Harutyunyan et al. 2008) and our estimated explosion date is consistent with the phases of the best fitting spectra found in those databases. So, we adopt JD = 245650.0 ± 0.9 as the explosion date of SN 2013df and use it as reference in the rest of the chapter.

4.2 Photometric results

4.2.1 UV-optical light curves

The optical *UBVRI* and *SWIFT UVW2*, *UVM2*, *UVW1* light curves of SN 2013df spanning from discovery up to approximately 250 d post discovery are shown in Figure 4.2. The SN UV magnitudes along with their errors are shown in Table

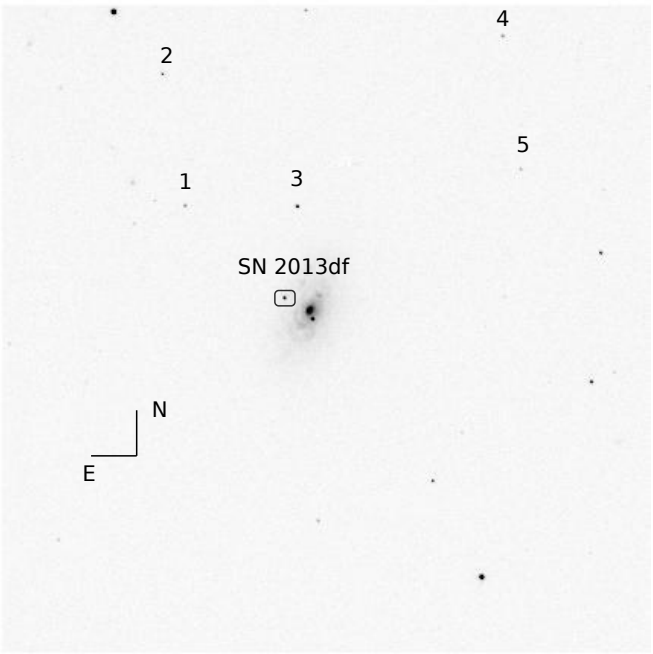

Figure 4.1: V band image of NGC 4414 taken with TJO+MEIA on 2013 June 20. The stars used for the photometric calibration of SN 2013df are labelled, and the field of view is approximately $12'.3 \times 12'.3$.

4.2. The optical apparent magnitudes together with their errors are reported in Table 4.3. The calibration of the optical photometry was done by using the stellar sequence shown in Figure 4.1 and whose magnitudes are presented in Table 4.1. We have included some filtered and unfiltered amateur data in our optical LCs. Note that *uri* Sloan data obtained at the LT (presented in Table 4.4) have been approximated to the Johnson Cousins (JC) *URI* by using the relations in Jordi et al. (2006) and then added to the *UBVRI* light curves of Figure 4.2 using filled symbols. The transformations in Jordi et al. (2006) are colour transformations between *ugriz* Sloan Digital Sky Survey (SDSS) photometry and JC photometry. When applied to our stellar sequence, we found a fair agreement with our own JC photometry (differences ranging $\sim$ 0.1-0.3 mag). The transformations seem to work fairly well for our SN photometry, specially at early phases, although they still should be considered approximations.

Table 4.2: *SWIFT* UV photometry of SN 2013df taken with UVOT on board *SWIFT* + MIC.

Date	JD (+2400000.00)	Phase[a] (d)	*UVW2* (mag)	*UVM2* (mag)	*UVW1* (mag)
2013/06/13	56456.90	6.9	15.57 ± 0.08	15.21 ± 0.06	14.77 ± 0.06
2013/06/15	56459.35	9.4	16.32 ± 0.08	16.00 ± 0.07	15.50 ± 0.07
2013/06/16	56460.17	10.2	16.35 ± 0.08	16.10 ± 0.07	15.37 ± 0.07
2013/06/18	56461.75	11.7	16.67 ± 0.09		
2013/06/19	56462.82	12.8	16.73 ± 0.10		
2013/06/20	56463.82	13.8	16.81 ± 0.09	16.58 ± 0.07	15.72 ± 0.07
2013/06/22	56466.19	16.2	16.82 ± 0.09	16.45 ± 0.08	15.79 ± 0.07
2013/06/24	56467.97	18.0	16.91 ± 0.09	16.63 ± 0.09	15.76 ± 0.07
2013/06/26	56469.56	19.6	17.08 ± 0.09	16.81 ± 0.08	15.95 ± 0.07
2013/06/30	56474.29	24.3	17.25 ± 0.09	16.99 ± 0.08	16.15 ± 0.07
2013/07/02	56475.91	25.9	17.49 ± 0.09	17.15 ± 0.09	16.43 ± 0.07
2013/07/04	56478.13	28.1	17.68 ± 0.11	17.39 ± 0.09	16.44 ± 0.08
2013/07/06	56479.76	29.8	17.70 ± 0.10	17.54 ± 0.09	16.60 ± 0.08
2013/07/08	56481.76	31.8	17.76 ± 0.10	17.43 ± 0.09	16.81 ± 0.09
2013/07/10	56484.25	34.2	18.18 ± 0.14	17.72 ± 0.14	17.01 ± 0.09
2013/07/12	56486.33	36.3	17.97 ± 0.13	17.73 ± 0.12	16.96 ± 0.10
2013/07/14	56487.64	37.6	17.84 ± 0.11	17.67 ± 0.11	17.11 ± 0.09
2013/07/16	56489.75	39.8	18.20 ± 0.17	17.73 ± 0.14	17.16 ± 0.09
2013/07/23	56496.68	46.7	18.29 ± 0.11	18.11 ± 0.09	17.39 ± 0.09
2013/07/27	56501.03	51.0	18.25 ± 0.17	18.01 ± 0.15	17.44 ± 0.11
2013/07/31	56504.73	54.7	18.23 ± 0.10	18.28 ± 0.10	17.57 ± 0.09
2013/08/04	56509.43	59.4	18.83 ± 0.39	18.68 ± 0.32	17.39 ± 0.22
2013/08/06	56511.01	61.0	18.49 ± 0.11	18.24 ± 0.09	17.59 ± 0.09

[a]Phase in days with respect to the adopted explosion date JD = 2456450.0 ± 0.9.

Table 4.3: Optical Johnson Cousins photometry of SN 2013df.

Date	JD	Phase[a]	U	B	V	R	I	Instrum.[b]
	(+2400000.00)	(d)	(mag)	(mag)	(mag)	(mag)	(mag)	
2013/06/07	56451.37	1.4				14.25 ± 0.08		F.C.
2013/06/08	56452.40	2.4				13.77 ± 0.07		S.D.
2013/06/09	56453.03	3.0				13.74 ± 0.08		K.I.
2013/06/09	56453.41	3.4			14.10 ± 0.01			S.H. T18
2013/06/10	56453.57	3.6		14.36 ± 0.30	14.20 ± 0.24	13.85 ± 0.23		N.S.
2013/06/10	56454.70	4.7			14.46 ± 0.18			S.H. T5
2013/06/11	56455.43	5.4		14.55 ± 0.09	14.53 ± 0.02	14.11 ± 0.07	13.96 ± 0.06	MEIA
2013/06/12	56456.42	6.4	14.11 ± 0.06	14.77 ± 0.08	14.55 ± 0.02	14.34 ± 0.04	14.13 ± 0.06	MEIA
2013/06/12	56456.70	6.7			14.55 ± 0.30			S.H. T5
2013/06/13	56456.57	6.6		15.05 ± 0.21	14.40 ± 0.11	14.37 ± 0.06		N.S.
2013/06/13	56456.90	6.9	14.15 ± 0.05	14.98 ± 0.04	14.73 ± 0.04			UVOT
2013/06/14	56458.43	8.4	14.66 ± 0.03	15.22 ± 0.01		14.62 ± 0.01	14.39 ± 0.01	MEIA
2013/06/15	56459.35	9.4	14.79 ± 0.05	15.40 ± 0.04	15.02 ± 0.05			UVOT
2013/06/15	56459.43	9.4	14.67 ± 0.05	15.24 ± 0.11	14.95 ± 0.03	14.66 ± 0.03	14.51 ± 0.06	MEIA
2013/06/16	56460.42	10.4	14.79 ± 0.06	15.31 ± 0.01				MEIA
2013/06/16	56460.17	10.2	14.88 ± 0.05	15.41 ± 0.05	15.06 ± 0.05			UVOT
2013/06/17	56460.59	10.6		15.45 ± 0.03	14.98 ± 0.11	14.50 ± 0.21		N.S.
2013/06/18	56461.92	11.9	15.16 ± 0.08	15.34 ± 0.01	14.87 ± 0.01	14.42 ± 0.02	14.46 ± 0.03	RATCam
2013/06/20	56463.82	13.8	15.14 ± 0.05	15.39 ± 0.04	14.85 ± 0.05			UVOT
2013/06/20	56463.88	13.9		15.31 ± 0.02	14.77 ± 0.11	14.34 ± 0.07	14.44 ± 0.03	RATCam
2013/06/22	56465.92	15.9	15.20 ± 0.32	15.25 ± 0.02	14.63 ± 0.01	14.38 ± 0.08	14.21 ± 0.04	RATCam
2013/06/22	56466.19	16.2	15.21 ± 0.06	15.28 ± 0.05	14.65 ± 0.05			UVOT
2013/06/22	56466.42	16.4	15.03 ± 0.07	15.26 ± 0.11	14.61 ± 0.03	14.26 ± 0.04	14.13 ± 0.06	MEIA
2013/06/23	56467.42	17.4	15.13 ± 0.09	15.18 ± 0.11	14.65 ± 0.06	14.24 ± 0.04	14.16 ± 0.07	MEIA
2013/06/24	56467.97	18.0	15.35 ± 0.05	15.31 ± 0.04	14.55 ± 0.06			UVOT
2013/06/24	56468.42	18.4	15.15 ± 0.08	15.15 ± 0.11	14.57 ± 0.04	14.19 ± 0.04	14.12 ± 0.07	MEIA
2013/06/24	56468.42	18.4	15.32 ± 0.04	15.18 ± 0.23	14.67 ± 0.08	14.21 ± 0.04	14.18 ± 0.08	TNG
2013/06/25	56469.42	19.4	15.14 ± 0.07	15.13 ± 0.13	14.57 ± 0.04	14.17 ± 0.04	14.06 ± 0.06	MEIA
2013/06/26	56469.56	19.6	15.39 ± 0.06	15.22 ± 0.05	14.63 ± 0.05			UVOT
2013/06/26	56470.42	20.4	15.18 ± 0.10	15.20 ± 0.11	14.55 ± 0.03	14.16 ± 0.08	14.02 ± 0.06	MEIA
2013/06/28	56472.44	22.4	15.39 ± 0.05	15.30 ± 0.03	14.55 ± 0.02	14.22 ± 0.12	14.03 ± 0.04	AFOSC
2013/06/29	56473.42	23.4	15.40 ± 0.07	15.47 ± 0.13	14.62 ± 0.03	14.18 ± 0.04	14.08 ± 0.06	MEIA
2013/06/30	56474.29	24.3	15.78 ± 0.06	15.60 ± 0.05	14.76 ± 0.05			UVOT
2013/06/30	56474.42	24.4	15.69 ± 0.16	15.63 ± 0.14	14.68 ± 0.03	14.22 ± 0.05	14.08 ± 0.07	MEIA
2013/07/02	56475.91	25.9	16.07 ± 0.06	15.87 ± 0.05	14.94 ± 0.05			UVOT
2013/07/03	56477.42	27.4	16.19 ± 0.09	15.98 ± 0.14	15.02 ± 0.04	14.43 ± 0.05	14.26 ± 0.07	MEIA
2013/07/03	56478.13	28.1	16.39 ± 0.08	16.20 ± 0.06	15.11 ± 0.06			UVOT

Table 4.3: (continued)

Date	JD (+2400000.00)	Phase[a] (d)	U (mag)	B (mag)	V (mag)	R (mag)	I (mag)	Instrument[b]
2013/07/04	56478.42	28.4	16.27 ± 0.10	16.16 ± 0.13	15.15 ± 0.05	14.55 ± 0.07	14.43 ± 0.07	MEIA
2013/07/05	56479.42	29.4	16.48 ± 0.11	16.34 ± 0.13	15.23 ± 0.04	14.55 ± 0.05	14.52 ± 0.04	MEIA
2013/07/05	56479.76	29.8	16.78 ± 0.09	16.32 ± 0.06	15.35 ± 0.06			UVOT
2013/07/06	56480.42	30.4	16.49 ± 0.08	16.48 ± 0.15	15.34 ± 0.06	14.65 ± 0.02	14.50 ± 0.06	MEIA
2013/07/07	56480.58	30.6		16.40 ± 0.16	15.43 ± 0.06	14.60 ± 0.09		N.S.
2013/07/07	56481.42	31.4	16.66 ± 0.10	16.62 ± 0.14	15.43 ± 0.10	14.73 ± 0.20	14.51 ± 0.04	MEIA
2013/07/08	56481.76	31.8	16.82 ± 0.09	16.63 ± 0.06	15.52 ± 0.06			UVOT
2013/07/09	56482.58	32.6		16.73 ± 0.11	15.52 ± 0.20	14.96 ± 0.25		N.S.
2013/07/10	56484.25	34.2	17.06 ± 0.10	16.93 ± 0.07	15.84 ± 0.09			UVOT
2013/07/12	56486.33	36.3	17.20 ± 0.14	17.00 ± 0.09	15.73 ± 0.08			UVOT
2013/07/14	56487.64	37.6	17.24 ± 0.12	17.05 ± 0.08	15.79 ± 0.07			UVOT
2013/07/15	56488.58	38.6		17.05 ± 0.03	15.80 ± 0.22	15.26 ± 0.22		N.S.
2013/07/16	56489.75	39.8	17.33 ± 0.11	17.18 ± 0.10	16.18 ± 0.11			UVOT
2013/07/18	56492.38	42.4		17.19 ± 0.07	15.99 ± 0.03	15.30 ± 0.20	14.93 ± 0.05	AFOSC
2013/07/20	56493.93	43.9	17.77 ± 0.17	17.33 ± 0.02	16.03 ± 0.09	15.25 ± 0.01	15.18 ± 0.01	IO:O
2013/07/23	56496.68	46.7	17.62 ± 0.11	17.26 ± 0.07	16.19 ± 0.06			UVOT
2013/07/22	56496.42	46.4		17.39 ± 0.19	16.13 ± 0.07	15.37 ± 0.07	15.08 ± 0.08	MEIA
2013/07/22	56495.94	45.9	17.89 ± 0.20	17.34 ± 0.04	16.05 ± 0.04	15.34 ± 0.01	15.16 ± 0.02	IO:O
2013/07/24	56498.40	48.4	17.57 ± 0.10	17.41 ± 0.17	16.13 ± 0.11		15.11 ± 0.08	MEIA
2013/07/27	56501.03	51.0	17.75 ± 0.21	17.50 ± 0.13	16.23 ± 0.11			UVOT
2013/07/29	56503.40	53.4		17.46 ± 0.16	16.27 ± 0.04	15.49 ± 0.06	15.17 ± 0.07	MEIA
2013/07/30	56504.40	54.4		17.40 ± 0.16		15.56 ± 0.01	15.20 ± 0.05	MEIA
2013/07/31	56504.73	54.7	17.77 ± 0.11	17.50 ± 0.07	16.38 ± 0.07			UVOT
2013/08/06	56511.01	61.0	17.78 ± 0.11	17.54 ± 0.07	16.52 ± 0.07			UVOT
2013/11/20	56617.21	167.2		18.73 ± 0.07	18.28 ± 0.06	17.88 ± 0.04	17.01 ± 0.03	IO:O
2013/12/05	56632.72	182.7			18.42 ± 0.07	17.92 ± 0.05	17.12 ± 0.09	AFOSC
2013/12/12	56638.68	188.7		19.18 ± 0.04	18.81 ± 0.04	17.97 ± 0.04	17.19 ± 0.12	AFOSC
2013/12/18	56645.13	195.1		19.10 ± 0.07	18.69 ± 0.04	18.34 ± 0.04	17.38 ± 0.04	IO:O
2013/12/25	56652.28	202.3		19.30 ± 0.07	18.84 ± 0.06	18.51 ± 0.05	17.46 ± 0.03	IO:O
2014/01/08	56666.73	216.7		19.51 ± 0.09	19.23 ± 0.05	18.39 ± 0.03	17.55 ± 0.13	AFOSC
2014/01/27	56685.21	235.2		19.62 ± 0.08	19.44 ± 0.08	19.10 ± 0.06	18.03 ± 0.05	IO:O
2014/02/11	56700.17	250.2		20.07 ± 0.08	19.91 ± 0.08	19.38 ± 0.08	18.28 ± 0.06	IO:O

[a] Phase in days with respect to the adopted explosion date JD = 2456450.0 ± 0.9

[b] F.C. = 0.5 m Newtonian + FLI Proline; S.D. = 0.3 m Schmidt Cassegrain + SBIG ST10; S.H. T18 = 0.25 m Telescope + ST10; K.I. = Itagaki Astronomical Observatory + KAF-1001E; N.S. = 0.20 m Schmidt Newtonian + Orion Star Shoot Pro V2; S.H. T5 = 0.32 m Telescope + SBIG STL-6303; MEIA = TJO 0.82 m + MEIA; RATCam = LT 2.2 m + RATCam; LRS = TNG 3.58 m + LRS; AFOSC = Asiago 1.82 m + AFOSC; IO:O = LT 2.2 m + IO:O; UVOT = UVOT on board *SWIFT* + MIC. More details in Chap. 2.

Table 4.4: Optical Sloan photometry of SN 2013df.

Date	JD (+2400000.00)	Phase[a] (d)	u (mag)	r (mag)	i (mag)	Instrument[b]
2013/06/18	56461.92	11.9	15.94 ± 0.02	14.63 ± 0.02	14.78 ± 0.02	RATCam
2013/06/20	56463.87	13.9		14.64 ± 0.04	14.74 ± 0.02	RATCam
2013/06/22	56465.92	15.9	15.99 ± 0.32	14.53 ± 0.05	14.58 ± 0.02	RATCam
2013/07/20	56493.93	43.9	18.71 ± 0.07	15.54 ± 0.01	15.52 ± 0.01	IO:O
2013/07/22	56495.94	45.9	18.85 ± 0.01	15.59 ± 0.01	15.52 ± 0.01	IO:O
2013/11/20	56617.21	167.2		18.05 ± 0.03	17.53 ± 0.02	IO:O
2013/12/18	56645.13	195.1		18.50 ± 0.03	17.92 ± 0.03	IO:O
2013/12/25	56652.28	202.3		18.65 ± 0.03	18.02 ± 0.02	IO:O
2014/01/27	56685.21	235.2		19.22 ± 0.04	18.59 ± 0.04	IO:O
2014/02/11	56700.17	250.2		19.58 ± 0.05	18.85 ± 0.04	IO:O

[a] Phase in days with respect to the adopted explosion date JD = 2456450.0 ± 0.9.
[b] RATCam = LT 2.2 m + RATCam; IO:O = LT 2.2 m + IO:O. More information about the telescopes and instruments can be found in Chapter 2.

We have estimated the decline rate at the first peak, and the rise and decline rate at the secondary peak of SN 2013df through linear interpolation of the observed magnitudes. The results are presented in Table 4.5. Similar to SN 2011fu, the decline rates measured from the late time data are steeper than the rate expected for the decay of ^{56}Co $\rightarrow^{56}$ Fe. The minimum magnitudes after first decline and those at secondary maximum of the *BVRI* light curves of SN 2013df were estimated by fitting low order polynomials as were the times at which these minima ($t_{\rm min}$) and maxima ($t_{\rm max}$) took place (see Table 4.6). We were unable to fit the U band light curve given its flatness after first decline. As mentioned before, in the R band light curve of SN 2013df, we perceived the rise to the first maximum thanks to the early amateur data points. We also fitted this first maximum with low order polynomials and estimated that it occurred on $\rm JD_{R1stmax} = 2456453.5 \pm 0.1$ at $m_{\rm R1stmax} = 13.78 \pm 0.04$ mag.

4.2.2 Bolometric light curve

To derive the UV-optical-NIR pseudo-bolometric LC of SN 2013df, we followed two steps. In the first place, we derived the UV-optical pseudo-bolometric LC from the photometry presented in Section 4.2.1. This was done in the same way we calculated the optical-NIR pseudo-bolometric LC for SN 2011fu. That is, integrating the SED given by the fluxes at specific effective wavelengths obtained from the extinction-corrected apparent magnitudes. The next step was to estimate a NIR contribution to the LC, since SN 2013df was not observed in these wavelengths. To do this, we calculated two pseudo-bolometric LCs of SN 1993J (using the photometric data from Richmond et al. 1994 and Matthews et al. 2002). Following the same procedure as for the UV-optical pseudo-bolometric LC of SN 2013df, one calculation was done considering, and the other omitting, the NIR contribution. The difference in luminosity

Table 4.5: Decline and rise rates in the *UBVRI* LCs of SN 2013df.

Band	Decline from 1st peak [a] (mag d^{-1})	Rise to 2nd peak [b] (mag d^{-1})	Decline from 2nd peak [c] (mag d^{-1})	Decline tail [d] [mag (100d)$^{-1}$]
U	0.15 ± 0.02		0.15 ± 0.01	2.82 ± 0.68
B	0.15 ± 0.02	-0.03 ± 0.02	0.13 ± 0.01	1.26 ± 0.02
V	0.13 ± 0.01	-0.06 ± 0.01	0.07 ± 0.01	1.81 ± 0.03
R	0.16 ± 0.01	-0.04 ± 0.01	0.07 ± 0.01	1.94 ± 0.04
I	0.14 ± 0.01	-0.05 ± 0.01	0.06 ± 0.01	1.46 ± 0.05

[a] Considering the interval from $\sim$ 4 to 10 d after explosion.
[b] Considering the interval from $\sim$ 10 to 20 d after explosion.
[c] Considering the interval from $\sim$ 20 to 35 d after explosion.
[d] Considering the interval from $\sim$ 40 d after explosion. Note that for the *U* band, the calculation was done with few data points.

Table 4.6: Minimum and secondary maximum *BVRI* magnitudes of SN 2013df and the corresponding times at which they occurred.

Band	App. 1max. mag.[a] mag	$t_{\rm min}^{\rm (b)}$ (d)	App. min. mag.[c] (mag)	$t_{\rm max}^{\rm (b)}$ (d)	App. 2max. mag.[d] (mag)	Ab. max. mag.[e] (mag)
B	–	11.27 ± 1.08	15.39 ± 0.02	18.46 ± 0.91	15.19 ± 0.01	-16.86 ± 0.31
V	–	10.90 ± 0.90	14.99 ± 0.03	20.15 ± 1.06	14.57 ± 0.02	-17.38 ± 0.30
R	13.78 ± 0.04	8.97 ± 0.90	14.69 ± 0.30	20.81 ± 1.20	14.18 ± 0.01	-17.71 ± 0.31
I	–	11.02 ± 1.20	14.50 ± 0.03	21.60 ± 1.25	14.03 ± 0.01	-17.80 ± 0.31

[a] App. 1max. mag. = Apparent first maximum magnitude.
[b] $t_{\rm min}$ and $t_{\rm max}$ are calculated with respect to our adopted explosion date JD $= 245650.0 \pm 0.9$.
[c] App. min. mag. = Apparent minimum magnitude.
[d] App. 2max. mag. = Apparent secondary maximum magnitude.
[e] Ab. max. mag. = Absolute secondary maximum magnitude estimated considering $\mu = 31.65 \pm 0.30$ and $E(B-V)_{\rm Total} = 0.098 \pm 0.016$ mag.

between SN 1993J's optical and optical-NIR pseudo-bolometric LCs was then added to SN 2013df's UV-optical LC, thus obtaining its UV-optical-NIR pseudo bolometric LC. If instead of using the NIR contribution estimated for SN 1993J we use the one obtained for SN 2011dh from the data of Ergon et al. 2014, the shape of the UV-optical-NIR pseudo bolometric LC of SN 2013df does not change. However, the LC results a little less brighter around the minimum after first peak and at secondary peak. The only explosion parameter affected by this is then the ^{56}Ni mass, which has a slightly lower uncertainty: $0.1 - 0.11$ M$_\odot$.

SN 2013df's luminosities at the minimum after the first peak and at the secondary maximum were estimated by fitting low order polynomials to the light curve. This resulted in $L_{\rm min} = 2.2 \times 10^{42}$ erg s^{-1} and $L_{\rm 2nd\ max} = 2.5 \times 10^{42}$ erg s^{-1} respectively. We also derived a lower limit to the luminosity at first peak from our *R* band observations $L_{\rm 1st\ peak} \gtrsim 2.5 \times 10^{42}$ erg s^{-1}.

In order to derive the explosion parameters of SN 2013df, we have modelled the bolometric light curve as described in Valenti et al. (2008). The SN luminosity

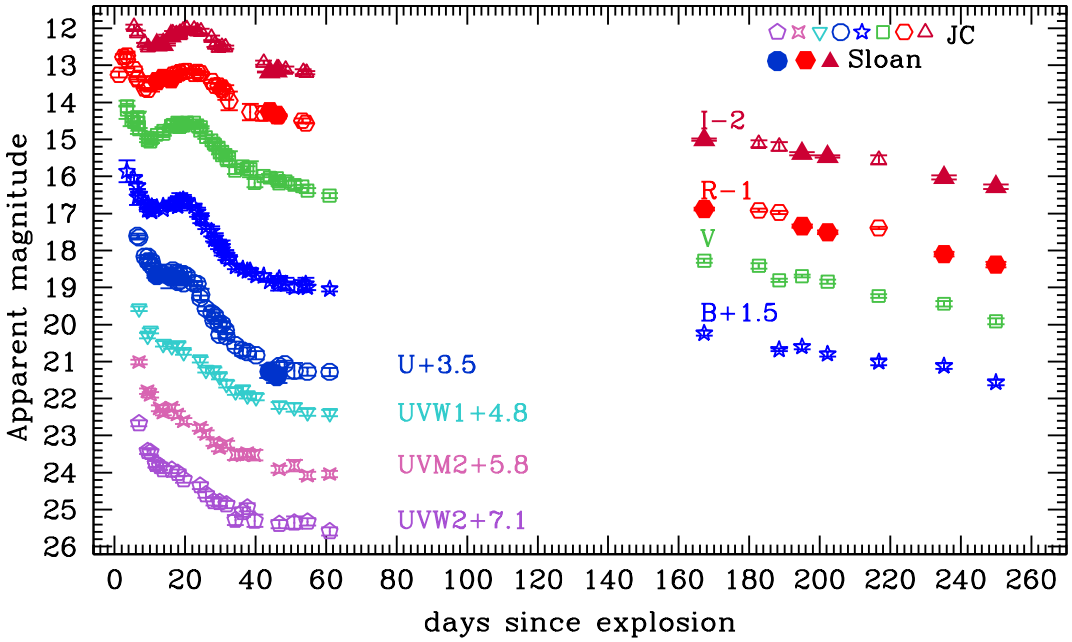

Figure 4.2: UV-optical light curves of SN 2013df. The *uri* Sloan data have also been included in these light curves by using the approximations to the JC system given in Jordi et al. (2006). The transformed Sloan data points are depicted in the figure with filled symbols. The assumed explosion epoch is JD = 2456450.0 ± 0.9. The LCs have been shifted for clarity by the values indicated in the figure.

evolution is divided into the photospheric phase ($t \leq 30$ d) and the nebular phase ($t \geq 60$ d). The simple analytical model by Arnett (1982) is adopted, and in addition we have included the energy produced by the ^{56}Co $\rightarrow$ ^{56}Fe decay. In the nebular phase, the luminosity is powered by the energy deposition of the γ-rays produced by the ^{56}Co decay, the electron-positron annihilation and the kinetic energy of the positrons (Sutherland & Wheeler, 1984; Cappellaro et al., 1997). Since the model cannot reproduce the shock breakout that dominates the early phases after explosion, we have not attempted to fit the early LC. We limited the photospheric phase to 25 d after the secondary peak, assumed a constant optical opacity $\kappa_{\rm opt} = 0.10\,{\rm cm^2 g^{-1}}$, and adopted a range of photospheric velocities (derived from the minimum of the Fe II spectral lines) spanning 7000 to 9000 km s^{-1}. The pseudo-bolometric UV-optical-NIR light curve of SN 2013df, as well as its best fit model, are presented in Figure 4.4, whereas the explosion parameters derived from the model are displayed in Table 4.7. As can be seen in Figure 4.4, the model overall reproduces the behaviour

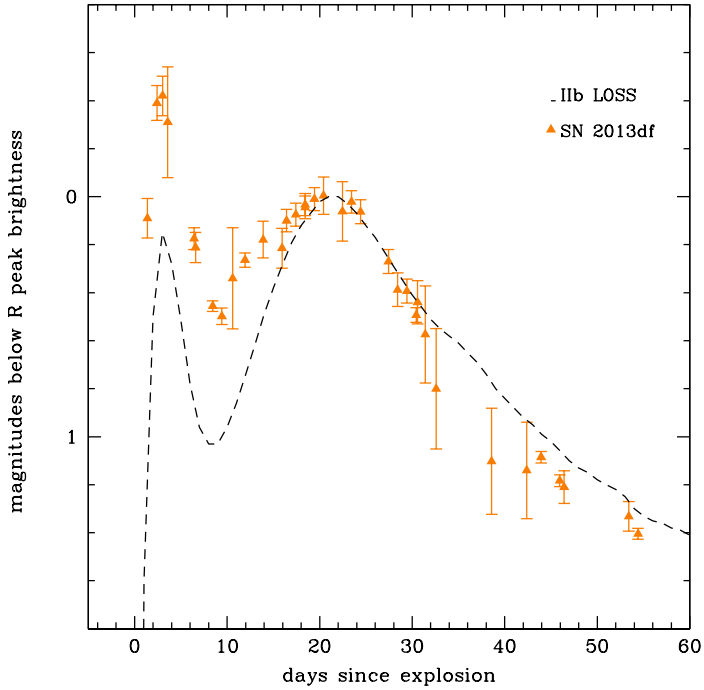

Figure 4.3: Comparison of the R band magnitudes since explosion of SN 2013df and the template for type IIb SNe derived in Li et al. 2011.

Table 4.7: Explosion parameters derived from the modelling of the second peak in SN 2013df's pseudo-bolometric LC.

Parameters	
$E_{\rm kin}$ (10^{51}erg)	0.4-1.2
^{56}Ni mass ($M_\odot$)	0.10-0.13
$M_{\rm ej}$ ($M_\odot$)	0.8-1.4

of the observational data points. We measured the width of both the observed and model bolometric LCs, and found that, close to peak, the widths are very similar but the observed LC is wider by one day. However, as can be seen in Figure 4.4 the model seems broader at around phase 40 d. Most likely, this is related to the fact that it cannot accurately reproduce fast declining LCs, and may indicate that the ejecta mass derived from the model may be slightly overestimated.

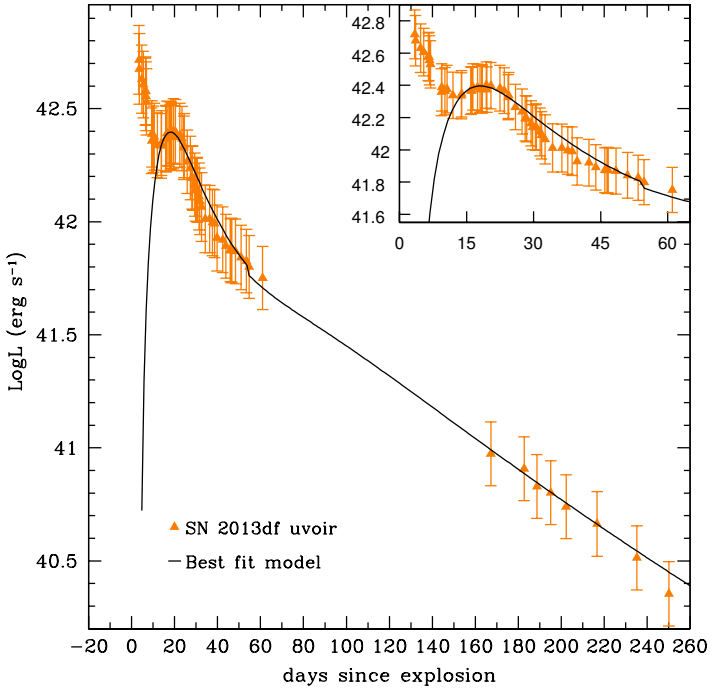

Figure 4.4: Pseudo-bolometric UV-optical-NIR LC of SN 2013df (calculated assuming the same NIR contribution as SN 1993J) and its best fit model computed by omitting the first peak. For clarity, we have zoomed in on the light curves up to phase $\sim$ 70 d in the upper right corner of the figure.

4.3 Spectroscopic results

4.3.1 Spectral evolution

The log of our spectral observations is presented in Table 4.8.

Our spectral sequence of SN 2013df (Figure 4.5) covers the evolution from 9 up to 243 d post explosion, with a seasonal visibility gap between 42 and 183 d. The most prominent lines are identified in the figure.

In the spectrum at 9 d (that is, near the minimum after the first peak in the LCs), we identify a clear P-Cygni Hα feature and an absorption component of Hβ at around 4700 Å, although the latter possibly has contributions of Fe II λ4924 (Barbon et al., 1995; Taubenberger et al., 2011; Hachinger et al., 2012). Both the absorption components of Hα and Hβ exhibit a flat-bottom profile indicating the presence of a thick expanding H shell (Barbon et al., 1995). Other than the flat bottom, and as seen before in type IIb SNe 1993J, 2001ig (Silverman et al. 2009), 2011dh (Marion et al. 2014) and 2011ei, the Hα absorption seems to have two components which may

Table 4.8: Log of spectroscopic observations of SN 2013df.

Date	JD (+2400000)	Phase [a] (d)	Set-up[b]	Spectral Range Å
2013/06/15	56459.41	9.4	AFOSC+g4,VPH6	3500-10000
2013/06/20	56464.35	14.4	B&C+g300	3350-7850
2013/06/28	56472.41	22.4	AFOSC+VPH6	4500-10000
2013/07/18	56492.35	42.2	AFOSC+g4	3500-8450
2013/12/05	56632.66	182.7	AFOSC+g4,VPH6	3500-10000
2014/02/04	56693.25	243.3	OSIRIS+R500R	4800-10000

[a]Phase in days with respect to the adopted explosion date JD = 2456450.0 ± 0.9.
[b]AFOSC = Asiago 1.82 m + AFOSC; B&C = Asiago 1.22 m + B&C; OSIRIS = Gran Telescopio de Canarias 10.4 m + Osiris. More information about the telescopes and instruments can be found in Chapter 2.

be due to the presence of two peaks in the radial distribution of the H density or to contamination by Si II. The spectrum also shows He I λ5876 absorption probably blended with Na I λ5890 − 5896 (Taubenberger et al., 2011). The absorption at approximately 5000 Å is likely to be a blend of Fe II λ5018, He I λ5015 and Si II λ5016 (Hachinger et al., 2012; Silverman et al., 2009), and that around 4300 Å a blend of Mg II λ4481 and He I λ4471 (Hachinger et al., 2012; Silverman et al., 2009). We believe the feature around 4100 Å could be Hγ, and there are also traces of Ca II H & K at 3934 Å & 3968 Å (Taubenberger et al., 2011; Hachinger et al., 2012).

The spectrum taken at 14 d past explosion exhibits the same features as our previous spectrum. However, the features identified as Hα and Hβ have increased by a factor in equivalent width of approximately 1.2 with respect to our previous spectrum, while the feature identified as He I λ5876 has diminished approximately by the same quantity. The spectrum taken at 22 d since explosion (near to the secondary maximum light), is characterised by an increase in intensity of the λ5876 He I line by a factor of about 1.4 while the increase of the Hα and Hβ lines is by a factor of approximately 1.1. This spectrum also shows conspicuous absorptions of Ca II NIR $\lambda\lambda\lambda$8498, 8542, 8662 (Taubenberger et al., 2011; Hachinger et al., 2012).

The spectrum at 42 d presents a significant decrease in flux at blue wavelengths compared to earlier data. The Hα line diminished by a factor of 4 approximately, while He I lines increased in intensity with respect to the preceding spectra by a factor of 1.3 approximately. Furthermore, the He I features at λ6678 and λ7065 respectively, can be identified in this spectrum (Taubenberger et al., 2011) while they were absent in the previous spectra. The profiles of the absorption lines of He I λ5876 and Hα seem to be similar to the ones seen in the hydrogen rich type Ib SN 2000H at phases 19 and 30 d (Branch et al., 2002).

The last two spectra of our sequence, taken at phases of 183 and 243 d after explosion, exhibit a relative increase in flux at blue wavelengths as well as strong lines of [O I] $\lambda\lambda$ 6300, 6364, [Ca II] $\lambda\lambda$7291, 7324, O I λ7774, and Ca II NIR. We also have identified Na I around 5890Å possibly contaminated by residual He I λ5876, and Fe II around 5000 Å (Matheson et al., 2000a; Taubenberger et al., 2011; Shivvers et al., 2013). We believe the feature around 6500-6600Å might be associated to Hα emission, and we discuss this possibility below. The [Ca II] $\lambda\lambda$7291, 7324 feature is noticeably more intense than [O I] in both of our last spectra.

The work by Woosley & Heger (2007) on the nucleosynthesis in massive stars of solar metallicity, shows that oxygen production strongly increases for progenitors over ~ 16 M$_\odot$. In Jerkstrand et al. 2015, a comparison between the observational and modelled [O I] $\lambda\lambda$6300, 6364 luminosities relative to the ^{56}Co decay power for SNe 1993J, 2008ax, and 2011dh is shown. All of the SNe exhibit luminosities consistent with progenitors of initial masses ranging 12 to 17 M$_\odot$. We have attempted to do a rough estimate of SN 2013df's progenitor mass by comparing the luminosities derived from [O I] $\lambda\lambda$6300, 6364 in our nebular spectra with the model tracks for type IIb SNe represented in figure 15 of Jerkstrand et al. 2015. In order to calculate such luminosities, first we deblended the emission feature of [O I] $\lambda\lambda$6300, 6364. Then, the integrated flux was obtained adjusting a Gaussian to the feature and subtracting the continuum flux level. We converted the resulting flux in luminosity by using our adopted distance and the extinction estimated, and then normalized this value relative to the ^{56}Co decay power (see equation 1 of Jerkstrand et al. 2015). Therefore, we derived $L_{\rm norm}(183) = 0.0088^{+0.0020}_{-0.0010}$ and $L_{\rm norm}(243) = 0.0075^{+0.0025}_{-0.0013}$ at 183 d and 243 d respectively. These two values are found to be closer to those for models 12C and 13D at similar phases (see figure 15 of Jerkstrand et al. 2015). The main properties of these models can be seen in table 3 of the mentioned manuscript. Still, we stress that $M_{\rm ZAMS}$ for these models are 12 M$_\odot$ and 13 M$_\odot$. These values are consistent with the lower limit for SN 2013df's progenitor mass derived by Van Dyk et al. (2014) from the analysis of the HST pre-explosion images of the SN site (13 M$_\odot$). SN 2013df has luminosities most similar to those of SNe 2011dh and 2008ax, for which the values are also consistent with 12-13 M$_\odot$ progenitors, while they are below the ones for SN 1993J which match best with a slightly higher mass progenitor ($M \sim 15$ M$_\odot$).

We have measured the black-body temperature by fitting the continuum of our spectral sequence. The temperature increases slowly from 7700 K at 9 d to 7900 K at 14 d, and subsequently decreases to 6900 K at 22 d and 4000 K at 42 d past explosion. Considering that the errors of these measurements are about $\pm$500 K, we could say that the black-body temperature remained constant between 9 and 22 d and decreased after that. Our values are slightly below those reported for SN 2011dh at coeval epochs (Ergon et al., 2014). This means the black-body radius for SN 2013df, interpreted as the thermalization radius, should be greater than for SN 2011dh given that the two SNe have similar luminosity.

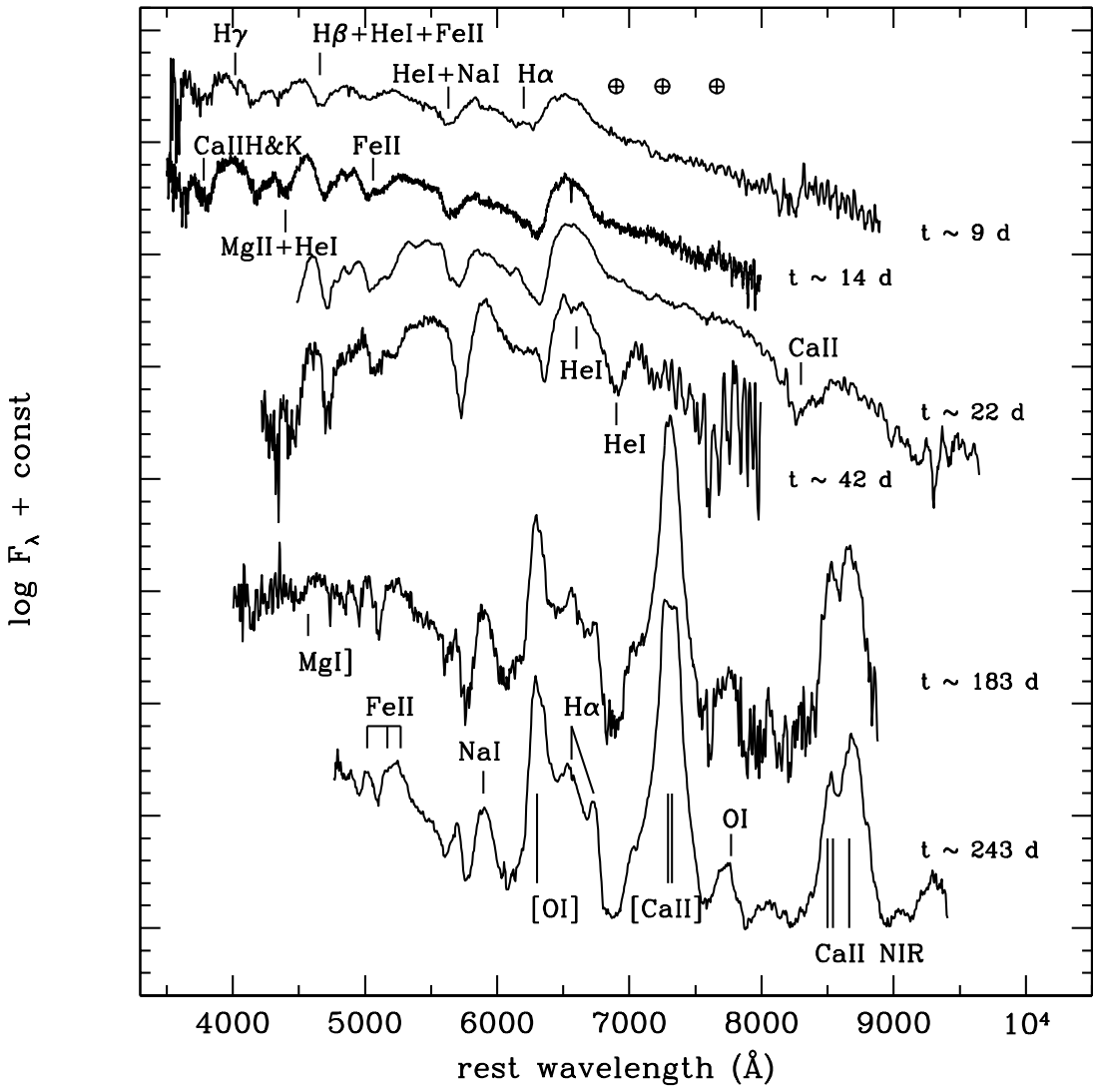

Figure 4.5: Optical spectral evolution of SN 2013df, where the most relevant features in the spectra are indicated. Residual telluric features have been marked with $\oplus$. The spectra have been corrected for the host galaxy redshift. Epochs indicated in the plot are with respect to our assumed explosion date of JD = 2456450.0 ± 0.9. Spectra have been shifted vertically for clarity.

In the top panel of Figure 4.6, we display the nebular profiles for the [O I] and the [Ca II] ions of SN 2013df in velocity space. Contrary to SN 2008ax and similar to SN 2011dh and 1993J, SN 2013df does not show a symmetrical double-peaked [O I] profile, but does seem to show some substructure indicative of clumping possibly related to Rayleigh-Taylor instabilities during the expansion of the SN ejecta (see e.g. Kifonidis et al., 2000). We note that the centroids of [O I] and [Ca II] in our spectra are slightly blue-shifted. This behaviour has been seen in other stripped envelope type Ib/c SNe and could result from residual opacity in the ejecta core (Taubenberger et al., 2009). We have followed the procedure described by Matheson et al. (2000b) to distinguish the possible different components forming the profiles. In the first place, we smoothed the profiles with boxcars of 5 pixels, and secondly we subtracted the smoothed profiles from the original ones. In the bottom panel of Figure 4.6, we zoom in on the small scale fluctuations we have obtained for [O I] λ6300, 6364 and [Ca II] $\lambda\lambda$7291, 7324. The dotted vertical lines marking 0 velocity in both panels of the plot refer to λ6300 for [O I] and λ7291 for [Ca II]. We identify 5 components in [O I] in both the 183 and 243 day spectra, while the [Ca II] line seems to consist of 6 features. For [O I], components 1 through 5 lie at approximately -3400, -1700, -500, 1300, 2600 km s^{-1} respectively, and components 1 through 6 of [Ca II] are at approximately -1500, -200, 800, 1900, 2750, 3900 km s^{-1}. Components 3, 4, and 5 in the [O I] λ6364 velocity space are shifted approximately by the same velocity as components 1, 2, and 3 in the [O I] λ6300 velocity space, which means that they are probably repetitions. The features that seem to be repeated in the [Ca II] profile are 2, 4, and 6 as they are shifted by approximately the same velocity as components 1, 3, 5 if the line is represented in the [Ca II] λ7324 velocity space.

We performed the same subtraction described above to try to extract the substructure present in the O I λ7774 line but were only able to distinguish one feature shifted -500 km s^{-1} in our spectrum at phase 243. We were unable to identify any small scale fluctuations for [O I] λ5777 and for the Mg I] λ4571 line profiles owing to the low S/N ratio of these features. For SN 1993J, Matheson et al. (2000b) found matches between the small scale fluctuations in the [O I] $\lambda\lambda$6300, 6364, [O I] λ5777 and O I λ7774 emission lines. However, no match was detected between the features present in Mg I] λ4571, [O I] $\lambda\lambda$6300, 6364, the various O I lines and [Ca II] $\lambda\lambda$7291, 7324 lines. This was interpreted as the emission of different species forming at different locations. Unfortunately, we cannot confirm whether there is a correlation between the different O I lines for SN 2013df, but we have found that the substructures in [O I] $\lambda\lambda$6300, 6364 and [Ca II] $\lambda\lambda$7291, 7324 are not correlated and probably originate in different clumps.

4.3.2 Late-time emissions between 6500 and 6800 Å

In our nebular spectra of SN 2013df there are two interesting emission lines around 6500 and 6800 Å. In Morales-Garoffolo et al. (2014), we speculated that both these

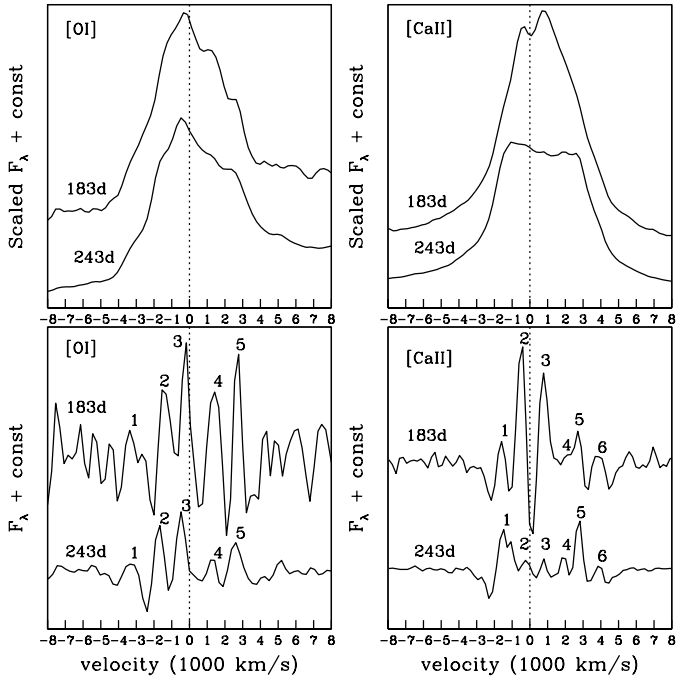

Figure 4.6: Top panel: Nebular profiles of SN 2013df's [O I] $\lambda\lambda$6300, 6364 and [Ca II] $\lambda\lambda$7291, 7324 lines at phases 183 and 243 d in velocity space. Bottom panel: Substructures present in the nebular profiles of the [O I] $\lambda\lambda$6300, 6364 and [Ca II] $\lambda\lambda$7291, 7324 lines at phases 183 and 243 d. The vertical lines at 0 km s^{-1} mark zero velocity with respect to 6300 and 7291 Å. The numbering in the lower panel corresponds to the different components identified in the profiles.

lines were Hα emerging after ejecta interaction with CSM. This was the interpretation for the 6600 Å band observed in the 367 day spectrum of SN 1993J (Patat et al., 1995), as well as in later time spectra (Matheson et al., 2000a). Jerkstrand et al. 2015 stress the fact that at phases above 150 d, no Hα emission is produced by their models. Instead, the features around 6550 Å in the late-time spectra of type IIb SNe are likely to be caused by [N II] $\lambda\lambda$6548, 6584. Given the similarity with SN 1993J, and the fact that for this SN the nebular emission around 6600Å was well modelled by Hα excited by CSM interaction, and the findings of Jerkstrand et al. 2015, we believe that the emission that is detected at 6500-6600 in SN 2013df's late time spectra is Hα on top of [N II] $\lambda\lambda$6548, 6584. Note that a recent analysis of late-time spectra of SN 2013df by Maeda et al. (2015) has confirmed our speculation about the interacting ejecta-CSM origin of this feature. Although in principle we could attribute the 6700-6800 Å feature to residual He I 6678 Å, Jerkstrand et al.

2015 stress that optical He lines start diminishing in spectra of type IIb SNe after 100 d and are difficult to detect. In Morales-Garoffolo et al. (2014) we hypothesised that the line was Hα originating from asymmetrical ejecta-CSM interaction. However, we have found that SN 2011fu also shows a line at ∼6700 Å at similar phases. In fact, as we discussed in Chapter 3, we believe that one possibility to explain the line in both these objects is that it is due to [S II] $\lambda\lambda$6716, 6731.

4.4 Further constraints on the progenitor's properties

Optical observations of CCSNe soon after shock breakout may help constrain progenitor characteristics. Clues can be given by early photometry (one day after explosion) as described in Chevalier & Fransson (2008) and Nakar & Sari (2010), thanks to colour temperature derived from early spectra (Rabinak & Waxman, 2011) and by flash spectroscopy, as described by Gal-Yam et al. (2014).

Recently, Nakar & Piro (2014) studied the conditions for double-peaked SN light curves. They found that non-standard progenitors formed by a compact massive core surrounded by an extended low-mass envelope can reproduce the main features of double-peaked light curves. They also derived a series of analytic formulae to constrain the mass of the extended material $M_{\rm ext}$, its radius $R_{\rm ext}$, and the radius of the core $R_{\rm core}$:

- From the time of the first peak in the LC ($t_{\rm p}$), the extended material mass prior to explosion is given by

$$M_{\rm ext} \approx 8 \times 10^{-3} E_{51}^{0.43} \kappa_{0.34}^{-0.87} \left(\frac{M_{\rm core}}{3{\rm M}_\odot}\right)^{-0.3} \left(\frac{t_{\rm p}}{1{\rm d}}\right)^{1.75} {\rm M}_\odot, \tag{4.1}$$

  where $M_{\rm ext}$ is taken to be the mass between the radii $R_{\rm ext}/3$ and $R_{\rm ext}$. E_{51} is the kinetic energy $E/10^{51}$erg, $\kappa_{0.34}$ is the opacity $\kappa/0.34$ cm^2 s^{-1}, $M_{\rm core}$ is the ejected core mass (not including mass of the compact remnant), and $t_{\rm p}$ is the time in days at which the first peak in the LC takes place.

- From the bolometric luminosity at the first peak (L), the radius of the extended material can be constrained by means of:

$$R_{\rm ext} \approx 10^{13} \kappa_{0.34}^{0.74} E_{51}^{-0.87} L_{43} \left(\frac{M_{\rm core}}{3{\rm M}_\odot}\right)^{0.61} \left(\frac{t_{\rm p}}{1{\rm d}}\right)^{0.51} {\rm cm}, \tag{4.2}$$

  where L_{43} is $\frac{L}{10^{43}{\rm erg\,s^{-1}}}$.

- From the luminosity at the minimum after the first peak ($L_{\rm min}$) an upper limit to the core radius may be derived:

$$R_{\rm core} \lesssim 2.5 \times 10^{11} \kappa_{0.2}^{0.9} E_{51}^{-1.1} \left(\frac{L_{\rm min}}{10^{41} {\rm erg\ s^{-1}}} \right)^{1.3} \left(\frac{M_{\rm core}}{3 {\rm M}_\odot} \right)^{0.85} {\rm cm}, \qquad (4.3)$$

where $\kappa_{0.2}$ is the opacity $\kappa/0.2$ cm^2 s^{-1}.

In order to derive some characteristics of SN 2013df's progenitor, we made use of the following considerations:

1. We assumed two different constant optical opacities depending on the stage of the SN evolution. At first (Equations 4.1 and 4.2) the LC is powered by the low mass extended hydrogen gas. As in Nakar & Sari (2010), for a hydrogen envelope with cosmic abundances we considered $\kappa = 0.34$ cm^2 g^{-1}. The second phase of the LC is powered by the compact hydrogen deficient core (Equation 4.3), for which we considered $\kappa = 0.1$ cm^2 g^{-1}, the same value as the one we used in the modelling of the bolometric LC.

2. As noted in Nakar & Piro (2014), estimates for $R_{\rm ext}$ can be obtained even if only the luminosity in one band is available, though less accurately. In our case the first maximum of the light curve was only detected in the R band, so we have used L and $t_{\rm p}$ as derived from that band and thus estimated only a lower limit to $R_{\rm ext}$.

3. We assumed the initial mass range for SN 2013df's progenitor to be that given by Van Dyk et al. (2014): $13 - 17$ M$_\odot$. We have estimated a range for the ejected core mass of $2 - 3.6$ M$_\odot$. To do this we considered the relation between the He-core mass and main sequence mass for the stellar evolution of a single star given by Sugimoto & Nomoto (1980), and assumed that the remnant mass is ~ 1.4 M$_\odot$. Although the core mass we have estimated here is for a single star and the progenitor of SN 2013df could potentially form part of a binary system, we do not expect the core mass to be much affected. For example, in the case of SN 2011dh, the core masses derived for its progenitor by Bersten et al. (2012) resulted similar to that obtained by Benvenuto et al. (2013), considering SN 2011dh's progenitor evolved in a binary system.

We characterised SN 2013df's progenitor as summarized in Table 4.9.

Our result for SN 2013df's $M_{\rm ext}$ is of the order of that obtained for SN 1993J in Nakar & Piro (2014), and an order of magnitude above the ones derived for SN 2011dh. As noted in Nakar & Piro (2014), $M_{\rm ext}$ is not the total mass of the envelope surrounding the core, but just the fraction distributed around $R_{\rm ext}$. The similarity between $M_{\rm ext}$ for SNe 2013df and 1993J suggests that the mass of the hydrogen shell in SN 2013df's progenitor prior to explosion is similar to that of SN 1993J, i.e. $M_{\rm H} \sim 0.2$ M$_\odot$ (Woosley et al., 1994), and slightly above the value for

Table 4.9: Estimates for the extended mass ($M_{\rm ext}$), radius ($R_{\rm ext}$) and core radius ($R_{\rm core}$) of SN 2013df's progenitor, calculated by following the procedure described in Nakar & Piro (2014) for "non standard progenitors". For comparison, the values obtained for SNe 1993J and 2011dh in Nakar & Piro (2014) are also presented.

SN	2013df	1993J	2011dh
$t_{\rm p}$ (d)	3.5	3	$0.27 - 0.85$
L (erg s^{-1})	$L_R = 2.5 \times 10^{42}$	$L_{\rm bol} = 1 \times 10^{43}$	$-16.8 \leq M_g \leq -15.5$
$L_{\rm min}$ (erg s^{-1})	2×10^{42}	4×10^{41}	$2 - 2.5 \times 10^{41}$
E_{51} (erg)	$0.4 - 1.2$	1.31	$0.6 - 1$
$M_{\rm core}$ (M$_\odot$)	$2 - 3.6$	2.23	2.5
$M_{\rm ext}$ (M$_\odot$)	$0.05 - 0.09$	0.06	$0.0007 - 0.006$
$R_{\rm ext}$/R$_\odot$	$64 - 169$	288	$288 - 503$
$R_{\rm core}$ (10^{11} cm)	$< 45 - 238$	< 9	$< 5 - 7$

SN 2011dh $M_{\rm H} \sim 0.1$ M$_\odot$ (Bersten et al., 2012). Concerning the extended radius of SN 2013df, we have derived a range of $64 - 169$ R$_\odot$. We stress that this range is based on the R luminosity instead of bolometric luminosity, which makes it a lower limit, as $L_R < L_{\rm bol}$. The difference between the R band specific luminosity and the bolometric luminosity for SN 1993J is about a factor two. Assuming the same difference for SN 2013df, this could increase the estimate for SN2013df's $R_{\rm ext}$ by a factor of 1.5. However, we must also take into account that for SN 1993J, $R_{\rm ext}$ derived by Nakar & Piro (2014) is a factor 1.9 below that obtained from the modelling of the light curve, and a similar underestimate could also take place for SN 2013df. Multiplying our lower limit range on the extended radius of SN 2013df's progenitor by these two factors brings it closer to the value derived by Van Dyk et al. (2014) from the pre-SN HST archival images, i.e. 545 ± 65 R$_\odot$. Finally we note that the range we have obtained for the upper limit to SN 2013df's core radius is much larger than the ones estimated for both SNe 1993J and 2011dh. Given the similar ejecta masses (Table 6.1) this could suggest that the progenitor core of SN 2013df was not as compact as for SNe 1993J and 2011dh.

4.5 Summary

In this chapter we have presented the analysis of our optical observations for the type IIb SN 2013df (complemented by UV data taken by *SWIFT*) spanning from a few days up to 250 d after explosion. SN 2013df's LCs present two peaks in all bands. The R absolute magnitude LC evolves from a first maximum of -18.12 mag to a minimum value of -17.20 mag, and then increases its brightness until reaching a secondary maximum of -17.72 mag approximately twelve days after the minimum. The late decline rates are faster than the radioactive decay of ^{56}Co.

From the modelling of the bolometric light curve (not including the first peak), we have obtained an explosion energy of $0.4 - 1.2 \times 10^{51}$erg, a ^{56}Ni mass in the range $0.1 - 0.13$ M$_\odot$ and a total ejected mass of $0.8 - 1.4$ M$_\odot$.

The earliest spectrum of our sequence shows a flat-bottomed Hα absorption indicative of the presence of an extended H shell in the ejecta, which is the outer layer of the progenitor's envelope.

Our nebular spectra are characterised by the presence of two components around 6500-6600 Å and 6700-6800 Å, the first of which is Hα in emission caused by interaction of the ejecta with circumstellar material. From the [O I] $\lambda\lambda$6300, 6364 luminosities we have derived a rough estimate to the initial mass of SN 2013df's progenitor $\sim$ 12–13 $M_\odot$. From the analysis of the nebular profiles of [O I] and [Ca II], we have concluded that the substructure they exhibit is indicative of the presence of different clumps where these species are being excited in the ejecta.

Finally, we have followed the procedure described in Nakar & Piro (2014) to add some additional constrains on some progenitor characteristics of SN 2013df assuming that it was a non-standard progenitor formed by a compact core and an extended low-mass envelope. We have estimated a mass range for the extended material similar to SN 1993J, which leads us to believe both SNe 1993J and 2013df had similar mass in their hydrogen shells prior to explosion. In addition, we estimated a lower limit to the radius for SN 2013df's progenitor of 64–169 $R_\odot$. At last, we have obtained an upper limit to the core radius of SN 2013df's progenitor $R_{\rm core} < (45\text{–}238) \times 10^{11}$ cm which is well above those derived for SNe 1993J and 2011dh.

Chapter 5

OGLE-2013-SN-100

In this chapter we present the observational data of OGLE-2013-SN-100 and their analysis, and discuss the possible physical conditions that gave rise to the observed properties of this rare transient.

5.1 OGLE-2013-SN-100, reddening and distance

OGLE-2013-SN-100 (see Figure 5.1), with coordinates $\alpha = 02^{\rm h}16^{\rm m}18^{\rm s}.55$ and $\delta = -74^{\rm o}45'23''.6$, was discovered by the OGLE IV survey (Wyrzykowski et al., 2014) on 2013 October 21.2 UT (Wyrzykowski et al., 2013). The first detection of OGLE-2013-SN-100 was on 2013 July 12 by OGLE IV. From this epoch on, OGLE IV started a follow-up campaign up to 2014 February 24. The majority of the observations were performed in the I band, except for two epochs of V band data that were taken on 2013 October 27 and December 1. OGLE-2013-SN-100 was classified 2013 December 1 as a peculiar type II SN (Dennefeld et al., 2013) by the PESSTO survey (see Appendix A). The classification spectrum, in addition to Hα, showed seemingly prominent He I λ5876. Since the spectrum was obtained after the secondary maximum of the OGLE IV I band LC (phase indicated by the first vertical line in Figure 5.2), approximate phase in which type IIb SNe show strong features of this element, we suspected that the transient could be a type IIb SN. This motivated us to study the object as part of our project on type IIb SNe, completing the dataset with data from the NTT and EFOSC2 in the observatory of La Silla (Chile) as part of the PESSTO survey. Specifically, we took *BVRI* band photometry and spectroscopy with grisms 16 and 13 from 2013 December 1 to 2014 January 22. In this chapter we include the analysis of both the photometric data obtained by the OGLE IV survey and the data obtained by PESSTO at the NTT.

As described in Section 5.3, the object shows prominent Hα emission lines in its spectra (see Figure 5.3), from which we obtained a redshift of 0.0855 ± 0.0002. Assuming $\rm H_0 = 73 \pm 5$ km s^{-1} Mpc^{-1}, $\Omega_{\rm m} = 0.27$, and $\Omega_{\rm v} = 0.73$ we derived a

luminosity distance to OGLE-2013-SN-100 of 376.7 ± 23.1 Mpc (Wright, 2006) and therefore $\mu = 37.9 \pm 0.3$ mag. The Milky Way reddening in the line of sight of OGLE-2013-SN-100 is $E(B-V)_{\rm MW} = 0.037 \pm 0.001$ mag (Schlafly & Finkbeiner, 2011). Since in our spectra we have not distinguished absorptions corresponding to Na ID lines at the host galaxy's redshift, we have assumed that the contribution to the reddening due to the host galaxy is negligible, and have adopted $E(B-V)_{\rm total} = 0.037 \pm 0.001$ mag as the total reddening in the line of sight of the object.

5.2 Photometry

The data obtained with EFOSC2 at the NTT were processed as described in Section 2.3.1, and the SN instrumental magnitudes were obtained by using the template subtraction technique as described in Section 2.3.2, using *BVRi* reference images acquired with EFOSC2 on 2014 December 11, 12, and 13. Calibration of the SN magnitudes was done relative to stars in the SN field (see Figure 5.1 and Table 5.1). The OGLE IV magnitudes were obtained by using an automated template subtraction technique for the survey data, using reference images taken by the survey 2010 November 27. Note that in this case, the reference image is calibrated (by means of observations of standard fields) before performing the template subtraction, thus the SN magnitudes obtained from the difference imaging are obtained in the same calibrated system as the template (Udalski et al., 2015). All the SN magnitudes are presented in Table 5.2, and in Figure 5.2 we have plotted the *BVRI* LCs.

As mentioned above, the *I* band LC shows two peaks. The LCs are plotted with respect to the second *I* band maximum, which by low order polynomial fitting, we have estimated to occur on JD $= 2456588.1 \pm 2.4$. We have selected this second maximum as reference epoch for the rest of this chapter. The first maximum at 20.38 ± 0.01 mag occurred on JD $= 2456503.1 \pm 1.4$, approximately 85 days before the second one that reached 19.20 ± 0.04 mag.

We have estimated the rise and decline rates of the LCs, and the results are indicated in Table 5.3. Although there is little photometric coverage, we have also estimated the rise rate to the first peak in the *I* band LC, which resulted -0.008 mag d^{-1}. While the rise to first peak in the *I* band is slower than that to the secondary maximum, the decline from the first peak occurs at a slightly faster rate than that from the second. Another characteristic observed in the LCs is that the tail declines are slower in the redder bands but all LCs decline at a faster rate than that expected for the decay of ^{56}Co.

5.3 Spectroscopy

In Table 5.4 we present our log of optical spectra for OGLE-2013-SN-100, and Figure 5.3 shows the spectral evolution of the object. As reflected in the figure, overall the

Table 5.1: *BVRI* optical Johnson Cousins photometry of the stars used in the EFOSC2 photometric calibration process.

Star	α (J2000) (h m s)	δ(J2000) ($^\circ$ ′ ″)	B (mag)	V (mag)	R (mag)	I (mag)
1	2:15:52.135	-74:43:55.14	20.65 ± 0.06	19.22 ± 0.10	–	–
2	2:15:50.226	-74:47:04.86	18.10 ± 0.03	17.44 ± 0.05	–	–
3	2:16:14.415	-74:46:35.43	18.41 ± 0.02	17.82 ± 0.02	–	–
4	2:16:31.933	-74:47:10.80	17.58 ± 0.02	16.89 ± 0.03	16.43 ± 0.03	16.08 ± 0.01
5	2:16:16.866	-74:47:10.40	19.91 ± 0.01	18.50 ± 0.01	–	–
6	2:16:16.011	-74:46:02.02	20.82 ± 0.04	19.31 ± 0.04	–	–
7	2:16:21.415	-74:44:10.51	20.11 ± 0.02	18.59 ± 0.02	17.58 ± 0.01	–
8	2:16:12.793	-74:43:30.00	22.08 ± 0.02	21.53 ± 0.04	–	–
9	2:16:31.073	-74:43:22.73	20.65 ± 0.01	19.08 ± 0.03	18.03 ± 0.03	17.06 ± 0.05
10	2:16:37.966	-74:44:48.55	21.75 ± 0.03	20.51 ± 0.02	–	–
11	2:15:50.172	-74:46:10.37	21.76 ± 0.01	21.17 ± 0.04	–	–
12	2:16:20.321	-74:43:43.33	16.38 ± 0.01	15.66 ± 0.01	15.41 ± 0.03	–
13	2:16:27.806	-74:46:02.55	22.29 ± 0.03	21.80 ± 0.03	21.47 ± 0.04	–

Table 5.2: *BVRI* optical Johnson Cousins photometry of OGLE-2013-SN-100.

Date	JD (+2400000.00)	Phase[a] (d)	B (mag)	V (mag)	R (mag)	I (mag)	Key[b]
2013/07/12	56485.93	-102.2	–	–	–	20.51 ± 0.10	OGLE
2013/08/04	56508.87	-79.2	–	–	–	20.41 ± 0.11	OGLE
2013/08/12	56516.89	-71.2	–	–	–	20.50 ± 0.17	OGLE
2013/08/16	56520.87	-67.2	–	–	–	20.63 ± 0.11	OGLE
2013/08/19	56523.76	-64.3	–	–	–	20.73 ± 0.19	OGLE
2013/08/22	56526.79	-61.3	–	–	–	20.82 ± 0.22	OGLE
2013/09/13	56548.75	-39.3	–	–	–	20.89 ± 0.13	OGLE
2013/09/20	56555.83	-32.3	–	–	–	20.53 ± 0.17	OGLE
2013/09/26	56561.74	-26.4	–	–	–	20.53 ± 0.11	OGLE
2013/09/29	56564.70	-23.4	–	–	–	20.44 ± 0.09	OGLE
2013/10/04	56569.75	-18.3	–	–	–	19.86 ± 0.04	OGLE
2013/10/08	56573.75	-14.3	–	–	–	19.43 ± 0.03	OGLE
2013/10/13	56578.72	-9.4	–	–	–	19.37 ± 0.04	OGLE
2013/10/18	56583.70	-4.4	–	–	–	19.26 ± 0.05	OGLE
2013/10/21	56586.67	-1.4	–	–	–	19.10 ± 0.05	OGLE
2013/10/27	56592.83	4.7	–	19.82 ± 0.04	–	–	OGLE
2013/10/28	56593.64	5.5	–	–	–	19.33 ± 0.05	OGLE
2013/11/07	56603.67	15.6	–	–	–	19.39 ± 0.05	OGLE
2013/11/19	56615.70	27.6	–	–	–	19.68 ± 0.09	OGLE
2013/11/23	56619.61	31.5	–	–	–	19.85 ± 0.05	OGLE
2013/12/01	56627.59	39.5	22.17 ± 0.04	20.99 ± 0.04	20.41 ± 0.05	20.10 ± 0.09	NTT
2013/12/01	56627.62	39.5	–	21.77 ± 0.15	–	–	OGLE
2013/12/02	56628.67	40.6	–	–	–	20.31 ± 0.13	OGLE
2013/12/09	56635.64	47.5	22.62 ± 0.13	21.33 ± 0.06	20.68 ± 0.04	20.27 ± 0.07	NTT
2013/12/11	56637.60	49.5	–	–	–	20.13 ± 0.12	OGLE
2013/12/29	56645.62	57.5	–	–	–	20.51 ± 0.14	OGLE
2013/12/24	56650.61	62.5	–	–	–	20.79 ± 0.11	OGLE
2013/12/25	56651.62	63.5	23.23 ± 0.07	21.99 ± 0.10	21.28 ± 0.07	20.81 ± 0.09	NTT
2013/12/30	56656.60	68.5	–	–	–	21.01 ± 0.15	OGLE
2014/01/03	56660.60	72.5	23.49 ± 0.14	22.29 ± 0.08	21.55 ± 0.05	20.98 ± 0.10	NTT
2014/01/09	56666.63	78.5	–	–	–	20.99 ± 0.16	OGLE
2014/01/10	56667.60	79.5	24.55 ± 0.15	22.46 ± 0.08	21.75 ± 0.17	21.17 ± 0.07	NTT
2014/01/20	56677.61	89.5	–	–	–	21.15 ± 0.19	OGLE
2014/01/23	56680.54	92.4	–	22.78 ± 0.14	22.16 ± 0.10	21.66 ± 0.12	NTT
2014/02/02	56690.53	102.4	–	–	–	21.35 ± 0.27	OGLE
2014/02/08	56696.55	108.5	–	–	–	21.92 ± 0.44	OGLE
2014/02/24	56712.52	124.4	–	–	–	21.17 ± 0.21	OGLE

[a] Phase with respect to the second maximum in the I LC, JD = 2456588.1 ± 2.4 d.

[b] OGLE=WT+OGLEIII; NTT=NTT+EFOSC2. More information about the telescopes and instruments can be found in Chapter 2.

Table 5.3: Decline and rise rates in the *BVRI* LCs of OGLE-2013-SN-100.

Band	Decline from 1st peak [a] (mag d^{-1})	Rise to 2nd peak [b] (mag d^{-1})	Decline from 2nd peak [c] (mag d^{-1})	Decline tail [d] (mag d^{-1})
B	–	–	–	0.040 ± 0.003
V	–	–	–	0.034 ± 0.002
R	–	–	–	0.033 ± 0.001
I	0.033 ± 0.001	-0.051 ± 0.005	0.017 ± 0.007	0.026 ± 0.003

[a] Considering the interval from $\sim$ 70 to 60 d before second *I* band maximum.
[b] Considering the interval from $\sim$ 40 to 1 d before second *I* band maximum.
[c] Considering the interval from $\sim$ 6 to 16 d after second *I* band maximum.
[d] Considering the interval from $\sim$ 40 to 90 d after second *I* band maximum.

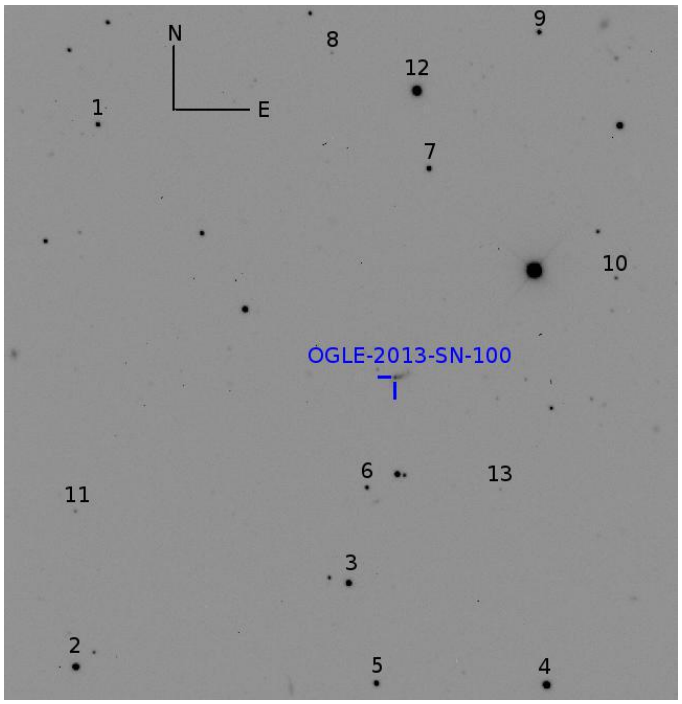

Figure 5.1: *V* band image of OGLE-2013-SN-100 taken with the NTT 2013 December 1. The field of view of the image is $30' \times 30'$.

spectra do not show a significant evolution. On one hand, they present Hα, Hβ and Hγ emissions, persisting up to 71.6 d since maximum. In addition, we have identified a broad absorption associated likely to He I line at λ5876 (likely to be contaminated by Na $\lambda\lambda$5880, 5896). Other possible traces of helium lines in the spectra include He I λ6768, and He I λ7065. We identify an absorption that is probably Fe II λ5169, but do not clearly recognise other Fe II features in the spectra. In addition, we distinguish other emissions that could be associated to Sc λ4670, 5527, 5658, and 6245. We also distinguish two narrow unresolved emissions likely to

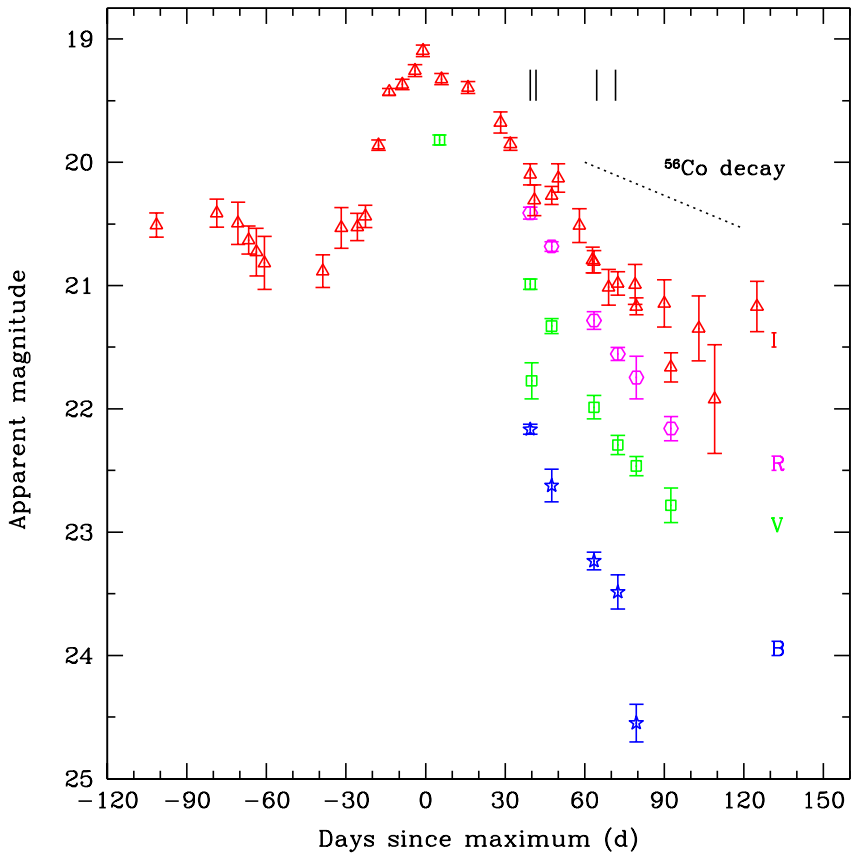

Figure 5.2: *BVRI* LCs of OGLE-2013-SN-100. Phases are given with respect to secondary *I* band maximum JD=2456588.1 ± 2.4. The vertical lines mark the epochs for which spectra were obtained. The trend of the linear ^{56}Co tail decay is also indicated in the figure.

be associated to [O III] $\lambda\lambda$4958.5, 5006.8, probably due to host galaxy contamination, given the horizontal-extended shape of the lines in the two-dimensional spectra. An alternative potential identification for the emission at $\sim$ 5000 Å could be He I λ5015. However, we find this less likely, basically since we do not identify other helium lines with a similar narrow emission-like shape in the spectra. In addition, the last three spectra show another feature that may be the unresolved [O II] $\lambda\lambda$3726, 3729 doublet which again is probably caused by host galaxy contamination. Another tentative line identification in our spectra is [O I] $\lambda\lambda$6300, 6364. This line could be associated to the transient (it has a broader shape than [O III]), this could mean that the observations correspond to relatively late phases since SN explosion, since such features start to appear in the nebular phases of CC-SNe (e.g. $\sim$ 60 d since explosion for SN 2011fu;

Table 5.4: List of spectroscopic observations of OGLE-2013-SN-100.

Date	Julian date (+2400000.00)	Phase[a] (d)	Telescope+Instrument[b]	Grism+Filter	Range (Å)	Resolving Power[c]
2013/12/01	56627.67	39.5	NTT+EFOSC2	Gr16+OG530	6000–9995	595
2013/12/03	56629.72	41.6	NTT+EFOSC2	Gr13	3650–9250	355
2013/12/26	56652.67	64.6	NTT+EFOSC2	Gr13	3650–9250	355
2014/01/02	56659.64	71.6	NTT+EFOSC2	Gr13	3650–9250	355

[a] Phase with respect to the second maximum in the I LC, JD = 2456588.1 ± 2.4 d.
[b] More information about the telescope and instrument can be found in Chapter 2.
[c] Measured from the FWHM of the night sky lines at a reference wavelength of 6563 Å.

see Chapter 3).

We have estimated the black-body temperatures from fitting black-body functions to our sequence spectra and have obtained a practically constant value of 5500 K for the first three cases, and a slightly lower value of 4900 K for our last spectrum. Nevertheless since the errors of these measurements are $\sim$ 500 K, we can say that the temperature remained constant over the period of our observations. Thus, the black-body temperatures could be comparable to those of CC-SNe at similar phases since secondary maximum (see e.g., figure 6 of Morales-Garoffolo et al. 2015a).

On the left panel of Figure 5.4, we show a blow-up of the Hα region of the spectra in velocity space. We have performed fits to the different profiles by decomposing them in components. Specifically, for the $\sim$ 40 d profile we found a good fit with three components, two associated to the Hα line (one broad Gaussian and one narrow Lorentzian), and another narrow Lorentzian component associated possibly to [N II] λ6583 from the host. For the 41.6 d spectrum of lower resolution, we obtained a good fit to the profile with two Lorentzian components, one narrow associated to the Hα line and another to [N II] λ6583 from the host. We attempted a three-component fit with an additional broad Hα component but the result was not satisfactory. For the last two profiles, also from spectra of lower resolution than the first, single component Lorentzian fits gave reasonable results. The Hα FWHM evolution is plotted on the right panel of Figure 5.4 and in Table 5.5 we show the results of the fits to the profiles.

5.4 Nature of OGLE-2013-SN-100

As shown in the previous sections, OGLE-2013-SN-100 shows two peaks in its I band light curve, the first of which reached an absolute magnitude of -17.59 ± 0.30 mag followed by a brighter second one of magnitude -18.77 ± 0.30 mag. Both of these maxima are consistent with the absolute magnitudes at peak of CC-SN LCs, which can range from > -15 mag (for faint objects; e.g. SN 2008ha, Valenti et al. 2009) to $\lesssim -21$ mag (superluminous events; e.g. Quimby et al. 2011). The spectra, all taken

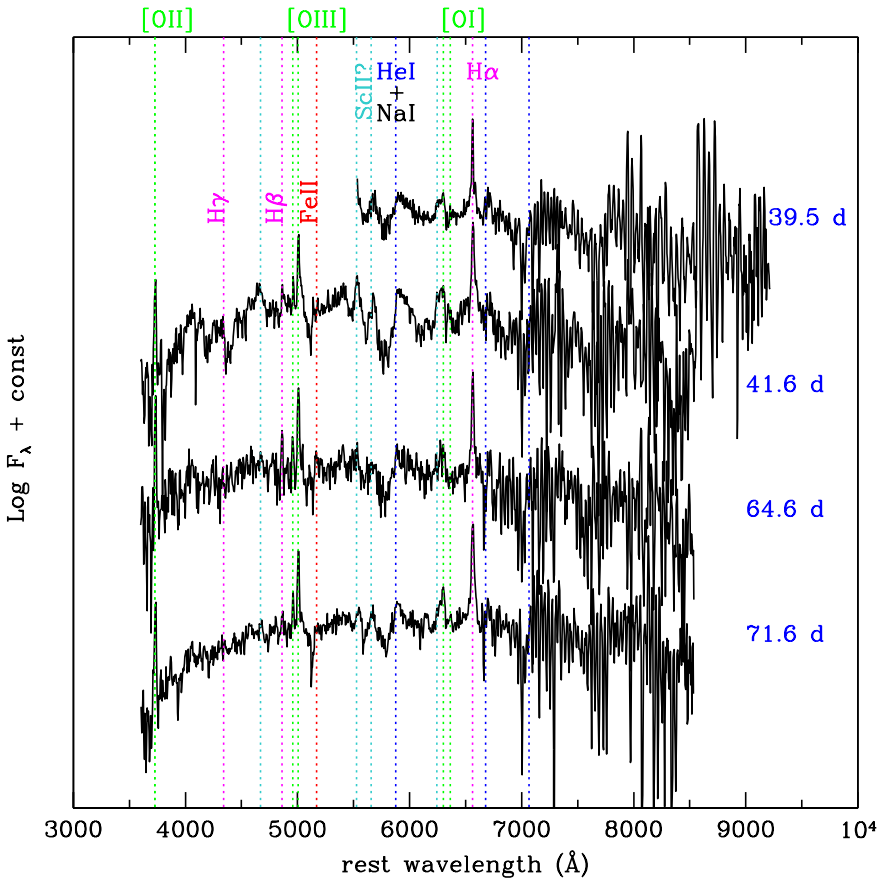

Figure 5.3: Optical spectral evolution of OGLE-2013-SN-100. The spectra are in the host galaxy rest-frame and have been shifted vertically for clarity. The most relevant features of the spectra are also indicated with vertical dashed lines. Phases indicated in blue are with respect to the second maximum in the I LC, JD = 2456588.1 ± 2.4 d.

after secondary maximum, show narrow Balmer emission lines with the Hα features exhibiting FWHM, which could be indicative of interaction between the transient's ejecta and H-rich CSM. In addition, the first spectrum of higher resolution shows a possible broad component underlying the narrow emission that could be compatible with SN emission (at later times this component could be hidden by the ejecta-CSM interaction). We have also identified absorptions likely to be associated to He I, a feature that is possibly Fe II λ5169, other lines that could be associated to scandium, and an emission probably due to [O I] $\lambda\lambda$6300, 6364. These features are common in the spectra of CC-SNe, which makes us suspect that a SN explosion has occurred at the site of OGLE-2013-SN-100. Below we explore several possible scenarios giving

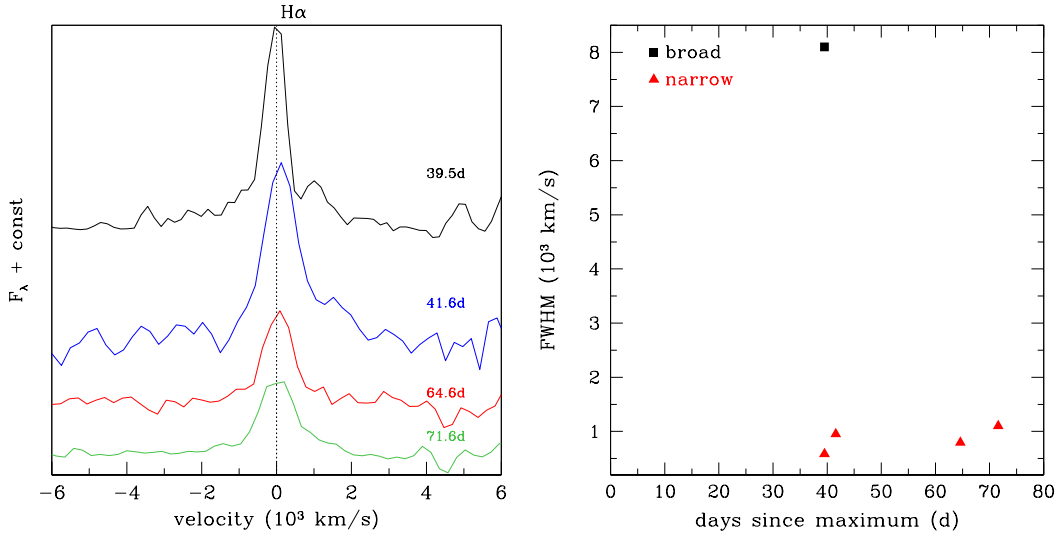

Figure 5.4: Left panel: Blow-up of the Hα region in the spectra of OGLE-2013-SN-100. Right panel: Time evolution of the FWHM of the Hα line in velocity space. Phases are with respect to secondary I band maximum, JD = 2456588.1 ± 2.4 d.

Table 5.5: Hα region profile fitting parameters for OGLE-2013-SN-100.

Date	Julian date (+2400000.00)	Phase[a] (d)	λ (Å)	Function	Flux (10^{-16} erg cm^{-2} Å^{-1})	Width (Å)
2013/12/01	56627.67	39.5	6564.32	Gaussian	4.59	177.20
2013/12/01	56627.67	39.5	6562.24	Lorentzian	5.60	12.77
2013/12/01	56627.67	39.5	6587.00	Gaussian	0.38	5.14*
2013/12/03	56629.72	41.6	6565.54	Lorentzian	8.29	20.79
2013/12/03	56629.72	41.6	6599.19	Lorentzian	1.12	18.05*
2013/12/26	56652.67	64.6	6564.19	Lorentzian	3.58	17.40
2014/01/02	56659.64	71.6	6563.69	Lorentzian	4.12	24.48

[a] Phase with respect to the second maximum in the I LC, JD = 2456588.1 ± 2.4 d.
* Likely the 6583 Å line of the [N II] doublet due to host contamination.

rise to the observed properties of this peculiar transient.

5.4.1 OGLE-2013-SN-100 compared to type IIb SNe with double-peaked LCs

To begin with, we study the possibility of OGLE-2013-SN-100 being a type IIb SN. With this purpose, in Figure 5.5, we represent the I absolute LC of OGLE-2013-SN-100 together with those of three type IIb SN that show two peaks in their I band LC, namely SNe 1993J, 2011fu, and 2013df.

The figure reflects that the first peak of SNe 1993J, 2011fu, and 2013df takes

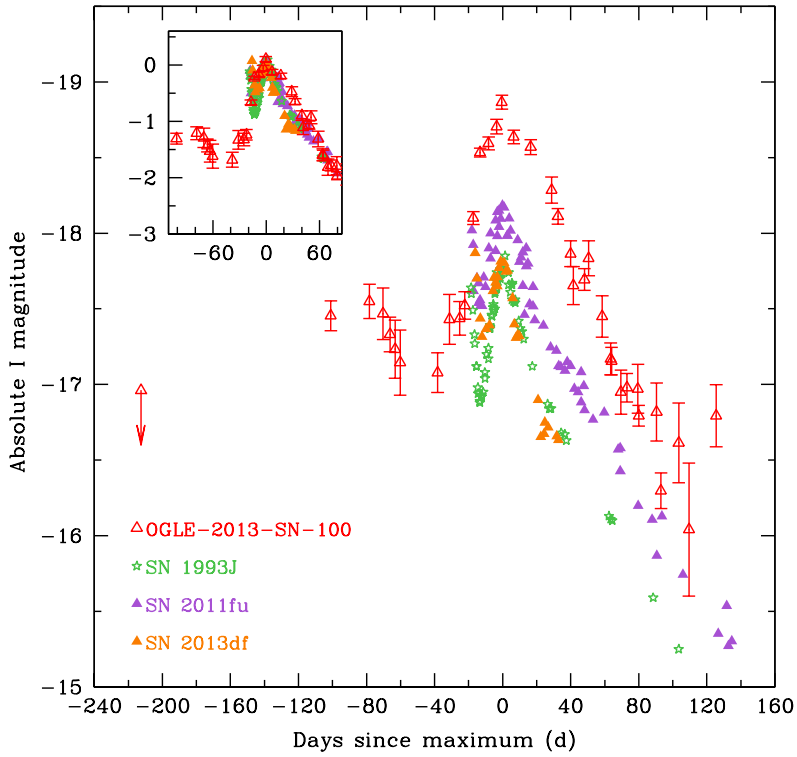

Figure 5.5: I band absolute LCs of OGLE-2013-SN-100, and the type IIb SNe 1993J, 2011fu, and 2013df. The magnitudes normalized to secondary peaks are depicted in the inset in the upper left. Phases are with respect to secondary I band maxima.

place at a much shorter timescale, while the second peak, apart from being brighter, is slightly broader for OGLE-2013-SN-100. On the other hand, the decay tails seem similar.

In Figure 5.6 we show the intrinsic $(V-I)_0$ colour evolution for SNe 1993J, 2011fu, and 2013df compared to that of OGLE-2013-SN-100. Note that for the $(V-I)_0$ of OGLE-2013-SN-100 at $\sim$ 5 d since secondary maximum, we have interpolated the I band magnitude from the nearest epoch. At this phase and at $\sim$ 40–50 d, the colour index of OGLE-2013-SN-100 seems comparable to the rest of the objects. However, OGLE-2013-SN-100 is redder at later phases.

From the minima of the P-Cygni broad absorption components of the He I λ5876 and Fe II λ5169 features, we have estimated the velocities of the OGLE-2013-SN-100 ejecta regions where these lines are formed. The results are presented in Figure 5.7. For comparison, we have also shown in the figure the velocities of these features for SNe 1993J, 2011fu, and 2013df. As can be seen, the velocities for OGLE-2013-SN-

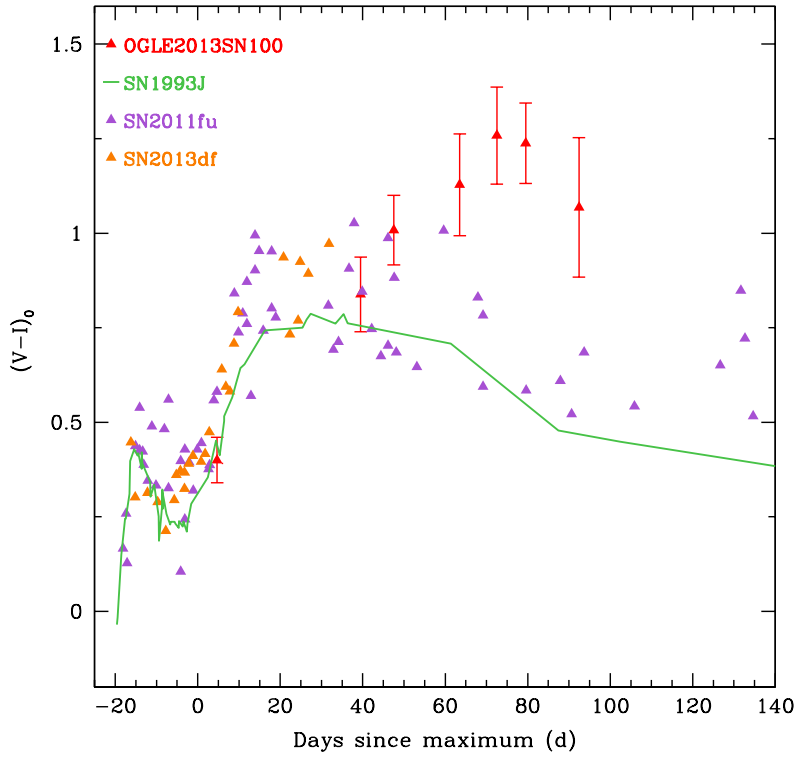

Figure 5.6: Comparison of the intrinsic $(V-I)_0$ colour evolution for OGLE-2013-SN-100 and type IIb SNe 1993J, 2011fu, and 2013df. The colour curves have been aligned in phase with respect to the I band LC secondary maximum.

100 are lower than those of the type IIb SNe. On the other hand, the FWHM of the Hα emission components of the P-Cygni profiles of the type IIb SNe 2011fu and 1993J at around 40 d, approximately double that which we have found for the broad component of the Hα profile of OGLE-2013-SN-100.

We present a comparison of OGLE-2013-SN-100 spectra to those of SN 1993J and 2011fu in Figure 5.8. The spectra for SN 1993J were downloaded from the Weizmann Interactive Supernova data REPository (WISeREP;[1] Yaron & Gal-Yam 2012), being their original reference Barbon et al. (1995), and those of SN 2011fu are from Chapter 3 of this thesis. The figure reflects that the spectra of OGLE-2013-SN-100 do not show evident similarities to those of SNe 1993J or 2011fu. Particularly, neither of the type IIb SNe show the prominent Hα emission that OGLE-2013-SN-100 does, while OGLE-2013-SN-100 does not show hints of absorption lines of He I λ6678.

[1] http://wiserep.weizmann.ac.il/

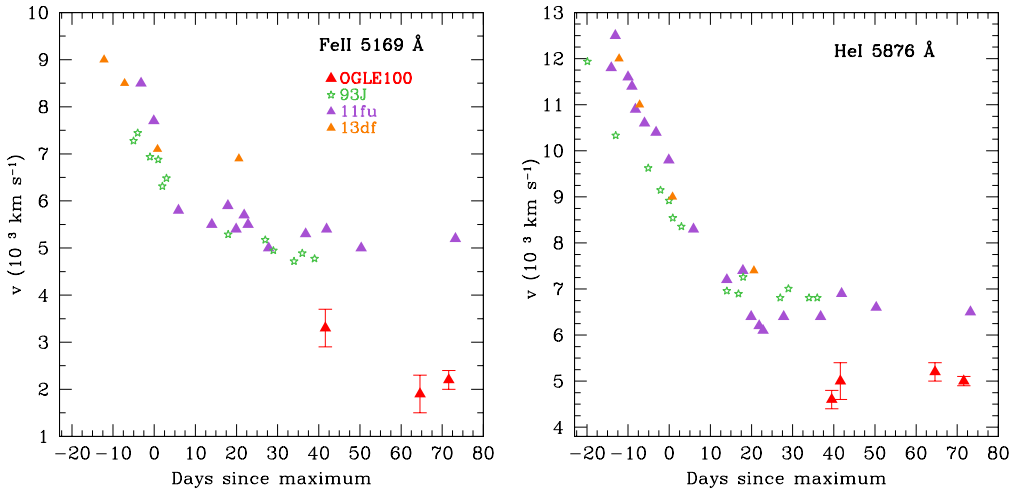

Figure 5.7: Fe II λ5169 and He I λ5876 velocities for OGLE-2013-SN-100 compared to type IIb SNe 1993J, 2011fu, and 2013df. The phases are with respect to their I band secondary maximum.

Was OGLE-2013-SN-100 a type IIb SN?

The completely different shape and duration of the first peak in the LC of OGLE-2013-SN-100 with respect to those of SNe 1993J, 2011fu, and 2013df suggest that its physical origin is completely different from that of those SNe. On the other hand, the spectral features of OGLE-2013-SN-100 are somewhat different as those observed in type IIb SNe. Specifically, the spectra show a clear narrow Hα emission, which type IIb objects do not present at similar phases. As a test, we have removed the narrow emissions from the first two spectra of OGLE-2013-SN-100 and compared them to spectra in the GELATO database, and have not obtained type IIb SNe as best fitting spectra but instead the best match was for SNe of types Ib/c. Other observables, such as the colour and the ejecta velocities or the temperature, are also different for this transient if we compare them with those of type IIb SNe. Thus, all in all, we are inclined to consider that OGLE-2013-SN-100 is not a type IIb SNe. However, given the limitations of the dataset, we cannot completely discard this possibility. If the object was a type IIb SN, the observational properties indicate that the progenitor of OGLE-2013-SN-100 and/or its circumstellar environment were somewhat different from those of the type IIb SNe observed up to now.

5.4.2 OGLE-2013-SN-100 compared to some other objects with double-peaked LCs

In Figure 5.9 we show a comparison of the I band LC of OGLE-2013-SN-100 with those of some other transients that exhibited two peaks in their LCs, namely, the

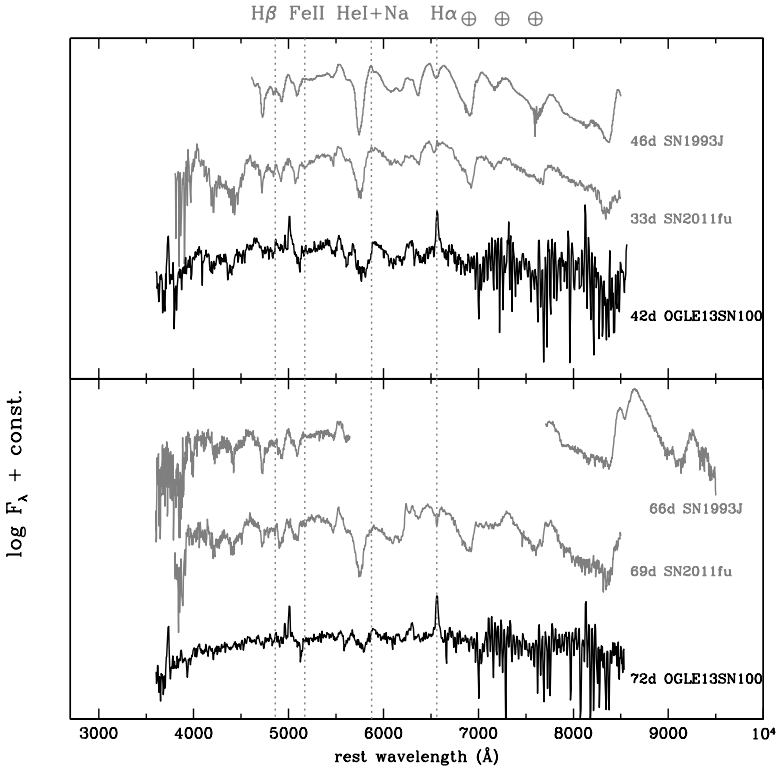

Figure 5.8: 42 and 72 d spectra for OGLE-2013-SN-100 compared to type IIb SNe 1993J, 2011fu at similar phases with respect to their I band secondary maximum. All spectra have been deredenned, redshift corrected, and shifted vertically for clarity.

transient SN 1961V (Zwicky, 1964; Bertola, 1967), the type Ibn SNe 2006jc (Pastorello et al., 2007), and the still debated SN impostor SN 2009ip (e.g. Mauerhan et al. 2013; Pastorello et al. 2013; Fraser et al. 2013; Margutti et al. 2014; Fraser et al. 2015).

As can be seen in the figure, all objects show a first event that is dimmer than the second. However, the first events have different shapes, for example that of SN 1961V is practically flat. SN 2006jc showed a first spiked outburst (for clarity, not shown in the figure) that ocurred about a year earlier than the second peak. Even if we compare the two R band upper limits before second peak of SN 2006jc, they are much dimmer than the first peak of OGLE-2013-SN-100. Furthermore, the first event in the LC of SN 2009ip is significantly narrower than that of OGLE-2013-SN-100. On the other hand, SNe 1961V, 2006jc, and 2009ip all exhibit a faster decline from second peak in comparison with OGLE-2013-SN-100.

We have plotted the $(V-I)_0$ colour evolution of OGLE-2013-SN-100 along with

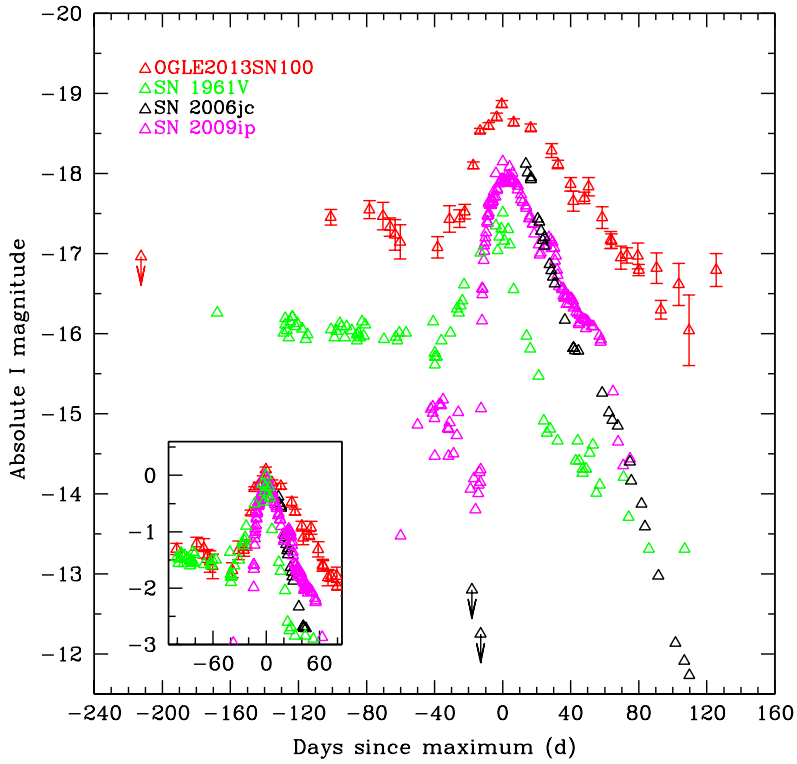

Figure 5.9: I band absolute LCs of OGLE-2013-SN-100, SNe 1961V, 2006jc, and 2009ip. The magnitudes normalized to secondary peaks are depicted in the inset in the bottom left. Phases are with respect to secondary I band maxima.

those of SN 2006jc and SN 2009ip in Figure 5.10. The figure shows that OGLE-2013-SN-100 exhibits a colour evolution seemingly parallel to that of SN 2009ip but that its indices are slightly redder. OGLE-2013-SN-100 is also somewhat redder than SN 2006jc up to about 70 d.

A spectral comparison of OGLE-2013-SN-100 to SN 2006jc and SN 2009ip is shown in Figure 5.11. The comparison spectra were downloaded from WISeREP but their original references are Anupama et al. (2009) for the $\sim$ 40 d and Pastorello et al. (2007) for the 72 d spectra of SN 2006jc, respectively. The spectra for SN 2009ip were obtained from Fraser et al. (2013). Compared to SN 2006jc, OGLE-2013-SN-100 exhibits different features. For example it lacks strong He I emissions such as He I λ5876 and presents stronger Hα.

The 42 d spectrum of OGLE-2013-SN-100 shows different features than that of SN 2009ip at a similar phase. For example, the line that we have identified as He I λ5876 is more intense, a Fe II λ5169 trace has tentatively been recognised,

and the hydrogen lines are weaker for OGLE-2013-SN-100. On the other hand, the spectra at $\sim$ 72 d share some common features. For example, between $\sim$ 5000 and $\sim$ 6000 Å, the He I λ5876 line is similar, as are the two absorptions that we have identified as Sc λ5527, 5658 in the spectrum of OGLE-2013-SN-100.

All in all, we find the spectra of OGLE-2013-SN-100 to be quite distinct from SN 2006jc but somewhat more similar to SN 2009ip.

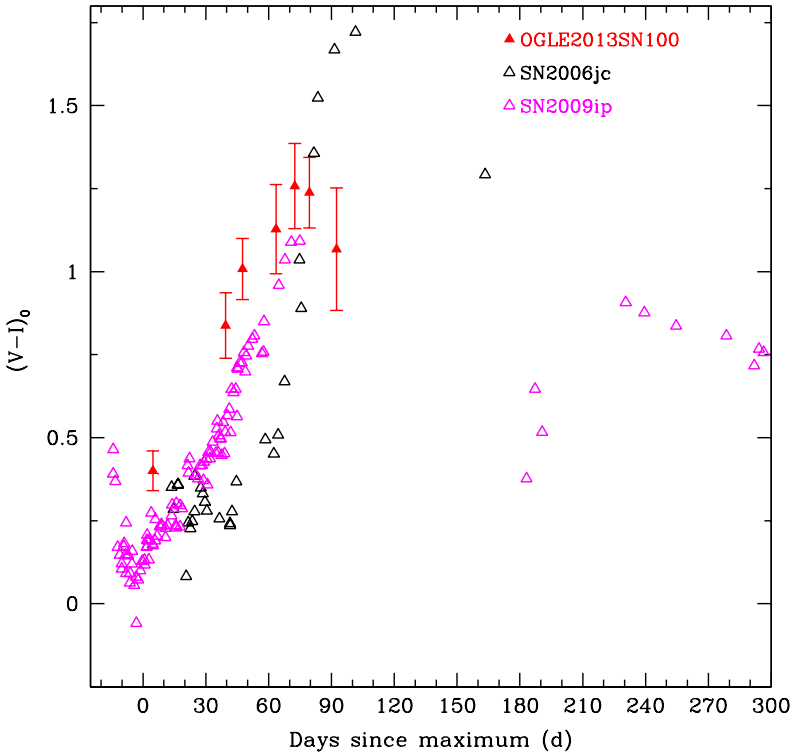

Figure 5.10: Comparison of the intrinsic $(V-I)_0$ colour evolution for OGLE-2013-SN-100 and SN 2009ip. Phases are with respect to secondary I band maxima.

Was the LC of OGLE-2013-SN-100 powered by a combination of an outburst and a SN explosion?

1. Outburst + SN explosion

One possibility that comes to mind to explain the LC and spectral behaviour of OGLE-2013-SN-100, and one which has been proposed for SNe 1961V, 2006jc, and 2009ip, is that the first maximum is caused by a mass-loss eruptive episode of the progenitor, while the second peak is powered by its core-collapse terminal explosion

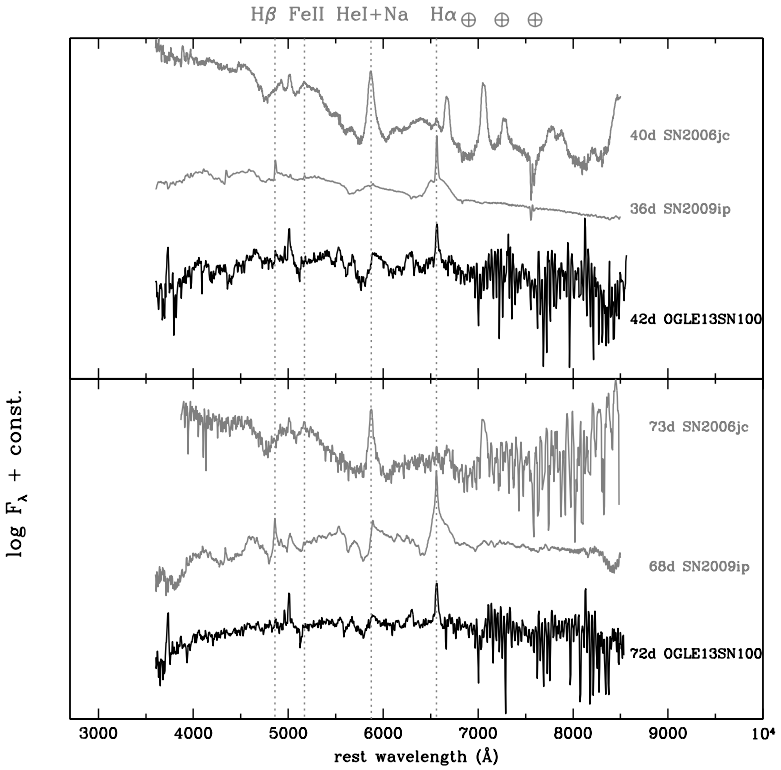

Figure 5.11: Comparison of 42 and 72 d spectra for OGLE-2013-SN-100 to the type Ibn SN 2006jc and the still-debated SN 2009ip at similar phases with respect to their I band secondary maximum. All spectra have been deredenned, redshift corrected, and shifted vertically for clarity.

(Smith et al. 2011; Pastorello et al. 2007; Mauerhan et al. 2013). Mass loss episodes are known to be the cause of the augmentation of luminosity in the LCs of for example the rare, unstable, and very massive ($M \gtrsim 40$ M$_\odot$) LBV stars (Humphreys & Davidson, 1994). An example of a LBV star is the Galactic η Carinae, whose episode of notable mass loss produced the naked-eye observed increase of its luminosity in the mid-19th Century. The main problem with this interpretation for OGLE-2013-SN-100 is the fact that the first peak in its LC is as bright as -17.59 ± 0.30 mag, whereas the absolute magnitudes of eruptive outbursts of massive stars have been observed to range from ~ -10 to -16 mag (Smith et al., 2011). Thus, we find the 'outburst + SN explosion' scenario unlikely to explain the nature of OGLE-2013-SN-100.

2. SN explosion + outburst

Another possible interpretation for the observational behaviour of OGLE-2013-SN-100 is that the first peak of the LC was powered by the core-collapse of a massive star, and then its ejecta encountered CSM, which caused an augmentation of the LC brightness producing the second peak. Smith et al. (2011) proposed this as a possible explanation for the LC of the transient SN 1961V, while for the still-debated SN 2009ip this possibility was also contemplated by Mauerhan et al. (2013) (however, see Fraser et al. 2013).

In this context, the delayed CSM-ejecta interaction powered peak could be explained if the CSM surrounding the progenitor had a double density distribution, one inner part with relatively low density and a denser outer zone, so that the second peak in the LC was caused when the ejecta collided with the external denser CSM. The origin of this higher density CSM could be mass-expelled by the progenitor of OGLE-2013-SN-100 before the CC-SN explosion. If the higher density CSM were H-rich, this would explain the narrow Balmer emission lines observed in the object's spectra. The clumpy inhomogeneous nature of the CSM or a rare geometrical configuration of the CSM could then explain the simultaneous observation of lines corresponding to both the SN ejecta and those caused by ejecta-CSM interaction. We can estimate when the progenitor of OGLE-2013-SN-100 expelled the dense CSM by assuming the first point in the I band LC as the SN explosion date, and supposing the SN ejecta began to interact with the dense CSM at the phase of the minimum between the two peaks in the I band LC (JD = 2456538.8 d). Additionally, we adopt the ejecta velocity at the time of explosion to be $\sim$ 8000 km s^{-1} (FWHM of the broad Hα component of our first spectrum; lower limit of the ejecta velocity at the time of explosion) and that of the unshocked dense CSM to be $\sim$1000 km s^{-1} (FWHM of the narrow Hα components in our spectra). With this, we find that the dense CSM should have been expelled $>$ 1 yr before CC-SN explosion.

The lack of earlier spectroscopic data makes it difficult to classify the plausible SN that exploded as OGLE-2013-SN-100. However, the observed signatures of ejecta-CSM interaction and the presence of a possible broad component in the Hα profile of our first spectrum, naturally makes us suspect that the object could be a type IIn SN. In fact, the FWHM of the broad component of the Hα profile of our first spectrum is comparable to broad components present in the spectra of type IIn SNe (FWHM $\gtrsim 10^4$ km s^{-1}; Stritzinger et al. 2012), which are usually associated with SN emission. To check the possibility of OGLE-2013-SN-100 being a type IIn SNe, we have plotted in Figure 5.12 a comparison of our latest spectrum of OGLE-2013-SN-100 and a spectrum at a similar phase since (first) maximum for the type IIn SN 1998S (e.g., Fassia et al. 2001). The spectrum for SN 1998S was downloaded from WISeREP but the original reference is Leonard et al. (2000). The reason for choosing a spectrum of SN 1998S as comparison, is that when comparing the spectra of OGLE-2013-SN-100 only to type IIn SNe with GELATO, SN 1998S gave

reasonable fits. The figure shows that the Hα profiles of the two objects are quite different. However, we also see some similarities in the lines we have identified as He I + Na and [O I]. Overall, we do not find the spectra strikingly similar, but we must bear in mind that type IIn SNe show diverse spectroscopic properties. For this reason, we cannot conclude that OGLE-2013-SN-100 was a type IIn SN, although we do not discard this possibility.

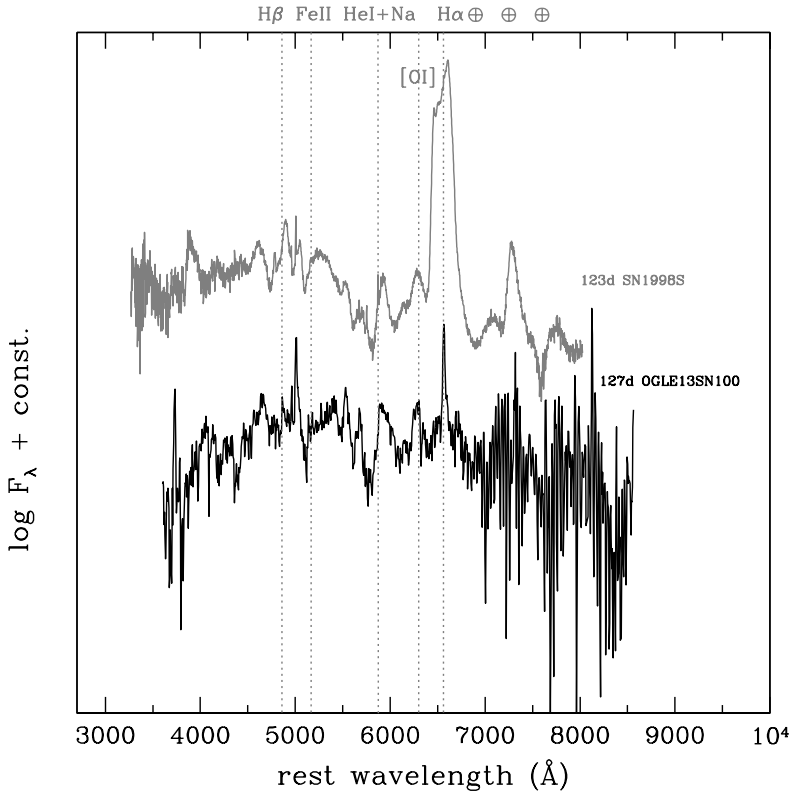

Figure 5.12: Comparison of the spectra of type IIn SN 1998S and OGLE-2013-SN-100 at $\sim$ 130 d since first maxima. The spectra have been deredenned, redshift corrected, and shifted vertically for clarity.

All in all, we find the 'SN explosion + CSM powered peak' a possible way, and in fact the most likely, to explain the observed properties of OGLE-2013-SN-100.

5.5 Summary

In this chapter we have presented the analysis of the observational data of OGLE-2013-SN-100. The transient shows a peculiar double-peaked LC, whose first peak is not similar to those observed for type IIb SNe such as SNe 1993J, 2011fu, or 2013df.

The spectra of OGLE-2013-SN-100 show common lines to those observed in CC-SN explosions, including Balmer emissions indicative of some degree of circumstellar interaction between ejecta and CSM. Both the spectral and photometric properties lead us to believe that there has been a CC-SN explosion at the site of OGLE-2013-SN-100 before the classification of this transient. The most likely possibility that explains the observational data, and specifically the LC, is that the first peak was due to the core-collapse of a massive star, and the second to the interaction of the SN ejecta and the CSM. If this were the case, the CSM has to have a configuration that permits the simultaneous observation of the SN spectral features and those caused by ejecta-circumstellar interaction. In any case, this object is an intruder in the small group of individual type IIb SNe that we selected to study in this thesis.

Chapter 6

Comparative Study of Type IIb SNe: Host Galaxies and Observables

The aim of this chapter is to establish correlations and differences among the observational properties of SNe IIb for a wavelength ranging from the UV to the NIR. To this end, beside the two type IIb SNe studied in this thesis, we have selected a sample of type IIb SNe found in the literature. The chapter is structured in the following way: To begin with, we investigate the host galaxies of the objects. Next their UV, optical, and NIR photometric data (when available) are compared, and at last we look at their optical spectral properties.

6.1 The sample

The sample of type IIb SNe studied throughout this chapter comprises 24 SNe: SNe 2011fu, 2013df, and 22 type IIb SNe from the literature for which individual studies exist and/or those for which there are some published UV and/or optical and/or NIR data (see Table 6.1). All the objects of the sample are confirmed type IIb SNe. Note that OGLE-2013-SN-100 was omitted from the sample since, as discussed in Chapter 5, we find it most likely not to be a type IIb SN.

6.2 Host galaxies

6.2.1 Galaxy colour

In Figure 6.1, we have depicted the g-r versus r absolute magnitudes for the host galaxies of the type IIb SNe of our sample. To compute the g-r indices, we used the photometric data from the SDSS when available. When they were not, we collected

Table 6.1: Properties of the sample type IIb SNe.

SN	Host galaxy	$M^a_{\rm max}$ (mag)	μ (mag)	Redshift[b]	$E(B\text{-}V)$ (mag)	$E_{\rm kin}$ (10^{51}erg)	^{56}Ni mass ($M_\odot$)	$M_{\rm ej}$ ($M_\odot$)	Ref.
1987K	NGC 4651	-17.61 ± 0.95 (R)	31.75 ± 0.95	0.00263 ± 0.00001	0.02 ± 0.01	–	–	–	(1)
1993J	M81	-17.88 ± 0.38 (R)	27.80 ± 0.03	-0.00011 ± 0.00001	0.19 ± 0.09	$0.7 - 1.4$	$0.10 - 0.14$	$1.3 - 3.5$	(2),(3)
1996cb	NGC 3510	-17.33 ± 0.22 (R)	29.95 ± 0.15	0.00238 ± 0.00001	0.12 ± 0.01	–	–	–	(4)
2001ig	NGC 7424	-17.9 (V*)	30.59 ± 0.15	0.00313 ± 0.00001	0.01	–	0.13	1.15	(5)
2001gd	NGC 5033	–	30.92	0.00292 ± 0.00001	0.10	–	–	–	(6)
2003bg	ESO 420-G009	-17.78 ± 0.25 (R)	31.68 ± 0.14	0.00456 ± 0.00001	0.00	5	$0.1 - 0.2$	4	(7),(8)
2006T	NGC 3054	-17.49 (r)	32.68	0.00809 ± 0.00002	0.07	–	–	–	(6)
2006ba	NGC 2980	–	34.79	0.01908 ± 0.00003	0.01	–	–	–	(6)
2006bf	UGC 8093	–	35.25	0.02387 ± 0.00001	0.02	–	–	–	(6)
2008aq	MCG-02-33-20	-16.74 ± 0.43 (V)	32.45 ± 0.43	0.00797 ± 0.00002	0.04	–	–	–	(6),(9)
2008ax	NGC 4490	-17.69 ± 0.39 (R)	29.92 ± 0.29	0.00189 ± 0.00001	0.40 ± 0.10	$1 - 6$	$0.07 - 0.15$	$2 - 5$	(10)
2008bo	NGC 6643	-15.98 ± 0.25 (r)	31.71 ± 0.25	0.00495 ± 0.00001	0.05	–	–	–	(6),(9),(11)
2008cw	PGC 2181396	–	35.82	0.0324	0.06	–	–	–	(6)
2009K	NGC 1620	–	33.55	0.01172 ± 0.00001	0.05	–	–	–	(6)
2009mg	ESO 121-G26	-17.69 ± 0.49 (V)	33.01 ± 0.48	0.00756 ± 0.00001	0.14 ± 0.02	0.15	0.10	0.56	(12)
2010P	Arp 299	–	33.26 ± 0.15	0.01030	2.27	–	–	–	(13)
2010as	NGC 6000	-17.85 ± 0.38 (R)	32.16 ± 0.36	0.00732 ± 0.00001	0.57 ± 0.10	0.7	0.12	2.5	(14)
2010jr	ESO 362-18	-16.84 ± 0.17 (V)	33.55 ± 0.15	0.01245 ± 0.00003	0.02	–	–	–	(9)
2011dh	M51	$-17.38^{+0.34}_{-0.29}$ (R)	$29.46^{+0.29}_{-0.27}$	0.00200	$0.07^{+0.07}_{-0.04}$	$0.6 - 1.0$	$0.05 - 0.10$	$1.8 - 2.5$	(15)
2011ei	NGC 6925	-16.08 ± 0.44 (R)	32.27 ± 0.43	0.00931 ± 0.00001	0.24 ± 0.02	2.5	0.03	1.6	(16)
2011fu	UGC 1626	-18.08 ± 0.15 (R)	34.36 ± 0.15	0.01849 ± 0.00004	$0.10^{+0.04}_{-0.03}$	1.3	0.15	3.5	Ch. 3
2011hs	IC 5267	-17.00 ± 0.34 (R)	31.85 ± 0.15	0.00571 ± 0.00001	0.17 ± 0.08	0.85	0.04	$1.8 - 2.5$	(17)
2013cu	UGC 9379	-18.65 (r)	35.16 ± 0.15	0.02524 ± 0.00014	0.00	–	–	–	(18)
2013df	NGC 4414	-17.71 ± 0.31 (R)	31.65 ± 0.30	0.00239 ± 0.00002	0.10 ± 0.02	$0.4 - 1.2$	$0.10 - 0.13$	$0.8 - 1.4$	Ch. 4

[a]For SNe 1987K, 1993J, 1996cb, 2003bg, 2009mg, 2011ei, and 2011hs we calculated the values of $M_{R\rm max}$ with the apparent magnitudes, distance moduli and extinctions given in the references described in the table.
[b]Host galaxy redshift taken from NED.
*synthetically estimated by Ben-Ami et al. (2015) from HST spectra.
(1) Filippenko (1988); (2) Richardson et al. (2006); (3) Young et al. (1995); (4) Qiu et al. (1999); (5) Silverman et al. (2009); (6) Bianco et al. (2014) and references therein; (7) Hamuy et al. (2009); (8) Mazzali et al. (2009); (9) Pritchard et al. (2014) and references therein; (10) Taubenberger et al. (2011); (11) Milisavljevic et al. (2010); (12) Oates et al. (2012); (13) Kankare et al. (2014); (14) Folatelli et al. (2014b); (15) Ergon et al. (2014); (16) Milisavljevic et al. (2013); (17) Bufano et al. (2014); (18) Gal-Yam et al. (2014).

the B and V magnitudes from NED or SIMBAD and used the transformations to the Sloan system presented in Jester et al. (2005). For the hosts of SNe 2011fu (UGC 1626) and 2006ba (NGC 2980) we were unable to compute a colour index since only B band data are available in the aforementioned databases. In addition, we have not included in the figure the host of SN 2010P (Arp 299), since it is an interacting galaxy, and no optical photometric data exist for the component where SN 2010P took place. For the hosts of SNe 2003bg (ESO 420-G009), 2006T (NGC 3054), 2009mg (ESO 121-G26), 2010as (NGC 6000), and 2010jr (ESO 362-18), the values reported in the figure are B-R versus R (in the AB magnitude system) since there was neither SDSS photometry nor V band data available. The dashed line in the figure represents the separation between blue and red galaxies proposed by Masters et al. (2010). As can be seen in the figure, there is a slightly larger number of red hosts in our sample. Specifically, 57 per cent of our galaxies belong to the red category and the remaining 43 per cent are blue hosts. Although our sample is highly constrained, this is in fair agreement with Galbany et al. (2014), who studied a sample of SN hosts from the CALIFA survey[1] and found that the hosts of type II and Ibc/IIb SNe are equally split in blue and red galaxies. This means that galaxies with both high star formation (blue) and low star formation (red) are favoured for hosting SNe IIb. In general, stronger connection with star formation implies shorter stellar lifetime from birth to SN explosion and, in consequence, larger progenitor $M_{\rm ZAMS}$. However, as indicated in Table 6.2, there are no significant differences between the estimated $M_{\rm ZAMS}$ of the progenitors of the SNe hosted in blue and red galaxies. In fact, the largest estimated progenitor $M_{\rm ZAMS}$ is for SN 2003bg. However, this object was hosted in a red galaxy. It is interesting to note that the hosts of the 'extended' type IIb SNe of our sample (progenitors with $R \sim 100$ R$_\odot$), with the exception of SN 2011hs, are red. At the moment we do not find an explanation for this over-abundance of 'extended' SNe in red hosts. A larger sample could help confirm this result. We would also like to remark that, as indicated in Table 6.2, the parameters of the SNe were obtained by using different methods by the different authors, which could lead to high uncertainties in the comparison of parameters for the different SNe.

If we assume the criteria of Arcavi et al. (2010) to separate giant ($M_{\rm r} < -18$ mag; metallicity $Z > 0.35\ Z_\odot$[2]) from dwarf hosts ($M_{\rm r} \geq -18$ mag; $Z \leq 0.35\ Z_\odot$), figure 6.1 would also reflect that all but the hosts of SNe 1996cb (NGC 2510) and 2008ax (NGC 4490) are giant. Tomasella et al. (2014) carried out a study of the distribution of the subtypes of 78 CC-SNe in dwarf compared to giant galaxies. In their sample, there were four type IIb SNe whose hosts were giant galaxies. In our sample of 21 type IIb SN hosts we have found that 90 % are also giant. Our results do not confirm the excess of type IIb SNe in dwarf hosts claimed by Arcavi et al. (2010), in agreement with Sanders et al. (2012) and Tomasella et al. (2014).

[1] http://califa.caha.es/

[2] or $12 + \log_{10}({\rm O/H}) > 8.23$ on the Pettini & Pagel (2004) scale.

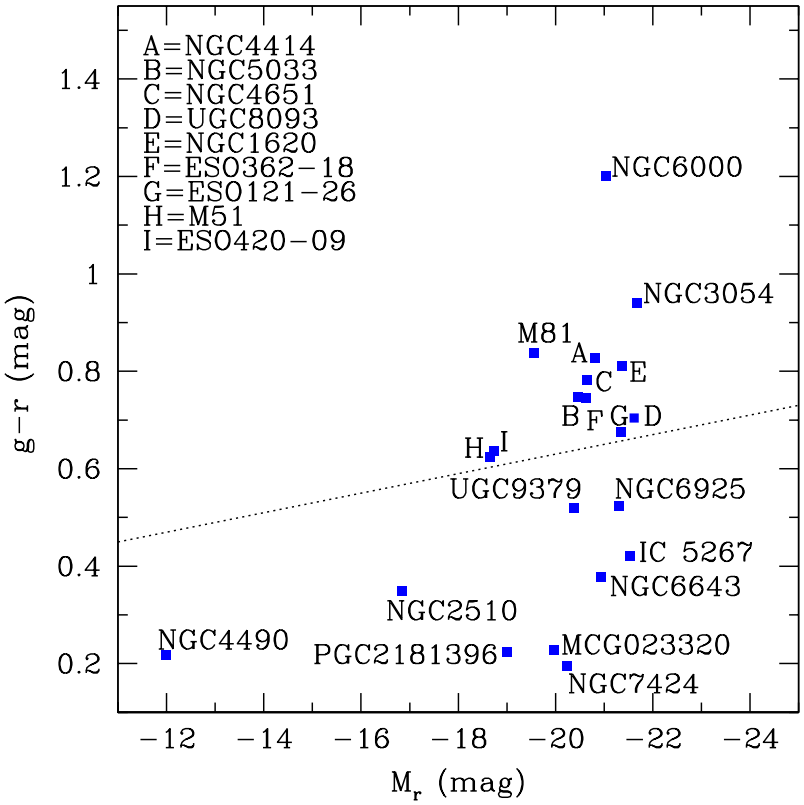

Figure 6.1: Colour-magnitude diagram for the host galaxies of the type IIb SNe in our sample. The dashed line represents the separation between blue and red galaxies proposed by Masters et al. 2010. Note that for the hosts of SNe 2003bg (ESO 420-G009), 2006T (NGC 3054), 2009mg (ESO 121-G26), 2010as (NGC 6000), and 2010jr (ESO 362-18) the values reported in the figure are *B*-*R* versus *R* (in the AB mag system) since there were no SDSS photometry or *V* band data available to transform the magnitudes to the Sloan system.

It would be interesting, as part of a future work, to study in detail the metallicity at the SN sites and try to connect them with the SN/progenitor properties.

6.2.2 Morphology

A possible indicator of star formation, other than red versus blue galaxies (as discussed in the previous section), is the presence of bars. In Table 6.3, we indicate the morphological type of each of the hosts of the SN sample. In Table 6.4, we show the numbers of type IIb SNe in barred, unbarred or intermediate galaxies of different morphological types. Table 6.4 indicates that the majority of SNe of our sample are

Table 6.2: Summary of the progenitor properties and host ($g-r$) indices of the type IIb SNe of our sample for which this information is provided in the literature and/or have been obtained in this thesis.

SN	$M_{\rm ZAMS}$ $M_\odot$	R $R_\odot$	$M_{\rm H}$ $M_\odot$	References	$(g-r)_{\rm Host}$ mag
1993J	13-16	600	0.03-0.05*	(1)	0.78 (red)
1996cb	–	~ 1	–	(2)	0.35 (blue)
2001gd	–	~ 100	–	(2)	0.75 (red)
2001ig	15	~ 1	–	(3)	0.20 (blue)
2003bg	20-25	~ 1	0.05	(4)	0.64 (red)**
2008ax	13	~ 1	0.05	(5)	0.22 (blue)
2008bo	–	~ 1	–	(2)	0.38 (blue)
2010as	28-29/15	–	–	(6)	1.20 (red)**
2011dh	12-15	200	0.03*	(7)	0.62 (red)
2011ei	10-15	~ 1	0.01	(8)	0.52 (blue)
2011fu	13-18	450	0.08*	(9)	–
2011hs	12-15	500-600	<0.13*	(10)	0.42 (blue)
2013df	12-17	500	0.03-0.05*	(11)	0.83 (red)

* Obtained multiplying the total envelope mass by an assumed mass fraction of Hydrogen in the envelope of $X_{\rm H}$=0.25.
(1) Woosley et al. (1994); Bersten et al. (2012).
(2) Chevalier & Soderberg (2010).
(3) Ryder et al. (2004, 2006); Silverman et al. (2009).
(4) Hamuy et al. (2009); Mazzali et al. (2009); Chevalier & Soderberg (2010).
(5) Crockett et al. (2008); Taubenberger et al. (2011); Hachinger et al. (2012); Jerkstrand et al. (2015).
(6) Folatelli et al. (2014b). The different masses reported correspond to those derived from direct detection of progenitor in HST images, and hydrodynamical modelling, respectively.
(7) Bersten et al. (2012); Van Dyk et al. (2013); Jerkstrand et al. (2015).
(8) Milisavljevic et al. (2013).
(9) Chapter 3 of this thesis
(10) Bufano et al. (2014).
(11) Van Dyk et al. (2014); Chapter 4 of this thesis.
** The value corresponds to ($B-R$).

in spirals of types Sbc/c, and there is a slightly larger number in unbarred galaxies. This is in accordance with the results obtained by Hakobyan et al. (2014) for a large sample of galaxies hosting type II SNe. Note that we have not included in the table the hosts of SNe 2006bf and 2010P, since the former is listed only as morphological type S, and the latter belongs to an interacting system. Since the hosts of SNe 1996cb, 2003bg, 2008aq, 2008ax, 2009mg, and 2010as have bars (see Table 6.3), they are more prone to star formation, and we would expect their progenitors to present larger $M_{\rm ZAMS}$. This is the case for SN 2003bg and 2010as (if the mass of the progenitor is considered to be that derived from the direct detection) but not for the rest of the objects in barred hosts.

Also in Table 6.3 we have indicated the offsets and distances of the different SNe of our sample with respect to their host galaxies' nuclei. The distances of the SNe to their galactic nuclei were calculated taking into account the position angle and inclination of their hosts (see e.g. equations 1 and 2 of Hakobyan et al. 2009). The

Table 6.3: Properties of the IIb SNe host galaxies and locations within the hosts of our SN sample.

SN	Host galaxy	Morphology	Absolute B mag. (mag)	i[a] (°)	Offset EW[b] (″)	Offset NS[b] (″)	D_{GN}[c] (″)
1987K	NGC 4651	SA(rs)c	-20.30 ± 0.95	49	22W	5N	24
1993J	M81	SA(s)ab; LINER Sy1.8	-20.20 ± 0.04	65	45W	160S	187
1996cb	NGC 3510	SB(s)m	-17.36 ± 0.30	78	20.9W	65.7N	74
2001gd	NGC 5033	SA(s)c;HII Sy1	-20.21	70	52W	161N	169
2001ig	NGC 7424	SAB(rs)cd	-19.75 ± 0.17	32	139E	109N	183
2003bg	ESO 420-G009	SB(s)c	-18.01 ± 0.17	42	16.3W	24.6S	31
2006T	NGC 3054	SAB(r)bc HII?	-20.65	52	22E	21S	153
2006ba	NGC 2980	SAB(s)c? HII	-21.38	58	21E	8S	187
2006bf	UGC 8093	S	-20.44	59	3.1W	15.5N	17
2008aq	MCG-02-33-20	SB(s)m	-19.34 ± 0.46	63	15E	45S	48
2008ax	NGC 4490	SB(s)d pec HII	-19.78 ± 0.30	60	53.1E	25.8S	62
2008bo	NGC 6643	SA(rs)c	-20.22 ± 0.27	60	31E	15N	35
2008cw	PGC 2181396	–	-18.46	62	1E	2N	4
2009K	NGC 1620	SAB(rs)bc	-20.58	54	8.7W	1.5N	9
2009mg	ESO 121-G26	SB(rs)c	-20.59 ± 0.49	51	46E	4S	49
2010P	Arp 299	IBm/SBm	–	41	6.2E	0.3N	6
2010as	NGC 6000	SB(s)bc	-19.74 ± 0.37	79	3.1W	2.0N	4
2010jr	ESO 362-18	S0/a Sy1.5	-19.78 ± 0.18	43	16.8W	13.6N	22
2011dh	M51	SAbc LINER	-20.98 ± 0.40	48	150E	90S	271
2011ei	NGC 6925	SA(s)bc HII	-20.39 ± 0.44	74	26E	28N	200
2011fu	UGC 1626	SAB(rs)c	-20.53 ± 0.27	14	2W	26N	148
2011hs	IC 5267	(R)SA(rs)0/a	-20.72 ± 0.17	42	20W	41N	111
2013cu	UGC 9379	Scd:	-20.11 ± 0.34	57	4E	20S	22
2013df	NGC 4414	SA(rs)c?;HII LINER	-20.78 ± 0.30	57	32E	14N	35

[a]Host galaxy inclination taken from the Asiago Supernova Catalogue (ASC; Barbon et al. 1999; http://graspa.oapd.inaf.it/asnc.html) or the HyperLeda database http://leda.univ-lyon1.fr/.
[b] The SN EW and NS offsets from their host galaxies' nuclei were collected mainly from the ASC.
[c] Estimated distance of the SN to its galaxy nucleus.

Table 6.4: Numbers of type IIb SNe from our sample in barred, unbarred or intermediate galaxies of different morphology.

	S0/a	Sa	Sab	Sb	Sbc	Sc	Scd	Sd	Sdm	Sm	Total
Unbarred	2	0	1	0	2	5	1	0	0	0	10
Intermediate	0	0	0	0	2	2	1	0	0	0	5
Barred	0	0	0	0	1	2	0	1	0	2	6
Total	2	0	1	0	5	8	2	1	0	2	21

dispersion of distances to galactic nuclei indicates that there does not seem to be a preferential position for type IIb SNe explosions within their host galaxies.

The investigations performed in this section lead us to conclude that there is not an apparent correlation between the distances of the SNe to their hosts' nuclei, and host morphology or progenitor characteristics.

6.3 Light curves

In this section we compare the available UV, optical, and NIR photometric data of our SN sample. See Table 6.5 for a summary of the data sources, and reference epochs used to represent the LCs shown throughout this section. The reference epochs correspond to the JD of the LCs' maxima in the R or r and V (when there are no R data available) bands, obtained from the literature, their LCs, or, by approximation, from the phases of the classification spectra (see more details in Table 6.5).

6.3.1 UV

In Figure 6.2 we show the UV absolute LCs of the SNe of our sample. The absolute magnitudes were obtained correcting for SN distance and extinction in the line of sight, and the phases are computed with respect to the reference epochs given in Table 6.5. The extinction corrections were obtained at the central wavelength for each UVOT filter by means of the Cardelli et al. (1989) parametrization with $R_V = 3.1$.

The figure reflects a dispersion of UV brightness and LC shapes among the sample of SNe. Regarding LC shape prior to maximum, a trace of cooling of the progenitors' stellar envelope after shock breakout has clearly been covered by observations for SNe 2010jr, 2011dh, and 2013df (Pritchard et al., 2014). The similarity between the brightness and duration of this cooling for SNe 2010jr and 2013df could imply that their progenitors had similarly-sized hydrogen envelopes (Brown et al., 2015), while the dimmer and shorter duration of this phase for SN 2011dh translates into a smaller envelope. One interesting fact is that, for these SNe with traces of early

Table 6.5: Data used in the photometric comparison of our SN sample.

SN	JD_{expl} (+240000)	JD_{max}* (+240000)	UV	Optical	NIR
1987K	$46984.0^{(a)}$	$47014.5^{(a)}$	–	(1)	–
1993J	$49074.0 \pm 0.7^{(b)}$	$49096.5 \pm 1.0^{(b)}$	–	(2),(3),(4),(5)	(4),(5)
1996cb	$50429.5^{(c)}$	$50452.5^{(c)}$	–	(6)	–
2001gd	–	$52175.5^{(d)}$	–	(7)	–
2001ig	$52246.5^{(e)}$	$52265.5^{(f)}$	–	–	–
2003bg	$52695.5^{(g)}$	52716.0–$52720.0^{(g)}$	–	(8)	(8)
2006T	–	$53781.6 \pm 0.1^{(h)}$	–	(7)	–
2006ba	–	$53829.3^{(d)}$	–	(7)	–
2006bf	–	$53813.5^{(d)}$	–	(7)	–
2008aq	–	$54532.2 \pm 1.5^{(i)}$	(9)	(7),(9)	–
2008ax	$54528.8 \pm 0.2^{(j)}$	$54550.3 \pm 0.4^{(j)}$	(9),(10)	(11),(12),(13)	(10)
2008bo	–	$54569.2 \pm 0.2^{(h)}$	(9)	(7),(9)	–
2008cw	–	$54616.5^{(d)}$			
2009K	–	$54865.1^{(d)}$	–	(7)	–
2009mg	$55168.1 \pm 2^{(k)}$	$55190.3 \pm 1.8^{(k)}$	(9)		–
2010P	–	$\sim 55228^{(l)}$	–	–	(14)
2010as	55267.8–$55274.7^{(m)}$	$55289.9 \pm 0.5^{(m)}$	–	(15)	(15)
2010jr	–	$55532.6^{(n)}$	(9)	–	–
2011dh	$55713.0 \pm 0.2^{(o)}$	$55734.9^{(o)}$	(16)	(16)	(16)
2011ei	$55767.5 \pm 1.0^{(p)}$	$55787.0 \pm 1.5^{(p)}$	(17)	(17)	–
2011fu	$55824.5 \pm 0.7^{(q)}$	$55848.7 \pm 0.9^{(q)}$	–	Chap.3	Chap.3
2011hs	$55872.0 \pm 4.0^{(r)}$	$55889.5 \pm 1.0^{(r)}$	(18)	(18)	(18)
2013cu	$56415.4 \pm 0.1^{(s)}$	$56425.9 \pm 1.0^{(s)}$	–	(19)	–
2013df	$56450.0 \pm 0.9^{(t)}$	$56470.8 \pm 0.5^{(t)}$	Chap.4	Chap.4	(20)

*Reference epochs used to depict the photometric data.
(a)Filippenko (1988); maximum epoch corresponds to $\sim R$ band. (b) Lewis et al. (1994); maximum epoch corresponds to the R band. (c)Qiu et al. (1999); maximum epoch corresponds to the R band. (d)Defined on the basis of the phase given by the classification spectrum, thus can be uncertain. (e) Ryder et al. (2004) (f) Ben-Ami et al. (2015); maximum epoch corresponds to the V band LC. (g) Hamuy et al. (2009); maximum epoch corresponds to the V band and has been assumed to be JD=2452718.0 in the plots. (h) Bianco et al. (2014); maximum epoch corresponds to V band. (i) estimated by low order polynomial fits to the V band LC. (j) Taubenberger et al. (2011); maximum epoch corresponds to the R band. (k) Oates et al. (2012); maximum epoch corresponds o the V band (l) Kankare et al. (2014); maximum epoch corresponds to the pseudo bolometric LC. (m) Folatelli et al. (2014b); maximum epoch corresponds to the R band. (n) Roming et al. (2009); maximum epoch corresponds to that of the brightest point in the V band LC. (o) Ergon et al. (2014); maximum epoch corresponds to the R band. (p) Milisavljevic et al. (2013); maximum epoch corresponds to the R band. (q) Chapter 3; maximum epoch corresponds to the R band. (r) Bufano et al. (2014); maximum epoch corresponds to the R band. (s) Gal-Yam et al. (2014); maximum epoch estimated by low order polynomial fits to the r band LC. (t) Chapter 4; maximum epoch corresponds to the R band.
(1) Filippenko (1988); (2) Lewis et al. (1994); (3) Barbon et al. (1995); (4) Richmond et al. (1994); (5) Matthews et al. (2002); (6) Qiu et al. (1999); (7) Bianco et al. (2014); (8) Hamuy et al. (2009); (9) Pritchard et al. (2014); (10) Roming et al. (2009); (11) Taubenberger et al. (2011); (12) Pastorello et al. (2008); (13) Tsvetkov et al. (2009); (14) Kankare et al. (2014); (15) Folatelli et al. (2014b); (16) Ergon et al. (2015); (17) Milisavljevic et al. (2013); (18) Bufano et al. (2014); (19) Gal-Yam et al. (2014); (20) Van Dyk et al. (2014).

cooling, the LC shapes of both SNe 2010jr and 2013df past maximum are similar, although SN 2013df declines at a faster rate. For SN 2011dh, however, only the *UVm2* LC follows a similar trend (albeit dimmer) to that of SN 2013df. From a few days before maximum to past maximum, both the *UVW1* and the *UVW2* of SN 2011dh mimic the shape of the optical LCs (Ergon et al., 2014), as do those of SNe 2008ax, 2009mg, and possibly 2011ei. Note that although missed by UV observations, the U band data of SN 2008ax did exhibit a shock breakout tail in the work presented by Roming et al. (2009). Given the similarity of the LC shape of SN 2008bo and SN 2010jr past maximum, one possibility is that shock breakout cooling was also missed by observations for SN 2008bo, and the same could be true for SN 2008aq. For SN 2011hs, we know that a trace of cooling was observed in the optical (R band). In fact, even though there are few UV observations for this object, they do seem to follow the trend of SN 2013df.

Figure 6.3 shows that the $(UVw1-V)$, $(UVm2-V)$, $(UVw2-V)$ colour indices of SNe 2010jr, 2011dh, 2011hs, and 2013df undergo a red-ward trend over the first $\sim$ 20 days before maximum light. This also seems to be the case for the $(UVw1-V)$ index of SN 2011ei. After maximum, all colours of both SNe 2010jr and 2013df have a slight blue-ward tendency, while $(UVw1-V)$ and $(UVm2-V)$ for SN 2011dh moderately redden but seem follow a blue-ward trend from $\sim$ 50-60 days on. For SNe 2008ax, $(UVw1-V)$ and $(UVw2-V)$ seem to turn blue before maximum, then redden up to $\sim$ 10 days past maximum and possibly incline towards the blue thereon after. The $(UVw1-V)$ index for SN 2009mg seems to have a similar behaviour to that of SN 2008ax. Although SN 2008bo has less photometric coverage, its colour indices seem to evolve in a similar fashion to those of SNe 2010jr and 2013df. The same is true for the $(UVw2-V)$ colour of SN 2008aq.

6.3.2 Optical

In Figure 6.4 we have depicted a comparison of the time evolution of the absolute magnitudes of the SN of our sample. Note that for SNe 2009mg, 2008aq, and 2010jr the magnitudes shown in the figure are V band magnitudes, while those for SNe 2006T, 2006ba, 2006bf, 2008bo, 2008cw, 2009K, and 2013cu are for the r band (converted to the Vega system). The rest of the LCs correspond to the R passband.

As can be seen in the figure, there is an evident variety in LC shapes and peak brightness among the SNe. The LCs can be divided in those presenting two peaks (SNe 1993J, 2010jr, 2011fu, 2013df, and 2011hs) and others presenting a single maximum. The main difference in the progenitor properties of the SNe showing two and one peaks (see Table 6.2) is that the former have extended progenitors ($R \sim 100$ R$_\odot$) while the latter arise from the explosion of compact stars ($R \sim 1$ R$_\odot$). Thus, the progenitor of SN 2010jr, which presents a double-peaked LC, but for which modelling of the observed data has not been performed, could be extended as well. For SN 2001gd, we cannot confirm that the progenitor was extended, as claimed by

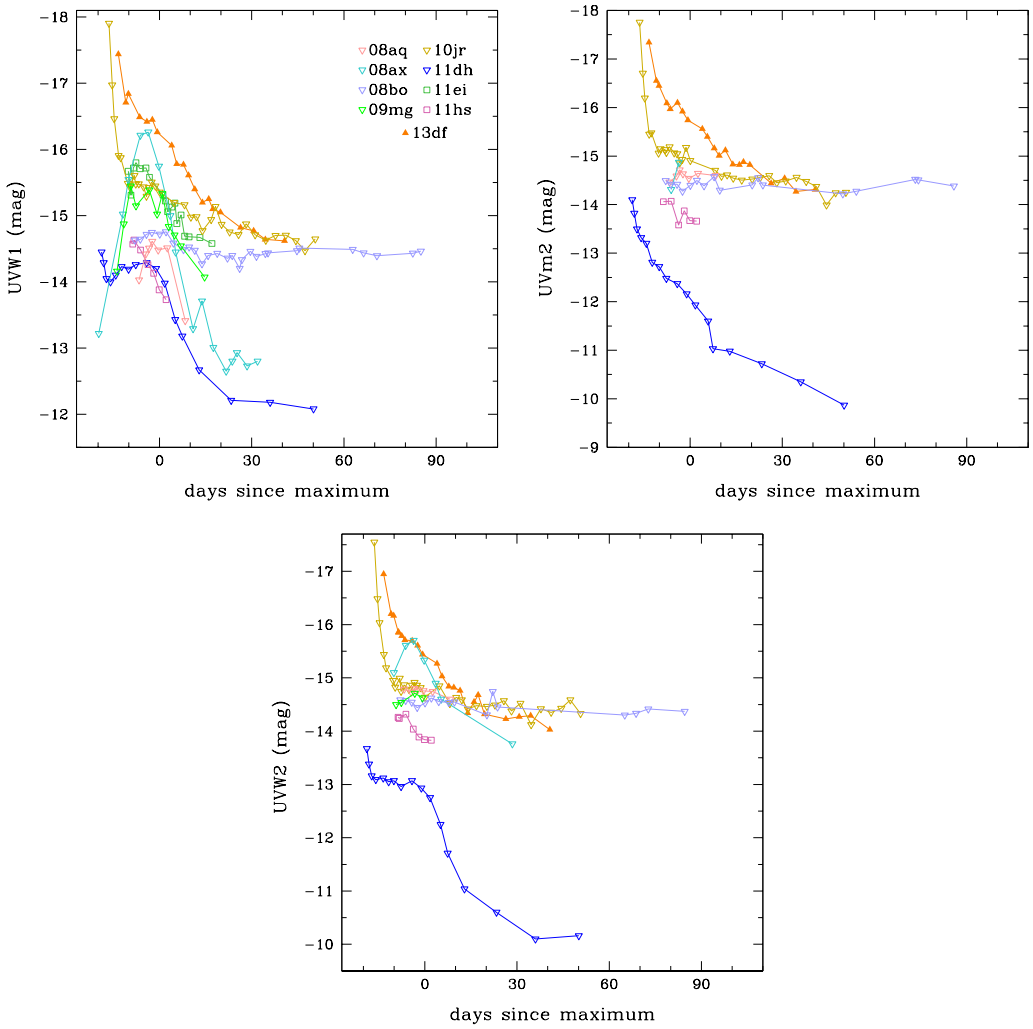

Figure 6.2: Absolute *UVw1*, *UVm2*, *UVw2* LCs of our SN sample. The absolute magnitudes were obtained by correcting for SN distance but not for dust extinction in the line of sight. Phase 0 corresponds to maximum light in V, R or r (see Table 6.5).

Chevalier & Soderberg (2010), since there are not early observations. On the other hand, as pointed out in Section 6.3.1, observations of cooling could have been missed for some of the other objects like 2006aq and 2008bo.

Noteworthy is the seemingly distinct behaviour of the LC of SN 2013cu with respect to the rest of the objects. It exhibits a single-peaked LC, but it spikes at an earlier time and its maximum is practically 1 magnitude brighter than the brightest single peaked object of the sample. One possible explanation is that the LC peak of SN 2013cu is actually powered by CSM interaction, as proposed by some authors

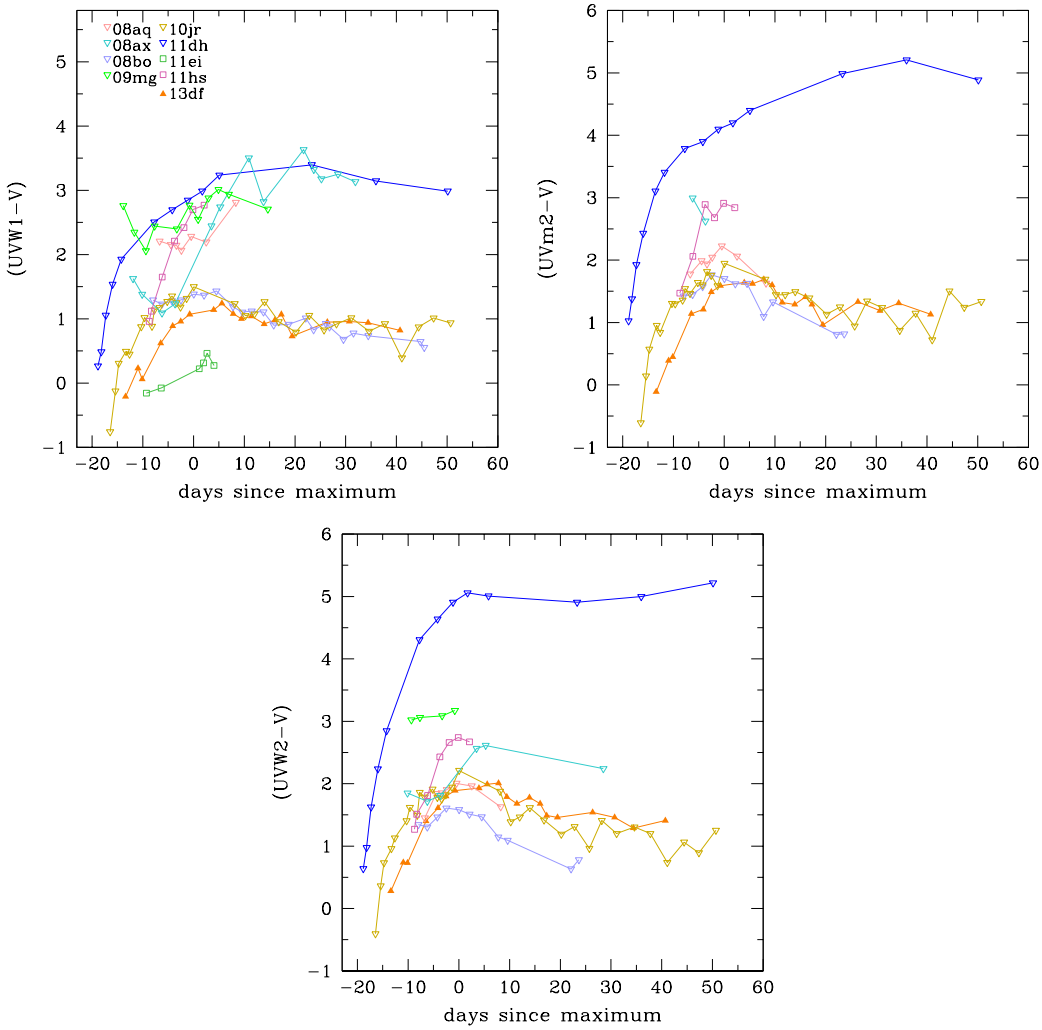

Figure 6.3: $(UVw1-V)$, $(UVm2-V)$, and $(UVw2-V)$ colour indices of our SN sample.

(e.g. Groh 2014; Strotjohann et al. 2015; Gräfener & Vink 2016).

The maximum magnitudes of the sample – note that in the case of the SNe with double-peaked LCs the maximum magnitudes refer to their secondary peak – lie between −15.98 mag (SN 2008bo) and −18.65 mag (SN 2013cu; see Table 6.1). The LC widths around peak also show some degree of diversity, with SN 2003bg being the broadest.

In Figure 6.5 we show a histogram of the distribution of the R band peak magnitudes of the SNe, (note that SNe 1987K, 2001ig, 2008aq, and 2009mg, were omitted from this plot since their data are not strictly in the R passband, while the magnitudes of SNe 2006T, 2008bo, and 2013cu were included in red after transforming

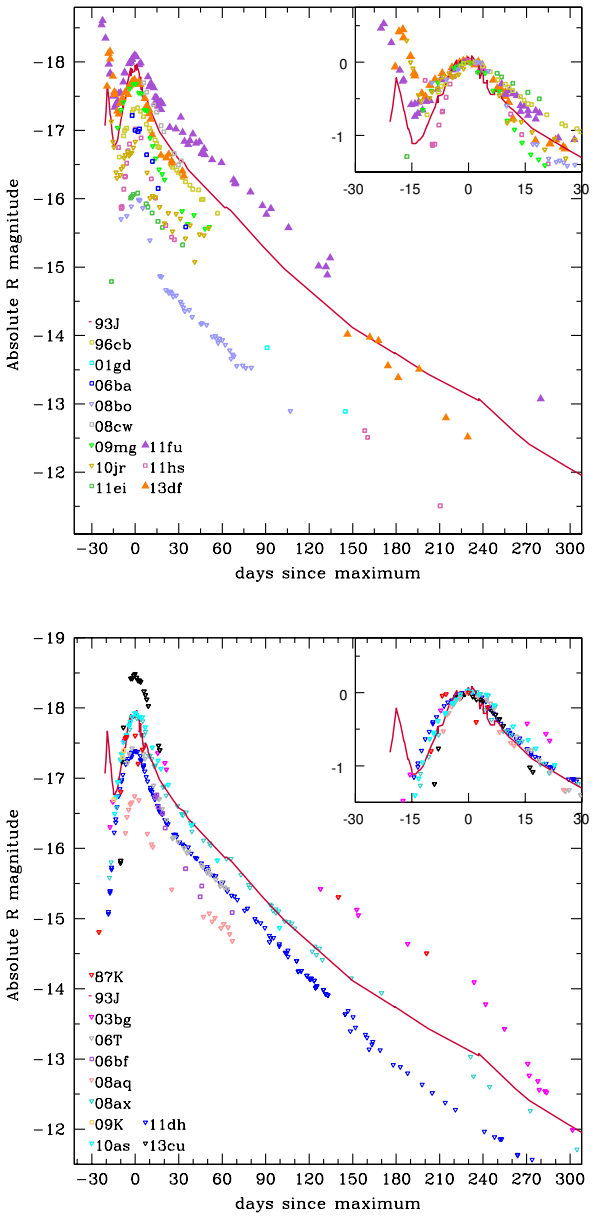

Figure 6.4: Time evolution of the absolute magnitudes of the sample of type IIb SNe. For SNe 2009mg, 2008aq, and 2010jr the magnitudes shown in the figure are in the V band. Those for SNe 2006T, 2006ba, 2006bf, 2008bo, 2008cw, 2009K, and 2013cu are for the r band (in the Vega system). The rest of the LCs correspond to the R band. For clarity we have divided the plot into two (with SN 1993J in both as reference). The insets in the upper-right corners of the plots are the magnitudes normalized to (secondary) peak. The absolute magnitudes were obtained by correcting for SN distance and extinction in the line of sight (see Table 6.1). Phase 0 corresponds to maximum light in V, R or r (see Table 6.5).

Table 6.6: Average absolute magnitudes for the sample of type IIb SNe. The calculations were done for all the SNe with R band data, secondary maxima of double-peaked R IIb SNe, single-peaked R IIb SNe, and all type IIb SNe, including those with data in the r band after transforming the maximal magnitudes to the Vega system.

Dataset	$M_{\rm R}$	σ
All R IIb	-17.48	0.58
Double-peaked R IIb	-17.67	0.47
Single-peaked R IIb	-17.35	0.66
All R and r IIb	-17.45	0.75

their r band maxima to the Vega system). Owing to the small sample, there is no clear peak in the distribution. We have calculated the mean absolute magnitudes and standard deviation of the whole sample, as well as that of only the type IIb SNe with two peaks in their LCs, and those with a single peak. We have also made a calculation of the average R band maximum of our sample by including those SNe with LCs in the r band after transforming them to the Vega system. The results of these calculations are shown in Table 6.6, which reflects that there are no significant differences between the average peak magnitudes of the different subsets. In a recent study about absolute magnitude distributions of different SN types by Richardson et al. (2014), they found that type IIb SNe show dimmer B absolute magnitudes than type Ib and Ic SNe. For the R band, we obtained $M_{\rm R}$ magnitudes within the uncertainties of $M_{\rm R} = -17.9 \pm 0.9$ mag, reported for a sample of 11 type Ib SNe by Drout et al. (2011), whereas our average is below $M_{\rm R} = -18.3 \pm 0.6$ mag obtained for a sample of 14 type Ic SNe by the same authors.

In Figure 6.6 we have represented the R and r (in Vega system; red points) peak absolute magnitudes of the type IIb objects of our sample versus their distance moduli. The lack of objects in the lower left part of the figure could indicate that low-luminosity ($M_{\rm R} > -17$ mag) type IIb SNe are not common events. Moreover, most objects seem to have absolute magnitudes ~ -18 mag and some ~ -16 mag. This could indicate that there are two luminosity classes of type IIb SNe. However, a larger sample is necessary to confirm this brightness separation.

In Figure 6.7 we show the pseudo-bolometric model-derived ^{56}Ni masses synthesized in the explosion of the type IIb SNe considered in this section versus their absolute R band magnitudes at (secondary) peak. For details on the construction and modelling of the bolometric LCs of the literature SNe see the references given in Table 6.1. We have performed a fit to the data and have obtained:

$$\log(M_{^{56}\rm Ni}) = (-0.39 \pm 0.05) \times M_{\rm R} - 7.9 \pm 0.8. \tag{6.1}$$

In fact, this relation is similar to that obtained by Drout et al. (2011) for a sample of type Ib and Ic SNe [$\log(\rm M_{^{56}Ni}) = -0.41 \times \rm M_R - 8.3$], but with a slightly higher amount of ^{56}Ni. We applied Equation 6.1 to estimate the ^{56}Ni masses synthesized in

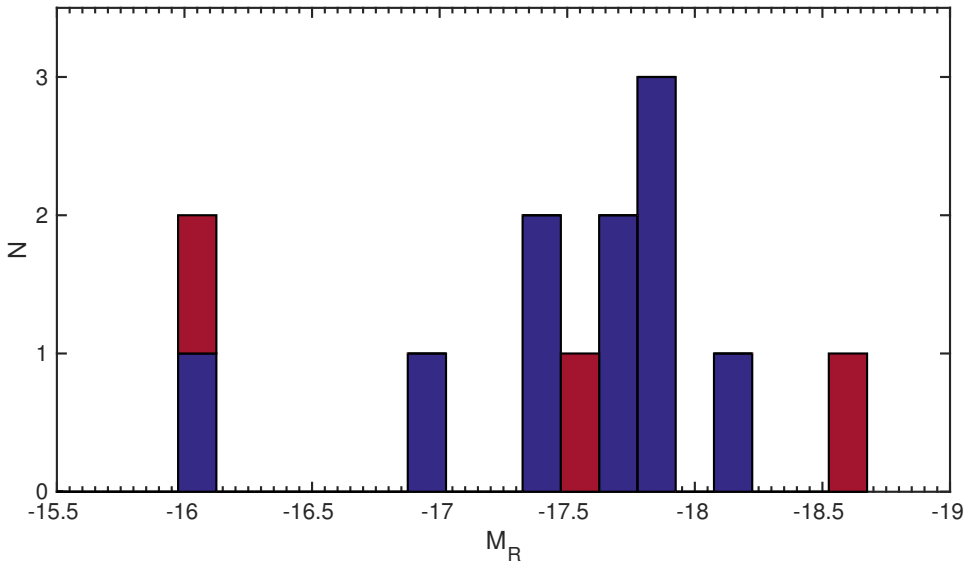

Figure 6.5: Distribution of R band peak magnitudes of the type IIb SNe studied in this chapter. The red data correspond to SNe 2006T, 2008bo, and 2013cu, for which their r band maxima were transformed to the Vega system.

the explosions of SNe 1987K, 2006T, 2008bo, and 2013cu using their peak absolute magnitudes given in Table 6.1, and have obtained 0.10, 0.09, 0.02, and 0.25 $M_{\odot}$, respectively.

By linear interpolation, we have estimated the decline and rise rates of various parts of the LCs. The results are shown in Table 6.7. The rise rate to the nickel-powered peak is relatively similar for all objects except for SNe 2006T, 2008ax, and 2011hs which have a slightly steeper slope to maximum light. The declines after maximum are somewhat similar, with SNe 2008bo evolving slightly faster than the rest of the objects, and SNe 2003bg and 2011ei declining at a slower rate. The decline tails are also similar to some extent, although for example SN 1996cb seems to decline at a slightly slower rate. Note also that for SN 2003bg, we used a different interval to calculate the tail decline rate and that it exhibits a change of slope at late times possibly due to dust formation (Hamuy et al., 2009).

In Figure 6.8 we show the decline rates from secondary peak in the R and r (transformed to the Vega system; red points) band LCs presented in Figure 6.4 versus secondary peak brightness. The figure reflects that there does not seem to be any correlation between secondary peak brightness and decline rate from secondary peak.

Regarding the SNe with two peaks in their LCs, as indicated in Table 6.7, we have obtained similar decline rates from the first R band LC peak for SNe 2011fu

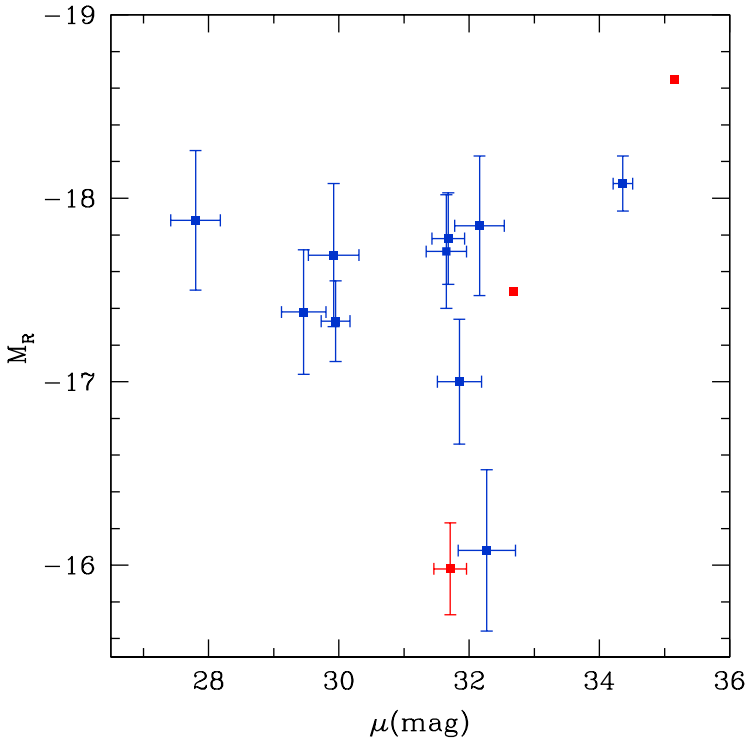

Figure 6.6: Maximum absolute R band magnitudes of the type IIb SNe of our sample versus their distance moduli. The points in red correspond to SNe 2006T, 2008bo, and 2013cu, with r band maxima in the Vega system.

and 2013df. SNe 1993J has a slightly steeper decline, and the decline of SN 2011hs is much faster. The V band decline rate from the first peak for SN 2010jr is 0.22 ± 0.01 mag d^{-1}, which is comparable with those of the before-listed SNe in the R band. In Table 6.8 we summarise the main photometric parameters of the first peak. The average maxima estimated at first peak in both the V and R bands is around -17.73 mag, with a standard deviation 0.52 mag and 0.72, respectively. The mean value of the minima after the V and R band first peaks is within -16.71 and -16.79 mag with a standard deviation of the order of 0.50 mag for both the V and R passbands. As indicated in Table 6.8 for SNe 2011fu and 2013df, the minimum in the V band occurs at a slightly later time than for SNe 1993J and 2010jr. In the R band, SN 2011hs reaches the minimum earlier than the rest of the SNe.

Considering the whole optical wavelength range, it is interesting to note that the minima occur later in the bluer bands than in the redder ones, as shown for SN 1993J (Kumar et al. 2013; table 4), or for SNe 2011fu and 2013df in Chapters 3 and 4 of this thesis. In Figure 6.9, we show the decline rates after first peak versus

Table 6.7: Decline and rise rates in the R and r (Vega system) LCs of our sample of type IIb SNe.

SN	Decline from 1st peak [a] (mag d^{-1})	Rise to 2nd peak [b] (mag d^{-1})	Decline from 2nd peak [c] (mag d^{-1})	Decline tail [d] [mag (100d)$^{-1}$]
1993J	0.20 ± 0.01	-0.03 ± 0.01	0.06 ± 0.01	2.19 ± 0.04
1996cb	–	-0.04*	0.04 ± 0.01	1.76 ± 0.11
2001gd	–	–	–	1.73*
2003bg	–	-0.03*	0.03*	1.25 ± 0.04
2006T	–	-0.07 ± 0.02	0.06 ± 0.01	1.91 ± 0.13
2006ba	–	–	0.05 ± 0.01	–
2006bf	–	–	–	1.37 ± 0.69*
2008ax	–	-0.06*	0.06 ± 0.01	2.09 ± 0.03
2008bo	–	-0.05*	0.08 ± 0.01	2.09 ± 0.04
2008cw	–	–	0.05 ± 0.01	–
2009K	–	-0.10 ± 0.01	–	–
2010as	–	-0.05 ± 0.01	0.05 ± 0.01	2.37 ± 0.12
2011dh	–	-0.03 ± 0.01	0.06 ± 0.01	2.20 ± 0.01
2011ei	–	-0.03 ± 0.01	0.03 ± 0.01	–
2011fu	0.13 ± 0.02	-0.03 ± 0.01	0.04 ± 0.01	2.05 ± 0.06
2011hs	0.46 ± 0.01	-0.06 ± 0.01	0.07 ± 0.01	2.06 ± 0.01
2013cu	–	-0.02 ± 0.01	0.05 ± 0.01	–
2013df	0.16 ± 0.01	-0.04 ± 0.01	0.07 ± 0.01	1.92 ± 0.11

*Fits done with a small number of data points.
[a] Considering the interval between first maximum and minimum.
[b] Considering the interval within 5 days before maximum, except for SN 2009K for which we estimated an earlier rise rate with the data available due to lack of photometric coverage.
[c] Considering the interval within 15 days after maximum.
[d] Considering the interval within 40 and 130 days past maximum. In the cases of SNe 2003bg and SN 2013df, due to lack of photometric coverage in the interval indicated, we used intervals within 40 to 130, and 34 to 180 days since maximum, respectively.

magnitudes at first peak in the V and R bands. Note that the decline from first peak for SN 2011hs was done with a small number of data points and since the magnitude at first peak is not available, we have represented the magnitude of the first LC data point. As can be seen in the left panel of Figure 6.9, our sample of SNe seem to not follow a particular behaviour in the V band between the magnitude and decline rate from first peak, while in the R band it could seem that a dimmer first peak declines at a faster rate. However, a larger sample of type IIb SNe with data obtained at first peak is necessary to further investigate this issue.

In Figures 6.10 and 6.11 we have plotted the intrinsic colour evolution of the SNe of our sample (using the reddening values given in Table 6.1). Note that we have not been able to compute colour indices for SNe 1987K, 2001ig, and 2013cu since there are no multi-band data in the literature for these objects.

In the first 20 to 10 d prior to maximum light, we have observed that while the $(U-V)_0$ and/or $(B-V)_0$ indices of the single-peaked type IIb SNe show a blue-ward trend, those of the double-peaked SNe, redden. On the other hand, we do not see a clearly distinct behaviour between the $(V-R)_0$ and $(V-I)_0$ indices of the SNe during this interval. Note that 20 to 10 d prior to maximum, the LCs of SNe 1993J,

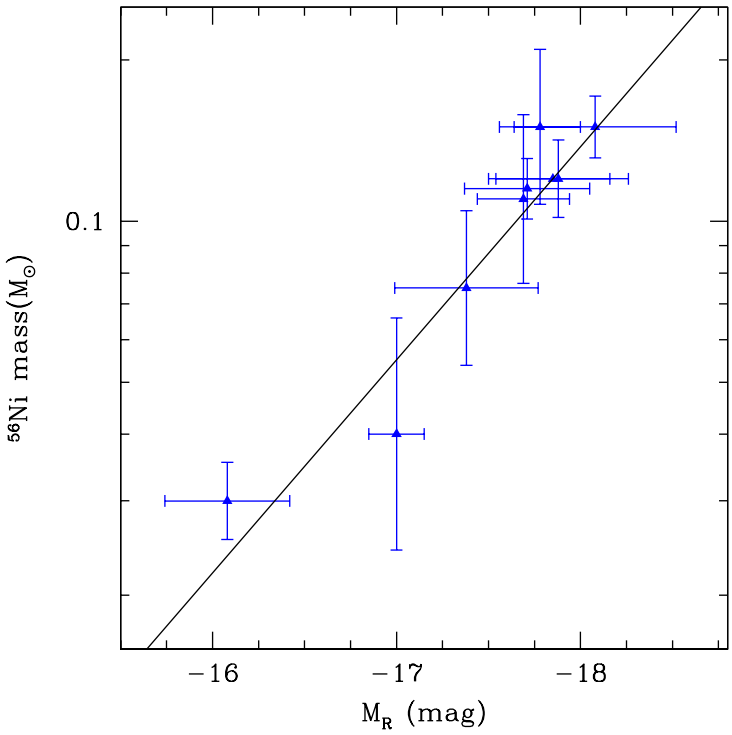

Figure 6.7: ^{56}Ni masses versus maximum absolute R magnitudes of the type IIb SNe considered in this section. The solid line represents the best fit.

Table 6.8: V and R absolute magnitudes at the first maximum and at minimum after first peak, and time and magnitude difference between them for those SNe of our sample with two peaks in their LCs.

SN	$M_{\rm V1stmax}$ (mag)	$M_{\rm Vmin}$ (mag)	ΔM_V (mag)	ΔJD_V (d)	$M_{\rm R1stmax}$ (mag)	$M_{\rm Rmin}$ (mag)	ΔM_R (mag)	ΔJD_R (d)
1993J	-17.61 ± 0.38	-16.48 ± 0.38	1.13	5	-17.68 ± 0.38	-16.77 ± 0.38	0.91	5
2011fu	-18.37 ± 0.15	-17.12 ± 0.15	1.25	8	-18.46 ± 0.15	-17.28 ± 0.15	1.18	8
2010jr	-17.13 ± 0.17*	-16.27 ± 0.17	0.86	4	–	–	–	–
2011hs	–	–	–	–	-16.75 ± 0.34*	-15.87 ± 0.34	0.88	2
2013df	-17.86 ± 0.31	-16.97 ± 0.31	0.89	8	-17.97 ± 0.31	-17.25 ± 0.31	0.72	6

*First point in the LC.

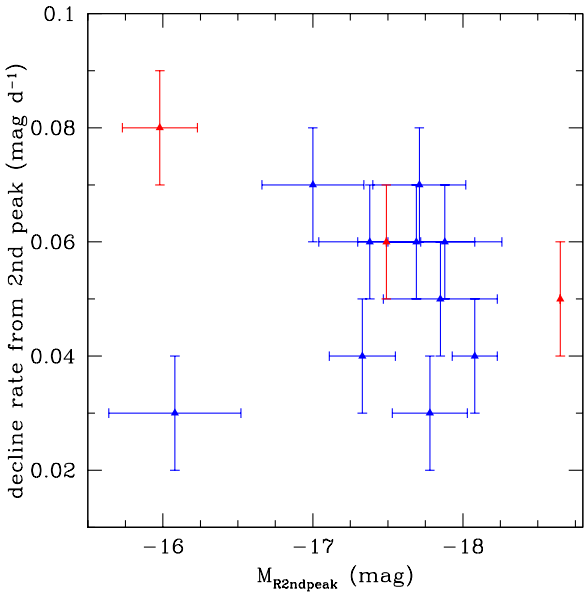

Figure 6.8: R band decline rate from secondary peak versus secondary peak brightness for our SN sample. The red points correspond to SNe 2006T, 2008bo, and 2013cu after transforming their r band maxima to the Vega system.

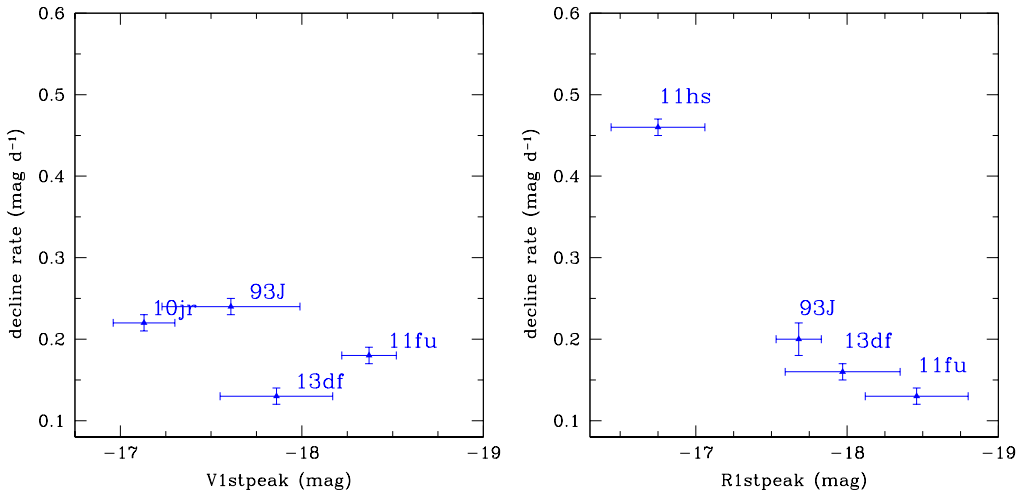

Figure 6.9: Decline rates from first peak versus absolute magnitudes at first peak for the double-peaked V and R LCs of our SN sample.

2010jr, 2011fu, and 2013df are adiabatically powered by the shock wave (Woosley et al. 1994). The behaviour of the colour indices thus reflects the main contribution of the bluer wavelengths to the first peak of these SNe.

From maximum to about 20 d past maximum, all colours become increasingly redder. From that point on, while the $(U-V)_0$ and $(B-V)_0$ indices have a continual blue-ward tendency, the $(V-R)_0$ slightly becomes bluer but shows a break around 100 d for some SNe like SN 1993J, and the $(V-I)_0$ colour evolves to some extent towards the blue (e.g. SN 2011fu) or remains practically constant (e.g. SN 2003bg).

Compared to the UV, the colours in the optical show a slower evolution, but the overall trend is similar. In general, we find a significant dispersion in the optical colour indices of the different type IIb SNe at similar phases. This implies that it is rather difficult to estimate the extinction towards a type IIb SN by comparison of its colour indices to those of extinction-corrected SNe of the same family.

6.3.3 NIR

In Figure 6.12 we show the NIR absolute LCs of the SNe of our sample. The figure reflects that, with the exception of the first peak of SN 1993J which is less pronounced, the shapes of the NIR LCs overall follow those of the optical bands. We find SNe 2010P and 2011fu to be the most NIR bright, with peak magnitudes around ~ -19 mag, and 2011hs to be the dimmest, with (secondary) peak brightness around ~ -17 mag.

Figure 6.13 shows the NIR intrinsic colour evolution of our sample SNe. From around maximum, all objects follow a similar trend to the optical colour indices, turning red up to 30 d and becoming bluer afterwards. Thus, the colour evolution in the NIR is slower than in the optical and, consequently, than in the UV. Although there are limited data in the NIR, it is possible to appreciate a significant dispersion (with a maximum value of about 0.8 mag) between the NIR colour indices of the different SNe.

6.4 Spectra

In this Section, we present a comparison of the spectra of the SNe of our sample. We have obtained most of the spectra from WISeREP, except the spectra of SNe 2009mg, 2010P, 2010as, and 2011ei.[3] The original references for all the spectra are given in Table 6.9. All the spectra have been dereddened and corrected for their host galaxy recession velocities assuming the values reported in Table 6.1. The phases in Figures 6.14 and 6.15 correspond to the JD with respect to the maxima in the SN LCs given in Table 6.5. On the left panels of both figures we have represented the SNe with

[3]These were obtained via private communication from the first authors of the published works on these SNe: Samantha Oates, Erkki Kankare, Gastón Folatelli, and Dan Milisavljevic, respectively

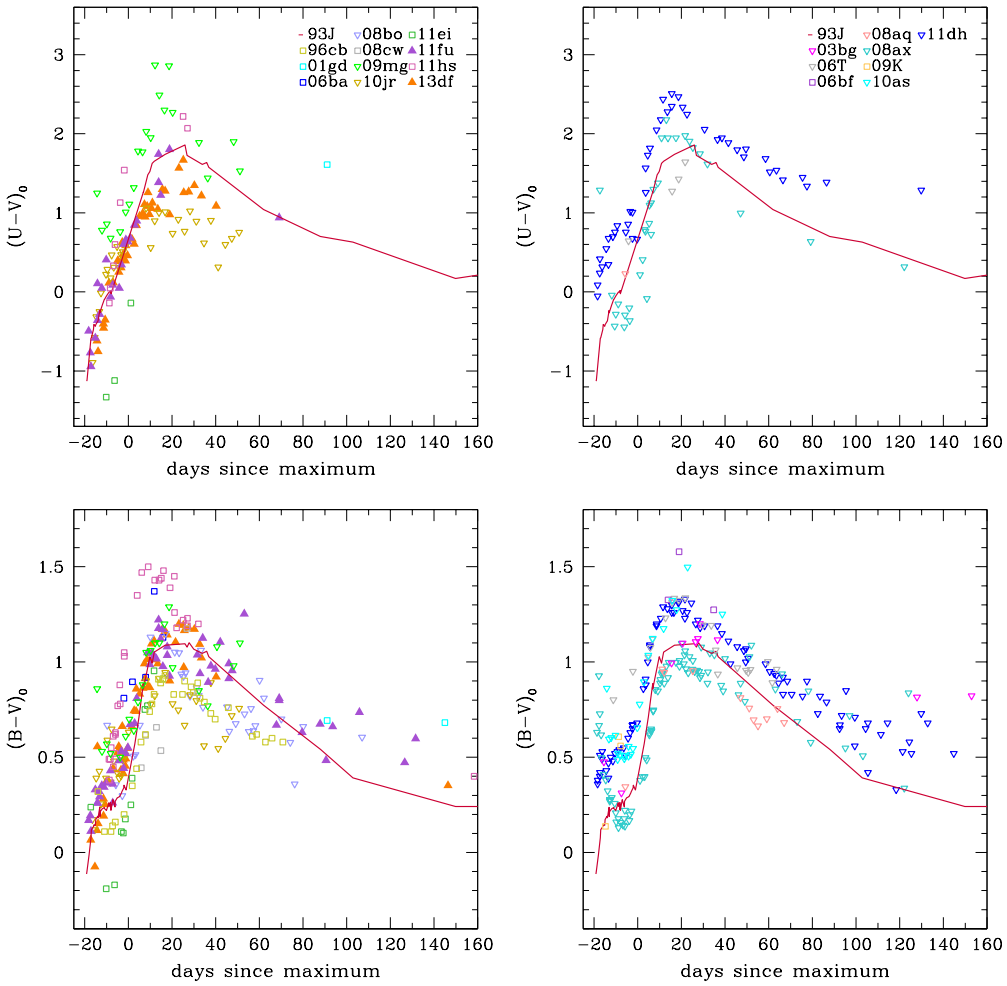

Figure 6.10: Comparison of the $(U-V)_0$ and $(B-V)_0$ colours of our type IIb SNe sample. All objects were corrected for extinction in their line of sight (see Table 6.1). Phase 0 corresponds to maximum light in V, R or r (see Table 6.5)

observed double-peaked LCs (at least in one band). The majority of the SNe with observed single-peaked LCs are plotted on the right panels of both figures. However, for the sake of clarity some single-peaked-LC SNe have also been plotted on the left panels. SN 1993J was plotted on both sides as reference.

As can be seen on the top panels of Figure 6.14, the spectra show diverse but gradual properties at early ($\sim$ 20 d before secondary maximum) times. SNe 1993J, 2011fu and 2013cu exhibit a blue almost featureless continuum. On the other hand, SNe 2013df, 2011hs, 2001ig, and 2003bg show shallow hydrogen and helium lines superposed on a redder continuum, and SNe 2008ax, 1996cb, 2011dh, and 2011ei

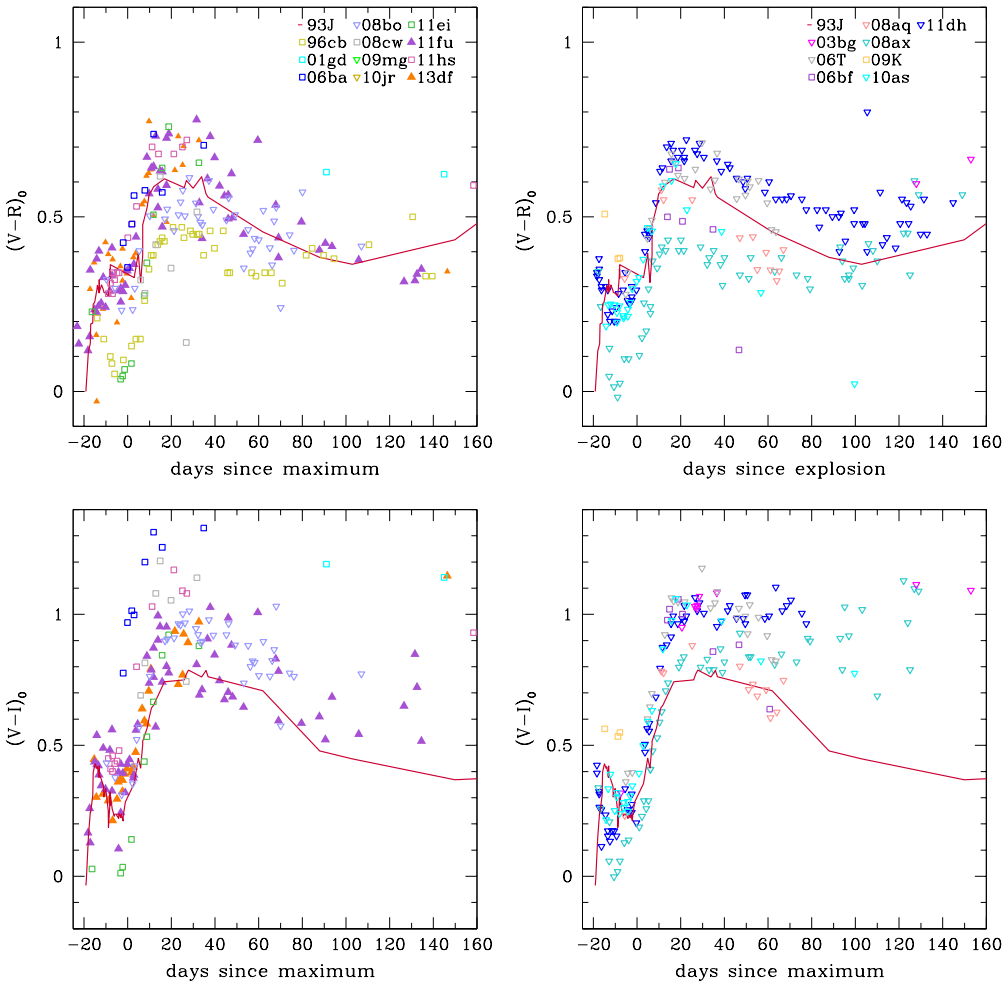

Figure 6.11: Comparison of the $(V-R)_0$ and $(V-I)_0$ colours of our type IIb SN sample. All objects were corrected for extinction in their line of sight (see Table 6.1). Phase 0 corresponds to maximum light in V, R or r (see Table 6.5)

present even stronger lines than the rest of the SNe. At these early phases, as is characteristic and expected in type IIb SNe, hydrogen lines predominate over helium. The main difference between double-peaked SNe and single peaked SNe at ~ -20 d is that the double-peaked objects exhibit bluer continuum and shallower lines.

On the bottom panels of Figure 6.14 we have depicted a spectral comparison at an intermediate phase ($\sim$ 20 d past maximum).[4] At this stage, helium lines have become stronger with respect to those at the earlier phase (as expected for type IIb

[4]Note that there are no available spectra at $\sim$ 20 d post maximum for SN 2008aq and we show a spectrum at an earlier phase for this SN.

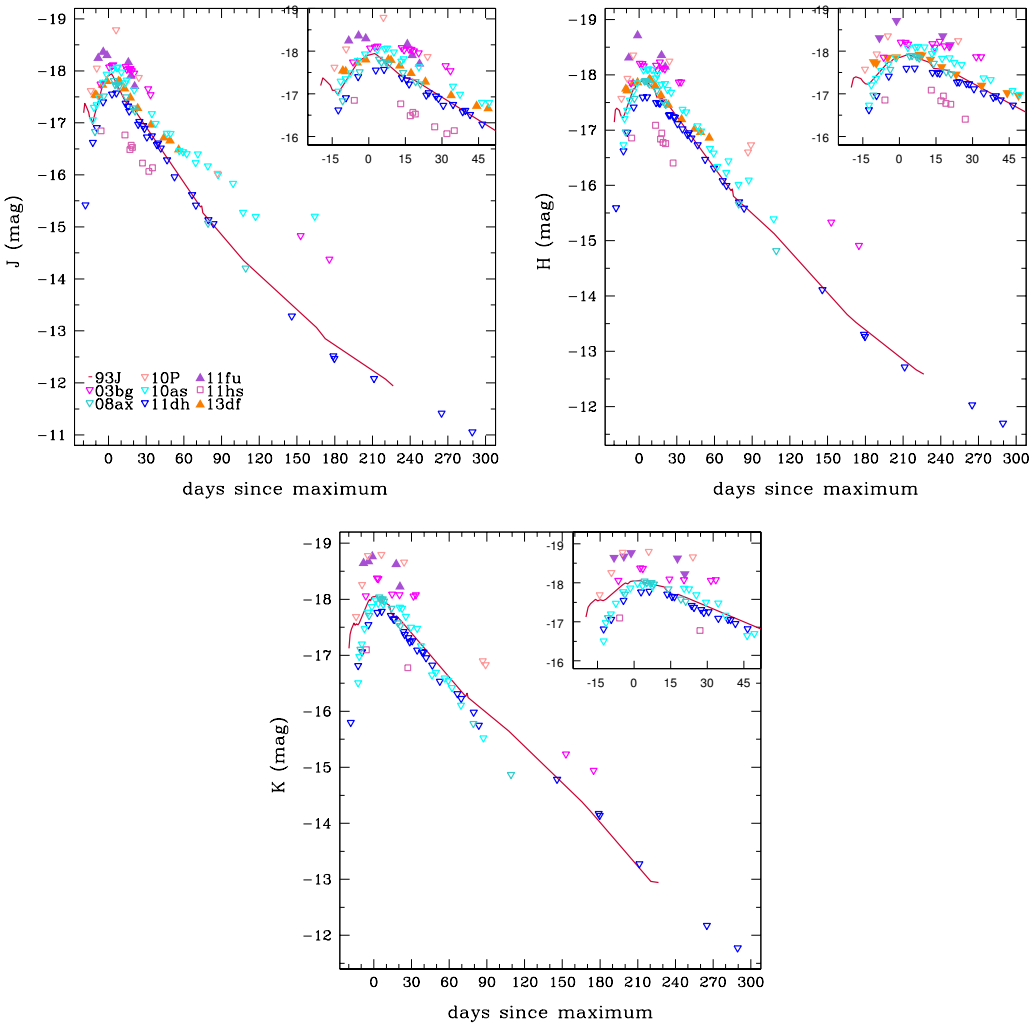

Figure 6.12: Absolute J, H, K LCs of our SN sample. The absolute magnitudes were obtained by correcting for SN distance and extinction in the line of site (see Table 6.1). Phase 0 corresponds to maximum light in V, R or r (see Table 6.5).

SNe). Although there is an overall resemblance in the spectra, the intensity of the lines varies from one SN to the other, indicating differences in the ionization state of their ejecta. In Table 6.10 we summarise the measured EWs of the Hα and He I λ5876 lines for the spectra at $\sim$ 20 d. Specifically, the EW of the Hα absorptions vary from $\sim$ 100 for SN 2009mg to $\sim$ 10 Å for SN 2011fu. About equal number of SNe show $\mathrm{EW_{H\alpha}/EW_{HeI\lambda5876}} > 1$ and $\mathrm{EW_{H\alpha}/EW_{HeI\lambda5876}} < 1$ at phase $\sim$ 20 d. Interestingly, all SNe with proposed extended progenitors show more intense He I λ5876 lines at this time.

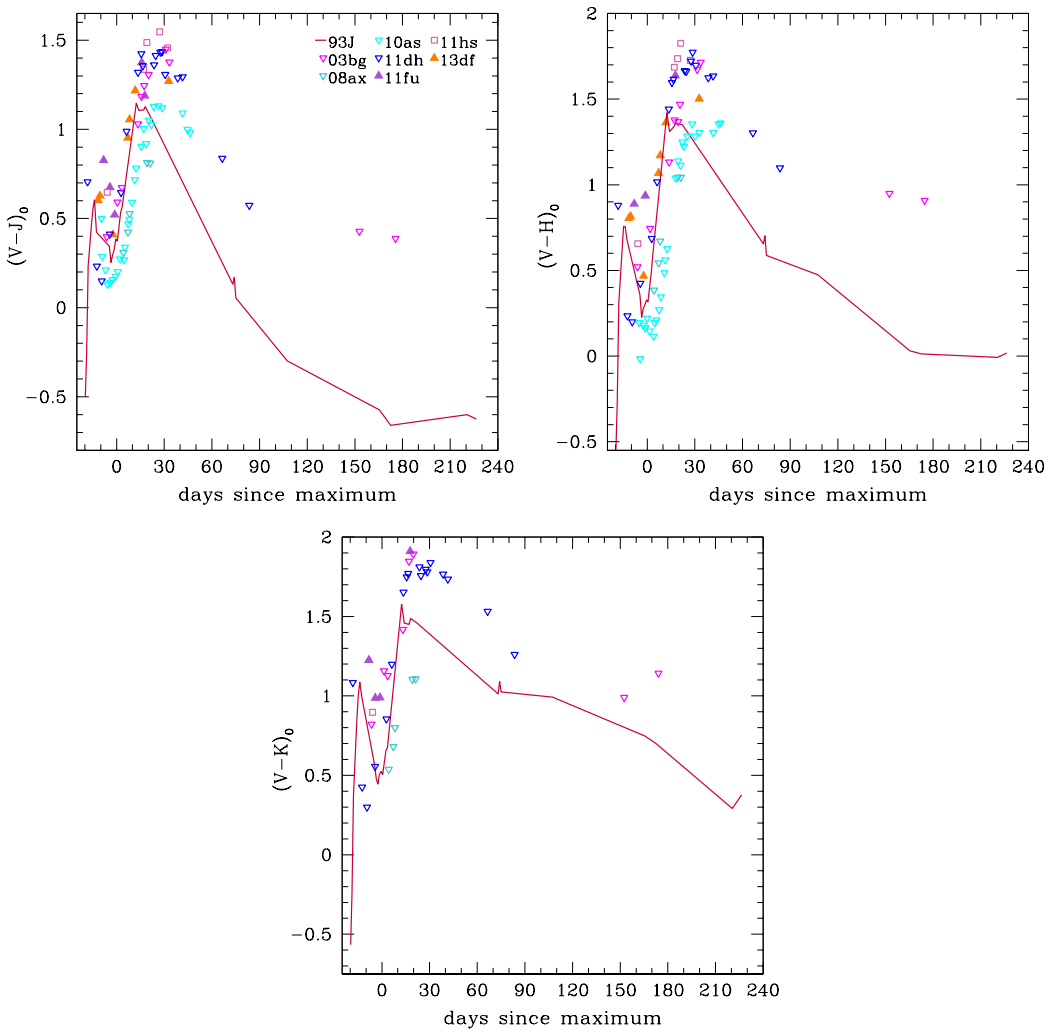

Figure 6.13: NIR colour evolution of the type IIb SNe of our sample. All objects were corrected for extinction in their line of sight (see Table 6.1). Phase 0 corresponds to maximum light in V, R or r (see Table 6.5).

The nebular spectra of the SNe at around $\sim$ 280 d are shown in Figure 6.15. As can be seen in the figure, Hα and He I λ5876 have basically disappeared. Instead, three of the most prominent features present in these nebular spectra are MgI] λ4571, [OI] $\lambda\lambda$6360,6364, and [CaII] $\lambda\lambda$7291,7324.[5] We have measured their integrated fluxes by means of an automated algorithm, which integrates the flux minus the continuum between $+V_{line}$ and $-V_{line}$, where V_{line} was assumed to be

[5]In the case of SN 2008bo, note that the spectrum is for an earlier phase and there is still a strong emission of likely He I λ7065 on the blue side of [CaII] $\lambda\lambda$7291,7324.

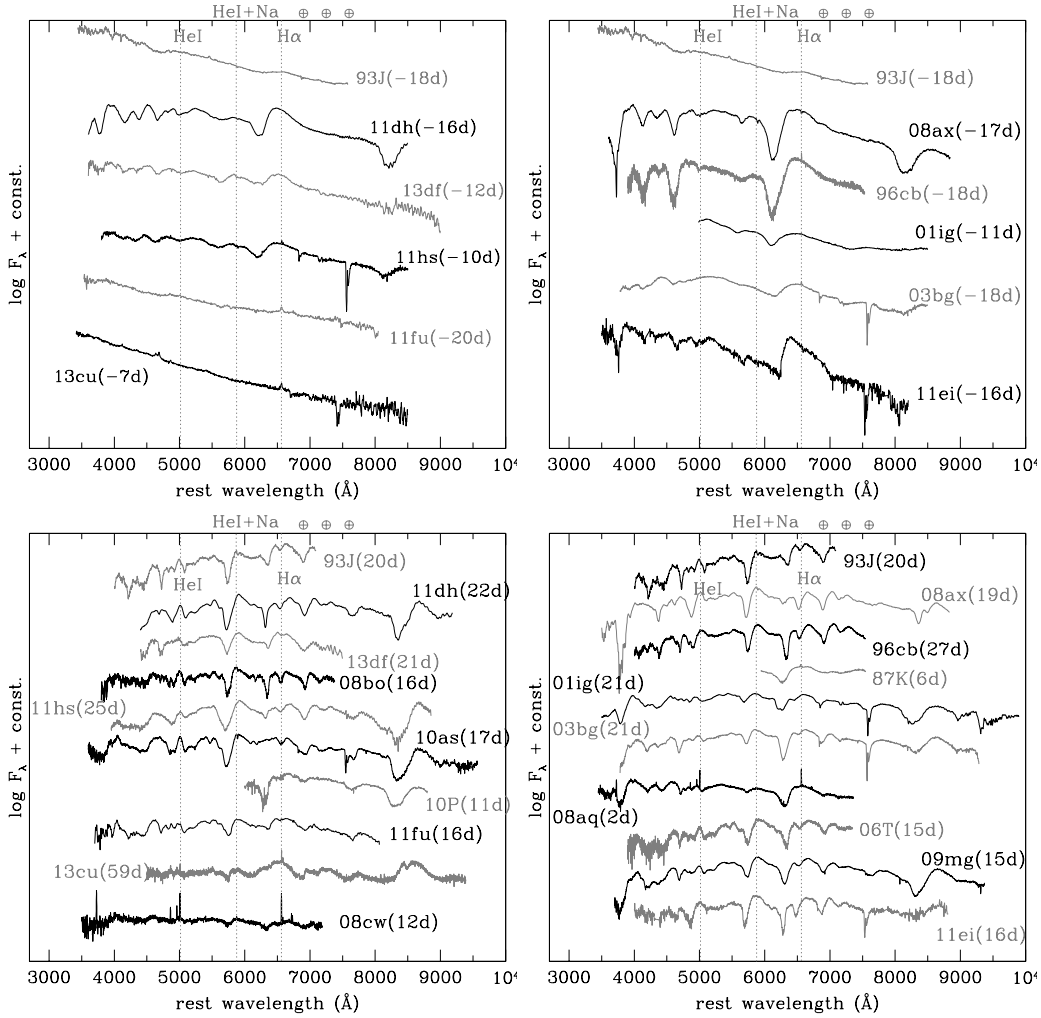

Figure 6.14: Top panels: comparison of the spectra of the type IIb SNe of our sample at ~ -20 d. Middle panels: Same as top panels for a phase ~ 20 d since maximum. Bottom panels: same as top and middle panels for nebular phases ~ 280 d. The spectra have been dereddened, redshift corrected (using the values given in Table 6.1), and shifted vertically for clarity. Phase 0 corresponds to maximum light in V, R or r; see Table 6.5.

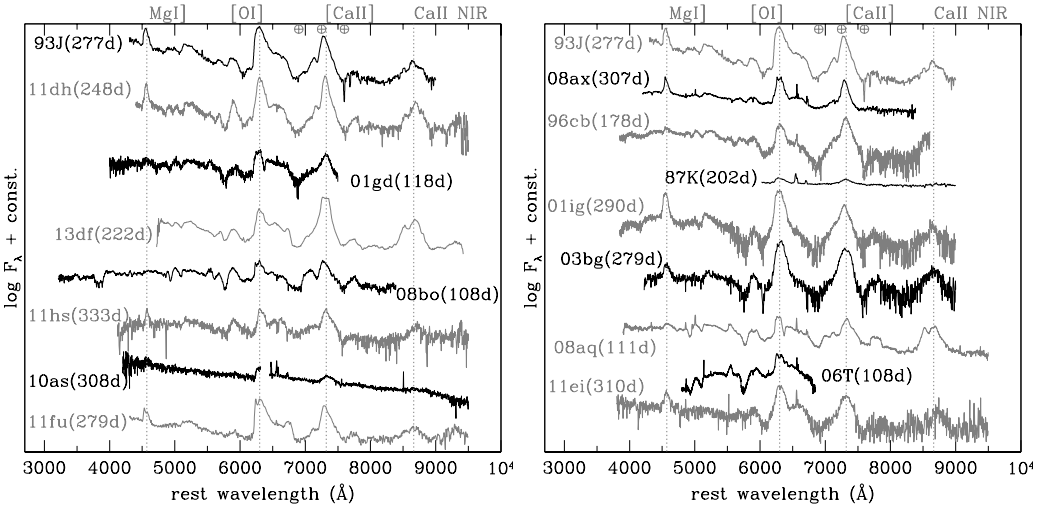

Figure 6.15: Comparison of spectra of our SN sample at $\sim$ 280 d since maximum. The spectra have been dereddened, redshift corrected (using the values given in Table 6.1), and shifted vertically for clarity. Phase 0 corresponds to maximum light in V, R or r; see Table 6.5.

4500 km s^{-1}, which corresponds to typical line widths of the emissions present in the spectra of SN 1993J (see also section 3.7 of Jerkstrand et al. 2015). The resulting line luminosities are shown in Table 6.11. At $\sim$ 280 d the SN with most luminous MgI] λ4571 and [OI] $\lambda\lambda$6360,6364 is SN 2011fu, while SN 2013df shows the most luminous calcium lines. On the other hand, the Mg/O ratios of SNe 1993J, 2001ig, 2008ax, 2011dh, and 2011ei are quite similar and slightly higher than those of SNe 1996cb, 2003bg, and 2011fu. In contrast, the SNe show a variety of [Ca II]/[O I] ratios, that of SN 2013df being significantly higher than the rest of the objects. The [Ca II]/[O I] ratios are expected to be sensitive to the progenitor's initial mass, increasing with decreasing main sequence mass (Fransson & Chevalier, 1987, 1989). However, it can be affected by many factors such as mixing. This explains the variety of [Ca II]/[O I] ratios seen among the SNe, and the little correspondence between their values and the estimates for the progenitor masses of the SNe (see Table 6.2). For example, this ratio is highest for SN 2013df. However, in Chapter 4 we estimated its progenitor to have a mass similar to those of other type IIb SNe ($\sim$ 12–13 M$_\odot$) like for example SN 2011dh, which exhibits a lower value of [Ca II]/[O I]= 0.9.

Concerning the nebular line profiles, the [O I] $\lambda\lambda$ 6300, 6364 and MgI] λ4571 emission profiles are double-peaked, in the case of SN 2011fu, and most similar to those of SN 2008ax. SNe 2006T, 2008bo, and 2010as also exhibit a double-peaked O I] $\lambda\lambda$ 6300, 6364 profile shape (at an earlier phase). The rest of the SNe show signatures of substructure underlying their nebular profiles but not as evident double peaks at the phases considered.

Table 6.9: Data used in the spectroscopic comparison of our SN sample.

SN	Early	Post-max	Nebular
1987K	–	(1)	(1)
1993J	(2)	(2)	(3)
1996cb	(4)	(4)	(4)
2001gd	–	–	(4)
2001ig	(5)	(5)	(5)
2003bg	(6)	(6)	(6)
2006T	–	(4)	(4)
2006ba	–	–	–
2006bf	–	–	–
2008aq	–	(4)	(4)
2008ax	(7)	(7)	(4)
2008bo	–	(4)	(4)
2008cw	–	(4)	–
2009K	–	–	–
2009mg	–	(8)	–
2010P	–	(9)	–
2010as	–	(10)	(10)
2010jr	–	–	–
2011dh	(11)	(11)	(12)
2011ei	(13)	(13)	(13)
2011fu	Chap.3	Chap.3	Chap.3
2011hs	(14)	(14)	(14)
2013cu	–	(15)	–
2013df	Chap.4	Chap.4	Chap.4

(1) Filippenko 1988; (2) Barbon et al. 1995; (3) unpublished spectrum taken at the 1.82-m telescope in Asiago (Italy); (4) Modjaz et al. 2014; (5) Silverman et al. 2009; (6) Hamuy et al. 2009; (7) Taubenberger et al. 2011; (8) Oates et al. 2012; (9) Kankare et al. 2014; (10) Folatelli et al. 2014b; (11) Ergon et al. 2014; (12) Shivvers et al. 2013; (13) Milisavljevic et al. 2013; (14) Bufano et al. 2014; (15) Gal-Yam et al. 2014.

Interestingly, as discussed in Chapters 3 and 4, SNe 2011fu and 2013df show an emission line at $\sim$ 6700 Å, although the line is broader in SN 2011fu. The rest of the objects do not exhibit a similar feature. Note that the lines at $\sim$ 6700 Å seen in the spectra of SNe 1987K, 2008aq, and 2008ax are much narrower, and are caused by sulphur from contamination by H II regions.

The minima of the P-Cygni absorptions of Hα and He I λ5876 provide an estimate of the velocities of the material ejected by SNe. Moreover, the photospheric velocities are expected to be similar to those derived from the Fe II λ5169 line (see e.g. figure 14 of Dessart & Hillier 2005). For SNe 2011fu and 2013df, we have taken such measurements from the spectra presented in Chapters 3 and 4. The results are shown in Figure 6.16 together with those obtained for the rest of the SNe of our sample. We also provide estimates of the velocities for Hα and He I λ5876 at three different epochs for SNe 2006T, 2008aq, and 2008bo, directly measured from their spectra presented in Modjaz et al. (2014). The velocities for the other SNe were

Table 6.10: Equivalent widths and ratios for Hα and He I λ5876 at phases $\sim$ 20 d since maximum. Note that for SN 2008aq there were no spectra at $\sim$ 20 d, and we have provided the measurements for an earlier time. Typical errors in the EW measurements are $\sim$ 10 Å.

SN	Phase (d)	$EW_{H\alpha}$ (Å)	$EW_{He\lambda5876}$ (Å)	$EW_{H\alpha}/EW_{He\lambda5876}$
1993J	20	44	93	0.5
1996cb	27	76	69	1.1
2001ig	21	73	27	2.7
2003bg	21	95	34	2.8
2006T	15	95	81	1.8
2008aq	2	122	21	5.8
2008ax	19	21	72	0.3
2008bo	16	59	69	0.9
2008cw	12	37	20	1.9
2009mg	15	104	55	1.9
2010as	17	–	135	–
2011dh	22	42	95	0.4
2011ei	16	64	54	1.2
2011fu	16	12	56	0.2
2011hs	25	37	132	0.3
2013cu	59	69	52	1.3
2013df	21	17	51	0.3

Table 6.11: Nebular line luminosities at phases $\sim$ 300 d since maximum. Note that for SN 2001gd, 2006T, and 2008aq we have provided the measurements at the latest phase for which spectra are available.

SN	Phase	L			ratio	
		MgI]λ4571 (10^{38}erg s^{-1})	[OI]$\lambda\lambda$6360,64 (10^{38}erg s^{-1})	[CaII]$\lambda\lambda$7291,7324 (10^{38}erg s^{-1})	$\frac{\text{[CaII]}}{\text{[OI]}}$	$\frac{\text{MgI]}\lambda4571}{\text{[OI]}\lambda\lambda6360,64}$
	(d)					
1987K	202	–	10	7.3	0.7	–
1993J	277	3.6	9.4	4.2	0.4	0.4
1996cb	178	0.7	3.4	4.8	1.4	0.2
2001gd	118	–	1.8	1.3	0.7	–
2001ig	290	2.4	5.8	1.8	0.3	0.4
2003bg	279	1.8	19	13	0.7	0.1
2006T	108	–	25	–	–	–
2008aq	111	–	24	17	0.7	–
2008ax	307	2.4	6.1	4.4	0.7	0.4
2008bo	108	–	13	16	1.2	–
2010as	308	*	–	2.8	–	–
2011dh	248	2.8	8.1	7.6	0.9	0.4
2011ei	310	0.5	1.4	0.8	0.6	0.4
2011fu	279	4.4	25	12	0.5	0.2
2011hs	333	0.4	0.8	0.7	0.9	0.5
2013df	222	–	11	35	3.2	–

*The low S/N in the region of the MgI]λ4571 line leads to uncertain values for its luminosity.

obtained from the literature.[6] Note that the first two He I λ5876 velocities reported for SN 2011fu in the figure were obtained from shallow, low contrast profiles, and in consequence are uncertain.

As we can see in Figure 6.16, the velocities are overall similar for all the SNe, with the exception of SN 2001ig which exhibits higher values, and SNe 2010as and 2011dh, which present different He I λ5876 velocity evolution at early times. Note that for SN 2011dh, the hydrogen lines were never seen below 11000 km s^{-1}, whereas the helium lines were always constrained to lower velocities. In fact the modelling of the SN data (Jerkstrand et al., 2015) suggested that 11000 km s^{-1} marked the interface between the H-rich envelope and the He core. Similar boundaries can be established for SNe 2003bg (11000 km s^{-1}), 2008ax (12000 km s^{-1}), 2011ei (10000 km s^{-1}) and 2011hs (12000 km s^{-1}). For SNe 1993J, 2001ig, 2011fu, and 2013df, however, analogous limits cannot be placed based solely on the observed velocities, since in the velocity space Hα is not separated from He.

As for the different behaviour of the He velocities for some of the SNe at early times, Ergon et al. (2014) pointed out that detailed modelling including non-thermal excitations might provide an explanation for SN 2011dh. Folatelli et al. (2014b) suggest that the flat velocity could be explained if there is a low density shell in the ejecta, and that SN 2010as and other type Ib/c transitional objects that show this flat He velocity evolution and traces of Hα features at early times, comprise a subgroup with the lowest hydrogen abundance within the type IIb SNe class. Further observations and modelling of the data of similar objects may help to confirm this hypothesis and the physical reasons giving rise to a dense shell in their ejecta.

6.5 Summary

In this chapter we have investigated several observational properties of a sample of type IIb SNe. To begin with, we find that galaxies with both high and low star formation rate host type IIb SNe. Specifically, about half of the hosts of our sample are blue and the other half red. It is interesting to note that, with the exception of SN 2011hs, all SNe of our sample with proposed extended progenitors were hosted by red galaxies. A larger sample and a more thorough study are needed to explore and provide an explanation if such an excess of extended SNe in red hosts is confirmed. On the other hand, the majority of the sample type IIb SNe are in spiral galaxies with an apparent preference for unbarred galaxies, and we do not find an excess of

[6]The velocities for SNe 1987K and 2003bg were obtained from Hamuy et al. (2009), those of SN 1993J from (Barbon et al., 1995; Taubenberger et al., 2011). For 1996cb we used the values reported by (Qiu et al., 1999), for 2001ig those of (Silverman et al., 2009), for 2008ax the ones given by (Taubenberger et al., 2011), for 2009mg they were obtained from (Oates et al., 2012), for SN 2010as they are those of Folatelli et al. (2014b), for 2011dh they are taken from (Ergon et al., 2014), for 2011ei they correspond to those of (Milisavljevic et al., 2013), and for 2011hs those given by (Bufano et al., 2014).

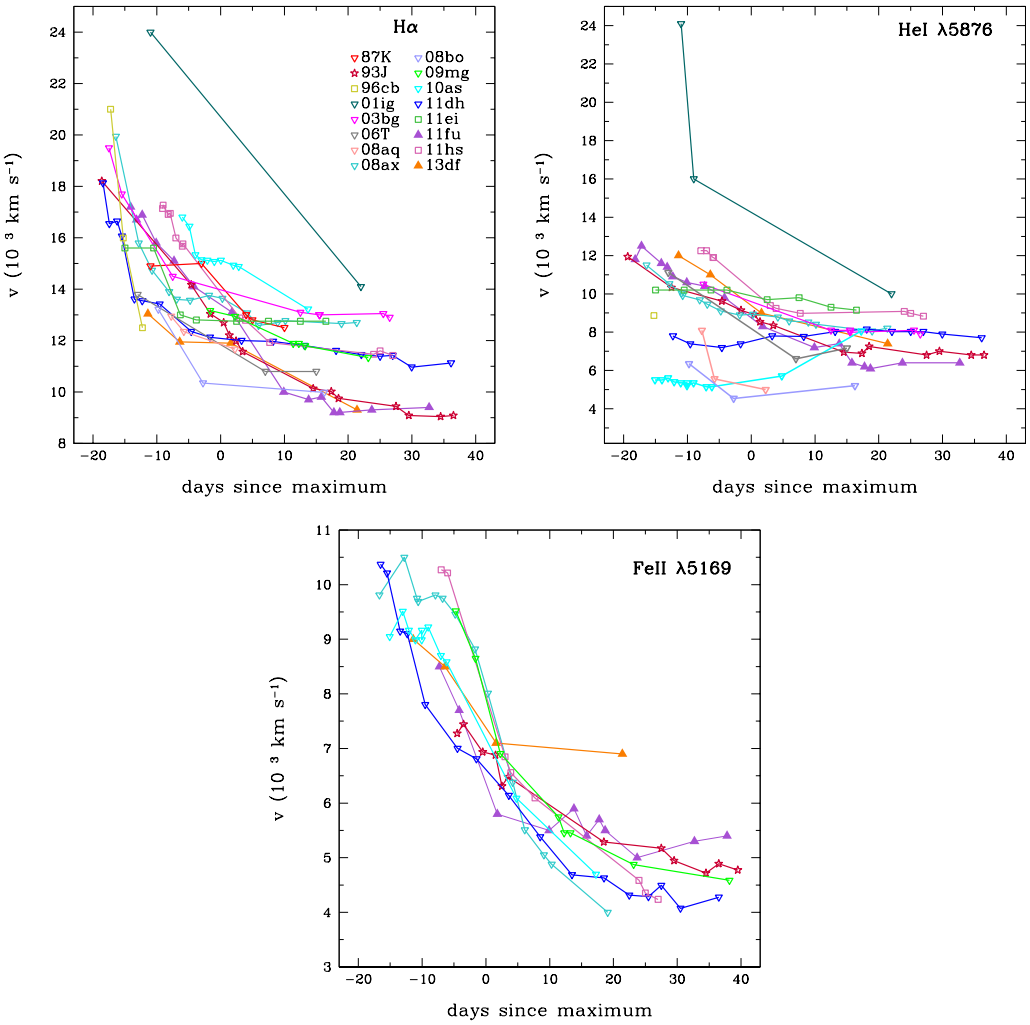

Figure 6.16: Velocity evolution of Hα, He I λ5876, and Fe II λ5169 for the sample of SNe studied along this chapter. Phase 0 corresponds to maximum light in V, R or r (see Table 6.5).

type IIb SNe in dwarf hosts, as has been claimed by other authors. Furthermore, the objects are not seen to explode in a preferred position within the hosts, except for the spiral arms.

As for the photometric properties, we find dispersion in the UV LC evolution, with SN 2011dh being the dimmest and SN 2013df one of the brightest. The shape of the UV LCs overall seems to mimic those in the optical with the exception of SN 2011dh ($UVm2$), and other SNe including SN 2013df which do not show a clear secondary maximum as do their optical LCs. The optical LCs show different shapes

and secondary peak brightness. We have obtained an average $M_{\rm R} = -17.48$ with standard deviation 0.58 mag at secondary peak for our SN sample. This value is below that reported for a sample of type Ic SNe, and lower but within the uncertainties of that reported for a sample of type Ib SNe by Drout et al. (2011). In the NIR, we find that the first peak in the LC of SN 1993J is much less pronounced than in the optical, and find a dispersion in the secondary maxima of our sample from about -17 to -19 mag.

Regarding the rise and decline rates for the SN LCs, the rise times to secondary peak are relatively similar for the sample of objects, with the exception of SN 2006T, 2011hs, and 2008ax, which present a slightly higher rate. Decline rates from secondary maximum are also similar, with SN 2008bo having a somewhat steeper decline (0.08 ± 0.01 mag d^{-1}). Likewise, there are similarities in the decline rates of the LC tails, with that of SN 1996cb seemingly slower (1.76 ± 0.11 mag (100d)$^{-1}$). A possible explanation of this behaviour could imply a higher ejected mass in the explosion than the rest of the objects. Respecting the SNe with two-peaks in their LCs, we find slightly different decline rates from first maximum, especially for the R band decline of SN 2011hs, which is significantly faster than the rest (0.46 ± 0.01 mag d^{-1}). While for the R band it seems that the SNe with brighter first peaks decline at a slower rate. This does not seem to be the case for the V band LCs. A larger sample of type IIb SNe with double-peaked LCs is necessary to further investigate this issue.

With regard to the optical colours, we find that the overall evolution is similar but slower than in the UV. There is significant dispersion between the colours of the different SNe, which implies that estimating type IIb SNe extinctions by comparison of their colour indices is rather difficult. The NIR colours evolve even slower than the optical, and again show a noticeable dispersion.

The optical spectra show diverse properties as well. At early phases the SNe with proposed extended progenitors seem to show blue continuum and shallow features, even more so those that were taken during the decline after first peak in their LCs. At phases post maximum light, the spectra are similar but exhibit different line intensities and EW. Specifically for the snapshot that we have shown at ~ 20 d post maximum, the EW ratio of Hα to He I λ5876 of the objects with proposed extended progenitors is below 1 at this time. At nebular phases, the most relevant features are MgI] λ4571, [O I] $\lambda\lambda$ 6300, 6364, and [CaII] $\lambda\lambda$7291,7324. We have found a variety of nebular line luminosities for the objects of our sample. Some of them present similar Mg/O line ratios, but we cannot find a clear explanation or connection between these and specific properties for the progenitors. On the other hand, the Ca/O line ratios are diverse, indicating that factors that are unrelated to specific progenitor properties, such as $M_{\rm ZAMS}$, affect the line intensities.

All the SNe of our sample show overall similar expansion and photospheric velocities except for SN 2001ig, which exhibits higher velocities for Hα and He Iλ 5876, and SN 2010as and 2011dh whose He I λ5876 velocities exhibit a flat behaviour at early times. The fact that SN 2001ig has higher velocities than the rest of the objects

could mean that it had higher explosion energy per unit mass. To explain the flat velocity behaviour of He I λ5876 for SN 2010as, Folatelli et al. (2014b) invoke the presence of a dense shell in the SN ejecta, while for SN 2011dh Ergon et al. (2014) claim that non-thermal excitations may play a role.

The relatively small sample of type IIb SNe that we have compared in this chapter shows that although they share some similar properties, type IIb SNe are overall heterogeneous in their observables showing different LC shapes, spreads in peak brightness, and spectral characteristics. Despite these differences, the binary progenitor scenario is favoured for many type IIb SNe. In the case of SNe 1993J, 2001ig, 2008ax, 2011dh, 2011ei, 2011fu, 2011hs, and 2013df, binarity is seconded by the estimates of their progenitor initial masses. The binary system scenario is further supported due to the direct detection of the companion star of the progenitor of SN 1993J (Maund & Smartt, 2009). In the case of SN 2010as, binarity was proposed by Folatelli et al. (2014b) to try to explain the discrepant initial mass estimates for the progenitor star from direct measurements and the modelling of the hydrodynamical LC. All in all, Roche-Lobe overflow is the preferential mechanism for the progenitors of the majority of type IIb SNe to have lost part of their outer envelope before explosion. The differences in the configuration and state of the binary interaction with the companion star at the time of the explosion could help explain the differences found in type IIb SN observables. The multiple ongoing and future surveys will continue to discover type IIb SNe. Further effort is needed to increase the statistics of this up to now poorly sampled SN subclass, which at the same time will help to shed light upon their progenitor systems, the conditions that lead to their explosions, and to try to further connect these with their observed properties.

Chapter 7

Conclusions

Throughout this thesis we have analysed the observational properties of SNe 2011fu and 2013df, which are amongst the very few type IIb objects that present double-peaked LCs in all optical bands. The observational analysis of the data for both these SNe leads to the conclusion that their properties, and consequently those of their progenitors, are somewhat similar.

On one hand, we interpret the optical and NIR observations of SN 2011fu as the consequence of the explosion of an extended star ($R \sim 450$ R$_\odot$), in which 1.3×10^{51} erg of kinetic energy were released and 0.15 M$_\odot$ of ^{56}Ni were synthesised. Our data point to a $M_{\rm ZAMS}$ of 13–18 M$_\odot$ and a hydrogen-rich envelope of $\sim$ 0.3 M$_\odot$ for SN 2011fu's progenitor. Secondly, the UV/optical data of SN 2013df can be explained by the terminal disruption of an extended ($R > 64 - 169\,$R$_\odot$) and massive ($\sim$ 12–13 M$_\odot$) star, that had retained a $\sim$ 0.2 M$_\odot$ hydrogen envelope. The 0.4–1.2 $\times$ 10^{51}erg explosion produced 0.1–0.13 M$_\odot$ of ^{56}Ni. In the nebular phase spectra we find that the O/Ca zones of SNe 2011fu and 2013df are clumped, being indicative of asymmetric ejecta. And in the case of SN 2013df, there is a late-time Hα emission that indicates ejecta interaction with H-rich material (analogously to SN 1993J).

The mass and radius constraints obtained in this thesis for the precursor stars of both SNe 2011fu and 2013df, imply that their progenitors could not have been wind-stripped WRs. Instead, they were extended stars that possibly formed part of binary systems, and which donated part of their outer envelope to a companion before their final demise.

Both SNe 2011fu and 2013df were included in a sample of type IIb SNe for the study of the global properties of UV/optical/NIR observables. From the somewhat limited data in the UV, we found that the LCs show dispersion both in brightness and shape. A group of SNe shows an early declining phase in their UV LCs due to shock breakout. The similarity of the UV shock breakout tails between SNe 2010jr and 2013df leads us to believe that their progenitors' extended-hydrogen-envelopes could be alike. We conclude that type IIb SNe UV LCs could form two groups, on one

hand those whose LCs exhibit the shock breakout cooling and no apparent secondary peak, and on the other, those that show no long duration shock breakout cooling but rather a rise and decline from a maximum. SN 2011dh could be an intermediate case between these two groups. There are some SNe in our sample for which it is possible that the UV shock breakout tails have been missed by observations.

In the optical, the LCs can be divided in those showing two clear peaks and those that exhibit single maxima (i.e., a similar subdivision than in the UV). We conclude that there are diverse first peak brightness, decline rates from first peak, and durations of the cooling after the first peaks among double-peaked type IIb SNe. The part of the LCs associated to the ^{56}Ni decay also show distinct properties, such as peak brightness and slightly different rise and decline rates to/from (secondary) peak, reflecting a dispersion of explosion parameters among the subclass. From an inspection of secondary peak brightness in the R band of the SN sample we conclude, however, that low luminosity events could be uncommon, and have obtained an average $M_{\rm R} = -17.48$ with standard deviation 0.58 mag.

In the NIR, data are scarce but we find that the properties of type IIb SNe also seem to be diverse, with peak magnitudes ranging ~ -17 to ~ -19 mag. The NIR colour evolution is slower than in the optical, which in turn is slower than in the UV. However, in all wavelength ranges there is significant dispersion, which reflects the difficulty of using colour comparisons to estimate extinctions towards type IIb SNe.

Concerning the optical spectra, we also find distinct properties among the different objects. The spectra taken during the declining phase after first peak in the LCs of those SNe that show double peaked LCs, are bluer and show shallower features than those taken at similar phases for the SNe that have single-peaked LCs. After secondary maximum, the spectra resemble one another but there are differences between the EW and intensities of the different features.

We have found a diversity of line luminosities in the nebular spectra for the most important lines: MgI] λ4571, [O I] $\lambda\lambda$ 6300, 6364, and [CaII] $\lambda\lambda$7291,7324. The different [CaII]/[O I] ratios of the sample reflect that they are not only affected by progenitor initial mass but also by other factors such as mixing.

The photospheric and expansion velocities of our sample are overall similar except for SN 2001ig, which exhibits higher velocities (maybe indicative of a higher explosion energy per unit mass than the rest of the sample SNe) and SNe 2010as and 2011dh, which show flat He velocity at early phases. This, as indicated in the literature, could be due to a dense shell in the SN ejecta or non-thermal effects.

We have found that both high and low star formation rate galaxies are the hosts of type IIb SNe. The most important result in this context is that almost all the type IIb SNe arising from extended progenitors are found to have been hosted in red galaxies (low star formation rate). We do not provide an explanation for this apparent excess of extended IIb SNe in red hosts, since a larger sample is needed to confirm this result. We have not found a majority of the type IIb SNe of our sample hosted in dwarf galaxies, as some authors have previously suggested, instead,

most of the SNe of our sample are hosted in spiral galaxies of type Sbc/c, with no preferred position within them, except for the galactic arms.

All in all, we have shown that type IIb SNe present some similarities, but overall a variety and dispersion of observed properties. The analysis and interpretation of type IIb SNe explosions is further challenged by the discovery of peculiar transients such as OGLE-2013-SN-100. The object showed a rare double-peaked I band LC, with the first peak taking place over a much longer time-scale than those of SNe 2011fu, 2013df, or 1993J, which makes us conclude that it was not caused by cooling of the progenitor's stellar envelope after shock breakout. Specifically, the first maximum seems to have taken place $\sim$ 85 d prior to the second one, and the minimum between the two peaks approximately 45 d before the second peak. Both LC peaks have absolute magnitudes that could be consistent with those of CC-SN at peak. The spectra of OGLE-2013-SN-100 do not show significant evolution at the phases at which they were taken (after the second peak). They exhibit some lines common to those observed in the spectra of CC-SN explosions such as helium and iron features. In addition, the spectra present Balmer emission lines, which could indicate SN ejecta-H-rich-CSM interaction. We conclude that the most likely scenario to explain the observed properties of OGLE-2013-SN-100 is that a CC-SN explosion occurred (causing the first peak of the LC) within a cavity surrounded by H-rich material, and that when the SN ejecta encountered the H-rich shell they provoked the second peak of the LC. Unfortunately, the lack of early-time spectra does not allow us to classify the CC-SN explosion that caused the first peak of the LC, but we find it likely to have been a type IIn SN, since our later-time spectra show narrow hydrogen emission lines indicative of ejecta CSM interaction. If instead the SN explosion had been a type IIb, we could conclude that the progenitor and/or CSM environment properties were quite different from those observed for other type IIb up to now.

This thesis contributes with detailed observations of two type IIb SNe that exhibit two peaks in all their optical LCs. Observational multi chromatic coverage of the first peaks in the LCs of type IIb SNe is rare, in fact there is only one more type IIb SN for which such data exist. Moreover, both of the SNe presented in this thesis are two additional type IIb SNe whose progenitors were likely part of a binary stellar system. In this context, many questions remain unanswered: How do the configuration and state of the binary interaction affect the observed properties of a type IIb SN? How do the physical characteristics of the progenitor companion affect the observables of the final type IIb SN? If some type IIb SNe come from single progenitors, how do their observables differ from those that arise from binary systems? In order to help answer these questions it is essential to observe more type IIb SNe and to increase the number of well-monitored events. Of particular interest would be to increase the statistics of type IIb SNe with double-peaked LCs. The various ongoing and future SN surveys will surely help in discovering more type IIb SNe at early phases, and thus aid in this task. On the other hand, future observations of type IIb SN fields once these have faded may help unveil further information about their

progenitors/progenitor systems and the conditions that gave rise to their observed properties.

Appendix A

PESSTO

The Public European Southern Observatory Spectroscopic Survey of Transient Objects (PESSTO; P.I. S. Smartt; Smartt et al. 2015) has the aim of classifying optical transients and performing spectroscopic and photometric follow-up of ∼150 targets related to the extremes of the SN population. PESSTO is formed by a broad collaboration of most of the SN research groups in Europe, as well as other groups around the world. The survey began in April 2012, and will continue up to 2017.

A.1 Science goals and strategy

The ongoing surveys dedicated to the search of optical transients (e.g. Palomar Transient Factory,[1] La Silla QUEST,[2] etc.) are discovering objects which question our current knowledge on stellar explosions. PESSTO's primary goal is to aid in classifying and providing follow-up data of such objects, thus helping to unveil the physical processes behind the diversity of the transient universe. Some of PESSTO's key science targets include luminosity extreme objects ($M_{\rm V} < -19.5$ and $M_{\rm V} > -15.5$ mag), objects with known variability history like SN 2009ip, transients taking place in peculiar environments (e.g. no host galaxy, hosts with $M_{\rm B} > -18$ mag, or galaxies that have hosted several SNe), and nearby objects, since they can be followed-up at multiple wavelengths (which may help to assess explosion and shock-CSM interaction mechanisms).

Up to now PESSTO has classified over 700 transients, over 150 of which are being followed up. In addition, 28 manuscripts including PESSTO data have already been accepted for publication in different journals.

PESSTO makes use of the 3.6-m New Technology Telescope (NTT) in the La Silla observatory (Chile). The visitor-mode time allocated for PESSTO is 90 nights

[1] http://www.ptf.caltech.edu/
[2] http://hep.yale.edu/lasillaquest

per year, which are divided in 10 nights per month from August to May. Classification spectra, as well as optical follow-up photometry and spectroscopy, are obtained with EFOSC2, while SOFI is used to acquire near infrared (NIR) data. The potential transient sources for PESSTO to classify are selected mainly from the La Silla QUEST, All-Sky Automated Survey for Supernovae (ASAS-SN)[3], Panoramic Survey Telescope & Rapid Response System (PAN-STARRS)[4], SkyMapper[5] and OGLE IV[6] surveys (to which PESSTO is partnered) although objects from other public sources, such as discoveries made by amateur astronomers, may also be considered for classification.

Usually, once per year each institution participating in the survey will constitute an observing team that will be in charge of one of the observational runs, which are typically split in 4, 3, and 3 nights sub-runs. In addition to the observers, for each sub-run, a support team is created to reduce the acquired data, classify the objects, send out an Astronomer's Telegram (ATel)[7] with the results of the classifications, and send the classification spectra to WISeREP within 24 h of the observations. Data reduction is done with a pipeline written in Python by members of the collaboration and provides reduced spectra and photometry for both EFOSC2 and SOFI data. The support team focuses only on the reduction of the optical spectra. Classifications are done with dedicated software, e.g. SNID or GELATO, which compare the input classification spectra with spectra in their database and return the best fit spectra and their phase. While the classification data are immediately public (via the ESO archive and WISeREP), the science follow-up data are made public once a year through official data releases.

A.2 Participation in PESSTO

In addition to the study of one object followed-up by PESSTO (see Chapter 5), and as part of the only Spanish node in the PESSTO collaboration, I have participated in the survey as both an observer and data reducer. Specifically, I was a member of the support team for two sub-runs in 2012 October, the complete 2013 April run, and one sub-run in 2014 August-September. I was part of the observing team in the 2013 January-February run.

A summary of the classifications performed as an observer and data reducer can be found in Table A.1. In Figure A.1, we show two examples of classification spectra obtained during two different PESSTO subruns (2013 April and 2014 August) compared to their best fitting spectra. On the top panel of the figure, LSQ13th is represented, which was classified as a type Ib/c SN about a week after maximum light.

[3]http://www.astronomy.ohio-state.edu/∼assassin/index.shtml
[4]http://pan-starrs.ifa.hawaii.edu/public/
[5]http://rsaa.anu.edu.au/observatories/telescopes/skymapper-telescope
[6]http://ogle.astrouw.edu.pl/
[7]http://www.astronomerstelegram.org/

Note that to classify this SN, not only did we compare the classification spectrum to spectral templates, but also and to better constrain its phase, we used available photometric data. On the bottom panel of Figure A.1, the LSQ14dud classification spectrum is presented. As can be seen, it fits nicely with type Ia SN 2006gz about a week after maximum light.

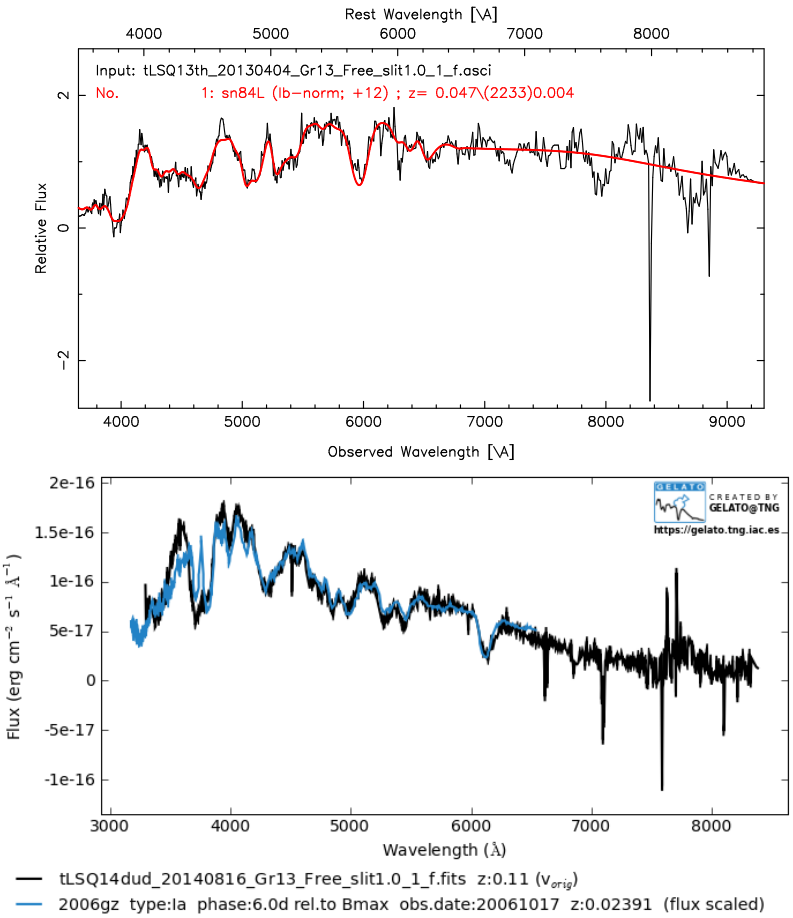

Figure A.1: Top panel: Classification spectrum of LSQ13th compared to one of the best fitting spectra given by SNID. The SN was classified as a type Ib/c SN about a week after maximum light. Bottom panel: LSQ14dud classification spectrum compared to the best fitting spectrum (given by GELATO) of type Ia SN 2006gz. LSQ14dud was classified as a type Ia SN about a week after maximum light.

Table A.1: Objects classified as data reducer or observer for PESSTO

Object	Right Ascension (J2000)	Declination (J2000)	Type	Reference
LSQ12fjm	04:36:10.93	-05:04:53.4	not a SN	Sternberg et al. (2012a)
LSQ12fiq	04:41:40.78	-09:53:34.4	Ia	Sternberg et al. (2012a)
LSQ12fkh	02:30:53.17	+09:35:40.8	Gal.	Sternberg et al. (2012b)
LSQ12fli	04 31 04.18	-07 12 13.7	Ia	Sternberg et al. (2012b)
LSQ12fmd	03 39 46.92	-07 30 19.1	Ia	Sternberg et al. (2012b)
LSQ12fnt	03 32 41.40	-01 11 11.0	Ic	Sternberg et al. (2012b)
SN 2013L	11 45 29.54	-50 35 53.0	IIn	Morales-Garoffolo et al. (2013c)
OGLE-2013-SN-012	05 09 52.38	-65 39 48.5	IIn?	Elias-Rosa et al. (2013a)
PSN J15213475-0722183	15 21 34.75	-07 22 18.3	Impostor?	Morales-Garoffolo et al. (2013a)
MASTER OT J093953.18+165516.4	09 39 53.18	16 55 16.4	Ia	Benitez-Herrera et al. (2013)
CSS130214:110748+243938	11 07 47.78	+24 39 38.4	Ia	Morales-Garoffolo et al. (2013b)
PSN J08175346+2328105	08 17 53.46	+23 28 10.4	Ia	Hachinger et al. (2013)
SSS130329:111742-203116	11 17 42.08	-20 31 16.4	star	Hachinger et al. (2013)
CSS130401:125031+090817	12 50 31.40	+09 08 16.9	Ia	Hachinger et al. (2013)
SNhunt178	13 10 21.31	-07 10 24.0	Ia	Hachinger et al. (2013)
LSQ13sj	13 18 17.76	-02 51 42.9	CC-SN?	Hachinger et al. (2013)
LSQ13rd	15 56 38.53	+00 21 09.6	II	Hachinger et al. (2013)
SSS130402:141135-282828	14 11 35.49	-28 28 27.6	star	Taubenberger et al. (2013)
LSQ13sd	10 21 35.56	+20 56 19.7	IIn?	Morales-Garoffolo et al. (2013d)
LSQ13th	09 28 48.97	-03 30 46.4	Ib/c	Morales-Garoffolo et al. (2013d)
CSS130403:150213+103846	15 02 13.09	+10 38 45.6	Ia	Morales-Garoffolo et al. (2013d)
SSS130404:102043-062657	10 20 42.87	-06 26 56.8	Ia	Elias-Rosa et al. (2013b)
PSN J14121396+1550315	14 12 13.96	+15 50 31.4	IIb	Elias-Rosa et al. (2013b)
MASTER OT J162412.26+091303.0	16 24 12.26	+09 13 03.0	Ia	Elias-Rosa et al. (2014a)
LSQ14drr	20 41 08.26	-55 28 16.1	IIP	Elias-Rosa et al. (2014a)
LSQ14dus	22 03 44.68	-52 43 19.8	Ia	Elias-Rosa et al. (2014a)
LSQ14dtt	21 33 10.24	-18 20 26.1	Ia	Elias-Rosa et al. (2014a)
OGLE-2014-SN-052	00 03 49.30	-69 59 00.3	Gal.	Elias-Rosa et al. (2014a)
LSQ14dvy	21 40 59.74	-45 23 02.0	Ia	Elias-Rosa et al. (2014a)
PSN J06363000-6643540	06 36 30.00	-66 43 54.0	Ia	Elias-Rosa et al. (2014a)
PSN J06335776-3448276	06:33:57.76	-34:48:27.6	Ia	Elias-Rosa et al. (2014a)
ASASSN-14fo	20:34:06.43	-01:58:03.5	Ia	Elias-Rosa et al. (2014b)
LSQ14drn	20:39:04.63	-61:10:27.0	Ia	Elias-Rosa et al. (2014b)
LSQ14drx	21:47:10.18	-49:36:53.7	IIn	Elias-Rosa et al. (2014b)
LSQ14dsj	21:53:25.57	-19:21:07.3	M-star	Elias-Rosa et al. (2014b)
LSQ14dss	23:02:57.76	-55:57:03.0	CV	Elias-Rosa et al. (2014b)
LSQ14dud	22:25:06.94	+00:31:49.4	Ia	Elias-Rosa et al. (2014b)
LSQ14dvq	21:03:10.63	-60:30:28.9	CV	Elias-Rosa et al. (2014b)

Table A.1: (continued)

Object	Right Ascension (J2000)	Declination (J2000)	Type	Reference
LSQ14dvx	20:38:43.63	-41:08:53.8	II	Elias-Rosa et al. (2014b)
LSQ14dxa	22:08:39.89	-56:09:24.9	Ia	Elias-Rosa et al. (2014b)
LSQ14ecb	21:53:41.32	-13:17:27.4	Ia	Elias-Rosa et al. (2014b)
LSQ14edn	21:58:10.26	-44:55:41.6	Ia	Elias-Rosa et al. (2014b)
LSQ14eer	22:48:14.65	+07:10:06.5	II	Elias-Rosa et al. (2014b)
OGLE-2014-SN-046	01:09:06.73	-74:30:46.4	IIP	Elias-Rosa et al. (2014b)
LSQ14eef	21 23 33.46	-08 45 36.6	Ia	Tartaglia et al. (2014a)
LSQ14eeh	21 05 29.94	-05 25 03.2	IIP	Tartaglia et al. (2014a)
LSQ14efn	20 26 35.43	-48 12 30.3	Ia	Tartaglia et al. (2014a)
LSQ14eek	21 36 50.32	-02 28 06.4	Ia	Tartaglia et al. (2014a)
LSQ14eet	22 50 11.71	+14 57 32.1	Ia	Tartaglia et al. (2014a)
LSQ14eew	23 20 42.10	+15 54 37.1	Ia	Tartaglia et al. (2014a)
LSQ14efd	03 35 38.76	-58 52 38.3	II	Tartaglia et al. (2014a)
LSQ14eey	23 38 11.68	+23 04 50.0	Ia	Tartaglia et al. (2014a)
LSQ14efh	20 36 22.65	-55 25 54.6	Ia	Tartaglia et al. (2014a)
LSQ14een	22 32 18.79	-02 42 50.5	Ia	Tartaglia et al. (2014a)
LSQ14eds	00 38 18.78	-17 58 16.6	Ia	Tartaglia et al. (2014a)
OGLE-2014-SN-047	03 30 15.46	-75 40 47.0	I	Tartaglia et al. (2014a)
PSN J14504990-1331037	14:50:49.90	-13:31:03.7	Ia	Tartaglia et al. (2014b)
LSQ14efs	21:00:18.82	-35:23:56.1	II	Tartaglia et al. (2014b)
LSQ14efq	20:47:50.29	-47:33:11.0	CV	Tartaglia et al. (2014b)
LSQ14dsx	23:04:09.83	-52:11:44.0	Ia	Tartaglia et al. (2014b)
LSQ14dxl	01:34:15.10	-17:05:59.8	IIP	Tartaglia et al. (2014b)
LSQ14efd	03:35:38.76	-58:52:38.3	I	Tartaglia et al. (2014b)

Bibliography

Aldering G., Humphreys R. M., and Richmond M., 1994. SN 1993J: The optical properties of its progenitor. *AJ*, **107**, 662–672.

Anupama G. C., Sahu D. K., Gurugubelli U. K., et al., 2009. Optical photometry and spectroscopy of the Type Ibn supernova SN 2006jc until the onset of dust formation. *MNRAS*, **392**, 894–903.

Arcavi I., Gal-Yam A., Kasliwal M. M., et al., 2010. Core-collapse Supernovae from the Palomar Transient Factory: Indications for a Different Population in Dwarf Galaxies. *ApJ*, **721**, 777–784.

Arnett W. D., 1982. Type I supernovae. I - Analytic solutions for the early part of the light curve. *ApJ*, **253**, 785–797.

Arnett W. D., Bahcall J. N., Kirshner R. P., and Woosley S. E., 1989. Supernova 1987A. *ARA&A*, **27**, 629–700.

Barbon R., Benetti S., Cappellaro E., Patat F., Turatto M., and Iijima T., 1995. SN 1993J in M 81: One year of observations at Asiago. *A&AS*, **110**, 513.

Barbon R., Buondí V., Cappellaro E., and Turatto M., 1999. The Asiago Supernova Catalogue - 10 years after. *A&AS*, **139**, 531–536.

Ben-Ami S., Hachinger S., Gal-Yam A., et al., 2015. Ultraviolet Spectroscopy of Type IIb Supernovae: Diversity and the Impact of Circumstellar Material. *ApJ*, **803**, 40.

Benitez-Herrera S., Taubenberger S., Garoffolo A. M., et al., 2013. PESSTO spectroscopic classification of optical transients. *The Astronomer's Telegram*, **4801**, 1.

Benvenuto O. G., Bersten M. C., and Nomoto K., 2013. A Binary Progenitor for the Type IIb Supernova 2011dh in M51. *ApJ*, **762**, 74.

Bersten M. C., Benvenuto O., and Hamuy M., 2011. Hydrodynamical Models of Type II Plateau Supernovae. *ApJ*, **729**, 61.

Bersten M. C., Benvenuto O. G., Nomoto K., et al., 2012. The Type IIb Supernova 2011dh from a Supergiant Progenitor. *ApJ*, **757**, 31.

Bertola F., 1967. Recent Observations of the Supernova in NGC 1058. *Information Bulletin on Variable Stars*, **196**, 1.

Bessell M. and Murphy S., 2012. Spectrophotometric Libraries, Revised Photonic Passbands, and Zero Points for UBVRI, Hipparcos, and Tycho Photometry. *PASP*, **124**, 140–157.

Bianco F. B., Modjaz M., Hicken M., et al., 2014. Multi-color Optical and Near-infrared Light Curves of 64 Stripped-envelope Core-Collapse Supernovae. *ApJS*, **213**, 19.

Blinnikov S. I., Eastman R., Bartunov O. S., Popolitov V. A., and Woosley S. E., 1998. A Comparative Modeling of Supernova 1993J. *ApJ*, **496**, 454–472.

Blondin S. and Tonry J. L., 2007. Determining the Type, Redshift, and Age of a Supernova Spectrum. *ApJ*, **666**, 1024–1047.

Branch D., Benetti S., Kasen D., et al., 2002. Direct Analysis of Spectra of Type Ib Supernovae. *ApJ*, **566**, 1005–1017.

Brown P. J., Roming P. W. A., and Milne P. A., 2015. The first ten years of Swift supernovae. *Journal of High Energy Astrophysics*, **7**, 111–116.

Bufano F., Pignata G., Bersten M., et al., 2014. SN 2011hs: a fast and faint Type IIb supernova from a supergiant progenitor. *MNRAS*, **439**, 1807–1828.

Burrows A., Livne E., Dessart L., Ott C. D., and Murphy J., 2007. Features of the Acoustic Mechanism of Core-Collapse Supernova Explosions. *ApJ*, **655**, 416–433.

Cappellaro E., Mazzali P. A., Benetti S., et al., 1997. SN IA light curves and radioactive decay. *A&A*, **328**, 203–210.

Cardelli J. A., Clayton G. C., and Mathis J. S., 1989. The relationship between infrared, optical, and ultraviolet extinction. *ApJ*, **345**, 245–256.

Chevalier R. A. and Fransson C., 2008. Shock Breakout Emission from a Type Ib/c Supernova: XRT 080109/SN 2008D. *ApJ*, **683**, L135–L138.

Chevalier R. A. and Soderberg A. M., 2010. Type IIb Supernovae with Compact and Extended Progenitors. *ApJ*, **711**, L40–L43.

Ciabattari F., Mazzoni E., Donati S., et al., 2013. Supernova 2013df in NGC 4414 = Psn J12262933+3113383. *Central Bureau Electronic Telegrams*, **3557**, 1.

Clocchiatti A., Wheeler J. C., Benetti S., and Frueh M., 1996. SN 1983N and the Nature of Stripped Envelope–Core Collapse Supernovae. *ApJ*, **459**, 547.

Crockett R. M., Eldridge J. J., Smartt S. J., et al., 2008. The type IIb SN 2008ax: the nature of the progenitor. *MNRAS*, **391**, L5–L9.

de Vaucouleurs G. and Corwin, Jr. H. G., 1985. S Andromedae 1885 - A centennial review. *ApJ*, **295**, 287–304.

Dennefeld M., Bersier D., Lyman J., et al., 2013. PESSTO spectroscopic classification of optical transients. *The Astronomer's Telegram*, **5617**, 1.

Dessart L. and Hillier D. J., 2005. Distance determinations using type II supernovae and the expanding photosphere method. *A&A*, **439**, 671–685.

Drout M. R., Soderberg A. M., Gal-Yam A., et al., 2011. The First Systematic Study of Type Ibc Supernova Multi-band Light Curves. *ApJ*, **741**, 97.

Elias-Rosa N., Garoffolo A. M., Benitez-Herrera S., et al., 2013a. PESSTO spectroscopic classification of optical transients. *The Astronomer's Telegram*, **4774**, 1.

Elias-Rosa N., Tartaglia L., Morales-Garoffolo L. T. A., et al., 2014a. PESSTO spectroscopic classification of optical transients. *The Astronomer's Telegram*, **6398**, 1.

Elias-Rosa N., Tartaglia L., Tomasella L., et al., 2014b. PESSTO spectroscopic classification of optical transients. *The Astronomer's Telegram*, **6399**, 1.

Elias-Rosa N., Taubenberger S., Hachinger S., et al., 2013b. PESSTO spectroscopic classification of optical transients. *The Astronomer's Telegram*, **4957**, 1.

Ergon M., Jerkstrand A., Sollerman J., et al., 2015. The Type IIb SN 2011dh: Two years of observations and modelling of the lightcurves. *A&A*, **580**, A142.

Ergon M., Sollerman J., Fraser M., et al., 2014. Optical and near-infrared observations of SN 2011dh - The first 100 days. *A&A*, **562**, A17.

Fassia A., Meikle W. P. S., Chugai N., et al., 2001. Optical and infrared spectroscopy of the type IIn SN 1998S: days 3-127. *MNRAS*, **325**, 907–930.

Filippenko A. V., 1982. The importance of atmospheric differential refraction in spectrophotometry. *PASP*, **94**, 715–721.

Filippenko A. V., 1988. Supernova 1987K - Type II in youth, type Ib in old age. *AJ*, **96**, 1941–1948.

Filippenko A. V., 1997. Optical Spectra of Supernovae. *ARA&A*, **35**, 309–355.

Filippenko A. V., Matheson T., and Barth A. J., 1994. The peculiar type II supernova 1993J in M81: Transition to the nebular phase. *AJ*, **108**, 2220–2225.

Filippenko A. V., Richmond M. W., Branch D., et al., 1992a. The subluminous, spectroscopically peculiar type IA supernova 1991bg in the elliptical galaxy NGC 4374. *AJ*, **104**, 1543–1556.

Filippenko A. V., Richmond M. W., Matheson T., et al., 1992b. The peculiar Type IA SN 1991T - Detonation of a white dwarf? *ApJ*, **384**, L15–L18.

Folatelli G., Bersten M. C., Benvenuto O. G., et al., 2014a. A Blue Point Source at the Location of Supernova 2011dh. *ApJ*, **793**, L22.

Folatelli G., Bersten M. C., Kuncarayakti H., Benvenuto O. G., Maeda K., and Nomoto K., 2015. The Progenitor of the Type IIb SN 2008ax Revisited. *ApJ*, **811**, 147.

Folatelli G., Bersten M. C., Kuncarayakti H., et al., 2014b. Supernova 2010as: The Lowest-velocity Member of a Family of Flat-velocity Type IIb Supernovae. *ApJ*, **792**, 7.

Fox O. D., Azalee Bostroem K., Van Dyk S. D., et al., 2014. Uncovering the Putative B-star Binary Companion of the SN 1993J Progenitor. *ApJ*, **790**, 17.

Fransson C. and Chevalier R. A., 1987. Late emission from SN 1987A. *ApJ*, **322**, L15–L20.

Fransson C. and Chevalier R. A., 1989. Late emission from supernovae - A window on stellar nucleosynthesis. *ApJ*, **343**, 323–342.

Fraser M., Inserra C., Jerkstrand A., et al., 2013. SN 2009ip à la PESSTO: no evidence for core collapse yet. *MNRAS*, **433**, 1312–1337.

Fraser M., Kotak R., Pastorello A., et al., 2015. SN 2009ip at late times - an interacting transient at +2 years. *ArXiv e-prints*.

Gal-Yam A., Arcavi I., Ofek E. O., et al., 2014. A Wolf-Rayet-like progenitor of SN 2013cu from spectral observations of a stellar wind. *Nature*, **509**, 471–474.

Gal-Yam A., Mazzali P., Ofek E. O., et al., 2009. Supernova 2007bi as a pair-instability explosion. *Nature*, **462**, 624–627.

Gal-Yam A., Mazzali P. A., Manulis I., and Bishop D., 2013. Supernova Discoveries 2010–2011: Statistics and Trends. *PASP*, **125**, 749–752.

Galama T. J., Vreeswijk P. M., van Paradijs J., et al., 1998. An unusual supernova in the error box of the γ-ray burst of 25 April 1998. *Nature*, **395**, 670–672.

Galbany L., Stanishev V., Mourão A. M., et al., 2014. Nearby supernova host galaxies from the CALIFA Survey. I. Sample, data analysis, and correlation to star-forming regions. *A&A*, **572**, A38.

Gräfener G. and Vink J. S., 2016. Light-travel-time diagnostics in early supernova spectra: substantial mass-loss of the IIb progenitor of SN 2013cu through a superwind. *MNRAS*, **455**, 112–126.

Groh J. H., 2014. Early-time spectra of supernovae and their precursor winds. The luminous blue variable/yellow hypergiant progenitor of SN 2013cu. *A&A*, **572**, L11.

Hachinger S., Mazzali P. A., Taubenberger S., Hillebrandt W., Nomoto K., and Sauer D. N., 2012. How much H and He is 'hidden' in SNe Ib/c? - I. Low-mass objects. *MNRAS*, **422**, 70–88.

Hachinger S., Taubenberger S., Elias-Rosa N., et al., 2013. PESSTO spectroscopic classification of optical transients. *The Astronomer's Telegram*, **4940**, 1.

Hakobyan A. A., Mamon G. A., Petrosian A. R., Kunth D., and Turatto M., 2009. The radial distribution of core-collapse supernovae in spiral host galaxies. *A&A*, **508**, 1259–1268.

Hakobyan A. A., Nazaryan T. A., Adibekyan V. Z., et al., 2014. Supernovae and their host galaxies - II. The relative frequencies of supernovae types in spirals. *MNRAS*, **444**, 2428–2441.

Hamuy M., Deng J., Mazzali P. A., et al., 2009. Supernova 2003bg: The First Type IIb Hypernova. *ApJ*, **703**, 1612–1623.

Hamuy M., Phillips M. M., Suntzeff N. B., et al., 2003. An asymptotic-giant-branch star in the progenitor system of a type Ia supernova. *Nature*, **424**, 651–654.

Hamuy M., Suntzeff N. B., Heathcote S. R., Walker A. R., Gigoux P., and Phillips M. M., 1994. Southern spectrophotometric standards, 2. *PASP*, **106**, 566–589.

Hamuy M., Walker A. R., Suntzeff N. B., Gigoux P., Heathcote S. R., and Phillips M. M., 1992. Southern spectrophotometric standards. *PASP*, **104**, 533–552.

Hartwig E., 1885. S and. *Astronomische Nachrichten*, **112**, 285.

Harutyunyan A. H., Pfahler P., Pastorello A., et al., 2008. ESC supernova spectroscopy of non-ESC targets. *A&A*, **488**, 383–399.

Heger A., Fryer C. L., Woosley S. E., Langer N., and Hartmann D. H., 2003. How Massive Single Stars End Their Life. *ApJ*, **591**, 288–300.

Horesh A., Stockdale C., Fox D. B., et al., 2013. An early and comprehensive millimetre and centimetre wave and X-ray study of SN 2011dh: a non-equipartition blast wave expanding into a massive stellar wind. *MNRAS*, **436**, 1258–1267.

Humphreys R. M. and Davidson K., 1994. The luminous blue variables: Astrophysical geysers. *PASP*, **106**, 1025–1051.

Immler S. and Lewin W. H. G., 2003. X-Ray Supernovae. In K. Weiler, ed., *Supernovae and Gamma-Ray Bursters*, vol. 598 of *Lecture Notes in Physics, Berlin Springer Verlag*, 91–111.

Inserra C., Pastorello A., Turatto M., et al., 2013. Moderately luminous Type II supernovae. *A&A*, **555**, A142.

Janka H.-T., Langanke K., Marek A., Martínez-Pinedo G., and Müller B., 2007. Theory of core-collapse supernovae. *Phys. Rep.*, **442**, 38–74.

Jeffery D. J., Kirshner R. P., Challis P. M., et al., 1994. A Hubble Space Telescope ultraviolet spectrum of SN 1993J. *ApJ*, **421**, L27–L30.

Jerkstrand A., 2011. *Spectral modeling of nebular-phase supernovae*. Ph.D. thesis, PhD Thesis, University of Stockholm, Faculty of Science, Department of Astronomy (2011). Advisor: Claes Fransson.

Jerkstrand A., Ergon M., Smartt S. J., et al., 2015. Late-time spectral line formation in Type IIb supernovae, with application to SN 1993J, SN 2008ax, and SN 2011dh. *A&A*, **573**, A12.

Jerkstrand A., Fransson C., Maguire K., Smartt S., Ergon M., and Spyromilio J., 2012. The progenitor mass of the Type IIP supernova SN 2004et from late-time spectral modeling. *A&A*, **546**, A28.

Jerkstrand A., Smartt S. J., Fraser M., et al., 2014. The nebular spectra of SN 2012aw and constraints on stellar nucleosynthesis from oxygen emission lines. *MNRAS*, **439**, 3694–3703.

Jester S., Schneider D. P., Richards G. T., et al., 2005. The Sloan Digital Sky Survey View of the Palomar-Green Bright Quasar Survey. *AJ*, **130**, 873–895.

Jordi K., Grebel E. K., and Ammon K., 2006. Empirical color transformations between SDSS photometry and other photometric systems. *A&A*, **460**, 339–347.

Kamble A., Margutti R., Soderberg A. M., et al., 2015. Radio and X-rays From SN 2013df Enlighten Progenitors of Type IIb Supernovae. *ArXiv e-prints*.

Kankare E., Mattila S., Ryder S., et al., 2014. The nature of supernovae 2010O and 2010P in Arp 299 - I. Near-infrared and optical evolution. *MNRAS*, **440**, 1052–1066.

Kifonidis K., Plewa T., Janka H.-T., and Müller E., 2000. Nucleosynthesis and Clump Formation in a Core-Collapse Supernova. *ApJ*, **531**, L123–L126.

Kotak R. and Vink J. S., 2006. Luminous blue variables as the progenitors of supernovae with quasi-periodic radio modulations. *A&A*, **460**, L5–L8.

Krisciunas K., Suntzeff N. B., Candia P., et al., 2003. Optical and Infrared Photometry of the Nearby Type Ia Supernova 2001el. *AJ*, **125**, 166–180.

Kumar B., Pandey S. B., Sahu D. K., et al., 2013. Light curve and spectral evolution of the Type IIb supernova 2011fu. *MNRAS*, **431**, 308–321.

Landolt A. U., 1992. UBVRI photometric standard stars in the magnitude range 11.5-16.0 around the celestial equator. *AJ*, **104**, 340–371.

Leibundgut B. and Suntzeff N. B., 2003. Optical Light Curves of Supernovae. In K. Weiler, ed., *Supernovae and Gamma-Ray Bursters*, vol. 598 of *Lecture Notes in Physics, Berlin Springer Verlag*, 77–90.

Leonard D. C., Filippenko A. V., Barth A. J., and Matheson T., 2000. Evidence for Asphericity in the Type IIN Supernova SN 1998S. *ApJ*, **536**, 239–254.

Lewis J. R., Walton N. A., Meikle W. P. S., et al., 1994. Optical Observations of Supernova 1993J from La-Palma - Part One - Days 2 TO 125. *MNRAS*, **266**, L27.

Li K. L. and Kong A. K. H., 2013. X-ray detection of SN 2013df. *The Astronomer's Telegram*, **5150**, 1.

Li W., 2008. Further analysis of the possible progenitor of SN 2008ax in NGC 4490. *The Astronomer's Telegram*, **1433**, 1.

Li W., Leaman J., Chornock R., et al., 2011. Nearby supernova rates from the Lick Observatory Supernova Search - II. The observed luminosity functions and fractions of supernovae in a complete sample. *MNRAS*, **412**, 1441–1472.

Liu Y.-Q., Modjaz M., Bianco F. B., and Graur O., 2015. Analyzing the Largest Spectroscopic Dataset of Stripped Supernovae to Improve Their Identifications and Constrain Their Progenitors. *ArXiv e-prints*.

Maeda K., 2012. Injection and Acceleration of Electrons at a Strong Shock: Radio and X-Ray Study of Young Supernova 2011dh. *ApJ*, **758**, 81.

Maeda K., Hattori T., Milisavljevic D., et al., 2015. Type IIb Supernova 2013df Entering into an Interaction Phase: A Link between the Progenitor and the Mass Loss. *ApJ*, **807**, 35.

Maeda K., Katsuda S., Bamba A., Terada Y., and Fukazawa Y., 2014. Long-lasting X-Ray Emission from Type IIb Supernova 2011dh and Mass-loss History of the Yellow Supergiant Progenitor. *ApJ*, **785**, 95.

Maeda K., Nomoto K., Mazzali P. A., and Deng J., 2006. Nebular Spectra of SN 1998bw Revisited: Detailed Study by One- and Two-dimensional Models. *ApJ*, **640**, 854–877.

Margutti R., Milisavljevic D., Soderberg A. M., et al., 2014. A Panchromatic View of the Restless SN 2009ip Reveals the Explosive Ejection of a Massive Star Envelope. *ApJ*, **780**, 21.

Marion G. H., Vinko J., Kirshner R. P., et al., 2014. Type IIb Supernova SN 2011dh: Spectra and Photometry from the Ultraviolet to the Near-infrared. *ApJ*, **781**, 69.

Masters K. L., Mosleh M., Romer A. K., et al., 2010. Galaxy Zoo: passive red spirals. *MNRAS*, **405**, 783–799.

Matheson T., Filippenko A. V., Barth A. J., et al., 2000a. Optical Spectroscopy of Supernova 1993J During Its First 2500 Days. *AJ*, **120**, 1487–1498.

Matheson T., Filippenko A. V., Ho L. C., Barth A. J., and Leonard D. C., 2000b. Detailed Analysis of Early to Late-Time Spectra of Supernova 1993J. *AJ*, **120**, 1499–1515.

Matthews K., Neugebauer G., Armus L., and Soifer B. T., 2002. Early Near-Infrared Observations of SN 1993J. *AJ*, **123**, 753–759.

Mauerhan J. C., Smith N., Filippenko A. V., et al., 2013. The unprecedented 2012 outburst of SN 2009ip: a luminous blue variable star becomes a true supernova. *MNRAS*, **430**, 1801–1810.

Maund J. R., Arcavi I., Ergon M., et al., 2015. Did the progenitor of SN 2011dh have a binary companion? *MNRAS*, **454**, 2580–2585.

Maund J. R., Fraser M., Ergon M., et al., 2011. The Yellow Supergiant Progenitor of the Type II Supernova 2011dh in M51. *ApJ*, **739**, L37.

Maund J. R. and Smartt S. J., 2009. The Disappearance of the Progenitors of Supernovae 1993J and 2003gd. *Science*, **324**, 486–.

Maund J. R., Smartt S. J., Kudritzki R. P., Podsiadlowski P., and Gilmore G. F., 2004. The massive binary companion star to the progenitor of supernova 1993J. *Nature*, **427**, 129–131.

Maurer I., Mazzali P. A., Taubenberger S., and Hachinger S., 2010. Hydrogen and helium in the late phase of supernovae of Type IIb. *MNRAS*, **409**, 1441–1454.

Mazzali P. A., Deng J., Hamuy M., and Nomoto K., 2009. SN 2003bg: A Broad-Lined Type IIb Supernova with Hydrogen. *ApJ*, **703**, 1624–1634.

Milisavljevic D., Fesen R. A., Gerardy C. L., Kirshner R. P., and Challis P., 2010. Doublets and Double Peaks: Late-Time [O I] $\lambda\lambda$6300, 6364 Line Profiles of Stripped-Envelope, Core-Collapse Supernovae. *ApJ*, **709**, 1343–1355.

Milisavljevic D., Margutti R., Soderberg A. M., et al., 2013. Multi-wavelength Observations of Supernova 2011ei: Time-dependent Classification of Type IIb and Ib Supernovae and Implications for Their Progenitors. *ApJ*, **767**, 71.

Minkowski R., 1941. Spectra of Supernovae. *PASP*, **53**, 224.

Modjaz M., Blondin S., Kirshner R. P., et al., 2014. Optical Spectra of 73 Stripped-envelope Core-collapse Supernovae. *AJ*, **147**, 99.

Modjaz M., Kirshner R. P., Blondin S., Challis P., and Matheson T., 2008. Double-Peaked Oxygen Lines Are Not Rare in Nebular Spectra of Core-Collapse Supernovae. *ApJ*, **687**, L9–L12.

Morales-Garoffolo A., Elias-Rosa N., Benetti S., et al., 2014. SN 2013df, a double-peaked IIb supernova from a compact progenitor and an extended H envelope. *MNRAS*, **445**, 1647–1662.

Morales-Garoffolo A., Elias-Rosa N., Benitez-Herrera S., et al., 2013a. PESSTO spectroscopic classification of optical transients. *The Astronomer's Telegram*, **4795**, 1.

Morales-Garoffolo A., Elias-Rosa N., Benitez-Herrera S., et al., 2013b. PESSTO spectroscopic classification of optical transients. *The Astronomer's Telegram*, **4827**, 1.

Morales-Garoffolo A., Elias-Rosa N., Benitez-Herrera S., et al., 2013c. PESSTO spectroscopic classification of optical transients. *The Astronomer's Telegram*, **4767**, 1.

Morales-Garoffolo A., Elias-Rosa N., Bersten M., et al., 2015a. SN 2011fu: a type IIb supernova with a luminous double-peaked light curve. *MNRAS*, **454**, 95–114.

Morales-Garoffolo A., Elias-Rosa N., and Isern J., 2015b. Early to late spectroscopic and photometric analysis of the type IIb SN 2013df. In A. J. Cenarro, F. Figueras, C. Hernández-Monteagudo, J. Trujillo Bueno & L. Valdivielso, eds., *Highlights of Spanish Astrophysics VIII*, 518–523.

Morales-Garoffolo A., Hachinger S., Taubenberger S., et al., 2013d. PESSTO spectroscopic classification of optical transients. *The Astronomer's Telegram*, **4955**, 1.

Mould J. R., Huchra J. P., Freedman W. L., et al., 2000. The Hubble Space Telescope Key Project on the Extragalactic Distance Scale. XXVIII. Combining the Constraints on the Hubble Constant. *ApJ*, **529**, 786–794.

Munari U. and Zwitter T., 1997. Equivalent width of NA I and K I lines and reddening. *A&A*, **318**, 269–274.

Nakar E. and Piro A. L., 2014. Supernovae with Two Peaks in the Optical Light Curve and the Signature of Progenitors with Low-mass Extended Envelopes. *ApJ*, **788**, 193.

Nakar E. and Sari R., 2010. Early Supernovae Light Curves Following the Shock Breakout. *ApJ*, **725**, 904–921.

Navasardyan H., Benetti S., Harutyunyan A., et al., 2008. Supernova 2008bo in NGC 6643. *Central Bureau Electronic Telegrams*, **1325**, 1.

Nicholl M., Smartt S. J., Jerkstrand A., et al., 2013. Slowly fading super-luminous supernovae that are not pair-instability explosions. *Nature*, **502**, 346–349.

Nomoto K. and Hashimoto M., 1988. Presupernova evolution of massive stars. *Phys. Rep.*, **163**, 13–36.

Nomoto K., Suzuki T., Shigeyama T., Kumagai S., Yamaoka H., and Saio H., 1993. A type IIb model for supernova 1993J. *Nature*, **364**, 507–509.

Oates S. R., Bayless A. J., Stritzinger M. D., et al., 2012. Multiwavelength observations of the Type IIb supernova 2009mg. *MNRAS*, **424**, 1297–1306.

Oke J. B., 1990. Faint spectrophotometric standard stars. *AJ*, **99**, 1621–1631.

Pastorello A., Cappellaro E., Inserra C., et al., 2013. Interacting Supernovae and Supernova Impostors: SN 2009ip, is this the End? *ApJ*, **767**, 1.

Pastorello A., Kasliwal M. M., Crockett R. M., et al., 2008. The Type IIb SN 2008ax: spectral and light curve evolution. *MNRAS*, **389**, 955–966.

Pastorello A., Smartt S. J., Mattila S., et al., 2007. A giant outburst two years before the core-collapse of a massive star. *Nature*, **447**, 829–832.

Patat F., Chugai N., and Mazzali P. A., 1995. Late-time Hα emission from the hydrogen shell of SN 1993J. *A&A*, **299**, 715.

Pérez-Torres M. A., Alberdi A., Marcaide J. M., et al., 2005. High-resolution observations of SN 2001gd in NGC 5033. *MNRAS*, **360**, 1055–1062.

Pettini M. and Pagel B. E. J., 2004. [OIII]/[NII] as an abundance indicator at high redshift. *MNRAS*, **348**, L59–L63.

Pignata G., Patat F., Benetti S., et al., 2004. Photometric observations of the Type Ia SN 2002er in UGC 10743. *MNRAS*, **355**, 178–190.

Podsiadlowski P., Hsu J. J. L., Joss P. C., and Ross R. R., 1993. The progenitor of supernova 1993J - A stripped supergiant in a binary system? *Nature*, **364**, 509–511.

Podsiadlowski P., Joss P. C., and Hsu J. J. L., 1992. Presupernova evolution in massive interacting binaries. *ApJ*, **391**, 246–264.

Poznanski D., Prochaska J. X., and Bloom J. S., 2012. An empirical relation between sodium absorption and dust extinction. *MNRAS*, **426**, 1465–1474.

Pritchard T. A., Roming P. W. A., Brown P. J., Bayless A. J., and Frey L. H., 2014. Bolometric and UV Light Curves of Core-collapse Supernovae. *ApJ*, **787**, 157.

Qiu Y., Li W., Qiao Q., and Hu J., 1999. The Study of a Type IIB Supernova: SN 1996CB. *AJ*, **117**, 736–743.

Quimby R. M., Kulkarni S. R., Kasliwal M. M., et al., 2011. Hydrogen-poor superluminous stellar explosions. *Nature*, **474**, 487–489.

Rabinak I. and Waxman E., 2011. The Early UV/Optical Emission from Core-collapse Supernovae. *ApJ*, **728**, 63.

Richardson D., Branch D., and Baron E., 2006. Absolute Magnitude Distributions and Light Curves of Stripped-Envelope Supernovae. *AJ*, **131**, 2233–2244.

Richardson D., Jenkins, III R. L., Wright J., and Maddox L., 2014. Absolute-magnitude Distributions of Supernovae. *AJ*, **147**, 118.

Richmond M. W., Treffers R. R., Filippenko A. V., et al., 1994. UBVRI photometry of SN 1993J in M81: The first 120 days. *AJ*, **107**, 1022–1040.

Romero-Cañizales C., Herrero-Illana R., Pérez-Torres M. A., et al., 2014. The nature of supernovae 2010O and 2010P in Arp 299 - II. Radio emission. *MNRAS*, **440**, 1067–1079.

Roming P. W. A., Pritchard T. A., Brown P. J., et al., 2009. Multi-Wavelength Properties of the Type IIb SN 2008ax. *ApJ*, **704**, L118–L123.

Ryder S. D., Murrowood C. E., and Stathakis R. A., 2006. A post-mortem investigation of the Type IIb supernova 2001ig. *MNRAS*, **369**, L32–L36.

Ryder S. D., Sadler E. M., Subrahmanyan R., Weiler K. W., Panagia N., and Stockdale C., 2004. Modulations in the radio light curve of the Type IIb supernova 2001ig: evidence for a Wolf-Rayet binary progenitor? *MNRAS*, **349**, 1093–1100.

Sanders N. E., Soderberg A. M., Levesque E. M., et al., 2012. A Spectroscopic Study of Type Ibc Supernova Host Galaxies from Untargeted Surveys. *ApJ*, **758**, 132.

Schlafly E. F. and Finkbeiner D. P., 2011. Measuring Reddening with Sloan Digital Sky Survey Stellar Spectra and Recalibrating SFD. *ApJ*, **737**, 103.

Shigeyama T., Suzuki T., Kumagai S., Nomoto K., Saio H., and Yamaoka H., 1994. Theoretical light curves of Type IIb supernova 1993J. *ApJ*, **420**, 341–347.

Shivvers I., Mauerhan J. C., Leonard D. C., Filippenko A. V., and Fox O. D., 2014. Early Emission from the Type IIn Supernova 1998S at High Resolution. *ArXiv e-prints*.

Shivvers I., Mazzali P., Silverman J. M., et al., 2013. Nebular spectroscopy of the nearby Type IIb supernova 2011dh. *MNRAS*, **436**, 3614–3625.

Silverman J. M., Mazzali P., Chornock R., et al., 2009. Optical Spectroscopy of the Somewhat Peculiar Type IIb Supernova 2001ig. *PASP*, **121**, 689–698.

Skrutskie M. F., Cutri R. M., Stiening R., et al., 2006. The Two Micron All Sky Survey (2MASS). *AJ*, **131**, 1163–1183.

Smartt S. J., 2015. Observational Constraints on the Progenitors of Core-Collapse Supernovae: The Case for Missing High-Mass Stars. *PASA*, **32**, 16.

Smartt S. J., Valenti S., Fraser M., et al., 2015. PESSTO: survey description and products from the first data release by the Public ESO Spectroscopic Survey of Transient Objects. *A&A*, **579**, A40.

Smith J. A., Tucker D. L., Kent S., et al., 2002. The u'g'r'i'z' Standard-Star System. *AJ*, **123**, 2121–2144.

Smith N., Li W., Silverman J. M., Ganeshalingam M., and Filippenko A. V., 2011. Luminous blue variable eruptions and related transients: diversity of progenitors and outburst properties. *MNRAS*, **415**, 773–810.

Smith N., Mauerhan J. C., Cenko S. B., et al., 2015. PTF11iqb: cool supergiant mass-loss that bridges the gap between Type IIn and normal supernovae. *MNRAS*, **449**, 1876–1896.

Soderberg A. M., Berger E., Page K. L., et al., 2008. An extremely luminous X-ray outburst at the birth of a supernova. *Nature*, **453**, 469–474.

Soderberg A. M., Chevalier R. A., Kulkarni S. R., and Frail D. A., 2006. The Radio and X-Ray Luminous SN 2003bg and the Circumstellar Density Variations around Radio Supernovae. *ApJ*, **651**, 1005–1018.

Spyromilio J., 1991. Supernova 1988A - Another clumped supernova. *MNRAS*, **253**, 25P–28P.

Sramek R. A. and Weiler K. W., 2003. Radio Supernovae. In K. Weiler, ed., *Supernovae and Gamma-Ray Bursters*, vol. 598 of *Lecture Notes in Physics, Berlin Springer Verlag*, 145–169.

Sternberg A., El-Hage P., Elias-Rosa N., et al., 2012a. PESSTO spectroscopic classification of optical transients. *The Astronomer's Telegram*, **4493**, 1.

Sternberg A., El-Hage P., Elias-Rosa N., et al., 2012b. PESSTO spectroscopic classification of optical transients. *The Astronomer's Telegram*, **4504**, 1.

Stockdale C. J., Weiler K. W., Immler S., et al., 2008. Supernova 2008bo in NGC 6643. *IAU Circ.*, **8939**, 2.

Stockdale C. J., Williams C. L., Weiler K. W., et al., 2007. The Radio Evolution of SN 2001gd. *ApJ*, **671**, 689–694.

Stritzinger M., Hamuy M., Suntzeff N. B., et al., 2002. Optical Photometry of the Type Ia Supernova 1999ee and the Type Ib/c Supernova 1999ex in IC 5179. *AJ*, **124**, 2100–2117.

Stritzinger M., Taddia F., Fransson C., et al., 2012. Multi-wavelength Observations of the Enduring Type IIn Supernovae 2005ip and 2006jd. *ApJ*, **756**, 173.

Strotjohann N. L., Ofek E. O., Gal-Yam A., et al., 2015. Search for Precursor Eruptions among Type IIb Supernovae. *ApJ*, **811**, 117.

Sugimoto D. and Nomoto K., 1980. Presupernova models and supernovae. *Space Sci. Rev.*, **25**, 155–227.

Sutherland P. G. and Wheeler J. C., 1984. Models for Type I supernovae - Partially incinerated white dwarfs. *ApJ*, **280**, 282–297.

Taddia F., Stritzinger M. D., Sollerman J., et al., 2012. The Type II supernovae 2006V and 2006au: two SN 1987A-like events. *A&A*, **537**, A140.

Tartaglia L., Elias-Rosa N., Morales-Garoffolo A., et al., 2014a. PESSTO spectroscopic classification of optical transients. *The Astronomer's Telegram*, **6400**, 1.

Tartaglia L., Elias-Rosa N., Morales-Garoffolo A., et al., 2014b. PESSTO spectroscopic classification of optical transients. *The Astronomer's Telegram*, **6403**, 1.

Taubenberger S., Hachinger S., Morales-Garoffolo A., et al., 2013. PESSTO spectroscopic classification of optical transients. *The Astronomer's Telegram*, **4952**, 1.

Taubenberger S., Navasardyan H., Maurer J. I., et al., 2011. The He-rich stripped-envelope core-collapse supernova 2008ax. *MNRAS*, **413**, 2140–2156.

Taubenberger S., Valenti S., Benetti S., et al., 2009. Nebular emission-line profiles of Type Ib/c supernovae - probing the ejecta asphericity. *MNRAS*, **397**, 677–694.

Tomasella L., Benetti S., Cappellaro E., et al., 2014. Asiago Supernova classification program: Blowing out the first two hundred candles. *Astronomische Nachrichten*, **335**, 841.

Tomasella L., Valenti S., Ochner P., Benetti S., Cappellaro E., and Pastorello A., 2011. Supernova 2011fu in UGC 1626 = PSN J02082141+4129123. *Central Bureau Electronic Telegrams*, **2827**, 2.

Tsvetkov D. Y., Volkov I. M., Baklanov P., Blinnikov S., and Tuchin O., 2009. Photometric Observations and Modeling of Type IIb Supernova 2008ax. *Peremennye Zvezdy*, **29**, 2.

Turatto M., 2003. Classification of Supernovae. In K. Weiler, ed., *Supernovae and Gamma-Ray Bursters*, vol. 598 of *Lecture Notes in Physics, Berlin Springer Verlag*, 21–36.

Turatto M., Benetti S., and Cappellaro E., 2003. Variety in Supernovae. In W. Hillebrandt & B. Leibundgut, eds., *From Twilight to Highlight: The Physics of Supernovae*, 200.

Turatto M., Mazzali P. A., Young T. R., et al., 1998. The Peculiar Type II Supernova 1997D: A Case for a Very Low ^{56}Ni Mass. *ApJ*, **498**, L129–L133.

Udalski A., Szymański M. K., and Szymański G., 2015. OGLE-IV: Fourth Phase of the Optical Gravitational Lensing Experiment. *Acta Astron.*, **65**, 1–38.

Valenti S., Benetti S., Cappellaro E., et al., 2008. The broad-lined Type Ic supernova 2003jd. *MNRAS*, **383**, 1485–1500.

Valenti S., Pastorello A., Cappellaro E., et al., 2009. A low-energy core-collapse supernova without a hydrogen envelope. *Nature*, **459**, 674–677.

Van Dyk S. D., Li W., Cenko S. B., et al., 2011. The Progenitor of Supernova 2011dh/PTF11eon in Messier 51. *ApJ*, **741**, L28.

Van Dyk S. D., Peng C. Y., King J. Y., et al., 2000. SN 1997bs in M66: Another Extragalactic η Carinae Analog? *PASP*, **112**, 1532–1541.

Van Dyk S. D., Sramek R. A., Montes M. J., Weiler K. W., and Panagia N., 1996. Supernova 1996cb in NGC 3510. *IAU Circ.*, **6528**, 1.

Van Dyk S. D., Zheng W., Clubb K. I., et al., 2013. The Progenitor of Supernova 2011dh has Vanished. *ApJ*, **772**, L32.

Van Dyk S. D., Zheng W., Fox O. D., et al., 2014. The Type IIb Supernova 2013df and its Cool Supergiant Progenitor. *AJ*, **147**, 37.

Weiler K. W., Panagia N., Montes M. J., and Sramek R. A., 2002. Radio Emission from Supernovae and Gamma-Ray Bursters. *ARA&A*, **40**, 387–438.

Weiler K. W., Williams C. L., Panagia N., et al., 2007. Long-Term Radio Monitoring of SN 1993J. *ApJ*, **671**, 1959–1980.

Wheeler J. C. and Harkness R. P., 1990. Type I supernovae. *Reports on Progress in Physics*, **53**, 1467–1557.

Woosley S. E., Eastman R. G., Weaver T. A., and Pinto P. A., 1994. SN 1993J: A Type IIb supernova. *ApJ*, **429**, 300–318.

Woosley S. E. and Heger A., 2007. Nucleosynthesis and remnants in massive stars of solar metallicity. *Phys. Rep.*, **442**, 269–283.

Wright E. L., 2006. A Cosmology Calculator for the World Wide Web. *PASP*, **118**, 1711–1715.

Wyrzykowski Ł., Kostrzewa-Rutkowska Z., Kozłowski S., et al., 2014. OGLE-IV Real-Time Transient Search. *Acta Astron.*, **64**, 197–232.

Wyrzykowski L., Udalski A., Kozlowski S., and Skowron J., 2013. OGLE-IV Transient Search report 22 October 2013. *The Astronomer's Telegram*, **5497**, 1.

Yaron O. and Gal-Yam A., 2012. WISeREP - An Interactive Supernova Data Repository. *PASP*, **124**, 668–681.

Young T. R., Baron E., and Branch D., 1995. Light Curve Studies of SN 1993J and SN 1994I. *ApJ*, **449**, L51.

Zimmermann H.-U. and Aschenbach B., 2003. XMM-Newton observation of SN 1993J in M 81. *A&A*, **406**, 969–974.

Zwicky F., 1964. NGC 1058 and its Supernova 1961. *ApJ*, **139**, 514.